PITTING CORROSION BEHAVIOR OF LEAN DUPLEX STAINLESS STEELS IN CHLORIDE AND THIOSULFATE CONTAINING ENVIRONMENTS

A Dissertation
Presented to
The Academic Faculty

By

Liang He

In Partial Fulfillment
Of the Requirements for the Degree
Doctor of Philosophy in Materials Science and Engineering

Georgia Institute of Technology

May, 2019

PITTING CORROSION BEHAVIOR OF LEAN DUPLEX STAINLESS STEELS IN CHLORIDE AND THIOSULFATE CONTAINING ENVIRONMENTS

Approved by:

Dr. Preet M. Singh, Advisor
School of Materials Science and Engineering
Georgia Institute of Technology

Dr. Hamid Garmestani
School of Materials Science and Engineering
Georgia Institute of Technology

Dr. Arun Gokhale
School of Materials Science and Engineering
Georgia Institute of Technology

Dr. Matthew McDowell
The George W. Woodruff School of Mechanical Engineering
School of Materials Science and Engineering
Georgia Institute of Technology

Dr. Faisal Alamgir
School of Materials Science and Engineering
Georgia Institute of Technology

Date Approved: February 19, 2019

ACKNOWLEDGEMENTS

The past five years at Georgia Tech has been a wonderful journey to me, which is beyond my imagination when I first came here. I cannot express enough gratitude to my advisor, Dr. Preet Singh, for his patient and inspiring guidance, knowledgeable advice and all the help during my phd study. I would also like to thank my committee members Dr. Faisal Alamgir, Dr. Hamid Garmestani, Dr. Arun M. Gokhale, and Dr. Matthew McDowell for their valuable guidance for this study. I would also like to thank my corrosion group members for their support and Mr. Jamshad Mahmood for his help in the laboratory.

This research was supported by the PSE fellowship from Renewable Bioproducts Institute at Georgia Institute of Technology.

Last but not least, I would also thank my whole family, especially my parents, Mr. Xing He and Mrs. Jing Chang, for their unconditional love and faith in me ever since I was young. I want to thank my husband, Mr. Zhaoxuan Zhang, who has always been there for me.

TABLE OF CONTENTS

LIST OF TABLES

LIST OF FIGURES

SUMMARY

A number of chemical process industry streams contain chlorides along with thiosulfate or sulfate ions. These industries include pulp and paper industry, mineral process industry, textile industry, and nuclear industry. Focus of this study is white water environment in paper machines, which is a neutral to acidic environment that mainly contains chloride, thiosulfate and sulfate ions. Surfaces of paper machine equipment, like drying or pressing rolls, are very smooth. Any surface imperfection on the surface due to corrosion can potentially cause problems with the paper making process. Because of the occurrence of problems like pitting corrosion, crevice corrosion and stress corrosion cracking, pulp and paper industry tends to select austenitic stainless steels and duplex stainless steels (DSSs) as construction materials for paper machine.

Duplex stainless steels (DSSs) are dual-phase Cr-Mo-Ni-Fe steels systems that possess both high mechanical strength and high corrosion resistance. The most common grade is the standard DSS 2205 that possesses the yield strength twice as that of austenitic stainless steels and superior corrosion resistance than 304L and 316L austenitic stainless steels. Compared to standard DSSs like DSS 2205, lean DSSs (LDSSs) such as UNS S32101 and UNS S32003 have lower Cr and Ni content, but have a pitting resistance equivalent or better than 316L austenitic stainless steels. Due to lower amount of alloying elements, especially nickel content, they can be more cost-effective than the standard DSSs as well as austenitic stainless steels in less aggressive environments such as paper machine white water. However, as newly developed grades, their corrosion behavior has not been widely investigated.

Among different corrosion problems, pitting corrosion is a very important issue since it is an autocatalytic process and is particularly dangerous once its growth is stable and it penetrates the thickness of the materials. In addition, corrosion pits are often the initiation sites for stress corrosion cracking. The small size of pits makes it even more difficult during regular equipment inspection. During the past few decades, pitting corrosion of austenitic stainless steels in environments containing chloride, thiosulfate, nitrate anions and other anions has been studied extensively. Because of the dual-phase microstructure of DSSs, pit initiation and pit growth mechanisms of pitting corrosion of DSSs are more complicated. Preferential dissolution of ferrite phase within pits has been observed in near-neutral thiosulfate -containing chloride solution and alkaline carbonated chloride solution. Pit initiation sites could also be altered due to the microstructure evolution of DSSs during heat-treatment like annealing and aging.

In this research, pitting corrosion behavior of LDSSs is studied in near-neutral environments that contain chloride, thiosulfate and sulfate. Effects of annealing and aging heat-treatment on the microstructure evolution, passive film properties and pitting corrosion are studied. Effects of chloride and thiosulfate concentrations on the stable pitting events, metastable pitting and repassivation behavior are studied. To study the mechanisms of pitting corrosion of DSSs in terms of pit initiation, pit propagation and any galvanic interactions between the two phases, the single-phase microstructures are selectively isolated and their passive film properties, active dissolution and the galvanic corrosion in the simulated pit solution are studied. The comparison between different grades of LDSSs in simulated white water has provided insights into invention and cost-effective selection of materials for paper machines or other chemical process industry with similar

environments. The study on the effects of annealing and aging processes has provided information on the effect of different heat-treatment procedures on the corrosion behavior of LDSSs. The study on the properties of ferrite and austenite single phase and the coupling effects of the two phases in both simulated white water and simulated pit solution also provided insights into the pitting corrosion mechanisms of LDSSs and has furthered our understanding of the phenomena of pitting corrosion in LDSSs.

CHAPTER 1. INTRODUCTION

1.1. Research Motivation

Duplex stainless steels (DSSs) are Fe-Cr-Ni steels systems that possess the dual-phase microstructure. The volume fraction of the ferrite phase and the austenite phase are roughly 50:50 to maintain the optimum performance of DSSs. The combination of the two phases gives the DSSs both high mechanical strength and excellent corrosion and stress corrosion cracking resistance compared with austenitic and ferritic stainless steels. Cr and Mo are ferrite stabilizers while Ni and N are austenite stabilizers and lower Ni content in the DSSs also makes their price more stable. Because of these features, DSSs have become cost-effective materials after the advancement in the production, fabrication, and welding techniques during the last several decades. The most common grade is the standard DSS 2205 that possesses the yield strength twice as that of austenitic stainless steels and superior corrosion resistance than 304 and 316 austenitic stainless steels. However, in less aggressive environments DSS 2205 is not the most cost-effective option, leading to the development of lean duplex stainless steels (LDSSs) that have lower content of alloying elements such as Cr and Ni. LDSSs now have applications in storage tanks, water heaters and in the pulp and paper industry.

Paper machine is the section of the paper mill where pulp is fed and formed into paper through forming, pressing and drying sections. Paper machine white water is neutral to acidic environment that mainly contains chloride, thiosulfate and sulfate anions. Chloride comes into the white water from wood feed, water and chemicals during the

processing of pulp and can cause localized corrosion. In paper mills that use hydrosulfite as the brightening agent, thiosulfate is produced during storage, especially when the solution is acidic.[1] Although the paper machine white water environment is considered less aggressive, corrosion problems such as pitting corrosion, crevice corrosion and stress corrosion cracking are observed in the paper machine materials. Because of these problems, pulp and paper industry tends to select austenitic stainless steels or DSSs as the construction materials for paper machine. A lot of research has focused on the corrosion behavior of austenitic stainless steels, but the mechanism of localized corrosion of DSSs is a less investigated issue, which becomes important as DSSs are being selected for a variety of applications in pulp and paper industry. This research focuses on the localized corrosion behavior of newly developed lean or low-alloyed DSSs grades such as UNS S32101, S32003, S32304 and S82441. The nominal composition of some grades of LDSSs, DSS 2205 and austenitic stainless steels 304L and 316L are shown in Table 1.1.

Table 1.1 Nominal composition of lower alloyed LDSSs, standard DSS 2205 and austenitic stainless steels 304L and 316L.

UNS number	S32101	S32304	S32003	S82441	S31803	S30403	S31603
Common name	2101	2304	2003	2404	2205	304L	316L
Cr (wt%)	21.3	22.9	21.7	24.0	22.6	18.0-20.0	16.0-18.0
Ni (wt%)	1.51	4.2	4.0	3.6	5.78	8.0-12.0	10.0-14.0
Mo (wt%)	0.3	0.24	1.64	1.6	3.07	-	2.0-3.0
Mn (wt%)	5.0	1.25	1.72	3.0	1.53	≤2.0	≤2.0
Cu (wt%)	0.31	0.24	0.17	-	0.36	-	-
C (wt%)	0.025	0.021	0.015	0.020	0.021	≤0.03	≤0.03
P (wt%)	0.017	0.027	0.025	-	0.028	≤0.045	≤0.045
S (wt%)	≤0.001	≤0.001	≤0.001	-	≤0.005	≤0.03	≤0.03
N (wt%)	0.25	0.13	0.17	0.27	-	≤0.10	≤0.10
Si (wt%)	0.69	0.37	0.32	-	0.48	≤0.75	≤0.75

1.2. Problem definition

Pitting corrosion is a type of localized corrosion where surface pits develop in stainless steels and other alloys due to local anodic dissolution of the alloy after the local breakdown of the passive film. Pitting corrosion is dangerous in that it can cause leaks in pipes and vessels if the pits penetrate the thickness of the construction materials. It can also cause surface imperfections on smooth surface, which may be a problem for some applications like paper-machine rolls. It is also often the precursor for the nucleation of fatigue or stress corrosion cracks. One example of pitting corrosion is shown in Figure 1.1

and pits are observed to form on 304L stainless steels in 10 ppm $S_2O_3^{2-}$ solution.[2] The difficulties in detecting pits because of their small size, and sometimes due to the presence of the pit cover, increase the detrimental effects of pitting corrosion. Thus the evaluation of pitting corrosion behavior of new materials in certain service environment and the investigation of mechanisms of pitting is of great significance. For stainless steels that form a protective passive film on the surface, localized corrosion such as pitting and crevice corrosion are major corrosion problems because of the local breakdown of the passive film.

The process of pitting corrosion involves pit initiation, pit growth, and sometimes repassivation in the case of metastable pitting. After the passive film on the stainless steels breaks down and aggressive anions like Cl^- migrate into the cavity/crevice created, the first step is the active dissolution of metals, followed by the hydrolysis of the metal ions. This hydrolysis reaction leads to the acidification of the pit solution, the pH of which can be much lower than the bulk solution. With the accumulation of metal ions in the pit solution, the saturation point or solubility limit can be reached and a salt film can form at the bottom of pits, which acts as a diffusion layer and is necessary to sustain the development of pits after the pit-cover is removed during pit propagation. Because of the partitioning of elements into ferrite phase and austenite phase of a duplex stainless steel, the electrochemical activity of the two phases are different, which can lead to the galvanic corrosion between the two phases in the pit solution and the corrosion rate of one phase may be promoted by the presence of the other phase. In addition, the complexity of microstructure can also change pit propagation rate and pit geometry. The active dissolution of one phase can be stopped when the edge of pits encounters the other phase which is more resistant. Because of this, both the orientation and the coarseness of ferrite

phase and austenite phase can affect the growth rate and size of stable pitting and metastable pitting, making pitting corrosion of DSSs a more complex problem than that for austenitic stainless steels.

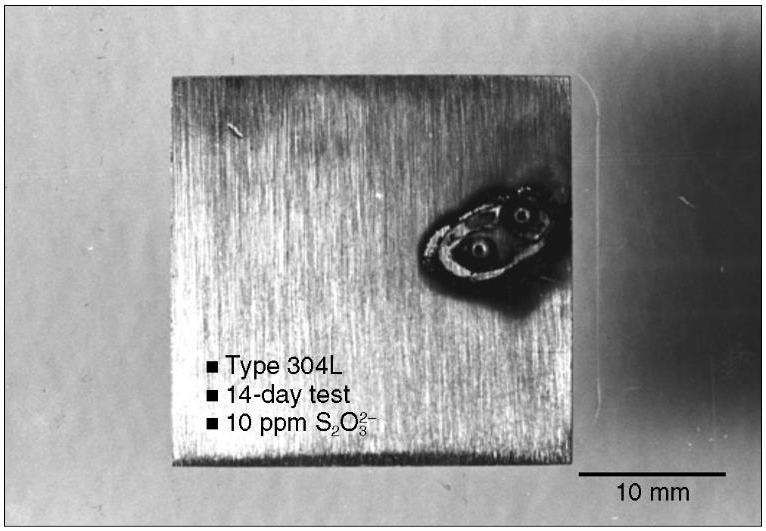

Figure 1.1 Pitting corrosion of stainless steels. 304L stainless steels in 10 ppm $S_2O_3^{2-}$ solution. [2]

1.3. Research Objectives

The objectives of this research are:

(1) To study the effects of chloride and thiosulfate ions on the stable pitting behavior and the repassivation behavior of LDSSs.

(2) To study the thermodynamics and kinetics of phase transformation, i.e. annealing and aging of LDSSs and their effects on the evolution of microstructure and pitting corrosion behavior.

(3) To study the pitting corrosion behavior and passive film properties of individual constituent phases of LDSSs in chloride and thiosulfate-containing environments including repassivation kinetics and defect concentrations.

(4) To develop an understanding of mechanisms of pitting corrosion behavior of LDSSs in chloride and thiosulfate- containing environment.

Literature review and background information related to this research are given in Chapter 2. Experimental procedures and technical approaches employed are introduced in Chapter 3. Effects of thiosulfate on the pitting corrosion behavior of different grades of lean duplex stainless steels are discussed in Chapter 4. Effects of annealing treatment on the microstructure and pitting corrosion behavior of UNS S32003 are studied in Chapter 5. In Chapter 6, effects of isothermal aging on the microstructural evolution as well as pitting corrosion of UNS S32003 are discussed. In Chapter 7, single ferrite phase and single austenite phase are isolated from the bulk UNS S32304 materials and their pitting corrosion resistance are compared using scratch test method. Galvanic corrosion between the ferrite phase and the austenite phase in simulated pit solution is also studied in this chapter. Chapter 8 gives recommendations on materials selection, processing and environment control to mitigate the pitting corrosion based on the results from this study and recommendations of future work related to this topic.

CHAPTER 2. BACKGROUND AND LITERATURE REVIEW

2.1. Duplex stainless steels

Duplex stainless steels are alloys that contain both ferrite phase and austenite phase in the microstructure with an optimum volume ratio of 50:50. The microstructure of duplex stainless steels is shown in Figure 2.1 and can be seen as the austenite island embedded in the ferrite phase matrix. The ferrite phase (α) appears darker while the austenite phase (γ) appears lighter in the SEM image. The ferrite phase has body centered cubic (BCC) crystal structure, while the austenite phase has a face centered cubic (FCC) crystal structure.

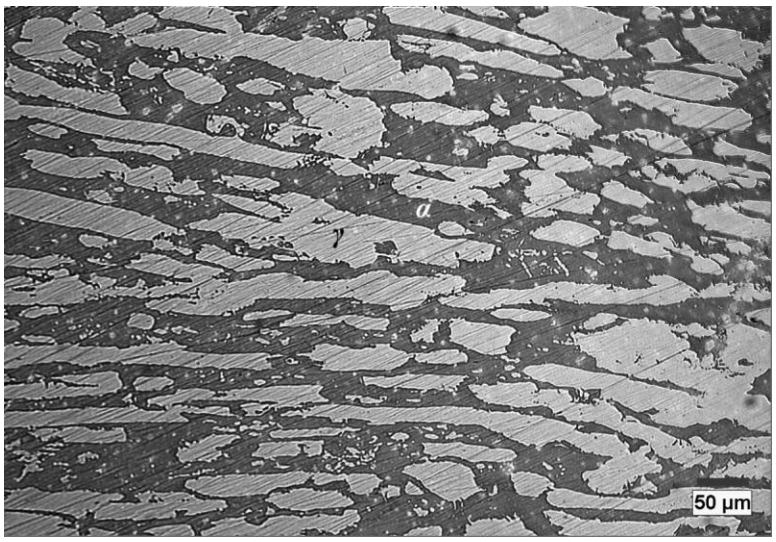

Figure 2.1 Microstructure of duplex stainless steels UNS S32003 in the transverse direction.

Compared with austenitic stainless steels, duplex stainless steels have lower Ni content, making the materials more cost-effective. The Ni content is compensated by N

and Mn to stabilize the austenite phase. The phases in the Fe-Cr-Ni alloys could be predicted from the Schaeffier diagram, as shown in Figure 2.2, where the x-axis represents the Cr equivalent while the y-axis is the Ni equivalent, calculated from Equation (1) and (2). [3] Elements in the Ni equivalent are the austenite stabilizers and those in the Cr equivalent are the ferrite stabilizers. The chemical composition of DSSs lies within the (γ+δ) region and where the γ: δ is 50: 50.

$$Ni\ equivalent = Ni + Co + 0.5Mn + 0.3Cu + 25N + 30C \quad (1)$$

$$Cr\ equivalent = Cr + 2Si + 1.5Mo + 5V + 5.5Al + 1.75Nb + 1.5Ti + 0.75W \quad (2)$$

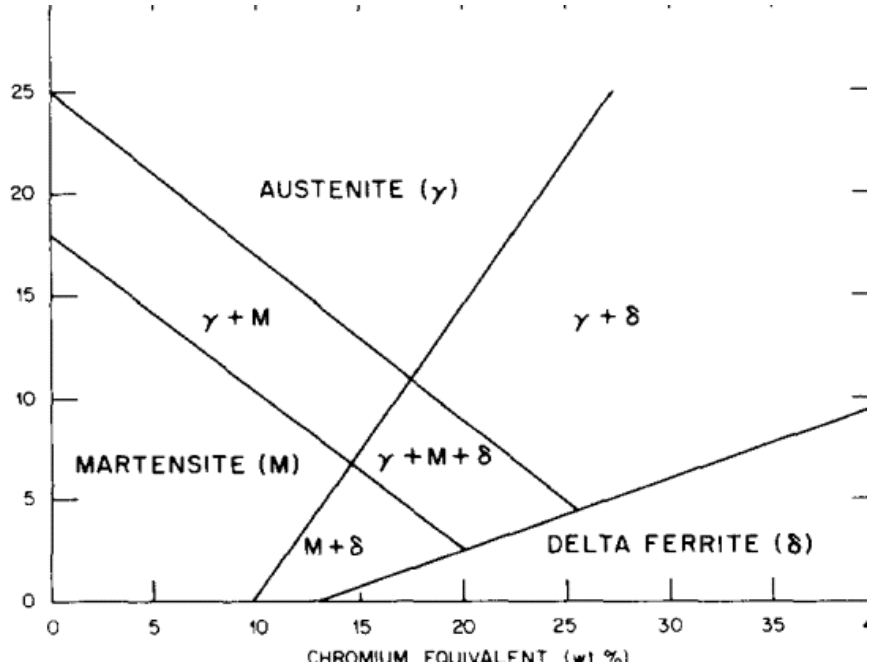

Figure 2.2 The Schaeffier diagram. [3]

The ferrite phase has high tensile strength and fatigue strength and the austenite phase provides good formability and high toughness. The combination of the two phases gives the DSSs both high mechanical strength and excellent corrosion and stress corrosion

cracking resistance compared with austenitic and ferritic stainless steels. Because of these features, DSSs have become cost-effective materials after the advancement in the production and fabrication techniques during the last several decades. Although the concept of duplex stainless steels was first introduced in the 1920s, the UNS S31803 (commonly referred to as DSS 2205) was the first widely used grade in 1970s. [4] DSS 2205 possesses the yield strength twice as that of austenitic stainless steels and superior corrosion resistance than 304 and 316 austenitic stainless steels. Nowadays, duplex stainless steels can be categorized into four different types, namely, lean, standard, super and hyper duplex stainless steels. They have applications in various industries including the pulp and paper industry, oil and gas industry, for storage tanks and as structure materials.

2.2.Properties of passive film on stainless steels

2.2.1. Passivation and passive film of metals

Compared with a metal in the active state, the passivated metal has a passive layer on the surface, which decreases the corrosion rate of the metal significantly. This passive layer is called passive film and is an oxide or oxyhydroxide layer with a thickness of several nanometers. Figure 2.3 shows the typical change in the anodic current density of a passivating metal and it can be divided into three regions, namely, the active region, the passive region and the transpassive region. In the active region, metals dissolve through the reaction:

$$M \rightarrow M_{(aq)}^{n+} + ne^{-} \quad (3)$$

As the potential reaches primary passivation potential (E_p or E_{pp}), anodic current density decreases markedly from critical current density (i_a) to passive current density (i_{pp}) by several orders of magnitude because of the formation of passive film. Transpassive potential (E_b) marks the end of passive behavior and the current density increases drastically because of one of the reactions described as follows. First, a component in the electrolyte oxidizes such as oxygen evolution:

$$2H_2O \rightarrow O_2 + 4H^+ + 4e^- \tag{4}$$

Second, a multivalent metal oxidizes to a higher oxidation state to form a soluble product. For example, for Cr, above transpassivation potential, the protective Cr_2O_3 (oxide) or $Cr(OH)_3$ (hydroxide) oxidizes to soluble CrO_3, which forms H_2CrO_4 (at pH lower than ~1), $HCrO_4^-$ (acidic environment) or CrO_4^{2-} (in alkaline environment) depending on the pH of the environment. The sudden increase in the current density could also be due to localized corrosion where there is local breakdown of the passive film, which will be discussed later.

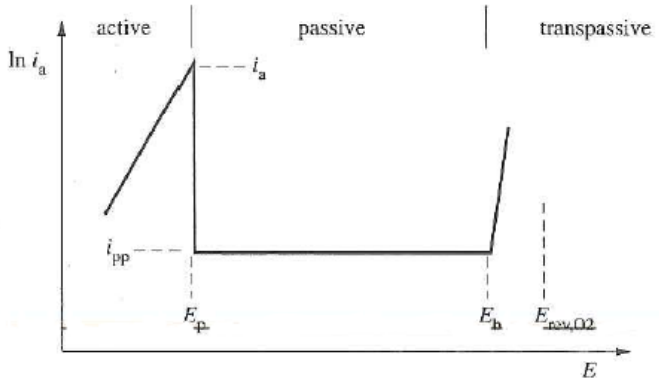

Figure 2.3 Partial anodic activity showing active to passive and transpassive transitions. [5]

Figure 2.4 shows the anodic polarization curves of Fe, Ni and Cr in sulfuric acid at 25 °C. [6] Cr has lower passivation potential as well as passive current density compared with that of both Ni and Fe. Thus, the addition of Cr to the alloy system helps with the formation of a Cr-enriched passive film and above a concentration of 12 wt% of Cr the corrosion resistance of alloys is significantly improved. [5] Typical oxidation states of elements in the passive film are the same with the most stable oxides, for example, Cr^{3+}, Ni^{2+}, Fe^{3+} and Al^{3+}. However, the situation for Fe is more complex and the oxidation state is a mixture of Fe^{2+} and Fe^{3+}.

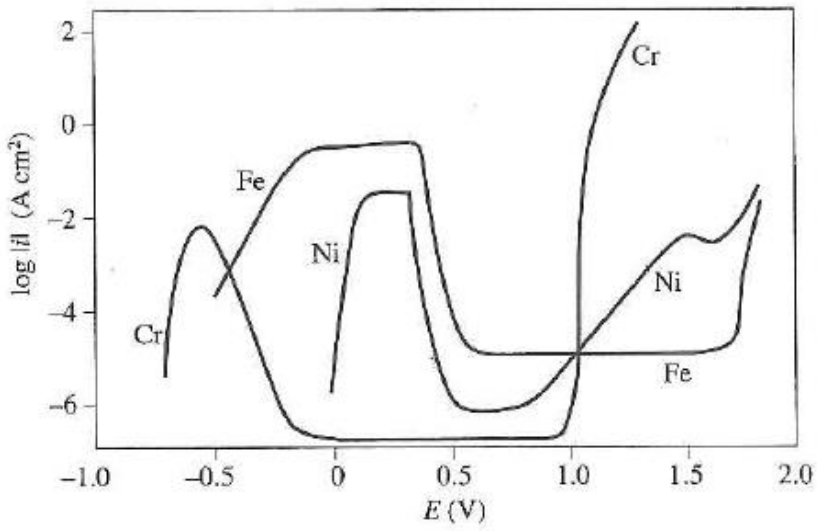

Figure 2.4 Polarization curves in 0.5 M H_2SO_4 of Fe, Ni and Cr. [6]

2.2.2. Passive film on stainless steels

The passive film on the stainless steels is enriched in Fe and Cr. The thickness is typically several nanometers. Properties of the passive film such as the thickness and the

chemical composition depend on a lot of factors, including passivation potential, passivation time, pH and temperature of the environment, as well as the composition of the solution. The thickness of the passive film increased with the applied potential as well as the environment temperature, as shown in Figure 2.5, where the film thickness was the highest when 304L stainless steel was polarized at 0.8 V_{SCE} in borate/boric acid solution at 70 °C. [7] At higher applied potential, the percentage of Fe^{2+} decreased while that of Fe^{3+} increased. [7] At high temperatures, although the passive film thickens, the passive potential range is decreased and the corrosion rate is higher, indicating a reduction in the passive film protectiveness. Because of the high solubility of iron oxide in acid, the outer layer of the passive film is enriched in Cr when exposed to acidic environment, while a higher Fe content is present in the outer layer of the passive film when formed in alkaline solution, which can be observed in Figure 2.6.

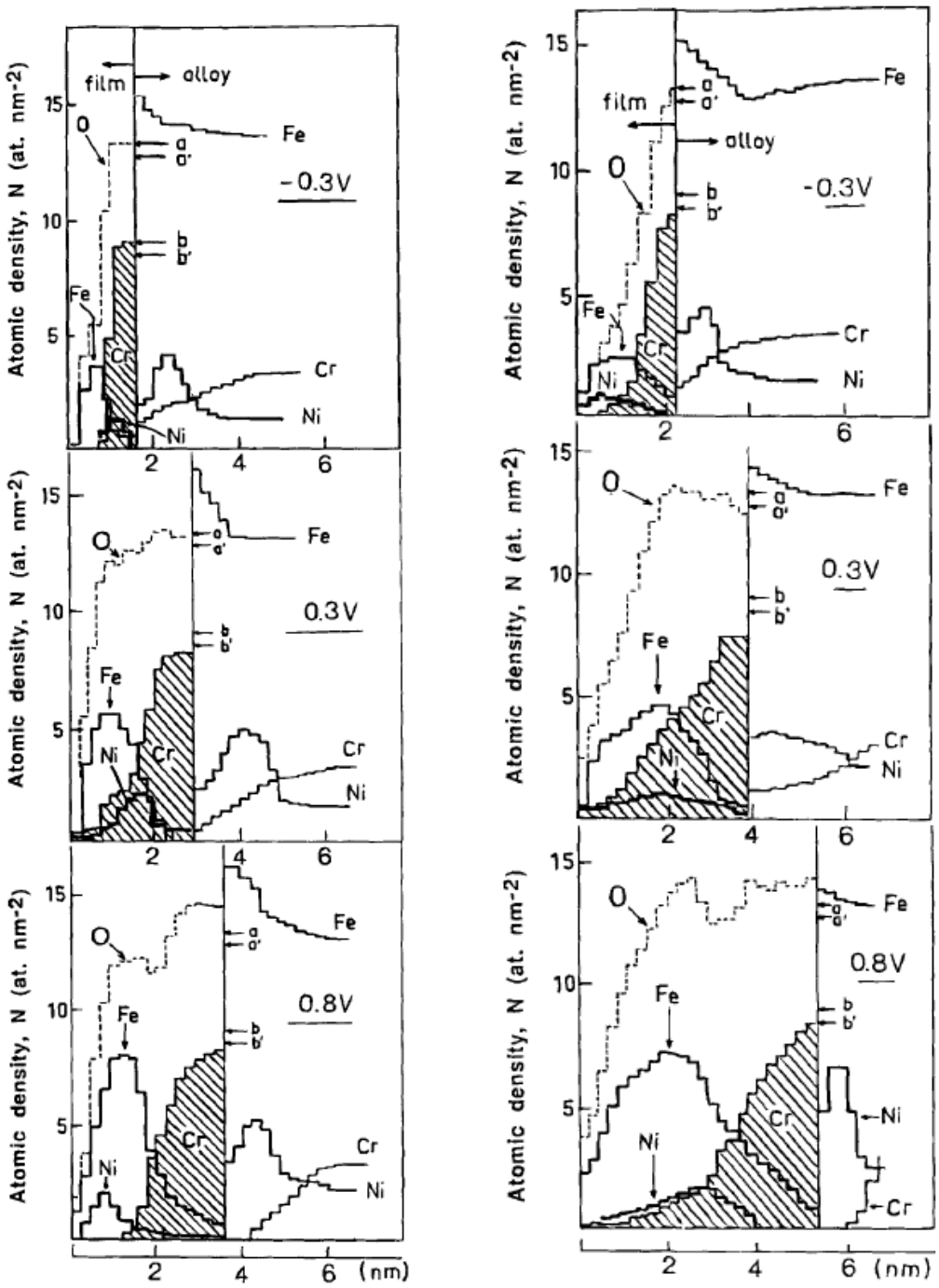

(a) (b)

Figure 2.5 Auger depth profiles for films formed on stainless steel AISI 304 in borate/boric acid solution for 2 hours at (a) 23 °C and (b) 70 °C.[7]

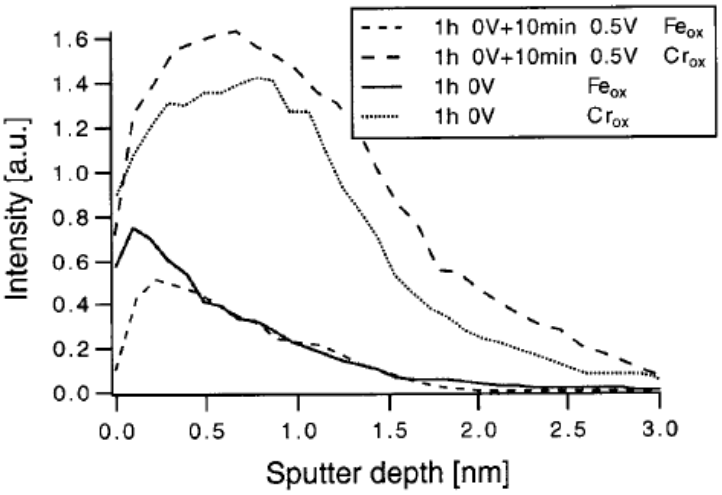

(a)

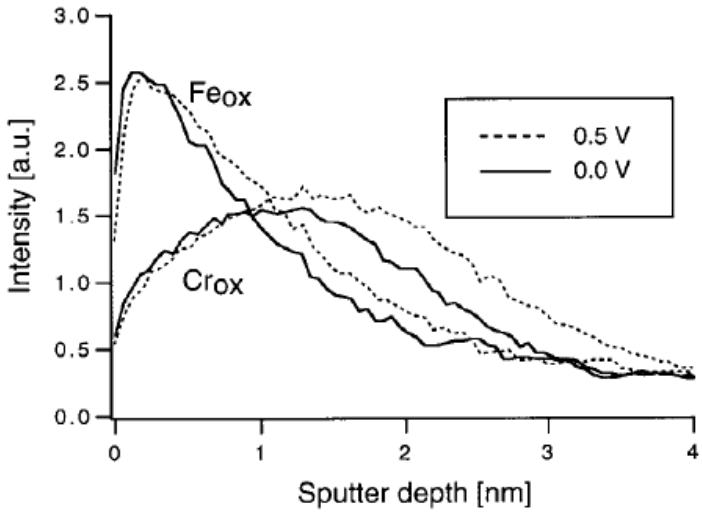

(b)

Figure 2.6 XPS depth profiles of film formed on Fe-25Cr alloy in (a) 0.1M H_2SO_4 + 0.4M Na_2SO_4 solution; (b) 0.1M NaOH solution. [8]

2.2.3. Repassivation of film

Breakdown of passive film can occur chemically in environments that contain aggressive ions such as chloride or through mechanical damage. The bare metal/alloy surface could repair the passive film during the repassivation process. Fast repassivation kinetics can minimize the probability of stable pit formation and other types of localized corrosion. Repassivation is an important process to corrosion problems such as pitting corrosion and stress corrosion cracking.

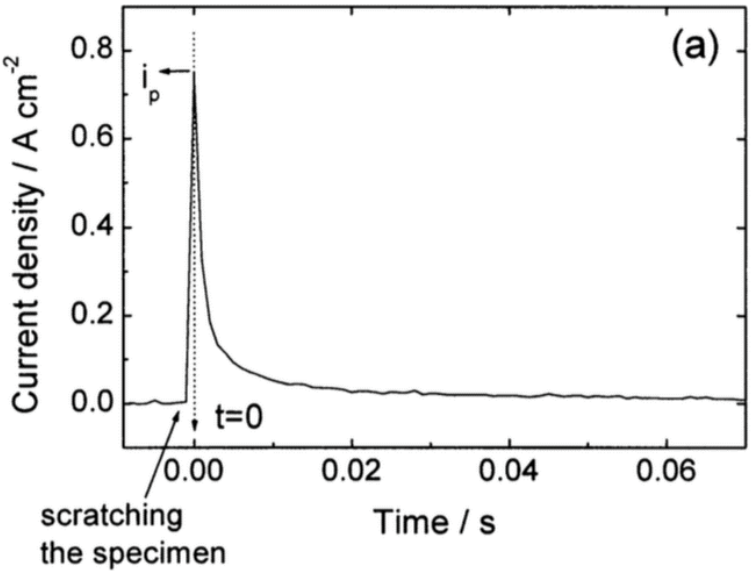

(a)

Figure 2.7 Current observations during scratch tests. (a) i(t) vs. t plot. (b) log i(t) vs. log t plot. [9]

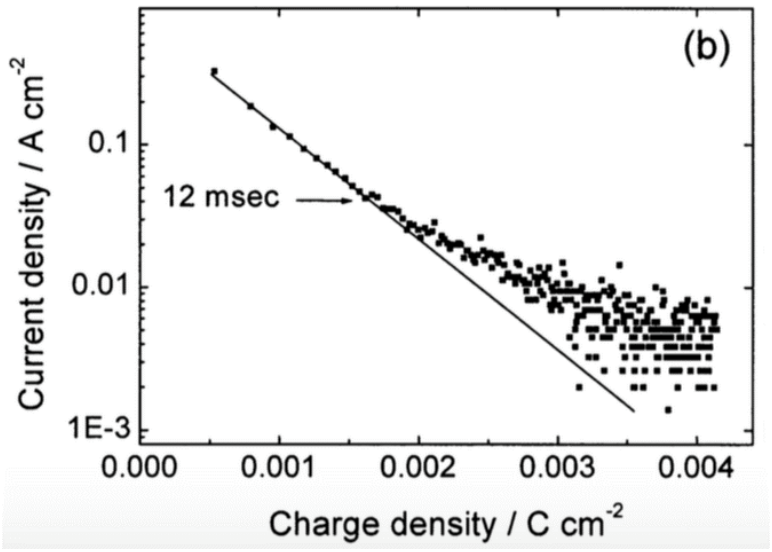

(b)

Figure 2.7 Continued.

Repassivation kinetics of the passive film could be studied through scratch tests where the decay of peak current caused by the scratch is studied, as shown in Figure 2.7, where both current (i) vs. time (t) and log i vs. log t are plotted. [9] Current decay after the scratch follows the empirical relationship given as $\partial \log i(t) / \partial t = -1$. With the assumption that all of the charge flow contributes to the formation of passive film on the bare metal surface, the high field conduction (HFC) model proposed by Verwey and Cabrera and Mott [10, 11] works well to simulate the repassivation of stainless steels. According to this model, the electric potential drop across the passive film leads to the flow of metal ions, which fill the interstitial sites in the oxygen lattice, as shown in Figure 2.8. The electrolytic current density can then be represented by Equation (5),

$$i(t) = \alpha \cdot \exp(B\frac{V}{x(t)}) \tag{5}$$

,where a and *B* are constant and (*V*/*x(t)*) is the electric field with *V* the potential drop and *x* the thickness of the passive film. If we assume that all of the current contributes to the growth of passive film and there is no metal dissolution, then the relationship between the charge density and the thickness of the passive film is expressed by Equation (6):

$$q(t) = \frac{\rho zF \cdot x(t)}{M}) \tag{6}$$

,where ρ is the density of passive film, *z* is the charge of metal ions, *F* is the Faraday's constant, *M* is the molecular weight of the film. Combining Equation (5) and Equation (6), the relationship between *i*(*t*) and *q*(*t*) is derived and represented by:

$$i(t) = \alpha \cdot \exp(\frac{B \cdot \rho VzF}{q(t) \cdot M}) \tag{7}$$

With $\frac{rzF}{M}$ constant and represented by *c*, the relationship is then being:

$$\log i(t) = \alpha \cdot \exp(\frac{cBV}{q(t)}) \tag{8}$$

According to Kwon et. al., value of *cBV* indicates the susceptibility of stainless steels to pitting corrosion and stress corrosion cracking. [9] The theory has been used to

study the effect of alloying elements and environmental factors on the repassivation kinetics and stress corrosion cracking susceptibility of stainless steels. [9]

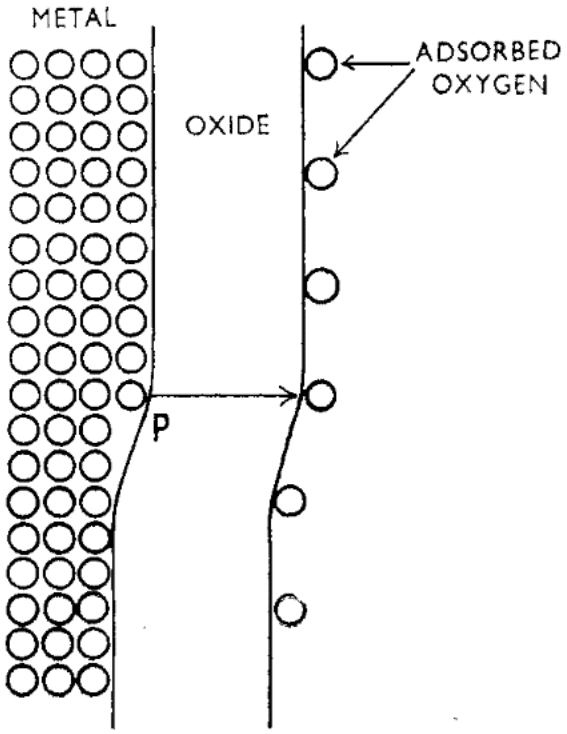

Figure 2.8 Mechanism proposed by Cabrera and Mott for oxide film formation.[11]

As mentioned above, in the high field conduction model, all the current flow is considered to contribute to the formation of passive film. However, during the initial stage after the breakdown of the passive film, current flow originates from both metal dissolution as well as film formation. Beck developed a model to fit the initial stage during repassivation, however, only current of metal dissolution was considered. [12] Lillard takes both anodic dissolution and film growth into consideration, where the passive film grows according to Avrami kinetics. [13] The mathematical expression is:

$$I_{tot} = I_{diss} + I_{film} = (1 - \theta)I_{bare} + \theta A t^{-b} \quad (9)$$

, where θ is the fraction of scratched surface covered with passive film, I_{bare} is the current on the bare metal surface, A is a characteristic charge density coefficient, t is time spent after the peak current is reached due to scratch, and b is a constant. One advantage of Lillard's model compared with Beck's is that it does not use Tafel expression for the film growth, which may result in large uncertainty during calculation.

2.3. Pitting corrosion mechanisms

Typical steps in pitting corrosion are: pit initiation, metastable pitting, and stable pit growth. Another important step that does not always happen is the repassivation when the stainless steels return to the passive state after the metastable pits fail to develop into stable pits or when the potential of metal decreases, as in the case of cyclic potentiodynamic polarization.

2.3.1 Pit initiation mechanisms

2.3.1.1 Penetration mechanism

Hoar et al. proposed the penetration mechanism to explain the passive film breakdown and pit initiation. [14] In this mechanism, aggressive anions migrate through the passive film to the metal/film interface due to the high electric field across the film (as high as 10^6 V/cm) and promote metal dissolution. The process is shown in Figure 2.9. [15] Electron spectroscopy for chemical analysis (ESCA) analysis of the passive film formed

on Ni in acid containing Cl^- showed the existence of Cl^- in the inner layer of film when Ni was polarized at high potentials, which supported the penetration mechanism. [16] However, another study showed that there was no presence of halide anions in the passive film formed on Fe in halide-containing solution. [17]

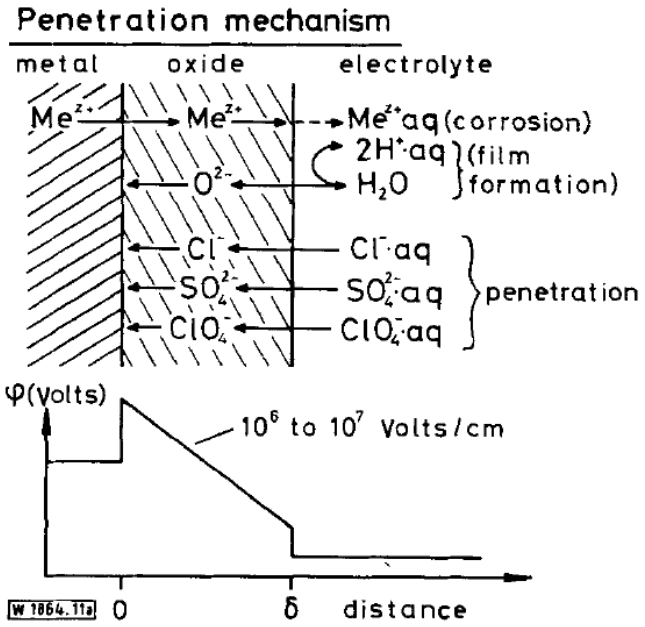

Figure 2.9 Schematic diagram showing penetration mechanism of film breakdown during pit initiation. Me^{z+}: metal cation. [15]

Another model that is related to the penetration mechanism is the point-defect model developed by D. D. Macdonald and the schematic diagram of the mechanism is shown in Figure 2.10. [18] Metal cation vacancy forms after dissolution of metal at the film/solution interface through the reaction:

$$M_M \rightarrow M^{\chi+}(aq) + V_{M}{}^{\chi\prime} \tag{10}$$

Where M_M is the metal cation in the cation site in the passive film, $M^{\chi+}(aq)$ is the metal cations dissolved in the aqueous solution, and $V_M{}^{\chi'}$ is the cation vacancy in the cation site in the passive film. The cation vacancies formed at the film/solution interface will migrate to the metal/film interface under electric filed across the film. At the metal/film interface, the cation vacancy combines with the bare metal to form metal cation in the cation site in the passive film, M_M, through the reaction:

$$m + V_{M}{}^{\chi\prime} \rightarrow M_M + \chi e' \tag{11}$$

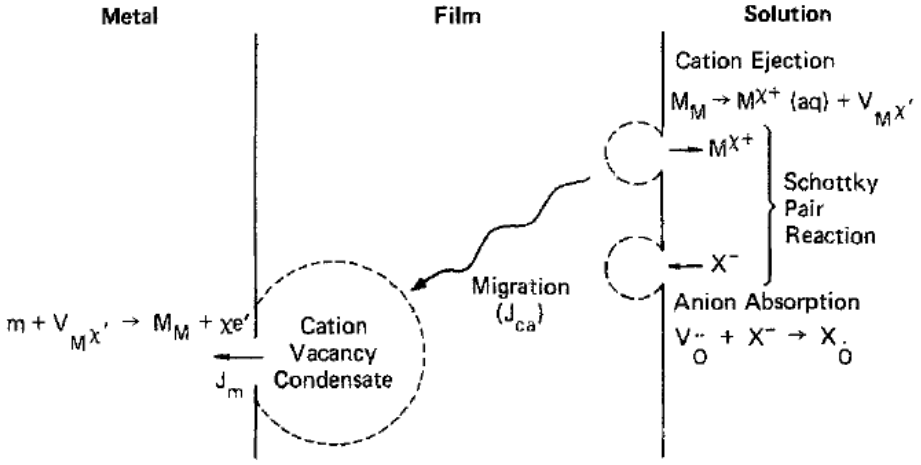

Figure 2.10 Point-defect model to explain passive film breakdown. $V_M{}^{\chi'}$: metal vacancy in the metal lattice in the film; M_M: metal cation in the metal lattice in the film; $V_o{}^{\cdot\cdot}$: oxygen vacancy in the oxygen lattice in the film; $X_o{}^{\cdot}$: aggressive anion in the oxygen lattice in the film. [18]

If the rate of formation of M_M is slow compared with the rate of cation vacancy accumulation, cation vacancies will condense at the metal/film interface, which will lead to the breakdown of passive film and pitting corrosion initiation. At the same time, oxygen anion vacancy can also be produced at the metal/film interface through the reaction: [19]

$$m \rightarrow \frac{\chi}{2} V_o^{\cdot\cdot} + M_M + \chi e' \tag{12}$$

Where $V_o^{\cdot\cdot}$ is the oxygen vacancy in the oxygen lattice in the passive film. Aggressive anions X^- such as Cl^- can combine oxygen vacancy at the film/solution interface:

$$V_o^{\cdot\cdot} + X^- \rightarrow X_o^{\cdot} \tag{13}$$

Where $X_o^{\cdot}$ is the aggressive anion occupying the oxygen site in the passive film. The reaction with oxygen vacancy at the film/solution interface will promote the oxygen vacancy flux and in turn promote the metal cation vacancy flux to the metal/film interface. As discussed above, this will lead to the faster condensation of metal cation vacancies at the metal/film interface, promoting pit initiation.

2.3.1.2 Adsorption mechanism

The adsorption theory that explains the breakdown of passive film was first proposed by H. H. Uhlig. [20] A detailed process was described by T. P. Hoar et al. [21] The process is shown in Figure 2.11. [15] The aggressive anions such as Cl^- have affinity for the metal and can adsorb on the metal surface. The adsorbed aggressive anions compete with passivating agents such as oxygen and displace passivating agents in the passive film.

In this way, the thickness of the passive film is reduced and the electric field across the film is increased due to the thinning of the film. [22, 23] Ultimately, the passive film locally is removed and pit initiates at that site.

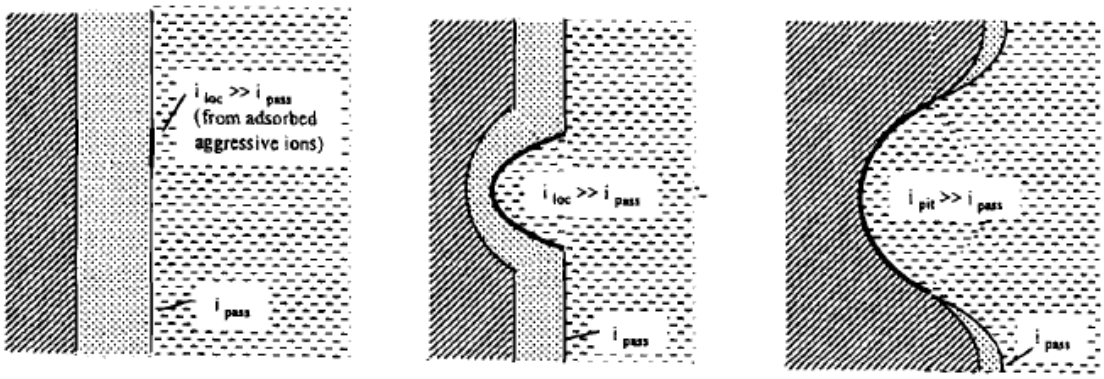

Figure 2.11 Schematic diagram showing adsorption mechanism for passive film breakdown during pit initiation. i_{pass}: passive current density; i_{loc}: corrosion current density at local site with adsorbed aggressive anions; i_{pit}: pit current density. [24]

2.3.1.3 Film breaking mechanism

In the film breaking model, pit initiation is a result of the mechanical breakdown of the passive film at local flaws caused by electrostriction. [25, 26] The mechanical breakdown of the passive film gives the aggressive anions access to the bare metal. Higher concentration of aggressive anion in the bulk solution can prevent more film flaws from passivating and lead to pit initiation, while pit initiates at less flaw sites when the aggressive anion concentration is low. [15]

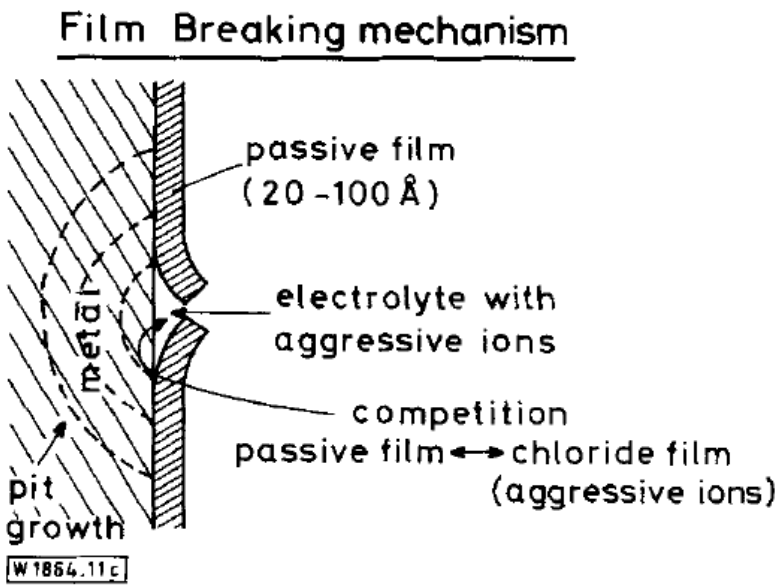

Figure 2.12 Schematic diagram showing film breaking mechanism of passive film breakdown during pit initiation.[15]

2.3.2 Metastable pitting

Metastable pitting involves pit initiation, pit growth for a limited time period followed by repassivation. Metastable pits can form below pitting potential or during the induction time of stable pit formation. In electrochemical polarization tests, metastable pitting events are current spikes that involves a current increase followed by a decrease to the passive current. For stainless steels, the metastable pitting spikes of stainless steels follow the transient pattern with gradual growth followed by a fast passivation, as shown in Figure 2.13. [27] Peak current is the highest current during a metastable pitting event. Pit growth time is the time span from pit initiation to peak current. Pit occurrence time is the time of occurrence of peak current relative to the beginning of potentiostatic polarization.

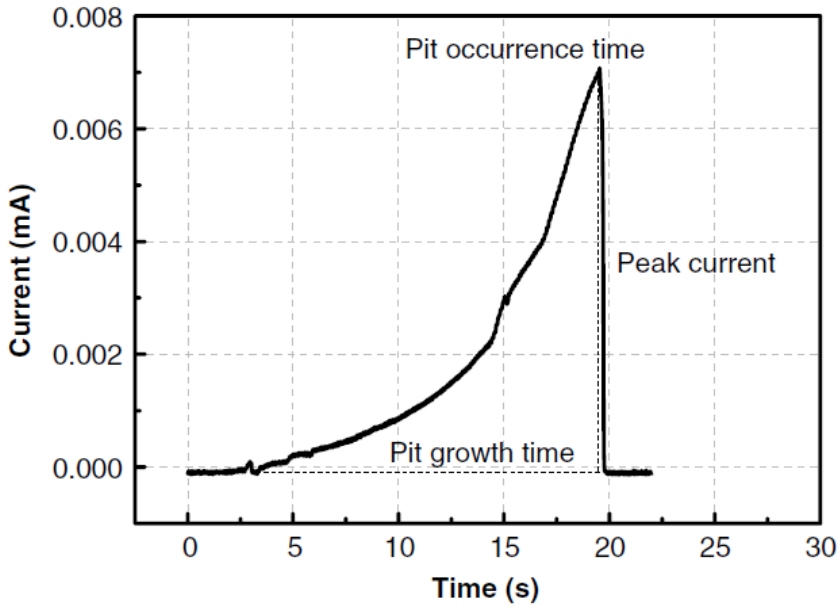

Figure 2.13 Metastable pitting current during potentiostatic polarization at 420 mV_{SCE} of 302 stainless steel in 0.1 M NaCl solution. [27]

Metastable pit radii can be calculated by integration of the current over time during metastable pit growth and according to Faraday's law and it should be assumed that the metastable pit has a hemispherical shape. The current density during metastable pit growth can then be calculated by dividing the current by the area of pit. It has been found that the current density is constant during the growth of metastable pit. [28] Pistorius and Burstein proposed that the metastable pit growth is under diffusion control based on the fact that the growth time of metastable pit is much longer than the time needed to establish a steady state for diffusion. [29] However, based on the observation that the current density increased with applied potential, it was argued that the metastable pit growth was under ohmic control. [28]

A lot of factors have effects on the metastable pitting events, including presence of anions species other than Cl^-, anion concentration, pre-treatment and surface roughness. Peak current of metastable pit transients is increased in environment containing higher Cl^- concentration. [28, 30] Nucleation rate of metastable pitting on 316L stainless steel is reduced when anions such as CrO_4^{2-}, SO_4^{2-}, NO_3^- and PO_4^{3-} are added to the NaCl solution, indicating an inhibiting effect of these anions on the metastable pitting. [30] Study on metastable pitting on 304 stainless steel in NaCl solution showed that higher surface roughness increased the occurrence of metastable pitting events through exposing more susceptible sites on the surface. [31] Addition of $S_2O_3^{2-}$ to NaCl solution also promote the occurrence and the growth of metastable pitting on 304L stainless steel and UNS S32101 DSS. [27]

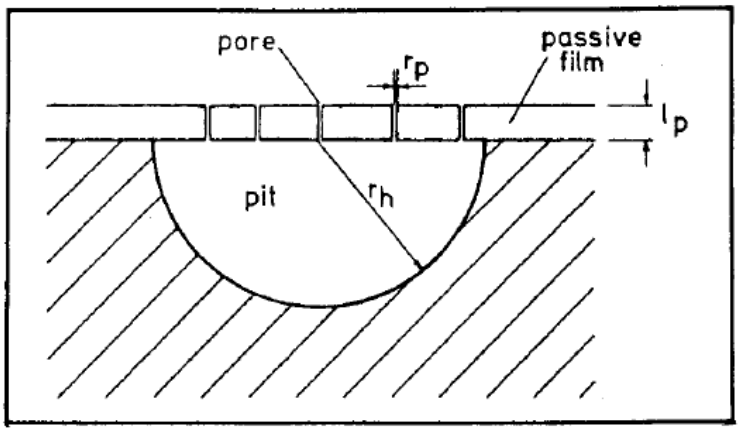

Figure 2.14 Schematic diagram showing the pit cover on top of a metastable pit. R_p: pore radii; l_p: pore length; r_h: pore radii. [28]

As shown in Figure 2.14, the metastable pit is usually covered by a porous pit cover, which sustains the aggressive environment within the pit. [28] The final stage of metastable

pitting event is the rupture of the pit cover and the dilution of the solution within pit, leading to the passivation of a metastable pit. The rupture of the pit cover is usually captured in current density vs. time curve where there is an increase in the current density at the end of event following constant current density region. In contrast, if the pit survives and continues to grow, it enters the stable pitting regime.

2.3.3 Stable pit propagation

The propagation mechanism of pits proposed by Galvele is illustrated in Figure 2.15. [32] After the passive film on the stainless steels breaks down and aggressive anions like Cl^- propagates into the cavity, the first step is the active dissolution of metal through the anodic reaction:

$$M_e \rightarrow M_e^{n+} + ne^- \tag{14}$$

Metal cations then hydrolyze:

$$M_e^{n+} + H_2O \rightarrow M_e(OH)^{n-1} + H^+ \tag{15}$$

The hydrolysis of metal cations produces protons within the pit, decreasing the pH of the pit solution. A pH of as low as 0.06 to 0.17 has been observed within the pit formed on 316L stainless steels while the bulk solution is neutral 0.5M NaCl solution. [33] The accumulation of the positively charged Me^{n+} and H^+ inside a pit attracts more Cl^- to migrate to the pit solution. These two facts lead to an increase in the aggressiveness of the pit solution, making the pit propagation an autocatalytic process.

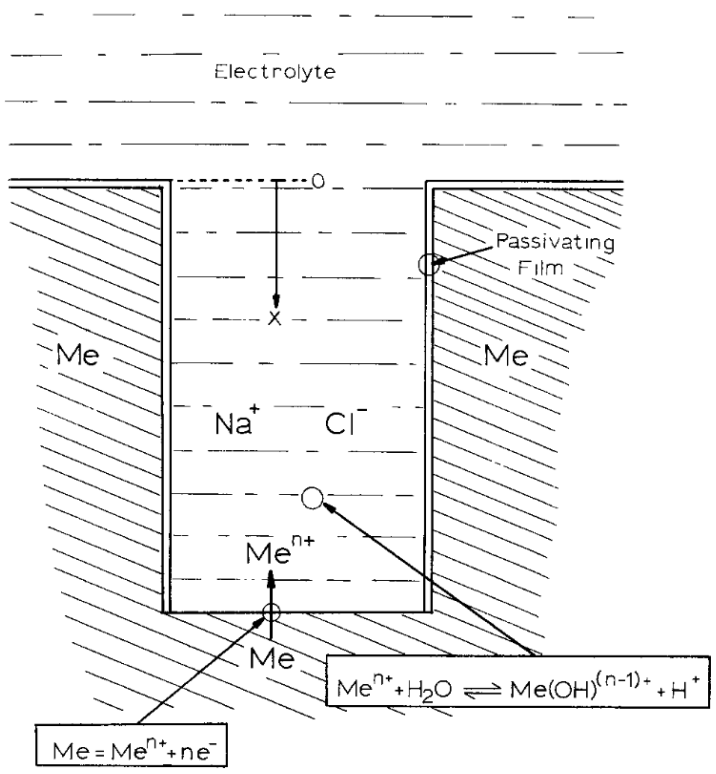

Figure 2.15 Pitting corrosion model proposed by Galvele. [32]

Pits formed at lower potentials tend to be crystallographically etched with hexagon or square shapes.[34, 35] These pits were found to form under activation control and the crystallographic planes with high dissolution rate dissolves during pit propagation and leaving the planes with the lowest dissolution rate on the surface of pits.

However, since the pit solution contains high concentration of metal cations and aggressive anions, a salt film can form on the surface of pits upon saturation at high potentials.[36-40] With the presence of salt film within pits, pits propagate under diffusion control as hemisphere with polished surface. Laycock and Newman used artificial pits formed on stainless steel wires to study the dissolution kinetics of pits and the relation with

salt film.[40] As shown in Figure 2.16, an artificial pit is first formed at 750 mV_{SCE} and then the potential is decreased, till current density is 80% of the limiting current density $i_{lim.}$ During the decrease of potential, the current density remains at a constant value i_{lim}, indicating the pit propagation is under diffusion control. A peak occurs at a lower potential and then the current density decreases with decreasing potential due to the dissolution of salt film and pit propagation is under mixed activation/ohmic control in the film-free state. Transition potential, E_T, was defined as the potential at which the salt film is dissolved.

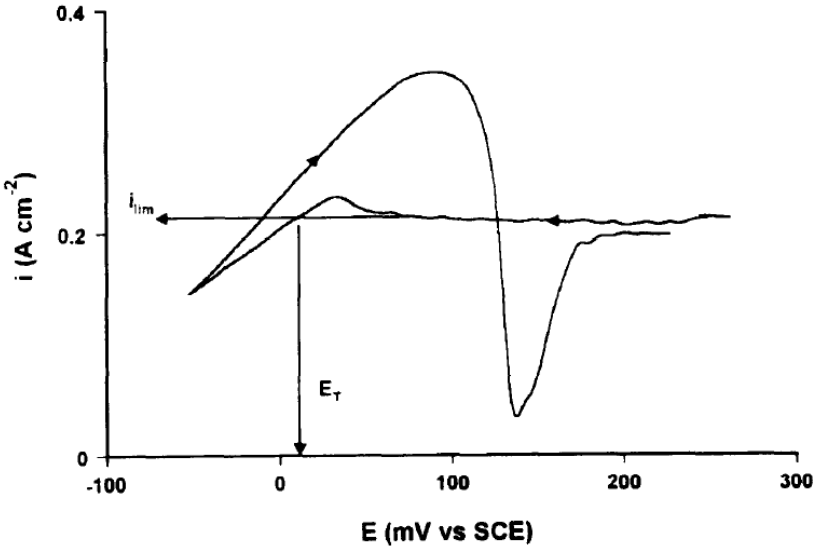

Figure 2.16 Definition of transition potential E_T and limiting current density i_{lim} on a current density vs. potential plot for 302 stainless steel artificial pit with 50 μm diameter. [40]

2.4. Factors that affect pitting corrosion

2.4.1 Chemical composition of alloy

Cr, Mo and N are the major alloying elements that contribute to the pitting corrosion resistance of stainless steels either by increasing the protectiveness of the passive film or through decreasing the active dissolution rate within the pits. An empirical term to estimate the pitting corrosion resistance is the pitting resistance equivalent number (PREN), which is typically calculated from Equation (16) for stainless steels that do not contain W. According to this equation, the PREN of some grades of DSSs are listed in Table 2.1.

$$PREN = Cr + 3.3Mo + 16N \quad (16)$$

Table 2.1 Calculated PREN of some grades of DSSs and austenitic SSs 304L and 316L according to the composition listed in Table 1.1.

Stainless steels (common names)	PREN
2101	26.3
2304	25.8
2003	29.8
2404	33.6
2205	32.7
304L	18.0-21.6
316L	22.6-29.5

Cr improves the pitting corrosion resistance of stainless steels by forming passive film on the surface and improving passive film protectiveness. As shown in Figure 2.17,

pitting potential in 0.1N NaCl at 25°C increases drastically when the Cr content is above 21 wt%. [41] Above 57.8 wt% of Cr, no pitting corrosion occurs, and the materials shows transpassive behavior at higher potentials with chromates formation.

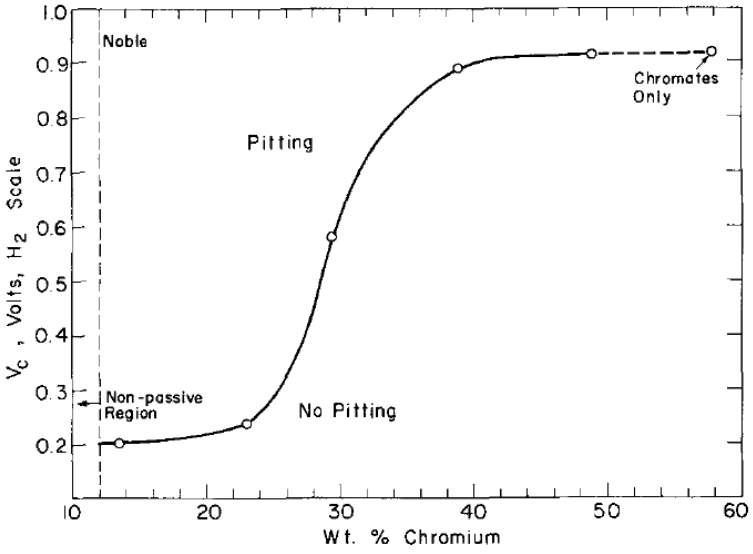

Figure 2.17 Change of pitting potentials with Cr addition for Cr-Fe alloys in 0.1N NaCl at 25 °C. [41]

The addition of Mo is also beneficial to the pitting corrosion resistance of stainless steels. Newman used artificial pits to study the effects of Mo on the pit growth kinetics and found that the anodic dissolution rate during pit propagation was 5-10 times lower with the addition of Mo.[42] Mo is also beneficial for stainless steels in environments containing sulfur compounds through promoting the desorption of S from the surface.[43, 44] It was found that the amount of the $K_2S_4O_6$ needed to fully achieve the activation effect of sulfur increases with the content of Mo in the stainless steels. [45] Through the use of radioisotope, Marcus et. al. were able to detect the surface coverage change with and

without the presence of Mo. Experimental data showed that there was little desorption of ^{35}S on Fe-Cr-Ni alloys but the desorption of ^{35}S was more than 50% on Fe-Cr-Ni-Mo alloys after 1 hour immersion at open circuit potential.

It has been demonstrated that the beneficial effect of nitrogen (N) in NaCl solution is also mainly through the reduction of anodic dissolution during pit propagation. [46, 47] As shown in Figure 2.18, anodic polarization curves in 2.5M HCl of two stainless steel samples are compared and anodic current density of alloy N with 0.22% nitrogen addition is much lower than that of alloy M without nitrogen addition.[46] The effects of other minor alloying elements such as Mn have also been studied.[48] Different from Cr, Mo and N, Mn has adverse effects on pitting corrosion resistance of stainless steel mainly because of the tendency to form MnS that act as active site prone to pit initiation.

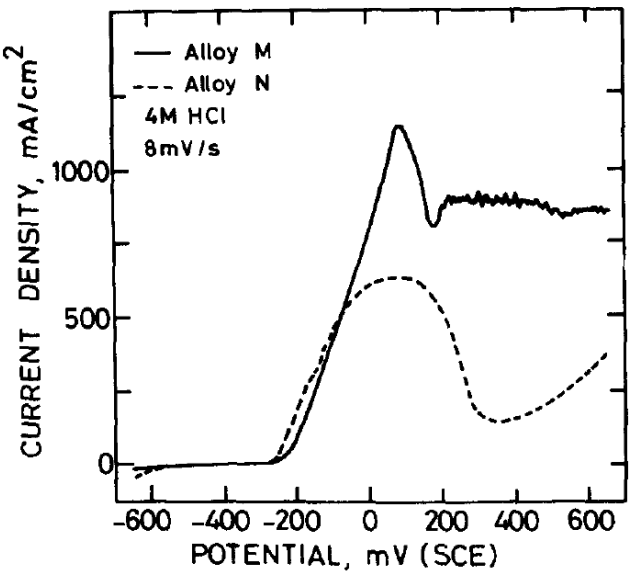

Figure 2.18 Anodic polarization of alloy M with low nitrogen and alloy N with 0.22% nitrogen in 2.5M HCl solution. [46]

2.4.2 Heat-treatment

2.4.2.1 Annealing treatment

Due to the two-phases, the microstructure evolution is more complex for DSS than single-phase stainless steels. Figure 2.19 shows a vertical section of the Fe-Ni-Cr system phase diagram with 70% Fe content and the vertical line represents the chemical composition with which the materials would have the dual-phase microstructure.[49] Typically annealing of DSSs done above ~1000 °C could lead to the transformation of the austenite phase (γ) into the ferrite phase (α). Cr and Mo preferentially partition into the ferrite phase while Ni and N preferentially partition into the austenite phase. According to thermodynamic predictions, the partitioning of alloying elements changes with annealing temperatures. While the Cr and Mo preferentially partition in the ferrite phase, the Mo content decreases at elevated temperatures but the partitioning of Cr is not affected much by the annealing temperature. Ni and N preferentially partition into the austenite phase, and the partitioning of Ni decreases while that of N increases with increasing annealing temperature. [49] However, N content also increases within the ferrite phase and Cr_2N may form when the ferrite phase is saturated with N. [50]

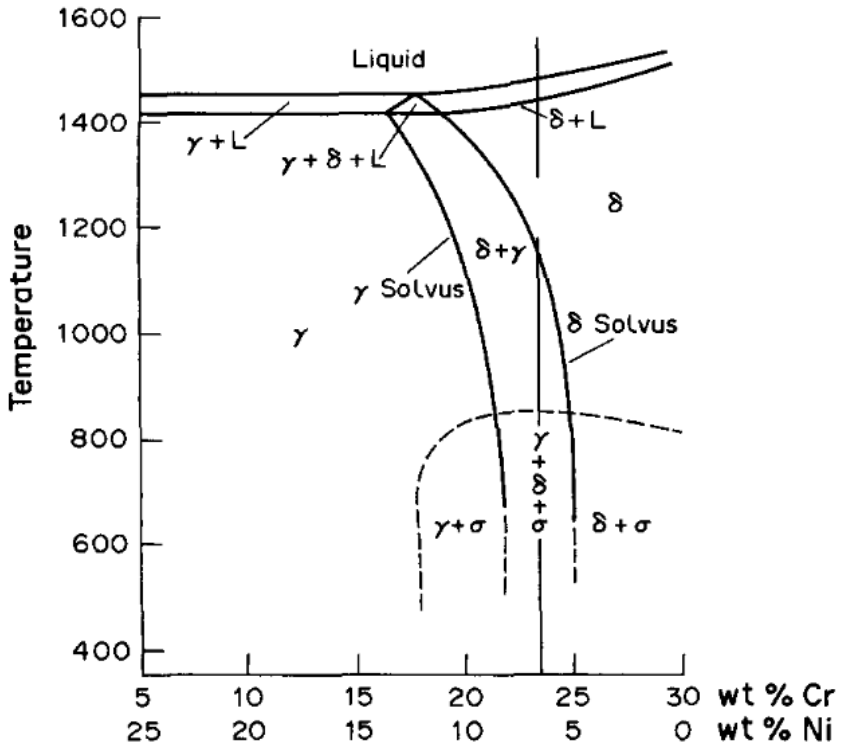

Figure 2.19 The constant Fe (70 wt%) vertical section of the Fe-Ni-Cr system phase diagram. The solidification sequence of the experimental alloy (duplex pipe) is shown by the vertical line. [49]

As discussed in 3.1.1, Cr, Mo and N benefit the corrosion resistance of stainless steels, therefore the pitting corrosion resistance of the two phases in DSSs is also affected by the composition change during annealing. With decreasing Cr and Mo content, the pitting corrosion resistance of the ferrite phase is expected to decrease while that of the austenite phase would increase when DSSs are annealed at higher temperatures. For UNS S32101 and UNS S82441, critical pitting temperature decreased with increasing annealing temperature above 1000 ºC because the ferrite phase is the weak phase and its PREN number is lower at high annealing temperature. [51, 52] Pitting corrosion resistance of UNS S32304 has a peak at 1080 ºC and below this temperature the austenite phase is more

susceptible to pitting corrosion while above this temperature, the ferrite phase is more susceptible to pitting. [53] These studies generally used potentiodynamic cyclic polarization to compare the pitting potential and potentiostatic polarization to measure the critical pitting temperature (CPT) of the DSSs specimens coupled with microstructure and pit morphology characterization. More comprehensive electrochemical tests have been carried out to investigate the effects of Cr_2N on the pitting corrosion behavior of DSS 2205. It is observed that the presence of Cr_2N reduces the limiting current density that is required to precipitate the salt film and increases the maximum dissolution current density within the pits, and the pitting corrosion resistance is decreased as a result. [50]

2.4.2.2 Isothermal aging treatment

Another important heat-treatment of DSSs is the isothermal high temperature aging, during which precipitates such as carbide and nitride and intermetallic phases like σ and χ are formed. σ phase and χ phase are enriched in Cr and Mo, but σ phase has higher Cr content while χ phase has higher Mo content. [54-56] For DSS 2205 and super DSSs, σ phase forms at the ferrite/austenite boundaries and grows into the ferrite phase within the 650 to 900 °C temperature range. [55, 57, 58] Compared with the fast precipitation of σ phase and χ phase in higher alloyed DSS grades, that is formed within minutes of aging, the formation of σ phase and χ phase in lower alloyed LDSSs is sluggish, following the precipitation of Cr_2N and $M_{23}C_6$, because of the lower Cr and Mo content in DSSs. [56, 59] For LDSS 2101, Cr_2N and $M_{23}C_6$ precipitate along the ferrite/austenite boundaries within minutes, while σ phase forms after 24 hours of aging at 690 °C. [58, 59]

Since the precipitates and intermetallic phases are enriched in Cr and Mo, secondary austenite that is depleted in Cr and Mo would form in their vicinity and is susceptible to pitting corrosion. [54, 59] J. Li et al used a potentiostatic polarization method to measure the critical pitting temperature of the aged DSSs specimens in NaCl solution and found that the CPT is sensitive to the microstructure evolution at shorter aging time. [52, 60-63] While breakdown potential in potentiodynamic polarization and CPT and CCT (critical crevice temperature) can reveal the pitting corrosion resistance of the most susceptible site in the microstructure, M. E. Wilms used critical current density during potentiodynamic polarization in simulated crevice solution as an indication of the general surface deterioration of super DSSs during aging. [58] While large drop in the pitting corrosion resistance occurs in aged DSSs specimens in chloride containing environment, similar effect was not observed in aged UNS S32101 specimens in caustic environment although precipitates and depleted areas are present in the microstructure. [64]

2.4.2.3 Welding

Welding is the process to join materials (typically metals or thermoplastics) together at high temperature. For metals, the temperature in the fusion zone and heat-affected zone (HAZ) can be as high as 1100 °C during welding. [65] Figure 2.20 shows different regions in the welded metals. For DSSs, problems often encountered in welding are excessively high content of the ferrite phase in the HAZ and the precipitation of secondary phases, lowering the toughness and corrosion resistance of DSSs. [65-71]

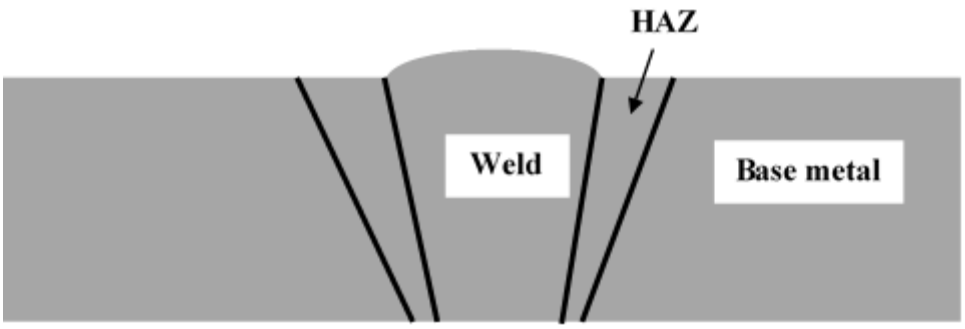

Figure 2.20 Different regions in the welded materials.

As shown in Figure 2.19, during welding the temperature is above the solvus line and the austenite phase transforms into the ferrite phase completely and the austenite phase reforms during cooling. If the cooling rate is too high, there is an excessive amount of the ferrite phase, especially in the HAZ where there is overheating. Volume percent of the ferrite phase as high as 72% has been observed in 2205 HAZ, but this is less a problem in the center of the weld where the cooling rate is lower. [66] When the austenite phase transforms into the austenite phase, N content in the austenite also dissolves into the ferrite phase, leading to the supersaturation of N and formation of Cr_2N precipitates in the ferrite phase.[67, 71] However, if the cooling rate is too slow or repeated heating occurs in the temperature range of 600-1000 °C, intermetallic phase will form, leading to the decrease in toughness and pitting corrosion resistance of DSSs.[66, 68]

2.4.3 Anion species

Pitting corrosion usually happens in environments that contain halide anions such as Cl^-, Br^- and I^- and the aggressiveness is in the order of: $Cl^- > Br^- > I^-$. [72, 73] Pitting corrosion resistance also decreases with increasing halide concentration. [72-74] As shown

in Figure 2.21, the critical potential (pitting potential) of 17.7%Cr-8.7%Ni-Fe stainless steel decreases linearly with increasing chloride anion activity. [74]

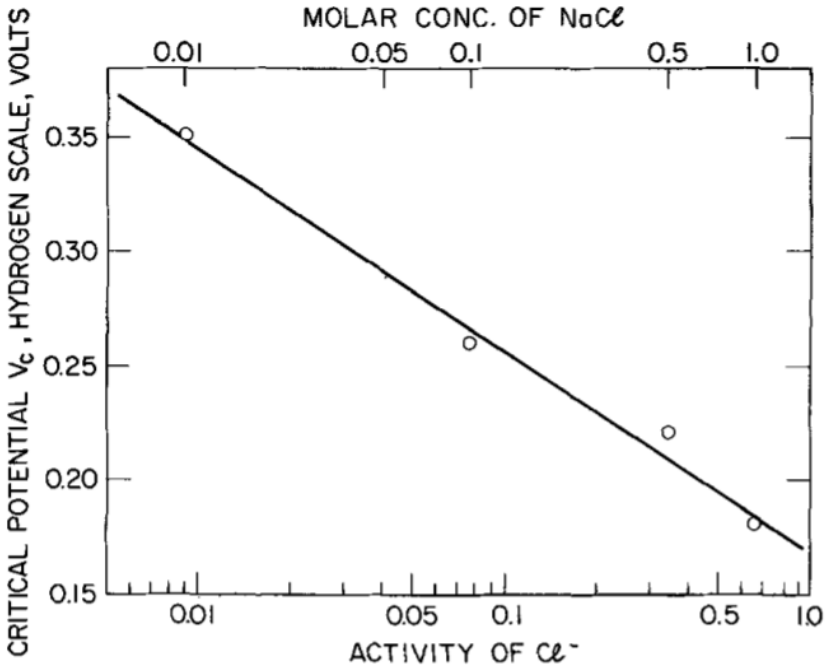

Figure 2.21 Change of critical potential (pitting potential) of 17.7%Cr-8.7%Ni-Fe stainless steel with different chloride anion activity. [74]

$S_2O_3^{2-}$ does not have significant effect on the breakdown of the passive film on stainless steels, which was shown through XPS analysis where $S_2O_3^{2-}$ decomposes on the bare alloy instead of on the passive film. [75-77] $S_2O_3^{2-}$ mainly activates the anodic dissolution of the bare metals after the passive film is broken by anions like Cl^- and SO_4^{2-}, or mechanically by scratching or stretching. [75, 76, 78-80] As shown in Figure 2.22, in solutions that contain Cl^-, $S_2O_3^{2-}$ and SO_4^{2-}, there is a critical $(Cl^-+SO_4^{2-})/S_2O_3^{2-}$ ratio range between which pitting corrosion would occur, and below the lower limit $S_2O_3^{2-}$ would act

as an inhibitor because of the preferential migration into the pit environment. [75] However, this critical range varies for different grades of stainless steels. [52, 80-82] Pit morphology in $S_2O_3^{2-}$ containing Cl^- environment is different for austenitic stainless steels and DSSs. In DSSs, the pit has a trenched shape with the ferrite phase preferentially attacked. [82] $S_2O_3^{2-}$ also affects the metastable pitting events of SSs, increasing both the peak current and dissolution kinetics. [27, 83]

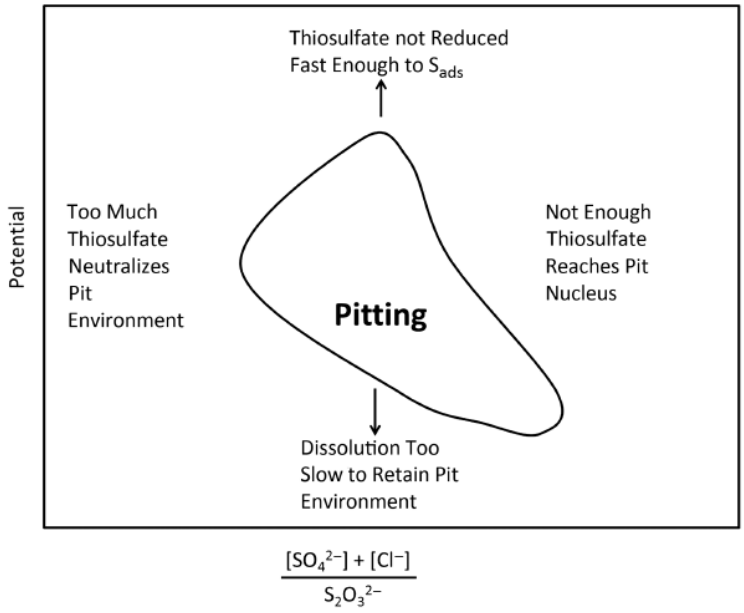

Figure 2.22 Summary of pitting corrosion in environments containing Cl^-, $S_2O_3^{2-}$, and SO_4^{2-}. [84]

SO_4^{2-} has been considered as a pitting inhibitor when a certain concentration is reached. H. H. Uhlig et.al. first reported the inhibition effects of SO_4^{2-} together with other anions such as NO_3^- and ClO_4^-. [74] Since SO_4^{2-} has higher charge than Cl^-, it is preferentially accumulated in the pit solution, and helps with the repassivation of pitting.

[32] The presence of SO_4^{2-} also decreases the frequency of pit initiation and the growth rate of pits. [85, 86] Other inorganic inhibitors include chromate, molybdate, perchlorate, and nitrate. [74, 87-90]

2.5 Preferential dissolution of constituent phases in DSSs

2.5.1 Preferential dissolution of one constituent phase in DSSs

For DSSs, during different corrosion processes such as active corrosion, pitting corrosion and stress corrosion cracking, it is often observed that one constituent phase is preferentially attacked while the other phase is retained, which is a unique characteristic of dual-phase steels. Factors including chemical composition of DSSs, corroding environment, as well as applied potential determine whether the ferrite phase or the austenite phase is preferentially dissolved.

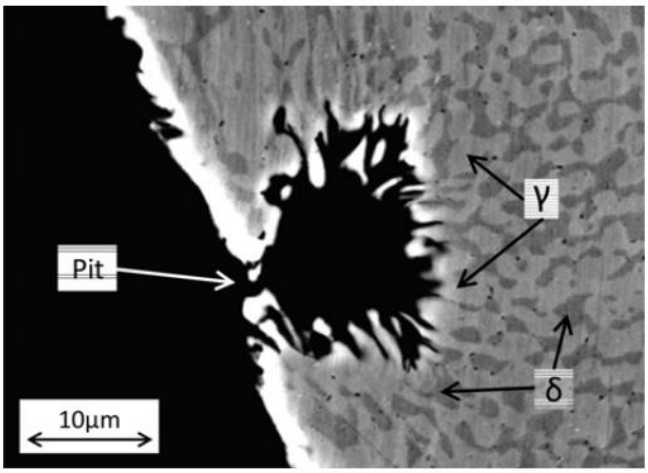

Figure 2.23 Cross-section of pits formed on UNS S32101 after testing in alkaline solution with 1M Cl^-showing the preferential dissolution of the ferrite phase (δ). [91]

Preferential dissolution of ferrite phase within pits has been observed in UNS S32101 and UNS S32304 in near-neutral $S_2O_3^{2-}$-containing Cl^- solution and alkaline carbonated Cl^- solution, as shown in Figure 2.23.[82, 91, 92] The ferrite stabilizer Mo content in these two grades of DSSs is lower than 0.3 wt%, leading to a higher pitting susceptibility of the ferrite phase. Lower maximum dissolution rate of the austenite phase than that of the ferrite phase in acidic (pH=0.5) 26% NaCl solution has been shown for UNS S32101 and S32202 that have N content of more than 0.2 wt%. On the other hand, the maximum dissolution rate is comparable in the same environment for UNS S32304, which has lower N content of 0.1 wt%. [93] This phenomenon indicates that N is very effective in increasing the corrosion resistance of the austenite phase in DSSs. Also, the preferential attack of one phase also depends on the potential at which the material is polarized. In (2M H_2SO_4 + 0.5M HCl) acid mixture, there are two peaks within the active region in potentiodynamic polarization curve of UNS S31803. Maximum dissolution of the ferrite phase occurs at a more negative potential of -320 mV_{SCE}, while the austenite phase preferentially dissolves at a more positive potential with the value of -245 mV_{SCE}, as shown in Figure 2.24. [94] At constant H_2SO_4 concentration, the maximum selective dissolution rate of the austenite phase is enhanced through increasing the HCl concentration. In contrast, the dissolution rate of the ferrite phase is increased if the H_2SO_4 to HCl concentration ratio is increased while keeping the HCl concentration constant. [95]

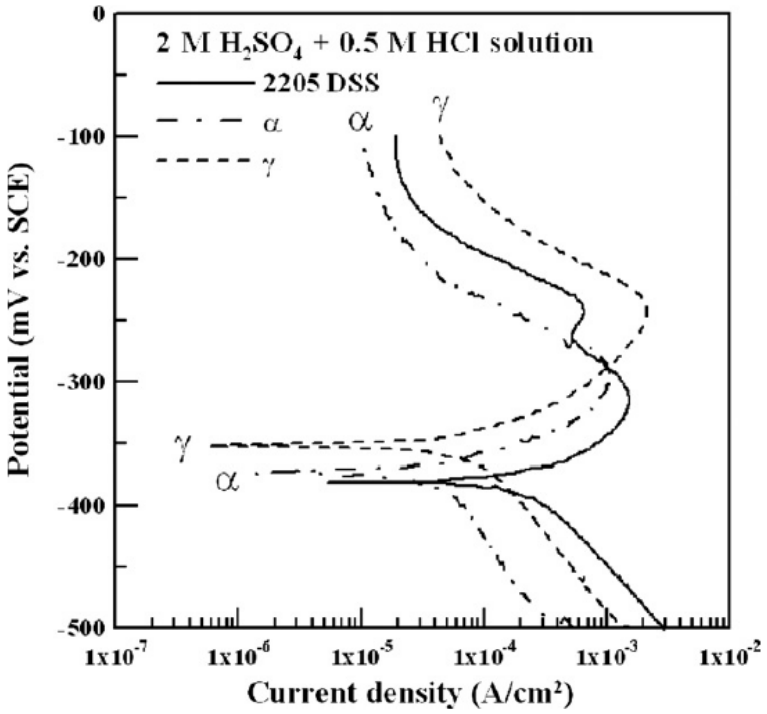

Figure 2.24 Potentiodynamic polarization curves of 2205 DSS and the respective constituent phases in (2M H_2SO_4 + 0.5 HCl) solution. [94]

2.5.2 Galvanic corrosion

Galvanic corrosion is "accelerated corrosion of a metal because of an electrical contact with a more noble metal or nonmetallic conductor in a corrosive environment" according to ASTM NACE /ASTMG193 - 12d. [96] The corrosion rate of the more active metal in the galvanic couple is promoted while the more noble metal is protected with much lower corrosion rate compared with the corrosion rate without coupling.

The mechanism is explained by the mixed potential theory and is shown in Figure 2.25.[97] Cu is more noble in the galvanic couple with Fe, while Fe acts as active metal in the couple. The corrosion rate of Cu without coupling is proportional to I_{corr}(Cu) and that

of Fe without coupling is proportional to I_{corr}(Fe). The anodic reaction for the metal dissolution is:

$$M_e \rightarrow M_e^{n+} + ne^- \tag{17}$$

Where M_e is metal and e^- is electron. And the cathodic reaction is usually hydrogen reduction:

$$2H^+ + 2e^- \rightarrow H_2 \tag{18}$$

When the two metals Cu and Fe are electrically contacted, the anodic current is the sum of the anodic current of the reaction of Cu and Fe. The cathodic current for hydrogen evolution should be equal to sum of the current for anodic reaction and the mixed potential for the galvanic couple, E_{couple}, is determined at the intersection of sum of cathodic current and anodic current. As can be seen in Figure 2.25, as the more noble electrode, the corrosion rate of Cu after galvanic coupling, $I_{coupled}(Cu)$ at mixed potential E_{couple} is much lower than $I_{corr}(Cu)$ without coupling. In comparison, the corrosion rate after coupling of more active electrode Fe, $I_{coupled}(Fe)$ is increased compared with uncoupled $I_{corr}(Fe)$.

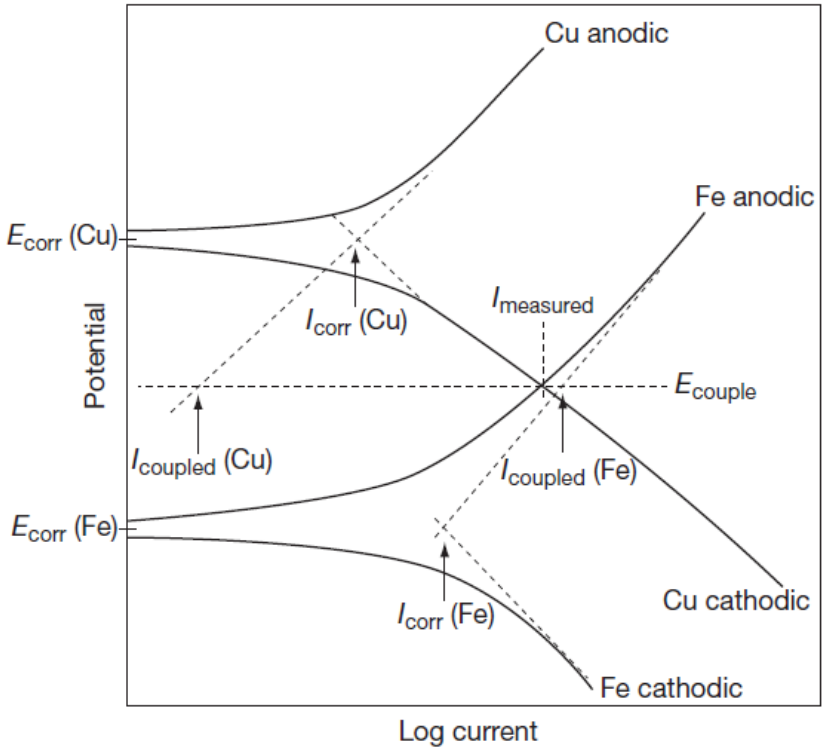

Figure 2.25 Polarization curves used to determine mixed potential E_{couple} and the corrosion rate of the coupled metals. [97]

Galvanic corrosion does not only occur on dissimilar metals or alloys, it has also been observed between constituent phases in multi-phase alloys, for example between the α and β phase in AZ91 magnesium alloy and between the ferrite phase and austenite phase in DSSs. [94, 98]

2.5.3 Properties of individual constituent phases and their coupling effects

The active corrosion behavior and preferential dissolution of the individual constituent phases of DSSs in (H_2SO_4+HCl) acid mixture has been studied extensively during the last two decades. The preferential dissolution of the individual constituent phases has also been used to obtain single-phase microstructure from a duplex stainless

steel to study the electrochemical behavior as well as passive film properties of the ferrite phase and the austenite phase individually, and their coupling galvanic effects in different environments. [94, 99-101]

In mixed (H_2SO_4 + HCl) solution, the ferrite phase is anodic while the austenite phase is more noble for UNS S31803 and super DSS. [94, 99] It was found that although the open circuit potential of the ferrite phase is lower than the of the austenite phase, the values are higher than that of the bulk DSS material. The increased open circuit potential was attributed to the elimination of phase boundaries that was previously present in the bulk DSS material.[99] In 3.5% sodium chloride solution, the passive film formed on the austenite phase has a higher Cr/Fe ratio and higher content of Ni, while that formed on the ferrite phase has higher Mo content.[101] Although as discussed above, the galvanic coupling effects between the two constituent phases in DSSs and the passive film properties have been studied, comparisons of pitting corrosion behavior between the two constituent phases in DSSs has not been studied before, which will lead to a better understanding about the preferential dissolution of one phase within pits.

CHAPTER 3. TECHNICAL APPROACH AND EXPERIMENTAL PROCEDURES

3.1 Materials selection

The materials selected in this research are wrought UNS S32101, S32304, S32003 and S82441 and their chemical composition is shown in Table 1.1. The samples were cut from the DSSs plates, and the typical microstructure is shown in Figure 3.1. These grades of DSSs are lower-alloyed than UNS S31803, a standard DSS, and thus more cost-effective in less aggressive environments. UNS S32101 (21.3 wt% Cr) and UNS S32003 (21.7 wt% Cr) have the lowest Cr content, followed by UNS S32304 (22.9 wt% Cr), and UNS S82441 has the highest Cr content. In terms of Mo content, UNS S32101 has 0.3 wt% Mo and UNS S32304 has 0.24 wt% Mo, while both UNS S32003 and UNS S382441 have ~1.6 wt% Mo. The difference in the chemical composition will affect the phase transformation as well as the pitting corrosion properties of DSSs.

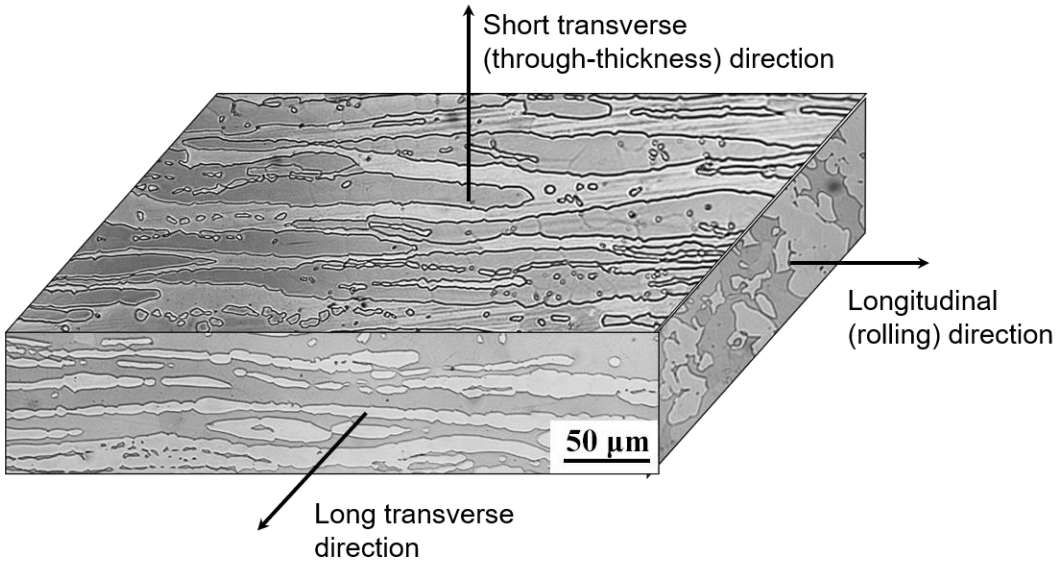

Figure 3.1 Three-dimensional representation of typical microstructure of DSSs plates in the as-received state.

3.2 Heat-Treatment of DSS materials

Specimens for heat-treatment are cut from as-received DSS materials into 10 mm x 10 mm x 3 mm pieces. Heat-treatment is done in a preheated furnace with atmosphere. Cooling through water quenching is used to preserve the high-temperature microstructure. After heat-treatment, oxide layer is formed on the surface of the specimens and is removed through grinding before electrochemical tests or other characterization.

3.3 Electrochemical tests

3.3.1 Sample preparation

For electric connection, a metal wire embedded in the insulating polymer is attached to the back of the specimen using electroplating tape. The specimen is then mounted in the epoxy resin. The surface of the sample is ground to 2000 grit and then ultrasonically cleaned using acetone and dried. To avoid crevice corrosion at the interface between the specimen and the epoxy, insulated electroplating tape is used to cover the interface. A hole with a certain area is punched in the center of the tape beforehand. The final sample used for polarization tests is shown in Figure 3.2.

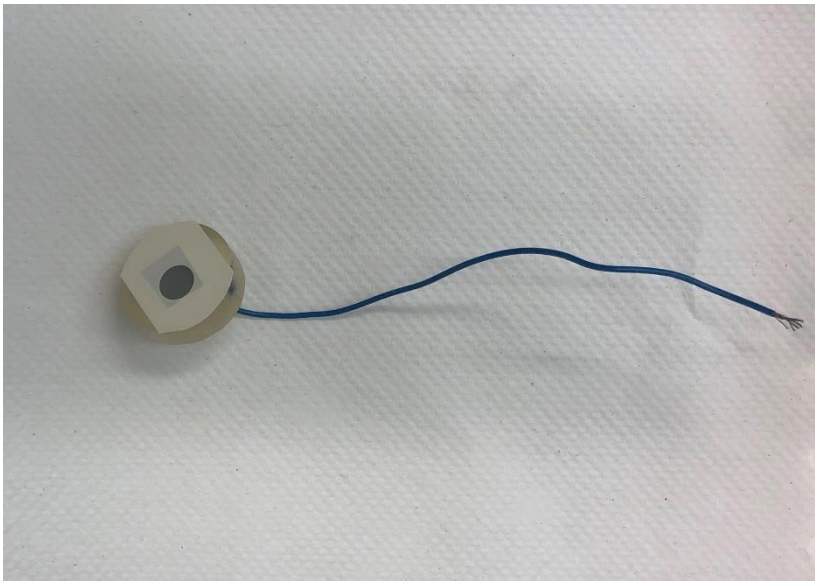

Figure 3.2 Sample used for electrochemical polarization.

3.3.2 Three-electrode system used for polarization tests

Electrochemical polarization tests were done using three-electrode cell connected to a potentiostat. As shown in Figure 3.3(a), saturated calomel electrode (SCE) was used as a reference electrode (RE) and the potentials in this work are all with respect to SCE and are denoted as V_{SCE}. A platinum foil is used as the counter electrode (CE). Tested sample as shown in Figure 3.2 works as working electrode. Tests at elevated temperatures are done in a water bath where the test temperature is kept constant within ±1 °C. For tests under deaerated condition, high-purity nitrogen is bubbled into the test solution for at least an hour before the test sample is introduced into the deaerated solution. Nitrogen is bubbled throughout the test solution using a diffuser. Figure 3.3(b) shows the schematics of the three-electrode system connected to a potentiostat. For potentiostatic and potentiodynamic polarization tests, the potential of the sample is controlled by the potentiostat and the corrosion rate of the sample is monitored at the same time.

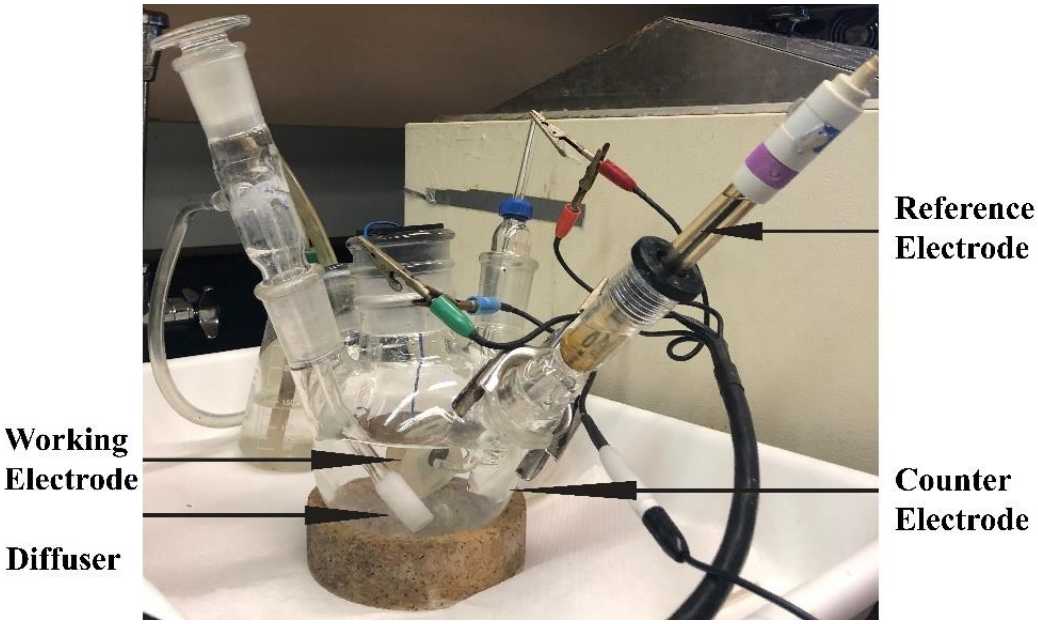

(a)

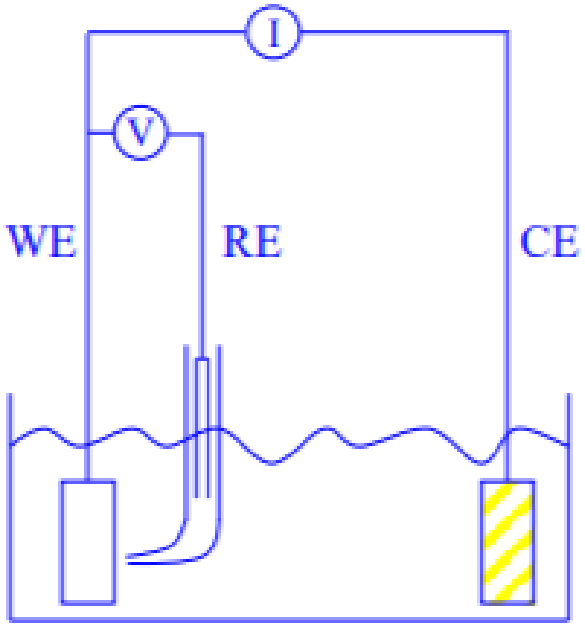

(b)

Figure 3.3 (a) Picture; (b) Schematic diagram: showing the three-electrode system used for polarization tests.

3.3.3 Potentiodynamic cyclic polarization

During potentiodynamic cyclic polarization, potential is swept from certain potential value below open circuit potential and in the anodic direction. When pitting corrosion occurs, there is a sudden increase in the current (or current density), as shown in Figure 3.4. The potential at which current density reaches 0.1 mA/cm^2 is defined as pitting potential, E_{pit}. When the current density exceeds certain value, usually above 0.1 mA/cm^2, the potential is scanned back in the cathodic direction. The current density does not decrease immediately with decreasing potential because of the metal dissolution within the pit and there is a hysteresis loop in the polarization curve. When the pit stops growing and the sample repassivates, current density decreases to the passive current density value. The potential at which the hysteresis loop closes is defined as the repassivation potential, E_{rp}. Higher E_{pit} and higher E_{rp} values indicate better pitting corrosion resistance.

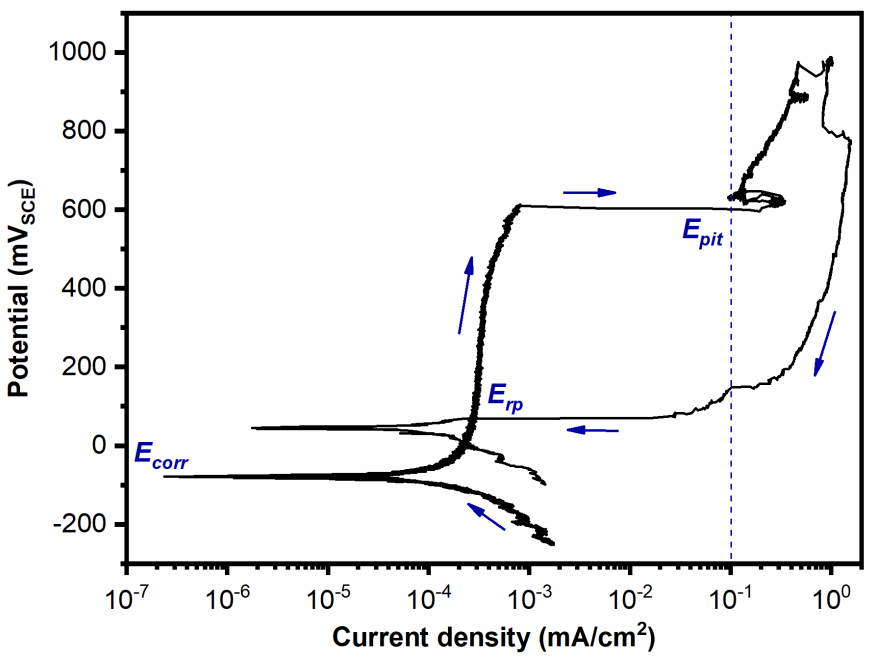

(a)

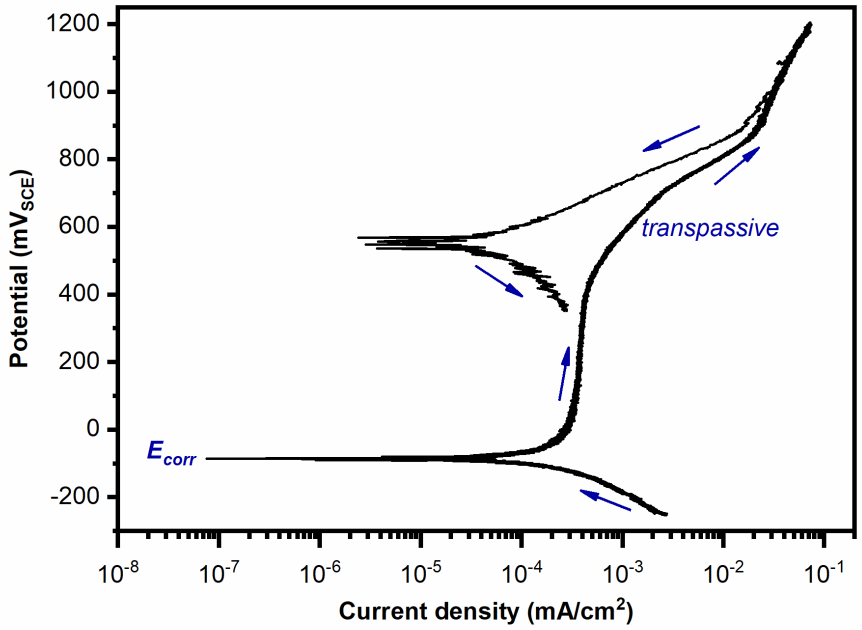

(b)

Figure 3.4 Potentiodynamic cyclic polarization curve showing (a) pitting corrosion behavior (b) transpassive behavior.

In comparison, for samples that are resistant to pitting, instead of sudden increase in the current density, current density increases gradually with potential above the passive region because of transpassive behavior or oxygen evolution. There is no hysteresis loop upon backward scan, as shown in Figure 3.4(b).

3.3.4 Potentiostatic scratch tests

Scratch tests are used to study the repassivation behavior of alloys and to study the interaction of the bare alloy surface with the environment after the removal of the passive film. The setup of the tests is shown in Figure 3.5. Three-electrode system is used with SCE as a reference electrode (RE) and platinum as counter electrode (CE). The test sample (WE) is under potentiostatic polarization throughout the tests and the current vs. time is recorded. The current is allowed to stabilize for 60 seconds at the passive current and then the scratch is made using a diamond scriber to remove the passive film. The current is recorded for another 120 seconds. Constant current increase indicates the development of localized corrosion.

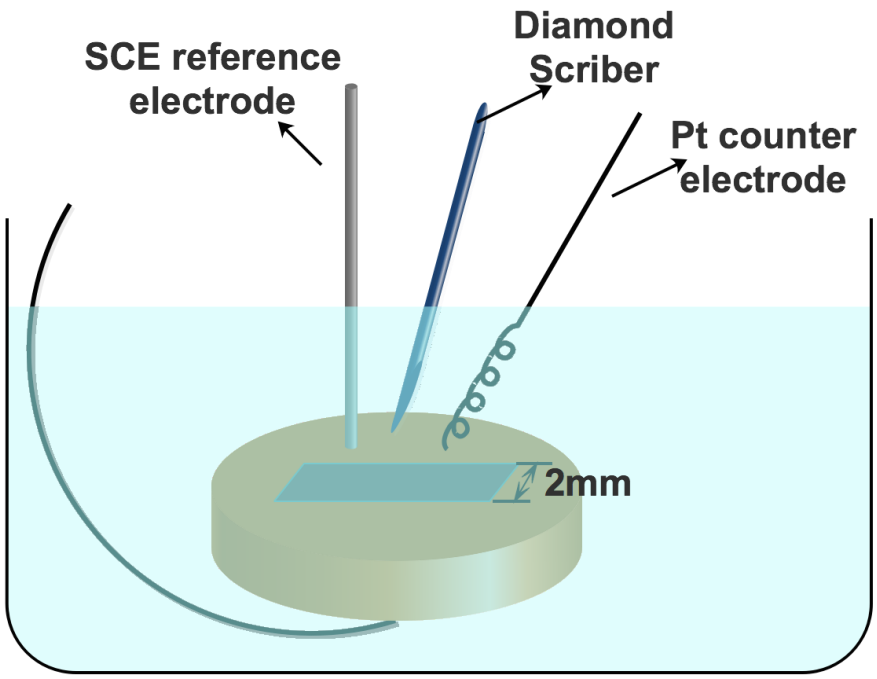

Figure 3.5 Schematics showing the setup of scratch tests.

3.3.5 Galvanic corrosion tests

The galvanic effect between the ferrite phase and the austenite phase is studied using galvanic corrosion tests. The test setup is shown in Figure 3.6. Sample 1 or the ferrite single-phase sample is the working electrode and sample 2 or the austenite single-phase sample is the counter electrode. A reference electrode is used to measure the mixed potential of the galvanic couple. As shown in Figure 3.7, a zero-resistance-ammeter (ZRA) is connected between the two tested samples and is used to monitor the galvanic current. With the setup of the potentiostat, positive current flow indicates the working electrode is anode, while negative current flow indicates that the working electrode is cathode.

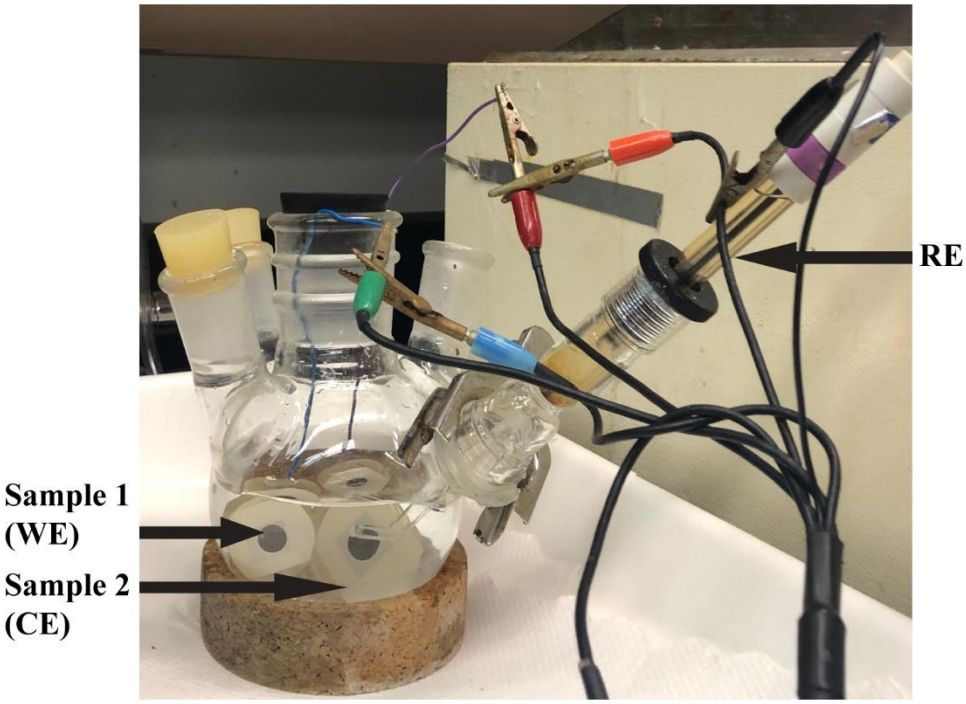

Figure 3.6 Setup of galvanic corrosion tests.

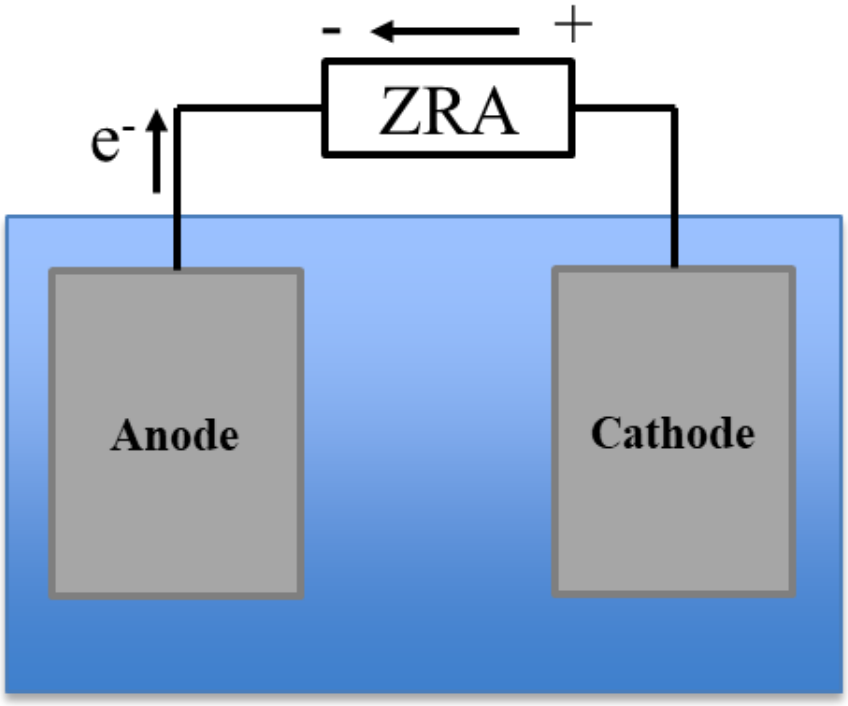

Figure 3.7 Configuration of galvanic corrosion tests.

3.3 Materials characterization

3.3.1 Microstructure characterization

3.3.1.1 Surface preparation

Microstructure of DSSs in as-received and heat-treated states is characterized using scanning electron microscopy and optical microscope. The mounted sample is ground and then polished to mirror finish using 0.05μm alumina.

Table 3.1 Etching conditions for metallographic preparation

Etchant	Composition	Volts	Time
40 wt% NaOH	60 mg NaOH 90 ml distilled water	2.5 V	10 seconds
Pellegrino's etchant	50 ml HCl (37%) 25 ml HNO_3 (70%) 50 ml distilled water	Chemical etching	20-180 seconds

To better distinguish between different phases, the polished surface is etched using different etching procedures. The conditions are shown in Table 3.1. Electrolytic etching in NaOH etchant is good for the phase contrast. The ferrite phase appears dark and intermetallic phases are revealed after etching. Nitrides and carbides are partially or completely dissolved after electrolytic etching in 40 wt% NaOH, leaving dark spots under optical microscope or SEM characterization. This leads to better phase contrast but makes positive identification of the chemical composition of the particles difficult using energy

dispersive X-ray diffraction (EDS) analysis. Compared with electrolytic etching, chemical etching in Pellegrino's etchant is less aggressive and precipitates remain in the microstructure after etching.[102]

3.3.1.2 SEM coupled with EDS analysis

For the chemical analysis of the phases in DSSs, SEM/EDS technique is used. Excitation voltage of 15 keV and 20 keV are usually used. Single-sided copper tape is used for the beam calibration. To avoid the overlapping of molybdenum (Mo) and sulfur (S) energy levels, L shell is used for the analysis of sulfur content. It should be noted that EDS analysis for elements lighter than sodium (Na), such as carbon (C) and nitrogen (N), is semi-quantitative. Usually carbon contamination within the SEM chamber is unavoidable.

3.3.1.3 Volume fraction calculation

To characterize the volume fraction of the ferrite phase, point-counting method is used. As shown in Figure 3.8, the microstructure of an annealed sample is polished to mirror finish and electrolytically etched in 40 wt% NaOH. The ferrite phase appears darker compared with the austenite phase. At least five fields of view are taken for analysis. For each field of view, the volume fraction of the ferrite phase is the number of points at the line intersections located in the ferrite phase divided by the number of total points at the line intersections, which as shown in Figure 3.8, is 100. For the analysis of volume fraction of precipitates, the surface is also etched in 40 wt% NaOH and images are analyzed by an image analysis software.

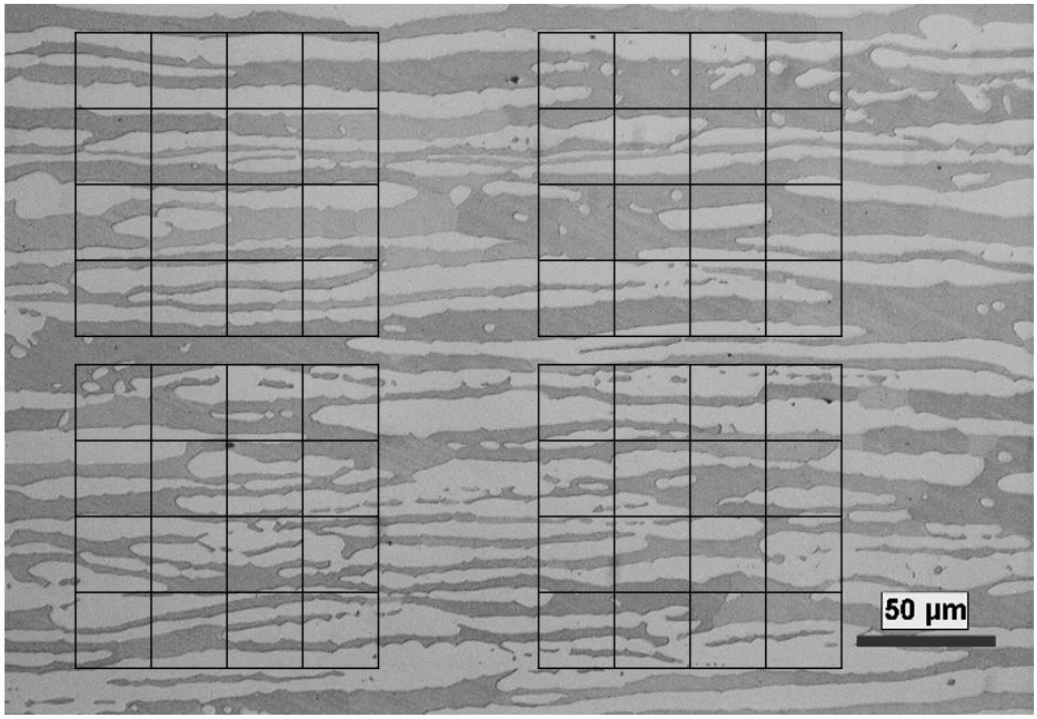

Figure 3.8 Point-counting method used to characterize the volume fraction of the ferrite phase in the microstructure. Polished surface is electrolytically etched in 40% NaOH.

3.3.1.4 Feritscope

In addition to the volume fraction calculation using point-counting method and image analysis software, a non-destructive Feritscope can also be used to characterize the ferrite number in the material using a magnetic induction method. However, in addition to the ferrite phase, other magnetizable phases such as strain-induced martensite is also measured using Feritscope.

3.3.2 Identification of phases

In addition to SEM/EDS analysis and Ferritscope, X-ray diffraction (XRD) was also used to identify the phases in the heat-treated specimens. The XRD patterns were

obtained using an X'Pert PROMRD X-ray diffractometer with Cu K_α radiation. The diffraction angles (2θ) were between 30° and 60°. The step size was 0.033° and time per step was 350 seconds.

3.3.2 Characterization of pits

After electrochemical tests, the surface of the test sample is rinsed in distilled water and then dried. For pitting corrosion, pit morphology is characterized using optical microscope and SEM. To characterize the depth of pits or surface scratch, a chromatic confocal profilometer is used. The step size used for the profilometer stage is as small as 10 nm, so a detailed characterization of a pit with the size of several microns can be realized.

CHAPTER 4. EFFECTS OF THIOSULFATE AND SULFATE ANIONS ON PITTING CORROSION OF LDSS

4.1 Introduction

Thiosulfate ions are present in a wide range of industrial environments such as in the pulp and paper industry, refinery environment, and gold leaching solutions. Thiosulfates can also be produced through the oxidation of sulfide or by the reduction of sulfate ions.[84] After sodium hydrosulfite was utilized as brightening agent in the pulp and paper industry, fast degradation of bronze wire, as well as pitting and crevice corrosion problems in steels occurred, which were found to be caused by the presence of thiosulfates in the white water environment of paper machines.[1] It has been proposed that thiosulfate mainly activates anodic dissolution on base metals where the passive film is broken either chemically by aggressive ions like chloride or sulfate-containing solutions,[76, 78] or mechanically through scratching or stretching.[75, 79, 80] The presence of thiosulfate ions in the paper machine white water has been shown to increase pitting susceptibility of UNS S30403 and UNS S31603 stainless steels. [75, 76, 82]

In this chapter, pitting corrosion behavior of lean duplex stainless steel grades UNS S32101, UNS S32304, UNS S32003 and UNS S82441 in thiosulfate-containing sodium chloride solutions was studied using both potentiodynamic cyclic polarization tests and scratch tests. The results not only provide insights into the performance of these alloys in

paper-machine environments, but also contribute to the understanding of mechanisms by which thiosulfate ions affect pitting in different lean duplex stainless steels.

4.2 Experimental details

Mill-annealed duplex stainless steels UNS S32003, S32304, S32101 and S82441 were used in this study. Chemical composition of these steels is shown in Table 1.1. Test samples, with dimension of 1 cm x 1 cm, were cut out of the steel plates and were in the as-received state. Alloy samples were mounted in epoxy. A metal wire was attached at the back of each alloy sample, prior to epoxy-mounting, for electric connection for electrochemical tests.

Simulated paper machine white water variants were made from reagent grade sodium chloride (NaCl), sodium sulfate (Na_2SO_4) and sodium thiosulfate ($Na_2S_2O_3$) in deionized water. The solution was naturally aerated and kept at 50 °C during the test. Before each test, the samples were polished to 2000 grit and cleaned with ethanol and acetone. Electrochemical tests were conducted using a potentiostat.

In potentiodynamic cyclic polarization tests, the polished and cleaned sample surface was covered with a punched electroplating tape, with exposed area of around 0.2 cm^2, to avoid crevice corrosion. The potential was swept from -0.6 V_{SCE} to 1.2 V_{SCE} or until a current density of 1 mA/cm^2 was exceeded. The forward scan rate was 0.1 mV/s and the reverse scan rate was 1.5 mV/s. Pit morphology in terms of size and shape was observed after each test using an optical microscope. Any data, where the sample showed any signs of crevice corrosion, was discarded. At least three tests were performed for each test condition. Pitting corrosion was confirmed from both cyclic polarization curves where

hysteresis loop was present, as well as by examining the tested sample using an optical microscope. Transpassive behavior, where there was no hysteresis loop in the cyclic polarization curve, was used as an indication that the alloy was not susceptible to localized corrosion attack under the tested environmental conditions. In subsequent analysis of data, pitting potential (E_{pit}) was defined as the potential at which the anodic current density exceeded 100 $\mu A/cm^2$ while the repassivation potential (E_{rp}) was determined by the potential where the backward potential scan curve intersected the forward potential scan curve and a hysteresis loop was formed. However, in tested thiosulfate containing environments, there was no crossover in the hysteresis loop and the E_{rp} was defined as the open circuit potential re-established from the reverse polarization scan.

Potentiodynamic cyclic polarization tests were conducted in solutions containing NaCl, ($NaCl + Na_2S_2O_3$), and ($NaCl + Na_2SO_4$), respectively, to see how different molar ratios of Cl^- and $S_2O_3^{2-}$, and that of Cl^- and SO_4^{2-} would affect the pitting corrosion behavior of selected grades of duplex stainless steels. Further, the tests were also conducted in solutions containing ($NaCl + Na_2S_2O_3 + Na_2SO_4$) ions to simulate the corrosion behavior of selected grades of duplex stainless steels in paper machine white water.

The objective of scratch tests was to investigate how thiosulfates interact with bare alloy surface and affect alloys' ability to repassivate in tested environments. The solution used was concentrated paper machine white water with (300 mg/L Cl^- + 58 mg/L $S_2O_3^{2-}$) by a concentration factor of twenty at 50 °C. The samples were polarized at 0, -100, -200 and -300 mV_{SCE}, respectively, for 60 seconds and then scratched using a diamond scriber. The current transient was recorded for 60 seconds after the surface was scratched. The peak

at 0 s corresponded to the moment when the passive film on the surface was removed by scratch.

Pit morphology and the corrosion product were characterized using SEM coupled with EDS. The samples were cleaned and lightly etched with 40 wt% NaOH solution to reveal their microstructure. Profilometer was used to characterize the shape and the depth of corrosion pits.

4.3 Potentiodynamic cyclic polarization behavior of LDSSs

4.3.1 LDSSs in solutions containing only NaCl

Potentiodynamic cyclic polarization curves of four different LDSSs in NaCl solution with 300 mg/L Cl^- at 50 °C are shown in Figure 4.1. Pitting corrosion occurred on both UNS S32101 and S32304. However, UNS S32003 and S82441 showed transpassive behavior and were resistant to pitting corrosion under this condition. Compared with UNS S32304, there were significantly more metastable pitting events during potentiodynamic polarization of UNS S32101. Average pitting potential and 95% confidence interval are shown in Figure 4.2. Average pitting potential of UNS S32101 is ~370 mV lower than that of UNS S32304. Based on these results, ranking of pitting corrosion resistance of the four LDSSs is: UNS S32101 < S32304 < S32003 and S82441.

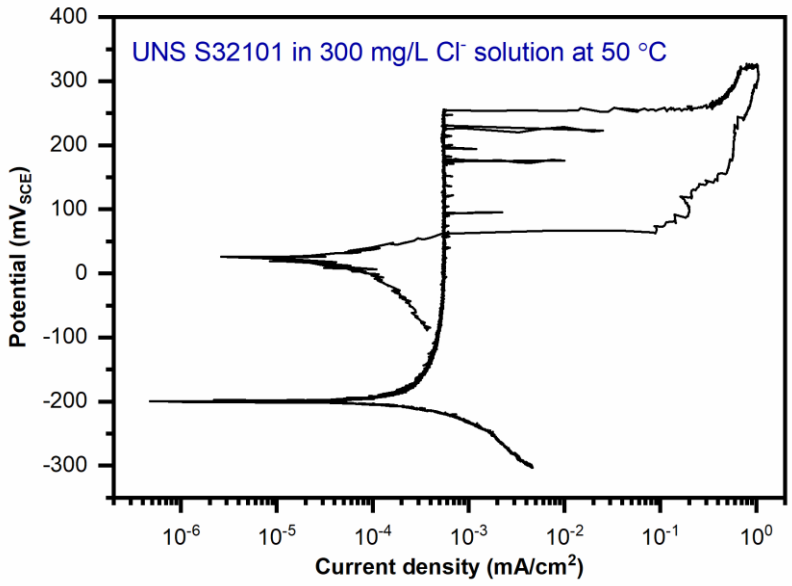

(a)

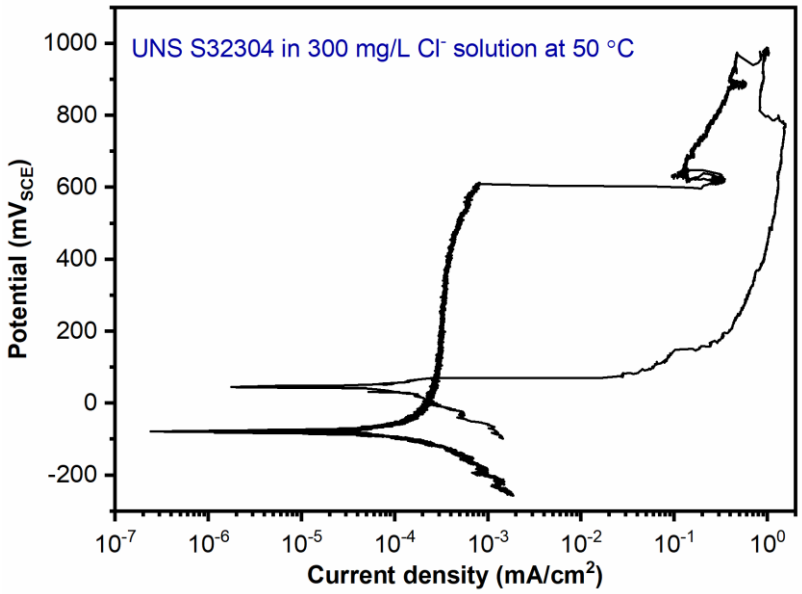

(b)

Figure 4.1 Potentiodynamic cyclic polarization curve in 300 mg/L Cl^- solution at 50 °C. (a) UNS S32101; (b) UNS S32304; (b) UNS S32003; (c) UNS S82441.

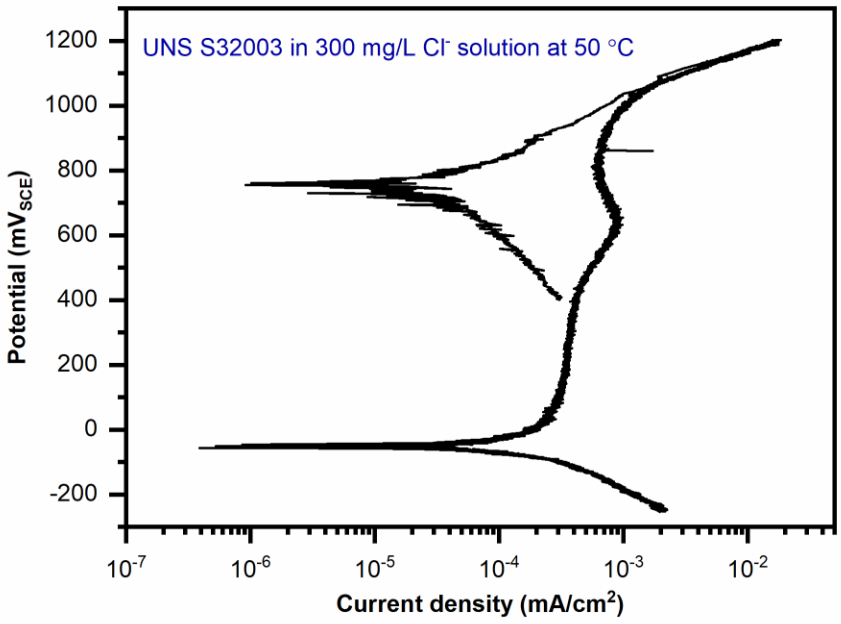

(c)

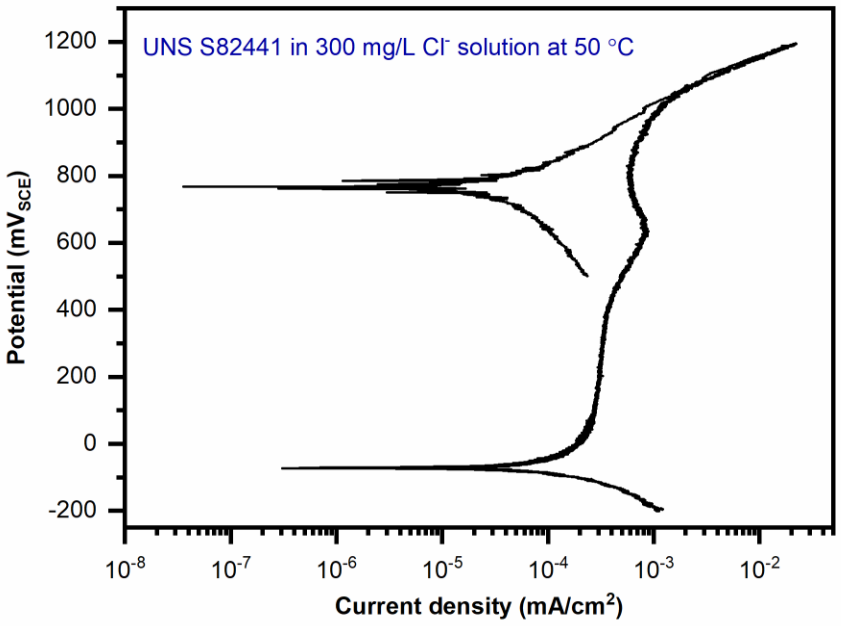

(d)

Figure 4.1 Continued

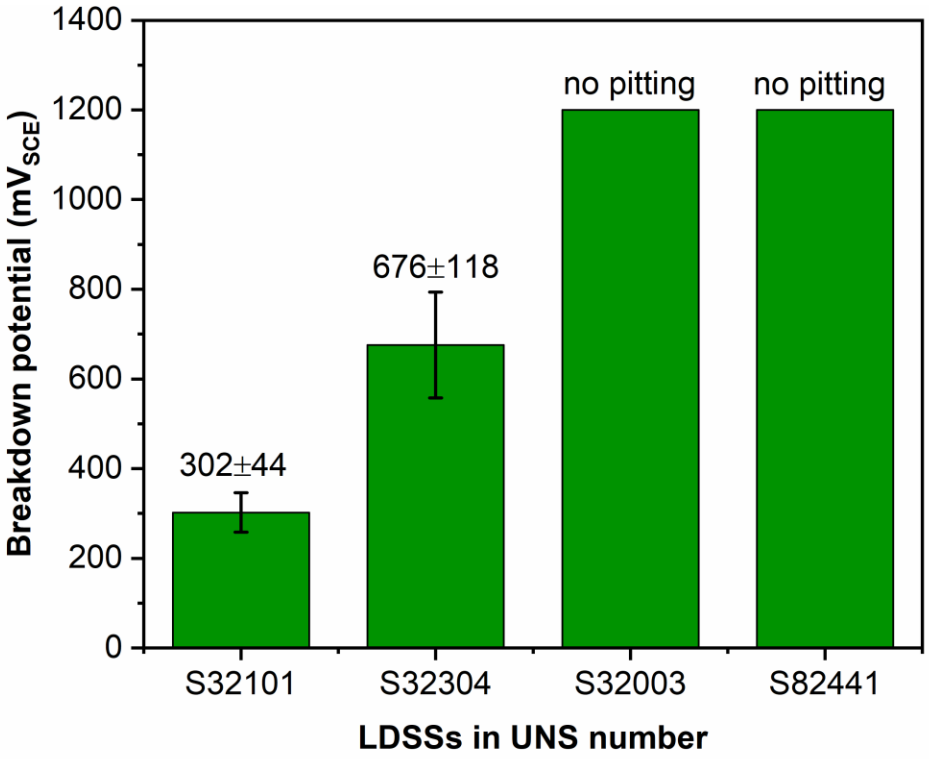

Figure 4.2 Breakdown potential of different LDSSs in NaCl solution with 300 mg/L Cl^- at 50 ℃.

Pits formed on UNS S32101 and S32304 in NaCl solution were observed under optical microscope and SEM. As shown in Figure 4.3, the pits have round shapes with diameters of tens of microns. A lacy pit cover was clearly visible on UNS S32304 sample, as shown in Figure 4.3(b).

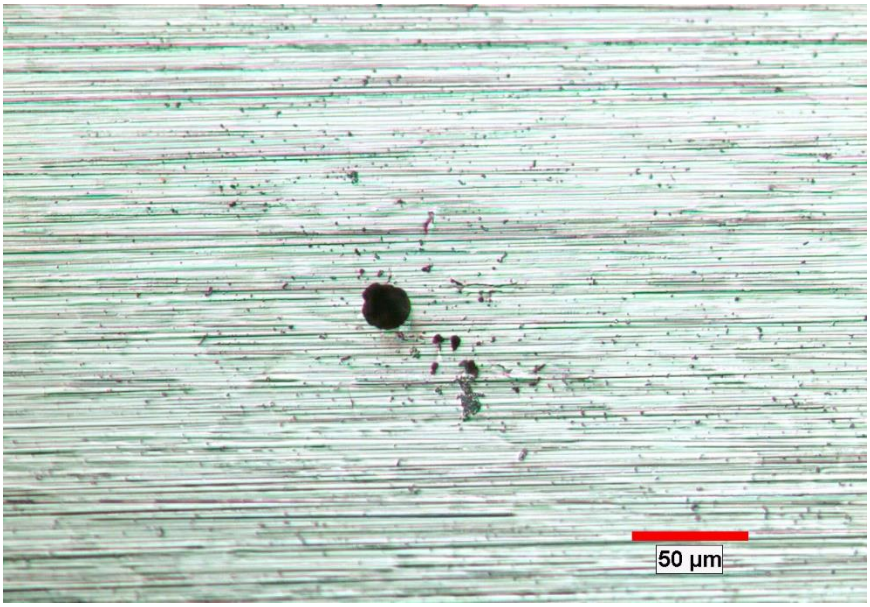

(a)

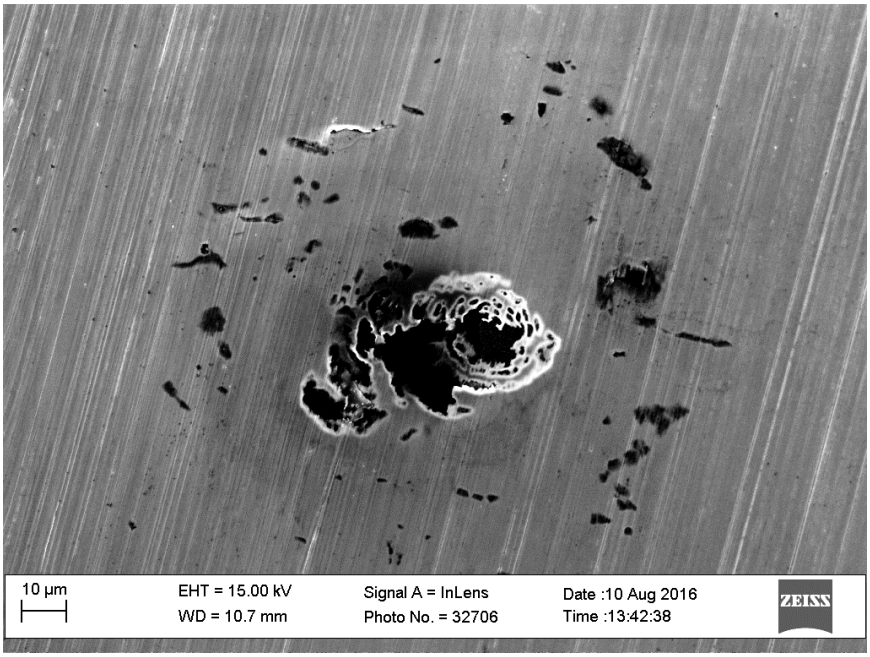

(b)

Figure 4.3 Pit morphology of (a) UNS S32101 and (b) UNS S32304.

4.3.2 Potentiodynamic cyclic polarization behavior of LDSSs in environments containing both sodium chloride and sodium thiosulfate

In this section, $Na_2S_2O_3$ was added to NaCl solution and the environments studied are shown in Table 4.1. Concentrations of Cl^- ions was kept constant at 300 mg/L and the $S_2O_3^{2-}$ concentration was changed so that the molar ratio of Cl^- to $S_2O_3^{2-}$ was varied from 33 and 16 to 8, respectively.

Table 4.1 Anion concentration of Cl^- and $S_2O_3^{2-}$ and $Cl^-/ S_2O_3^{2-}$ molar ratio used in this section.

Environment	Anion concentration		Molar ratio	Temperature (°C)
	Cl^- [mg/L]	$S_2O_3^{2-}$[mg/L]	[$Cl^-/ S_2O_3^{2-}$]	
Environment 1	300	29	33	50
Environment 2	300	58	16	50
Environment 3	300	116	8	50

Typical potentiodynamic polarization curves of LDSSs in environment 1 with 300 mg/L Cl^- and 29 mg/L $S_2O_3^{2-}$ are shown in Figure 4.4. Similar to the pitting results in NaCl-only solution, UNS S32003 and S82441 were resistant to pitting corrosion in environment 1. Hysteresis loop was present in cyclic polarization curves for UNS S32101 and S32304 in environment 1. Average pitting potential and 95% confidence interval are shown in Figure 4.5. Pitting potential of UNS S32101 is ~480 mV lower than that of UNS S32304. Repassivation potential for alloys UNS S32101 and UNS S32304 were below their open circuit potential in the presence of 29 mg/L $S_2O_3^{2-}$ in 300 mg/L Cl^- solution, as shown by

the results in Figure 4.4 (a) and (b). Ranking of pitting corrosion resistance of the four LDSSs in solution containing 300 mg/L Cl^- and 29 mg/L $S_2O_3^{2-}$ is the same with that in environment containing 300 mg/L Cl^-: UNS S32101 < S32304 < S32003 and S82441.

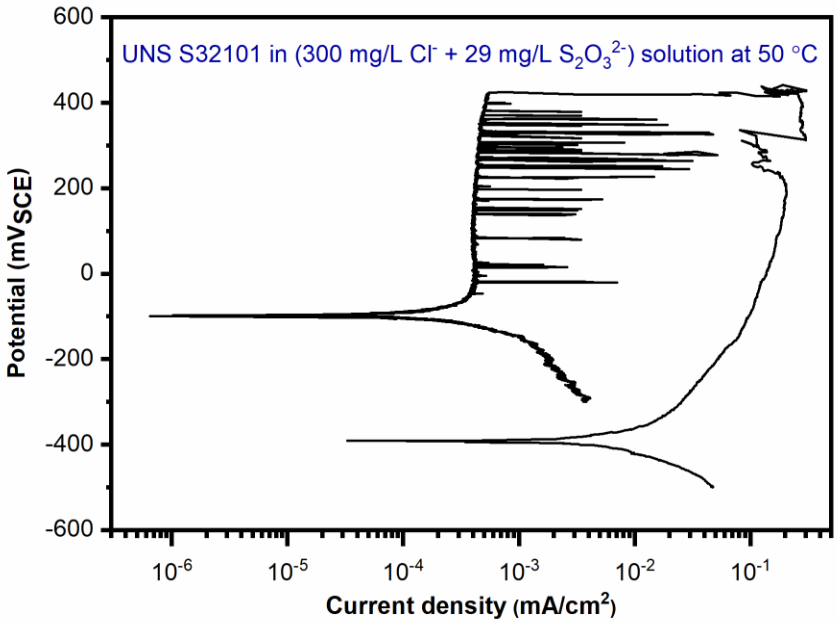

(a)

Figure 4.4 Cycylic potentiodynamic polarization curves of (a) UNS S32101; (b) UNS S32304; (c) UNS S32003; (d) UNS S32404 in (300 mg/L Cl^- + 29 mg/L $S_2O_3^{2-}$) solution at 50 °C.

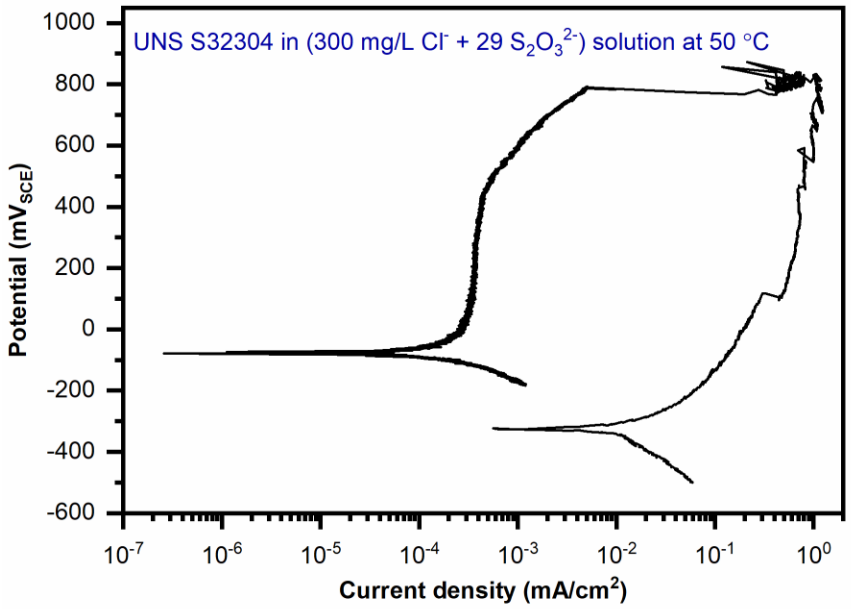

(b)

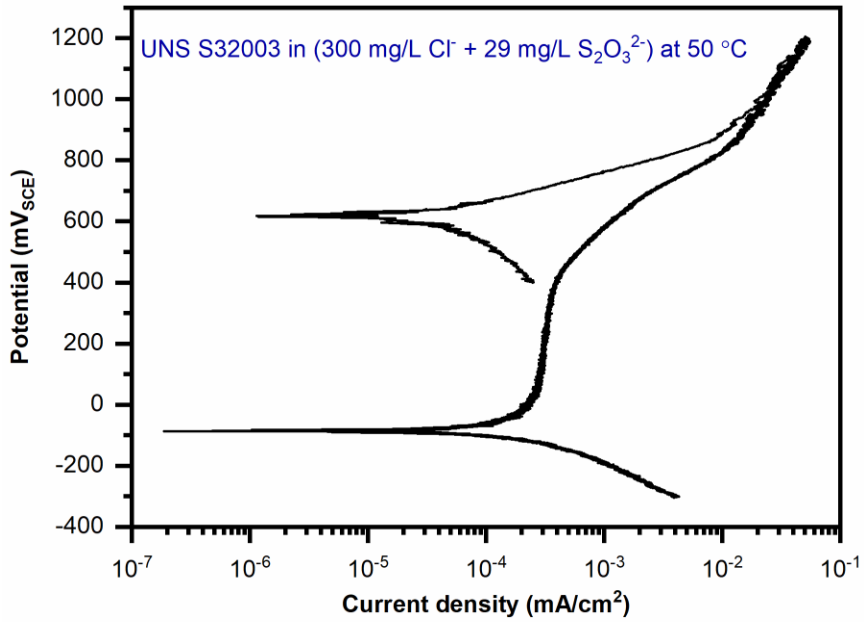

(c)

Figure 4.4 Continued.

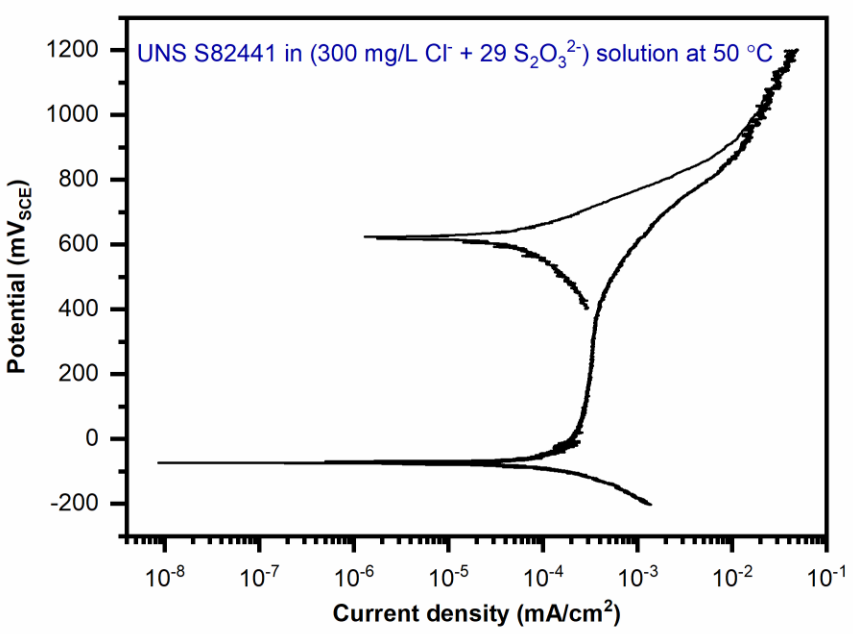

(d)

Figure 4.4 Continued.

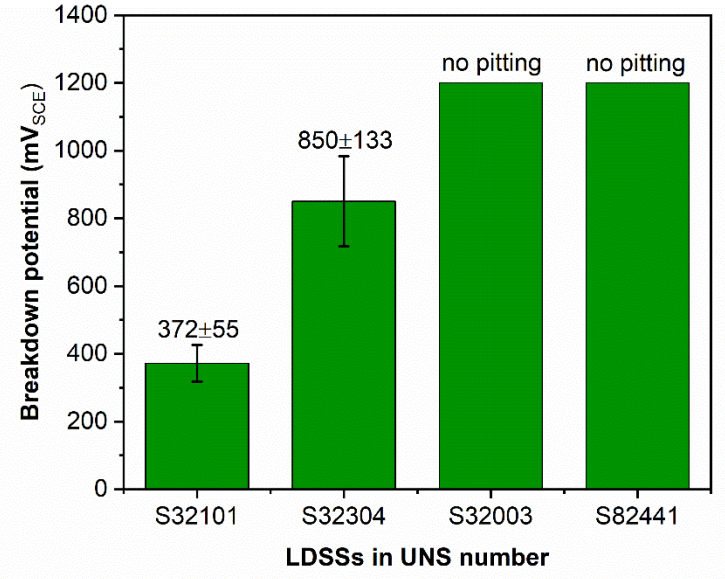

Figure 4.5 Breakdown potential of different LDSSs in solution containing NaCl and $Na_2S_2O_3$ with (300 mg/L Cl^- + 29 mg/L $S_2O_3^{2-}$) at 50 °C.

With the addition of $Na_2S_2O_3$, metastable pitting events on UNS S32101 were promoted and the number of metastable pitting events is increased when $Na_2S_2O_3$ is present, as shown in Figure 4.6. Comparisons of pitting potential and repassivation potential of UNS S32101 and S32304 in environments without and with the addition of $Na_2S_2O_3$ are shown in Figure 4.7. Pitting potential of UNS S32101 increased ~70 mV and that of S32304 increased ~170 mV when 29 mg/L $S_2O_3^{2-}$ is added to 300 mg/L Cl^- solution. In comparison, the decrease of repassivation potential of both LDSSs was more than 400 mV and the hysteresis loop was not closed, indicating a stronger effect of $S_2O_3^{2-}$ on the repassivation of pits.

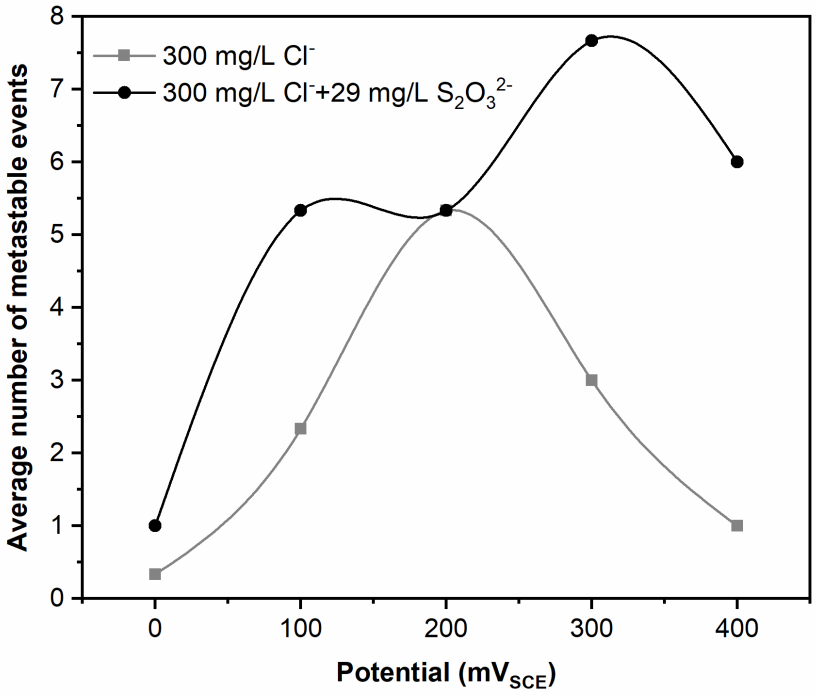

Figure 4.6 Average number of metastable pitting events within different potential range. 0: -100 to 0 mV_{SCE}; 100: 0 to 100 mV_{SCE}; 200: 100 to 200 mV_{SCE}; 300: 200 to 300 mV_{SCE}; 400: 300 to 400 mV_{SCE}. Potential scan rate was the same for the two sets of tests.

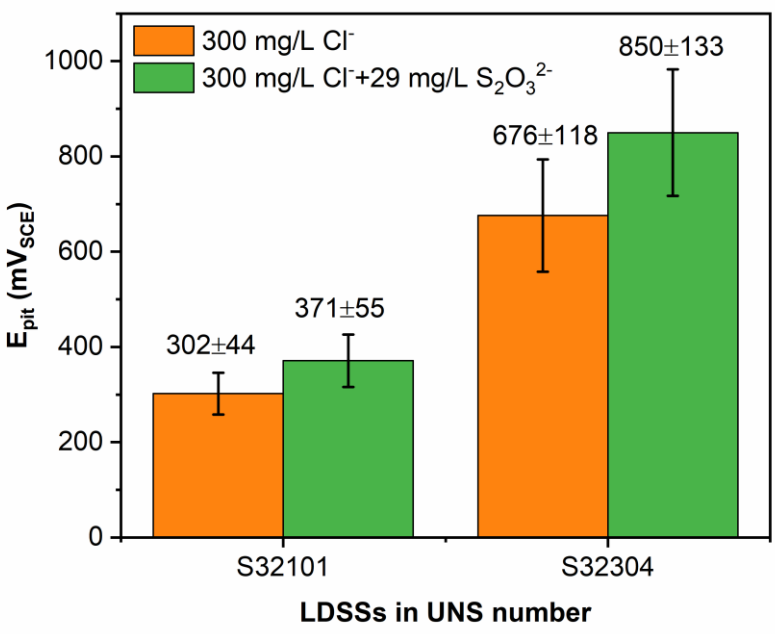

(a)

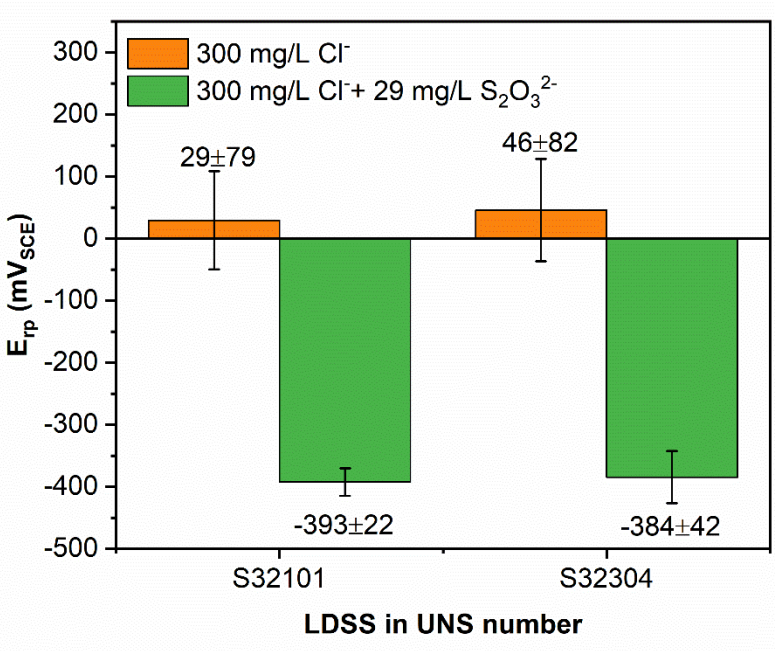

(b)

Figure 4.7 (a) Pitting potential and (b) repassivation potential of UNS S32101 and S32304 in environments containing 300 mg/L Cl^- and (300 mg/L Cl^- + 29 mg/L $S_2O_3^{2-}$).

Further, pitting corrosion behavior was only studied for UNS S32304, S32003 and S82441 in environments containing higher concentrations of $S_2O_3^{2-}$ in 300 mg/L Cl^- solutions, since pitting corrosion behavior of S32101 in similar environments has been studied elsewhere.[82] As shown in Figure 4.8 (c) and (d), similar to previous results, UNS S32003 and S82441 are resistant to pitting corrosion in the solution with 300 mg/L Cl^- and 58 mg/L $S_2O_3^{2-}$ and in the solution with 300 mg/L Cl^- and 116 mg/L $S_2O_3^{2-}$. However, for UNS S32304 samples, pitting corrosion was observed in some of the tests while in other equivalent tests the samples are resistant to pitting under otherwise similar conditions. Pitting corrosion susceptibility of LDSSs under the tested conditions is summarized in Table 4.2. When 58 mg/L $S_2O_3^{2-}$ is added, pitting corrosion was observed in 4 tests out of 9 tests done under similar conditions, while when 116 mg/L $S_2O_3^{2-}$ was added, pitting only occurs in 2 tests out of 9 tests, indicating an inhibitive effect of thiosulfate addition and a higher tendency of transpassive behavior at higher $S_2O_3^{2-}$ concentrations.

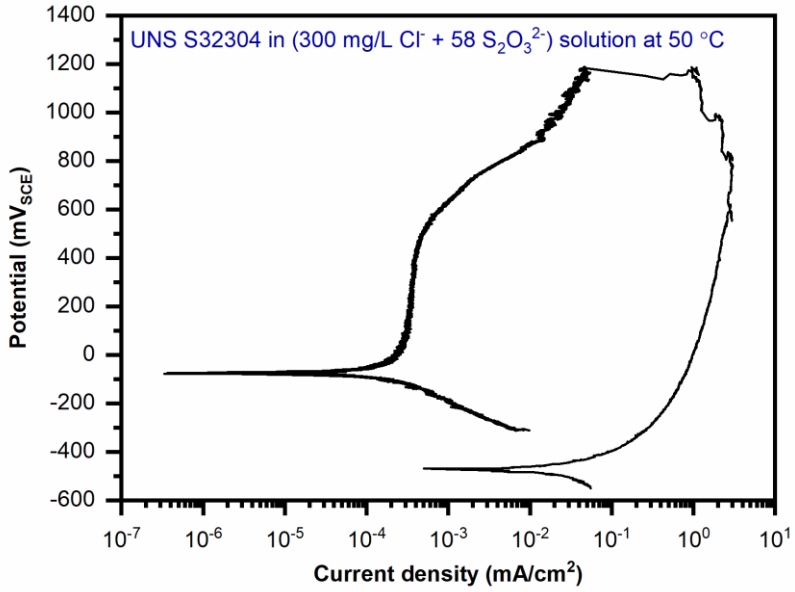

(a)

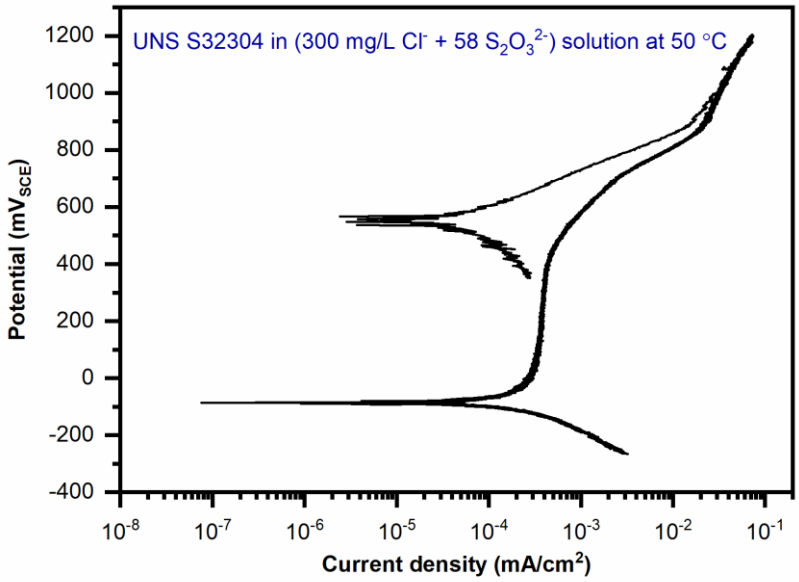

(b)

Figure 4.8 Typical cycylic potentiodynamic polarization curves of (a) UNS S32304 with pitting corrosion; (b) UNS S32304 showing transpassive behavior; (c) UNS S32003; (d) UNS S32404 in (300 mg/L Cl^- + 58 mg/L $S_2O_3^{2-}$) and (300 mg/L Cl^- + 116 mg/L $S_2O_3^{2})^-$ solution at 50 °C.

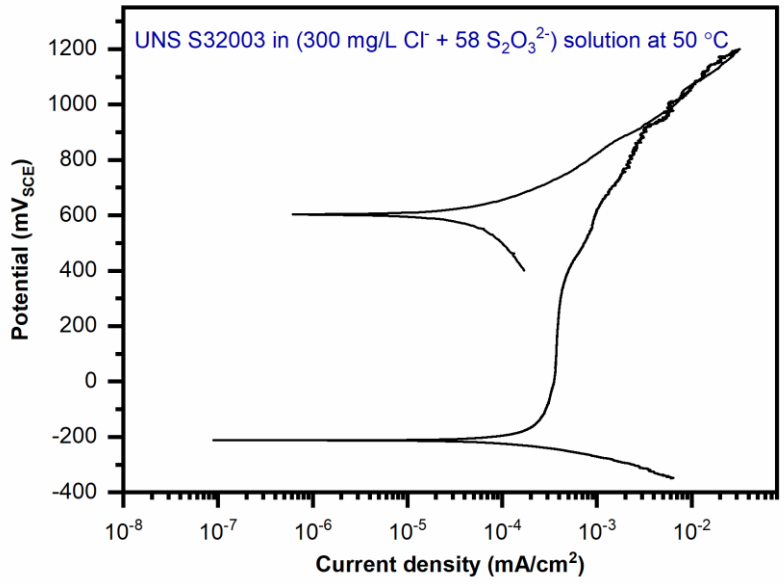

(c)

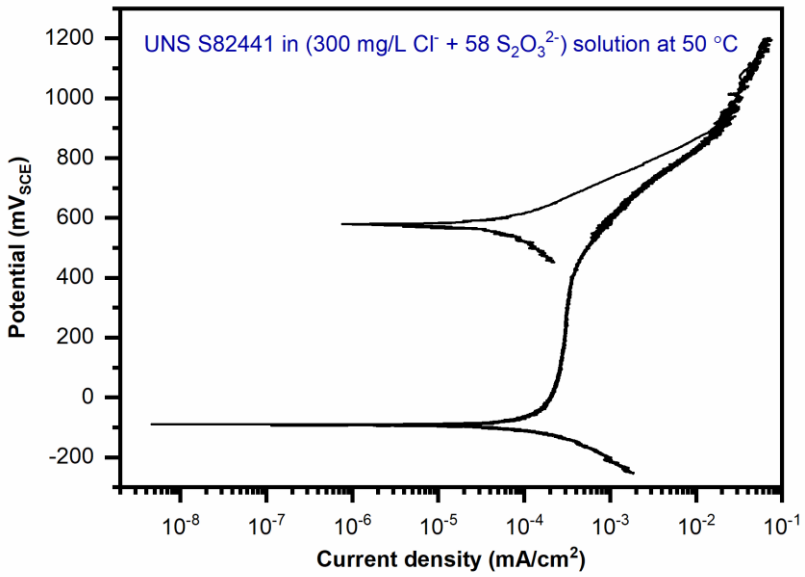

(d)

Figure 4.8 Continued.

Table 4.2 Pitting corrosion susceptibility of duplex stainless steels in solutions containing Cl^- and different amount of $S_2O_3^{2-}$.

Environment		Molar ratio	Pitting corrosion			
Cl^- [mg/L]	$S_2O_3^{2-}$ [mg/L]	[Cl^- /$S_2O_3^{2-}$]	UNS S32101	UNS S32304	UNS S32003	UNS S82441
300	0	-	Yes	Yes	No	No
300	29	33	Yes	Yes	No	No
300	58	16	-	4/9 *	No	No
300	116	8	-	2/9 *	No	No
6000	580	33	-	Yes	Prone to crevice corrosion	No
6000	1160	16	-	Yes	No	No

*Number of times pitting was observed from the 9 tests done under the same environmental conditions.

To see the effect of overall concentration of the test solutions on pitting behavior of duplex stainless steels, the concentration was increased by a factor of twenty while keeping the Cl^- to $S_2O_3^{2-}$ ratio at 17. Again, both UNS S32003 and UNS S82441 showed transpassive behavior and there was no pitting corrosion on specimens in the tested concentrated solutions. However, pitting occurred on all test samples of UNS S32304 in the concentrated environment and a typical potentiodynamic cyclic polarization curve is shown in Figure 4.9. Comparing the pitting corrosion behavior of UNS S32304 in environments with Cl^- to $S_2O_3^{2-}$ ratio of 33, pitting corrosion resistance in terms of pitting potential and repassivation potential decreases with the increase of the ionic strength in the concentrated solution, as shown in Table 4.3.

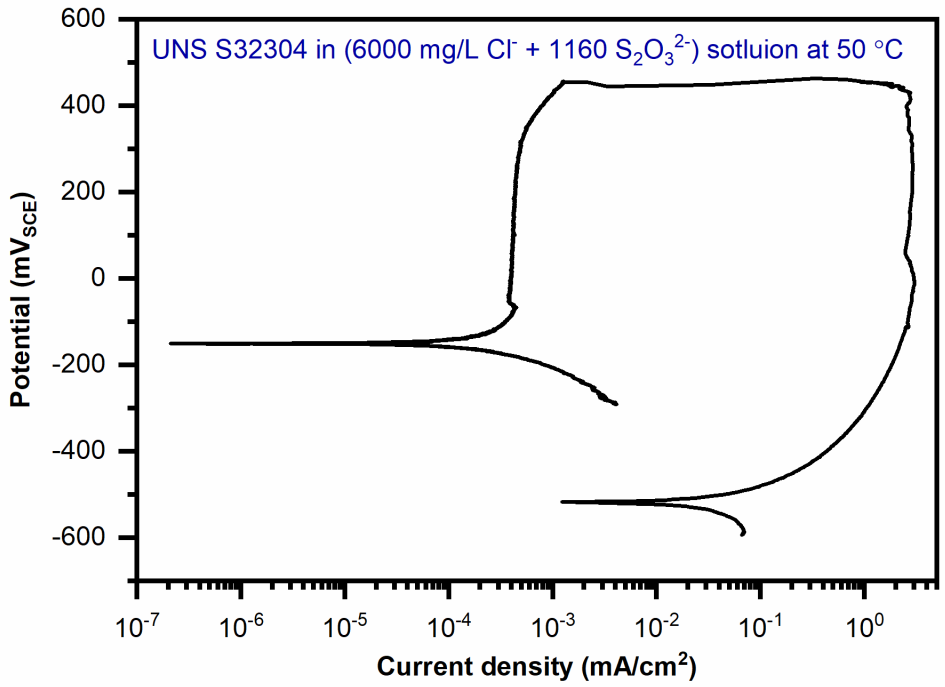

Figure 4.9 Potentiodynamic cyclic polarization curve of UNS S32304 in concentrated solution with 6000 mg/L Cl^- and 1160 mg/L $S_2O_3^{2-}$ at 50 °C.

Table 4.3 Pitting potential and repassivation potential of UNS S32304 in environments with Cl^- to $S_2O_3^{2-}$ ratio of 16.

Cl^- [mg/L]	$S_2O_3^{2-}$ [mg/L]	Molar ratio [Cl^- to $S_2O_3^{2-}$]	Pitting potential (mV_{SCE})	Repassivation potential (mV_{SCE})
300	29	33	676 ± 118	-384 ± 42
6000	580	33	454 ± 181	-514 ± 14

After cyclic polarization tests, surface of the tested samples was examined under an optical microscope or the scanning electron microscope (SEM). Different from the pits formed in solution containing only NaCl, pits formed on UNS S32101 and S32304 in environments containing Cl^- and $S_2O_3^{2-}$ showed preferential dissolution. An SEM image of

a pit formed on UNS S32304 in environment containing (300 mg/L Cl^- + 58 $S_2O_3^{2-}$) is shown in Figure 4.10 and there are branches extending from the center of the pit. Further, cross-sections of pits formed on UNS S32101 in environment containing (300 Cl^- + 29 $S_2O_3^{2-}$) were made and the optical micrographs are shown in Figure 4.11. Although the pits are formed on surfaces with different orientations, pits from both orientations showed a preferential dissolution of the ferrite phase.

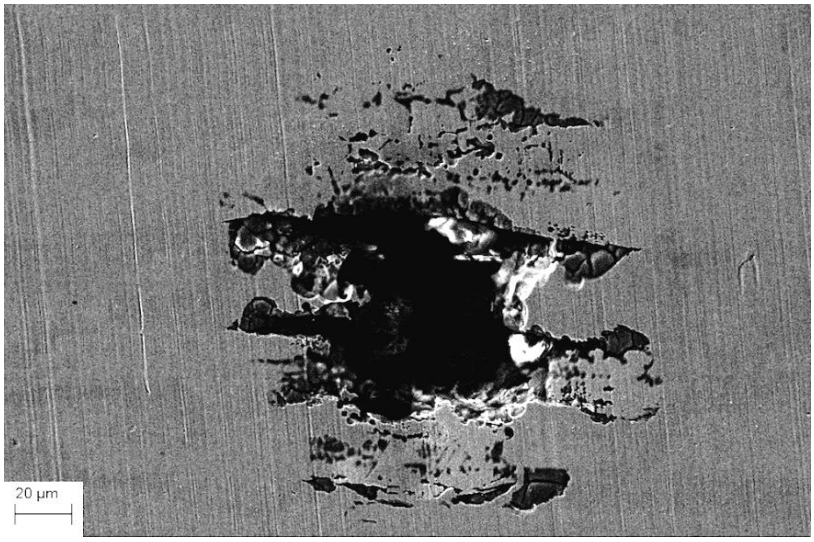

(a)

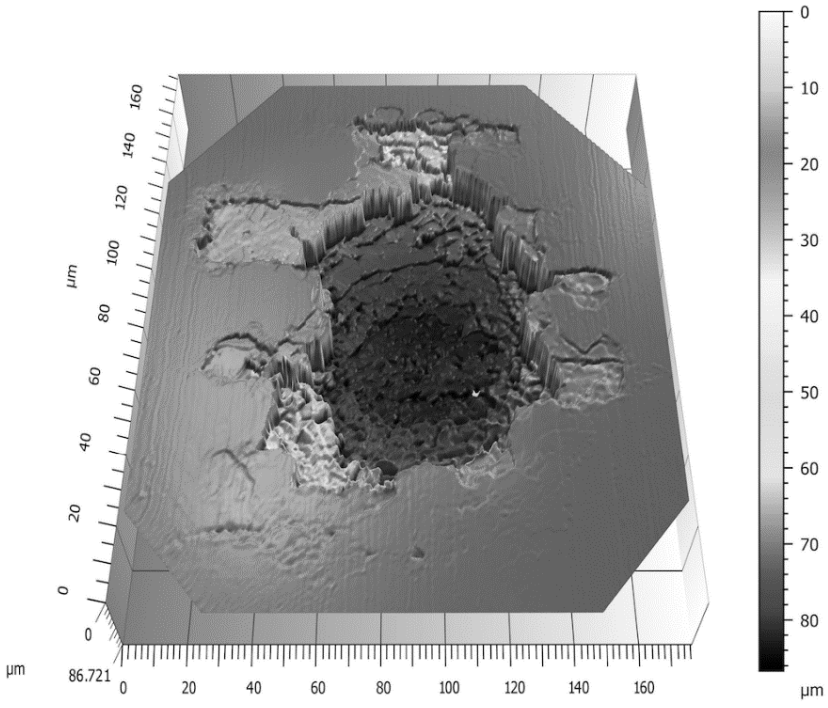

(b)

Figure 4.10 (a) SEM image and (b) profilometry of a pit formed on UNS S32304 in solution containing (300 mg/L Cl^- + 58 $S_2O_3^{2-}$).

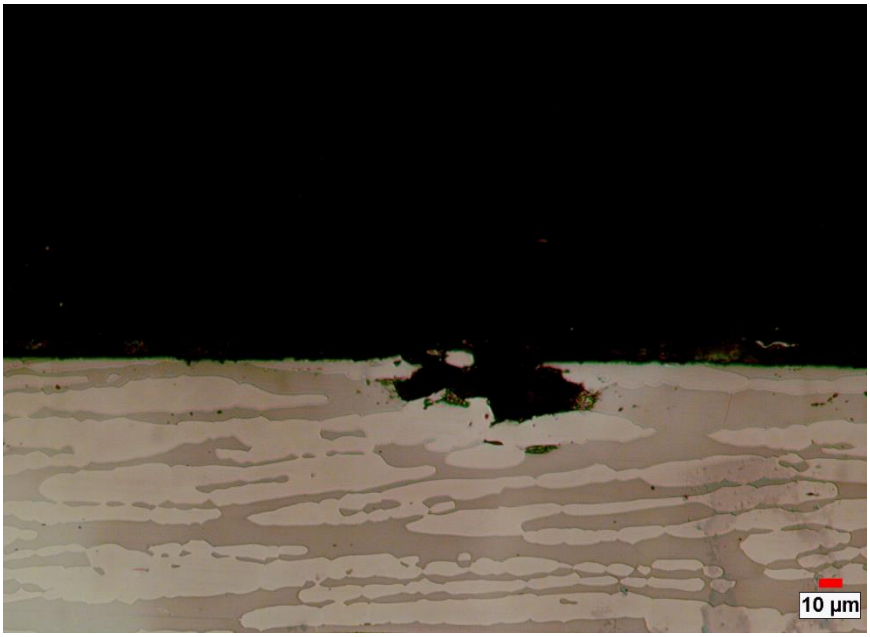

(a)

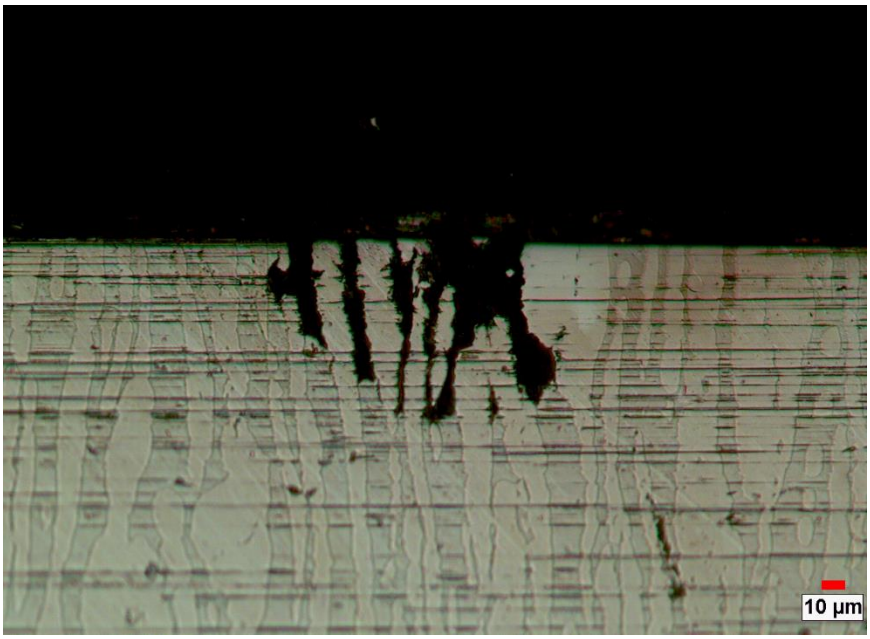

(b)

Figure 4.11 Cross-section of pits formed on UNS S32101 after polarization tests in environment containing Cl^- and $S_2O_3^{2-}$.

For the pits produced in environments containing $S_2O_3^{2-}$, corrosion product was accumulated inside the pits, especially when alloys were tested in concentrated solutions. A typical pit produced in (6000 mg/L Cl^- + 1160 mg/L $S_2O_3^{2-}$) solution was shown in Figure 4.11. EDS analysis was performed inside the pit and the corrosion product was found to be enriched in sulfur, and the chromium content was more than 50 wt% higher than the iron content inside the pit. The weight percent of each element in the corrosion product is listed in Table 4.4. Since the pit was rinsed and cleaned using deionized water, $S_2O_3^{2-}$ is expected to dissolve, therefore the sulfur content identified should be reduced sulfur formed inside the pit.

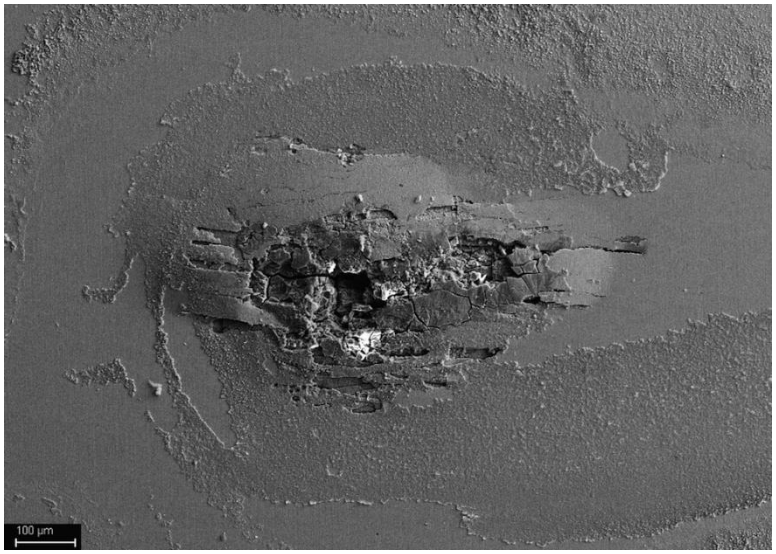

Figure 4.12 SEM image of pit formed on UNS S32304 in concentrated solution containing Cl^- and $S_2O_3^{2-}$.

Table 4.4 EDS analysis of corrosion product inside pits formed on UNS S32304 in concentrated solution containing $Cl^-$and $S_2O_3^{2-}$.

Element	Cr	Fe	Ni	Mo	Mn	Cu	S
Wt%	66.7	12.0	4.1	0.03	0.8	0.9	6.6

4.3 Effects of thiosulfate anions on repassivation behavior of DSSs

The objective of scratch tests was to investigate how thiosulfate ions may interact with the bare alloy surface and affect alloys' ability to repassivate in tested environments. The solution used was concentrated paper machine white water (300 mg/L Cl^- + 58 mg/L $S_2O_3^{2-}$), with a concentration factor of twenty, at 50 °C. The samples were polarized at 0, -100, -200 and -300 mV_{SCE}, respectively, for 60 seconds and then scratched using a diamond scriber. The current transient was recorded for 60 seconds after the surface was scratched. The peak at 0 s corresponded to the moment when the passive film on the surface was removed by scratch.

For UNS S2003 sample, the current after the scratch decreased to the passive current value when the sample was polarized at four different potentials, as shown in Figure 4.13 (a), indicating that there is no localized corrosion after the film was removed. This was confirmed by the observation of the scratched surface under an optical microscope after the test, as shown in Figure 4.13 (b), and no pit propagated from the scratch.

Similar to UNS S32003 sample, for S82441 sample, when polarized at -300 mV_{SCE}, -200 mV_{SCE}, -100 mV_{SCE} and 0 V_{SCE}, respectively, the current decreased to the passive current after scratch, as shown in Figure 4.14 (a). Metastable pitting occurred at 0 V_{SCE}. The micrographs of the scratched surfaces are shown in Figure 4.14 (b) and no pit was found to develop from the scratch when the sample was polarized at the four applied potentials.

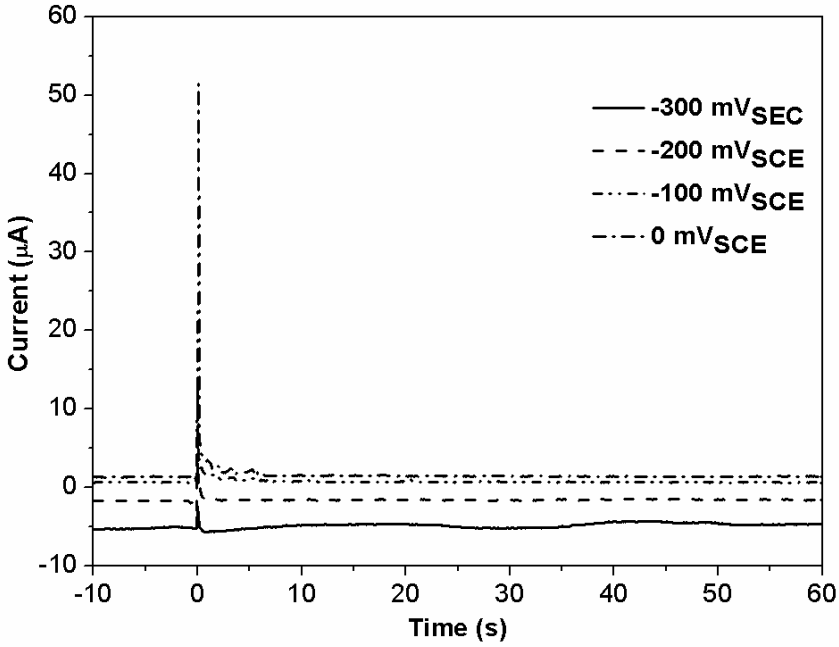

(a)

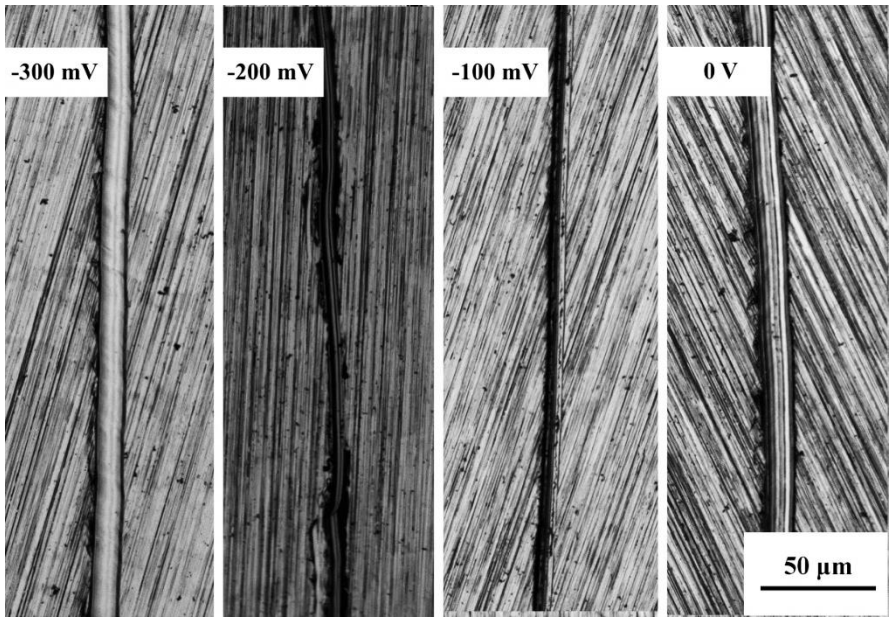

(b)

Figure 4.13 (a) Current transient during scratch test on UNS S32003; (b) Optical micrograph of scratches on UNS S32003 after scratch tests.

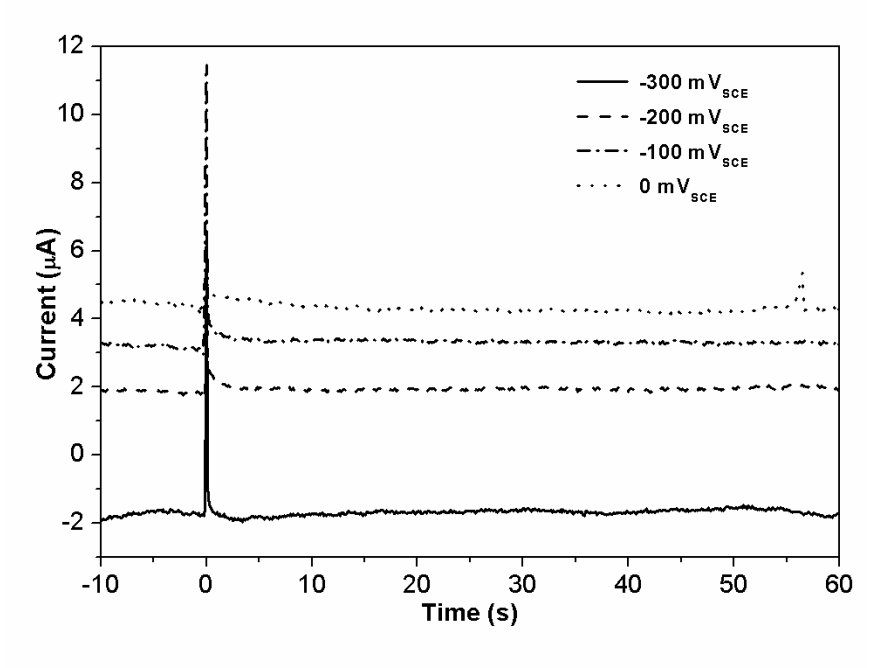

(a)

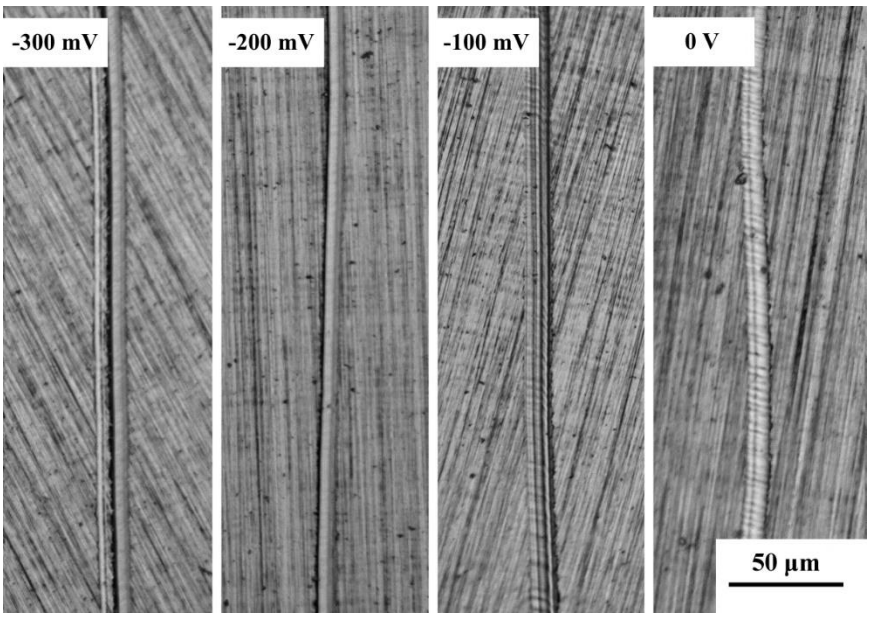

(b)

Figure 4.14 (a) Current transient during scratch test on UNS S82441; (b) Optical micrograph of scratches on UNS S82441 after scratch tests.

UNS S32304 sample was more prone to pitting corrosion compared with S32003 and S82441 samples when the passive film was removed through scratch. The S32304 sample repassivated within less than 0.2 seconds when the scratch test was done at -300 mV_{SCE}. When the samples were polarized at potentials higher than -300 mV_{SCE}, pits propagated from the scratch line, as shown in Figure 4.15 (b). For the same test time, the pits formed on the sample polarized at 0 V_{SCE} were larger than those formed on samples polarized at lower potentials, indicating a higher pit growth rate, which resulted in a higher current after scratch at $0V_{SCE}$, as shown in Figure 4.15 (a).

Figure 4.16 shows the SEM images of the scratched surface of UNS S32304 and S32101, which clearly show a preferential dissolution of the ferrite phase after the test. Since the scratch was made perpendicular to the rolling direction of the steels sample, the orientation of the pits is also perpendicular to the scratch line.

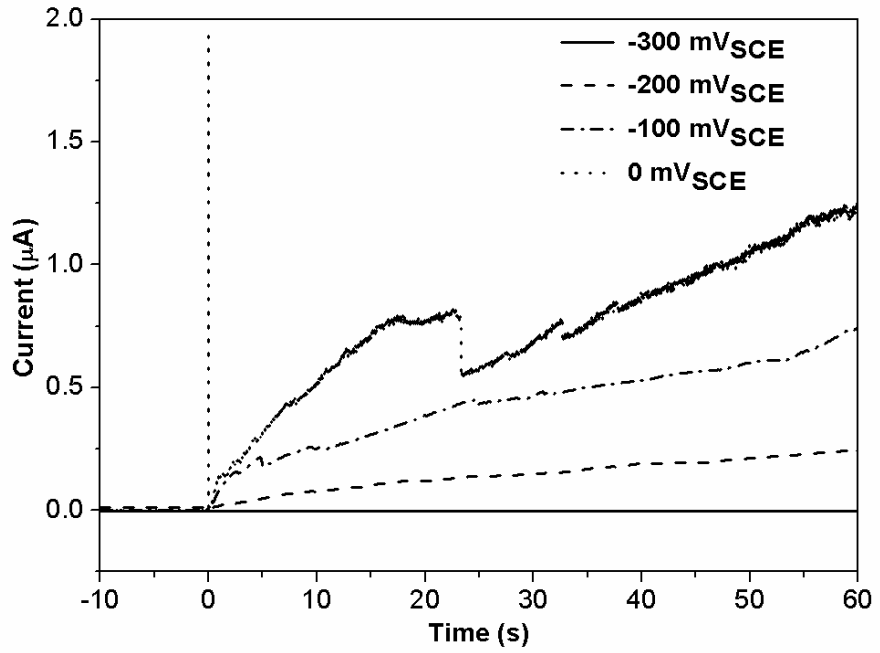

(a)

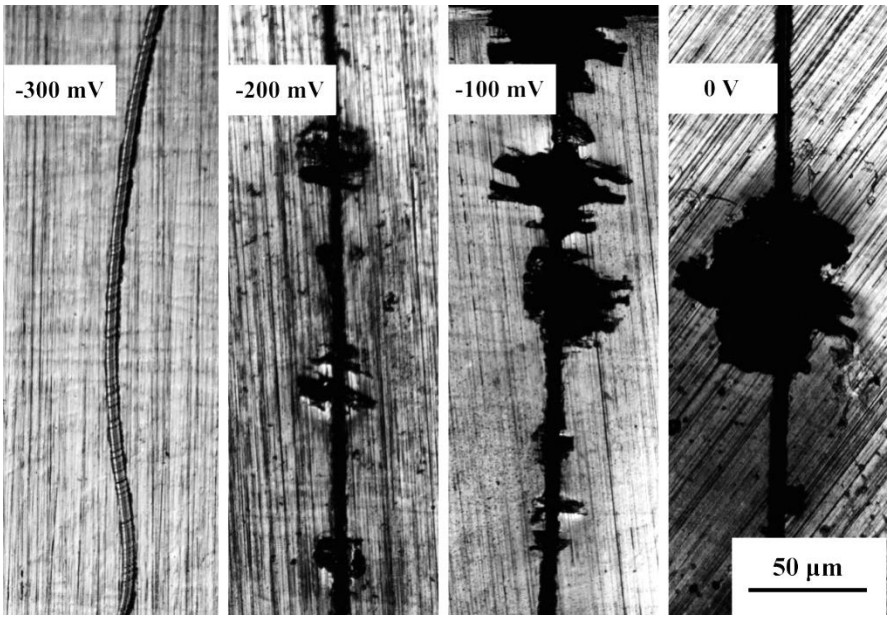

(b)

Figure 4.15 (a) Current transient during scratch test on UNS S32304; (b) Optical micrograph of scratches on UNS S32304 after scratch tests.

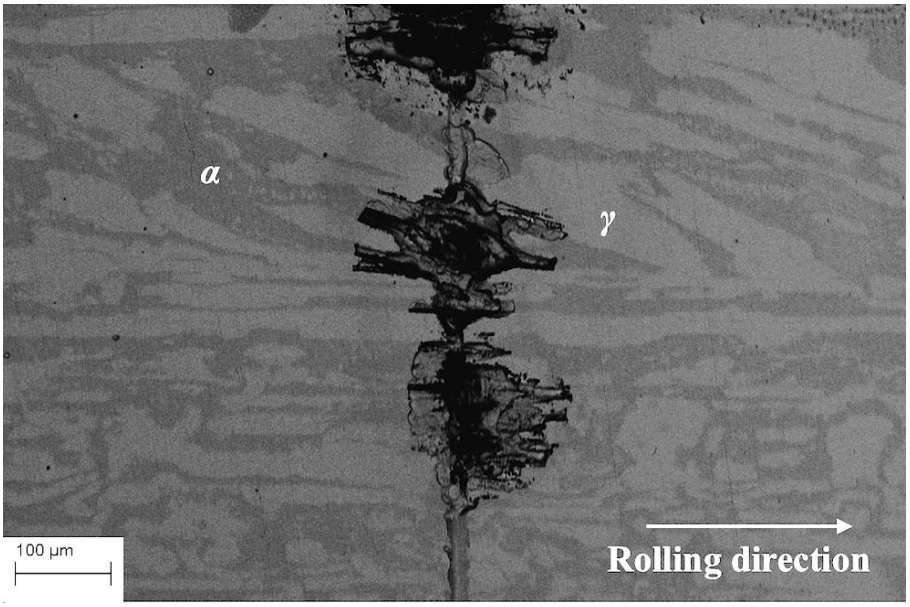

(a)

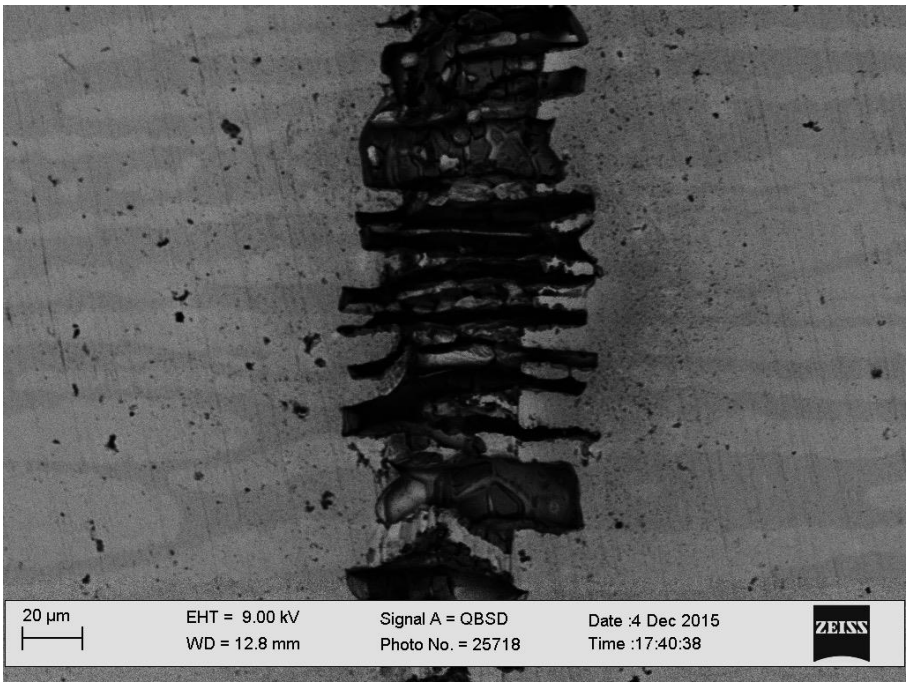

(b)

Figure 4.16 SEM image of scratch on the surface of (a) UNS S32304 and (b) S32101 after scratch test.

4.4 Combined effects of thiosulfate and sulfate anions on pitting corrosion of DSSs

To understand the behavior of LDSSs in simulated paper machine white water, both Na_2SO_4 and $Na_2S_2O_3$ were added to the solution containing NaCl. A series of tests were carried out in solutions with different amounts of $S_2O_3^{2-}$ added to a solution with a fixed amount of SO_4^{2-} and Cl^-. Environments tested in this study are shown in Table 4.5. Concentration of Cl^- and SO_4^{2-} in the base solution for this series of tests was kept constant at 300 mg/L and 50 mg/L, respectively. The molar ratio of $[(Cl^-+SO_4^{2-})/S_2O_3^{2-}]$ of tested solutions varied was infinity, 33, 16 and 8.

Table 4.5 Environments used to study the effects of sulfate.

Environment			Molar ratio $[(Cl^-+SO_4^{2-})/S_2O_3^{2-}]$	Temperature (°C)
Cl^- [mg/L]	SO_4^{2-} [mg/L]	$S_2O_3^{2-}$ [mg/L]		
300	50	0	-	50
300	50	31	33	50
300	50	62	16	50
300	50	124	8	50

Table 4.6 Pitting corrosion susceptibility of duplex stainless steels in solutions containing Cl^-, SO_4^{2-} and $S_2O_3^{2-}$.

Environment			Molar ratio	Pitting corrosion		
Cl^- [mg/L]	SO_4^{2-} [mg/L]	$S_2O_3^{2-}$ [mg/L]	$[(Cl^- + SO_4^{2-}) / S_2O_3^{2-}]$	UNS S32304	UNS S32003	UNS S82441
300	50	0	-	Yes	No	No
300	50	31	33	Yes	No	No
300	50	62	16	No	No	No
300	50	124	8	No	No	No

Test results are summarized in

Table *4.6*. Figure 4.17 shows the potentiodynamic polarization curves of UNS S32304 in solutions containing (300 mg/L Cl^- + 50 mg/L SO_4^{2-}) with different concentrations of $S_2O_3^{2-}$. No pitting corrosion was observed on UNS S32003 and S82441 specimens. However, when the $[(Cl^- + SO_4^{2-})/S_2O_3^{2-}]$ ratio was above 33, pits were observed on the UNS S32304 specimens. However, when more $S_2O_3^{2-}$ was added to the system and the $[(Cl^- + SO_4^{2-})/S_2O_3^{2-}]$ ratio was below 16, the specimens showed transpassive behavior and no pits were observed.

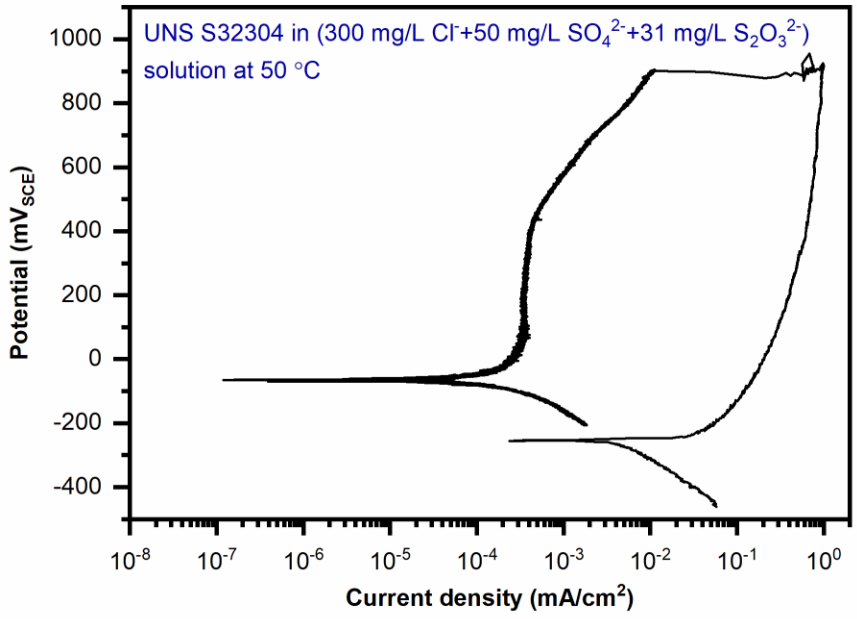

(a)

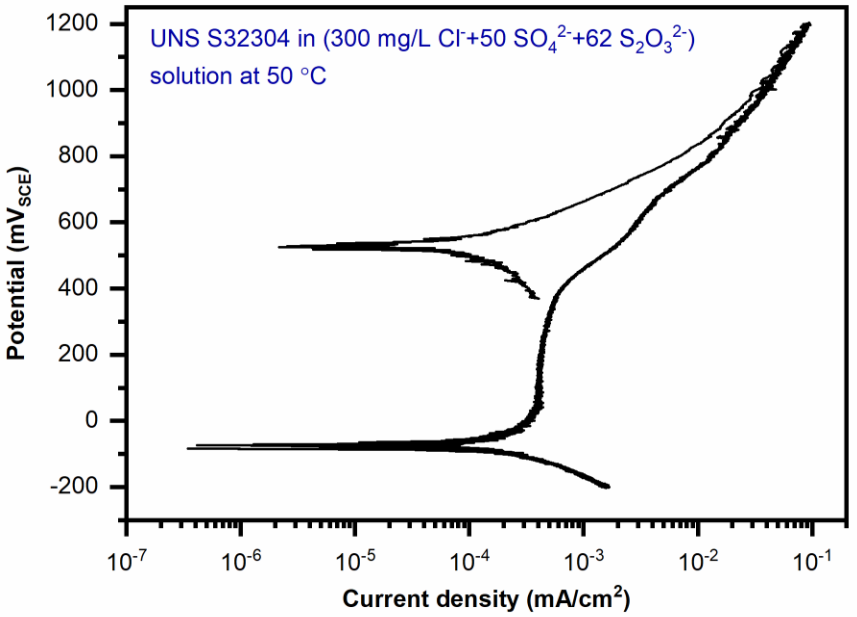

(b)

Figure 4.17 Potentiodynamic cyclic polarization curves of UNS S32304 in solution containing (a) 300 mg/L Cl^-+ 50 mg/L SO_4^{2-} + 31 mg/L $S_2O_3^{2-}$; (b) 300 mg/L Cl^- + 50 mg/L SO_4^{2-} + 62 mg/L $S_2O_3^{2-}$; and (c) 300 mg/L Cl^- + 50 mg/L SO_4^{2-} +124 mg/L $S_2O_3^{2-}$.

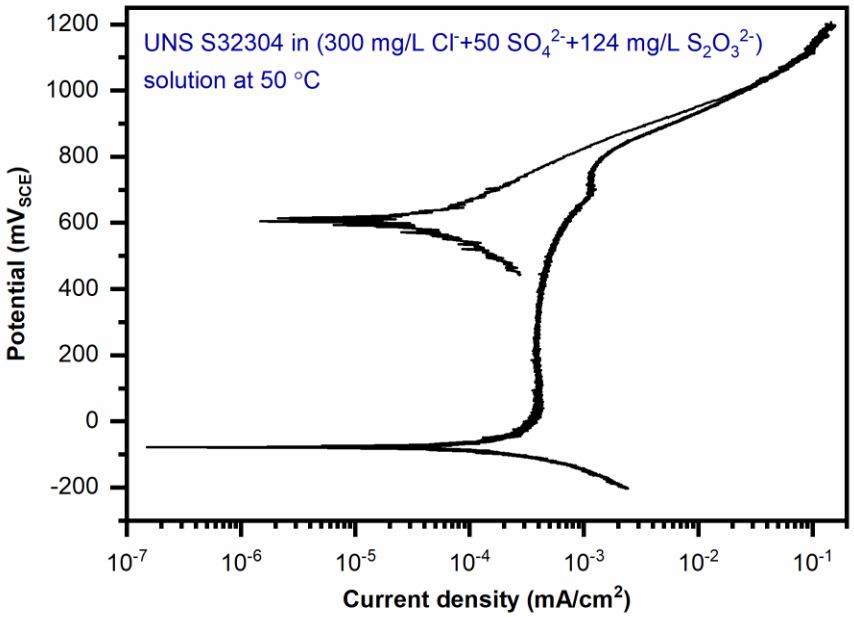

(c)

Figure 4.17 Continued.

4.6 Discussions

4.6.1 Chemical composition of alloys

The comparison of pitting corrosion susceptibility between the four grades of duplex stainless steels in environments containing (Cl^-+$S_2O_3^{2-}$) and (Cl^-+ $S_2O_3^{2-}$+ SO_4^{2-}) is summarized in Table 4.2, and

Table 4.6, respectively. No pitting corrosion was observed on UNS S32003 and UNS S82441 specimens in all tested environments, while UNS S32304 was found to be susceptible to pitting corrosion, especially in Cl^- containing solutions with relatively low concentrations of SO_4^{2-} and $S_2O_3^{2-}$. However, comparing the test results of UNS S32304 and S32101 in environments containing Cl^- and $S_2O_3^{2-}$, UNS S32304 demonstrated a higher pitting corrosion resistance than S32101, indicated by a higher pitting potential and repassivation potential of S32304. Thus, out of the four grades of duplex stainless steels, the pitting corrosion resistance of UNS S32101 was found to be the lowest, followed by the UNS S32304, while UNS S32003 and UNS S382441 possess the highest pitting corrosion resistance in simulated paper machine white waters. However, if we take into consideration the susceptibility of UNS S32003 to crevice corrosion in concentrated solutions, then the resistance to localized corrosion can be summarized as: UNS S32101 < S32304 < S32003 < S82441.

The difference in the pitting susceptibility of duplex stainless steels in paper machine white water can be attributed to the differences in their chemical composition. The Cr content in UNS S32003 and UNS S32101 is similar, which is around 21.5 wt%, while that for the UNS S32304 and UNS S82441 is around 23 wt% and 24 wt%, respectively. However, there is a significant difference in the Mo content in these lean grades of duplex stainless steels. UNS S32003 has 1.64 wt% Mo, while UNS S32101 has only 0.3 wt% Mo. Similarly, UNS S82441 has 1.6 wt% Mo and UNS S32304 only has 0.24 wt% Mo. With similar amount of Cr content, a higher Mo content in tested duplex stainless steels contributes to the higher pitting corrosion resistance. This effect of molybdenum is well known for the austenitic stainless steels, where UNS S31603 with higher Mo content

was more corrosion resistant than UNS S30403 in SO_4^{2-} and $S_2O_3^{2-}$ containing Cl^- solution.[81, 82] Prior published work has shown that the presence of Mo could promote desorption of sulfur species on the surface of steels. [42-45]

4.6.2 Effects of thiosulfate

Both the cyclic polarization test results and the scratch test results have shown that the main effect of addition of thiosulfate was in decreasing the repassivation potential. In cyclic polarization tests, with the presence of 29 mg/L $S_2O_3^{2-}$, UNS S32304 did not repassivate till the potential was below the initial open circuit potential. The hindering effect of $S_2O_3^{2-}$ on the repassivation of stainless steels was consistent with former findings, where no significant change in the pitting potential was observed while there was a noticeable decrease in the repassivation potential. [76, 82] These results also support the theory proposed by Newman et.al. that $S_2O_3^{2-}$ promoted the dissolution of bare metal where there was no intact passive film. [75] However, as shown in Table 4.6, when the $Cl^-/S_2O_3^{2-}$ was below 16 and relatively large amount to $S_2O_3^{2-}$ was added, pitting susceptibility of UNS S32304 was reduced. Because of the preferential electro-migration of $S_2O_3^{2-}$, the Cl^- concentration is decreased in the pit solution. In addition, $S_2O_3^{2-}$ gets reduced within the pit and the process consumes H^+ and form H_2O, and therefore, the acidic pit solution gets neutralized. Both facts contribute to the inhibition effect of $S_2O_3^{2-}$ on pitting corrosion of LDSSs. However, it should be noted that the inhibition effect only becomes dominant when $S_2O_3^{2-}$ is present in the environment in high concentration and for UNS S32304, the $Cl^-/S_2O_3^{2-}$ is below 16.

Pits formed in UNS S32304 after cyclic polarization tests in environment containing Cl^- and $S_2O_3^{2-}$ showed a preferential dissolution of the ferrite phase, which was confirmed by the SEM and profilometer results. Also, in scratch tests, pits propagated preferentially into the ferrite phase from the scratch on a UNS S32304 sample. In comparison, the pits formed on UNS S32304 in a solution containing only Cl^- or Cl^- and SO_4^{2-} possessed a round shape with a pit cover. Selective dissolution of either the austenite phase or the ferrite phase, depending on the segregation of alloy elements and the environment, has been observed in duplex stainless steels. [64, 82, 91, 103] Preferential corrosion of the ferrite phase in UNS S32101 and UNS S32304 was shown in the pits formed in alkaline and carbonate containing Cl^- solution. [91] While selective attack of the austenite phase was observed in UNS S32205 in hot alkaline-sulfide solution containing Cl^- ions. [64] Also, the chemical composition of each phase and the resulting pitting corrosion susceptibility may change with the heat-treatment conditions. [51, 104] In this case, since UNS S32304 is low in Mo, which is a ferrite stabilizer, the pitting susceptibility of the ferrite phase is higher than that of the austenite phase, leading to the preferential attack of the ferrite phase in environment containing Cl^- and $S_2O_3^{2-}$.

4.7 Conclusions

In this chapter, pitting corrosion behavior of four LDSSs are compared in environments containing Cl^-, $S_2O_3^{2-}$ and SO_4^{2-} at 50 °C using both cyclic potentiodynamic polarization test and scratch test method. The effects of $S_2O_3^{2-}$ and chemical composition of alloys on the pitting corrosion resistance of LDSSs are summarized as follows:

1. UNS S32003 and S82441 LDSSs were more resistant to pitting corrosion than S32304 and S32101 LDSSs in Cl^-, $S_2O_3^{2-}$ and SO_4^{2-} ions containing environments. The superior pitting corrosion resistance in this environment can be attributed to the higher Mo content in UNS S32003 and UNS S82441.

2. Potentiodynamic cyclic polarization tests revealed that $S_2O_3^{2-}$ increased the pitting susceptibility of duplex stainless steels mainly by lowering the repassivation potential. Repassivation behavior for the S32304 and S32101 indicated that the presence of $S_2O_3^{2-}$ hinders the repassivation on a bare alloy surface within the pits or on a scratched surface.

3. Preferential dissolution of the ferrite phase in UNS S32304 and S32101would occur with the presence of $S_2O_3^{2-}$ in Cl^- containing environment.

4. Addition of $S_2O_3^{2-}$ at higher concentrations can inhibit pitting corrosion. The lower concentration of Cl^- ions in the pit solution because of the preferential migration of $S_2O_3^{2-}$ and the higher pH due to the consumption of H^+ in $S_2O_3^{2-}$ reduction reaction both contribute to a less aggressive pit-solution chemistry. For UNS S32304, this inhibition effect becomes dominant when the $Cl^-/S_2O_3^{2-}$ ratio is below 16.

CHAPTER 5. EFFECTS OF ANNEALING HEAT-TREATMENT ON PITTING CORROSION OF LDSS

Chemical composition of the ferrite phase and the austenite phase in DSSs changes with annealing temperature above around 1000 ℃, which changes the pitting corrosion behavior of DSSs as a result.[50, 52, 105] In addition, since the N content in the ferrite phase increases with annealing temperature and may exceed the saturation point (0.05%), Cr_2N could precipitate, increasing the pitting corrosion susceptibility of DSSs by promoting the active dissolution within pits.[50, 60] However, it has been shown that the effects of annealing temperature are different for different grades of DSSs depending on their chemical composition. For example, for UNS S32101 and S82441, critical pitting temperature decreased with increasing annealing temperature above 1000 ºC because the ferrite phase is more susceptible to pitting corrosion as its pitting resistance equivalent number (PREN) is lower at higher annealing temperatures. [51, 52] Pitting corrosion resistance of UNS S32304 has a peak at 1080 ºC and below this temperature the austenite phase is more susceptible to pitting corrosion while above this temperature, the ferrite phase is more susceptible. [53] However, the effects of annealing treatment on the pitting corrosion behavior of UNS S32003 have not been studied.

In this chapter, UNS S32003 specimens were annealed at 1000, 1040, 1080, 1120 and 1160 ℃ for 1 hour, respectively and then water quenched. The resulting microstructure was observed using optical microscope and SEM coupled with EDS to characterize the volume fraction of each phase and their chemical compositions. Potentiodynamic cyclic

polarization tests were performed to study the pitting corrosion resistance of samples annealed at different temperatures.

5.1 Thermodynamic prediction of phase compositions at different annealing temperatures

Thermo-Calc software was used for thermodynamic calculations to predict the phase transformation of LDSS UNS S32003 at different annealing temperatures, and TCFE6 database was used for these calculations. Typical inputs for these calculations are chemical composition, temperature and pressure. Since the software only simulates equilibrium conditions, phases that are metastable will not be present in the results.

Thermodynamic prediction indicates that above 1000 °C the presence of second phase particles such as σ and χ and precipitation of carbides and nitrides is negligible, as shown in Figure 5.1. Ferrite, austenite and MnS were predicted as the equilibrium phases in UNS S32003 material annealed above 1000 °C, however, since the sulfur content in UNS S32003 is below 0.001, MnS is negligible and its volume fraction is close to 0, which is also indicated in Figure 5.1. Thus, only ferrite and austenite phase are present in the annealed UNS S32003. Thermodynamic calculations in Figure 5.1 show that the lower annealing temperatures favor higher volume fraction of the austenite phase whereas the ferrite phase volume fraction is higher at higher annealing temperatures.

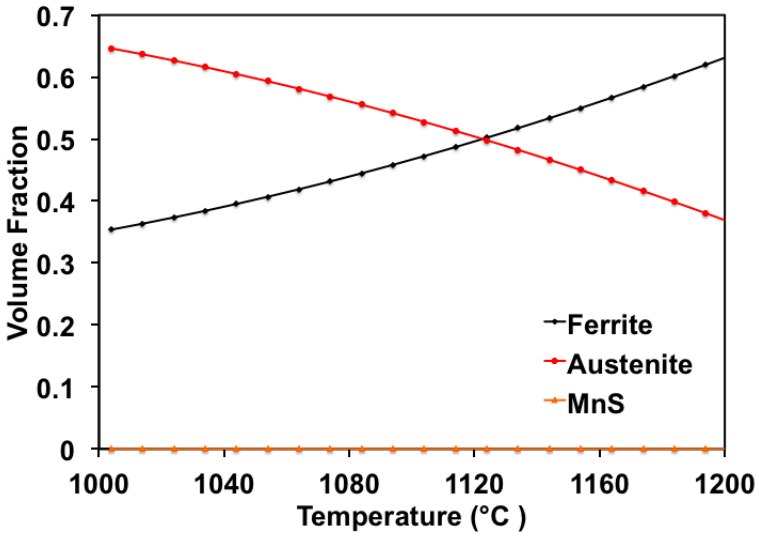

Figure 5.1 Volume fraction of ferrite phase and austenite phase at different temperatures.

Figure 5.2 shows the prediction of change in the contents of Cr, Mo and N as a function of annealing temperature. Since the saturation point of N in the ferrite phase is close to 0.05 wt%, which was reached at 1150 °C, so above this point, 0.05 wt% was used to predict the N content in the ferrite phase. PRENs of each phase were calculated based on the equation:

$$PREN = Cr + 3.3Mo + 16N$$

The calculated PRENs are plotted and shown in Figure 5.2(d). At annealing temperatures above 1000 °C, PREN of the austenite phase increases constantly with elevated temperature, while PREN of the ferrite phase decreases. At temperature close to 1200 °C, PRENs of the two phases reach the same value. Based on the thermodynamic prediction of PREN values, the austenite phase would be the sites susceptible to pit initiation compared to the ferrite phase.

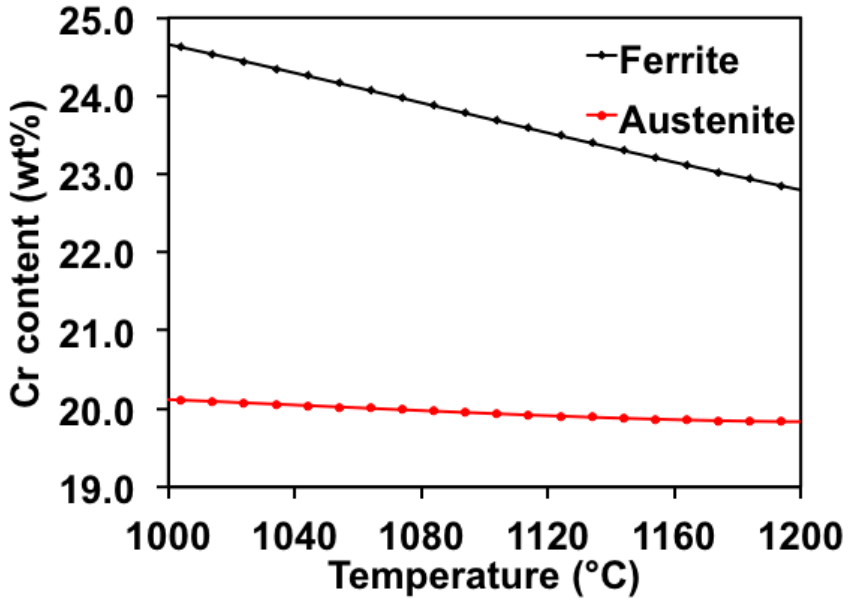

(a)

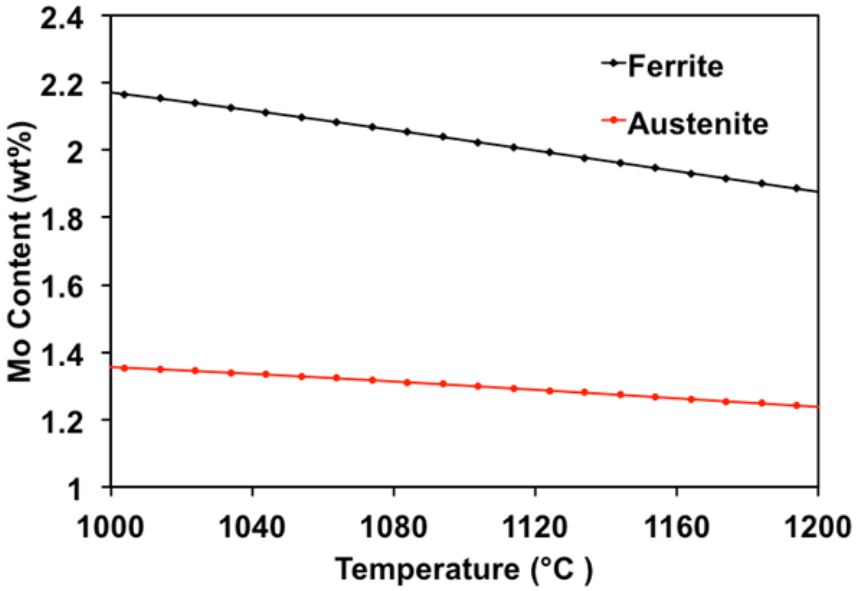

(b)

Figure 5.2 Weight percent of (a) Cr, (b) Mo, (c) N as a function of temperature and (d) calculated PREN according to the weight percent of Cr, Mo and N.

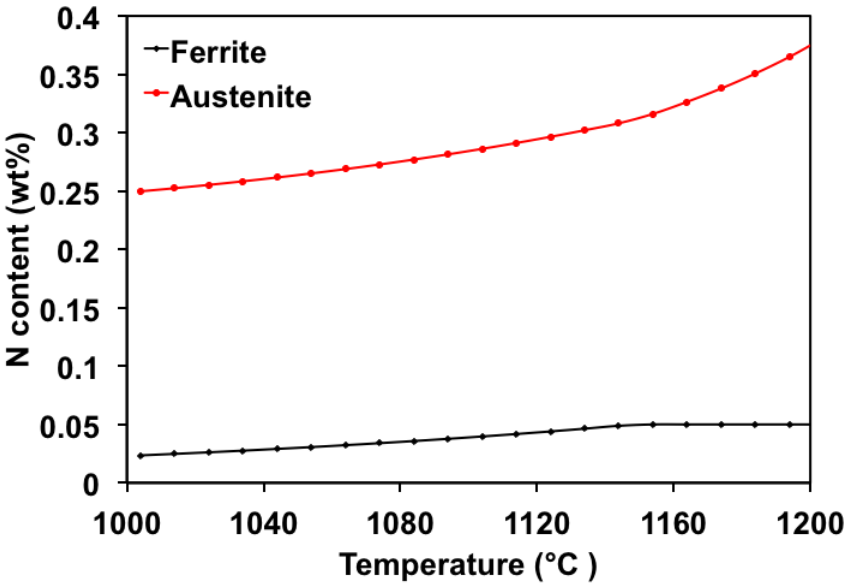

(c)

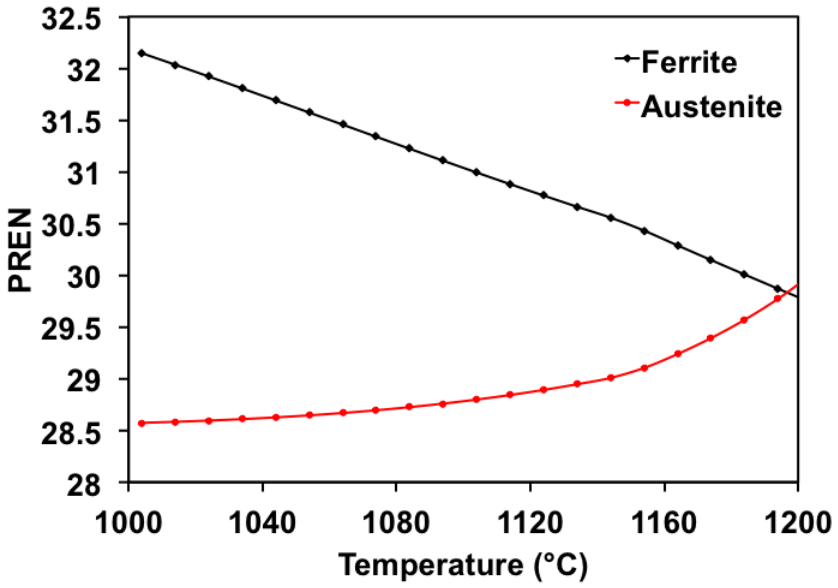

(d)

Figure 5.2 Continued.

5.2 Microstructure charactrization of annealed specimens

For annealing treatment, UNS S32003 specimens were cut into 10 mm x 10 mm x 5mm pieces, and were annealed at 1000 °C, 1040 °C, 1080 °C, 1120 °C and 1160 °C for 1 hour, respectively. The specimens were then water quenched to preserve the high-temperature microstructure. The specimens were mounted in epoxy and polished to mirror finish using 0.05 μm alumina. The samples were then electro-etched in 40 wt% NaOH solution at 2.5 V for 10 seconds. After etching, the ferrite phase appears dark and the austenite phase appears light when observed under an optical microscope or SEM.

Figure 5.3 shows the optical microscope images of microstructure of samples annealed at 1000 °C to 1120 °C. The phases coarsened as the annealing temperature increased. The volume fraction of the ferrite phase was characterized through point-counting method and the ferrite number was measured by FerritScope, as shown in Table 5.1. Both the point-counting results and FerritScope measurement indicate that the fraction of the ferrite phase increased at elevated annealing temperatures, as is predicted by the thermodynamic calculations shown in Figure 5.1. It should be noted that the Ferrite number measured by FerritScope would deviate from the actual volume fraction of the ferrite phase at higher ferrite percentage, however, it is a convenient tool to qualitatively compare the ferrite content in the microstructure. When UNS S32003 material is annealed at 1040 °C, the volume fraction of the two phases is the most balanced. In practice, this balanced microstructure is optimal for the performance of DSSs.

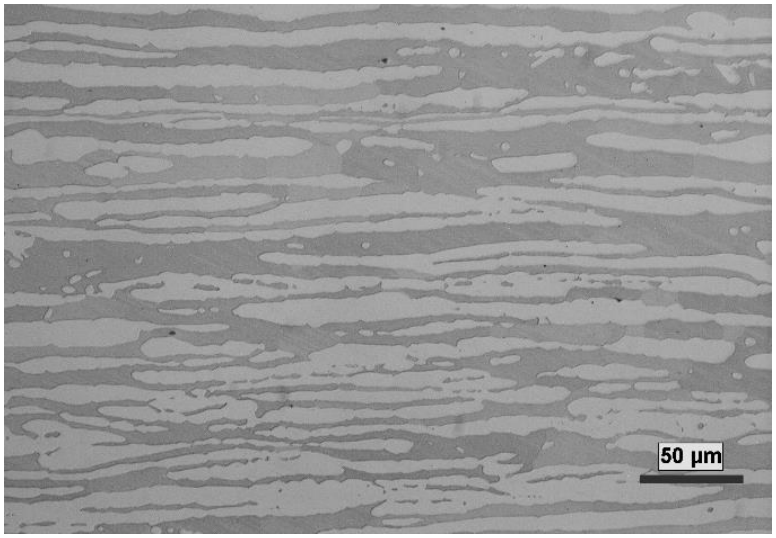

(a)

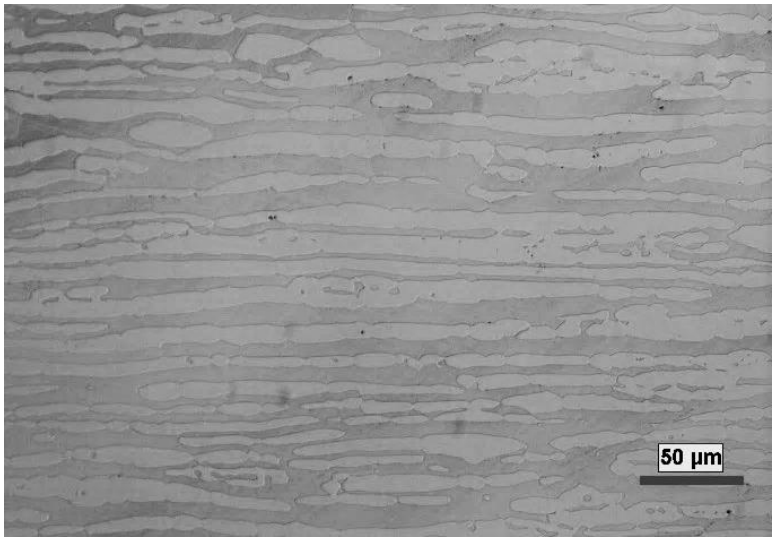

(b)

Figure 5.3 Microstructure evolution during annealing at different temperatures: (a) 1000 °C; (b) 1040 °C; (c) 1080 °C; (d) 1120 °C; (e) 1160 °C.

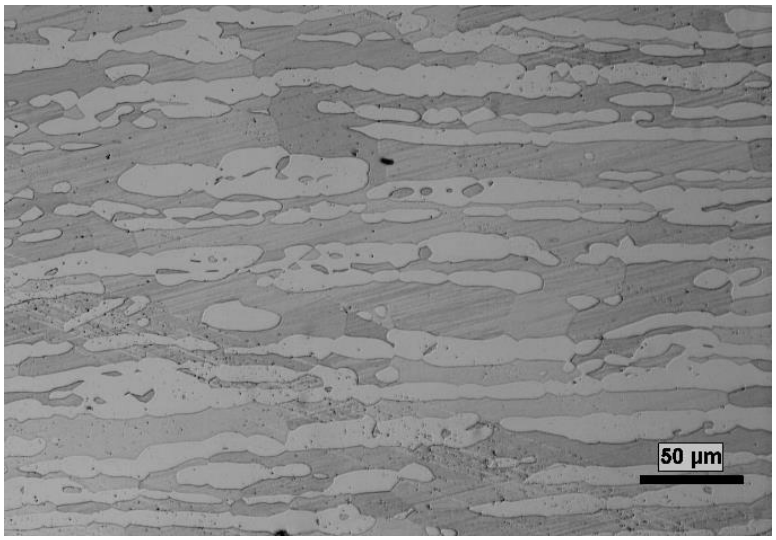

(c)

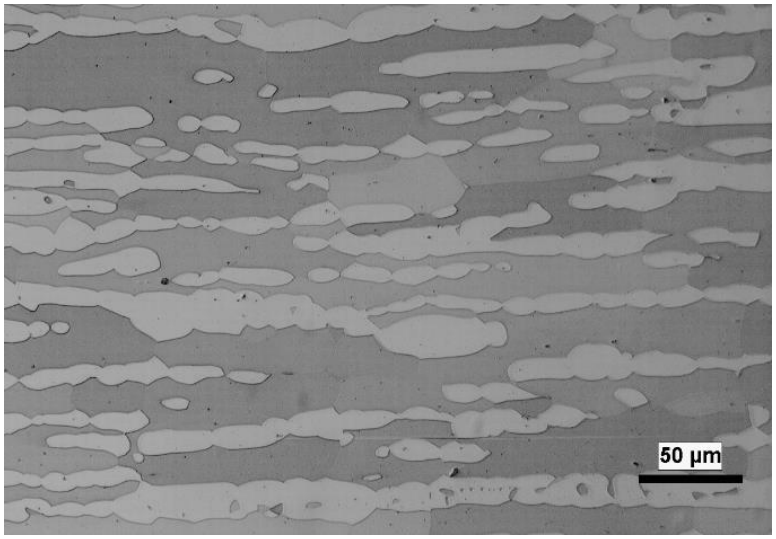

(d)

Figure 5.3 Continued.

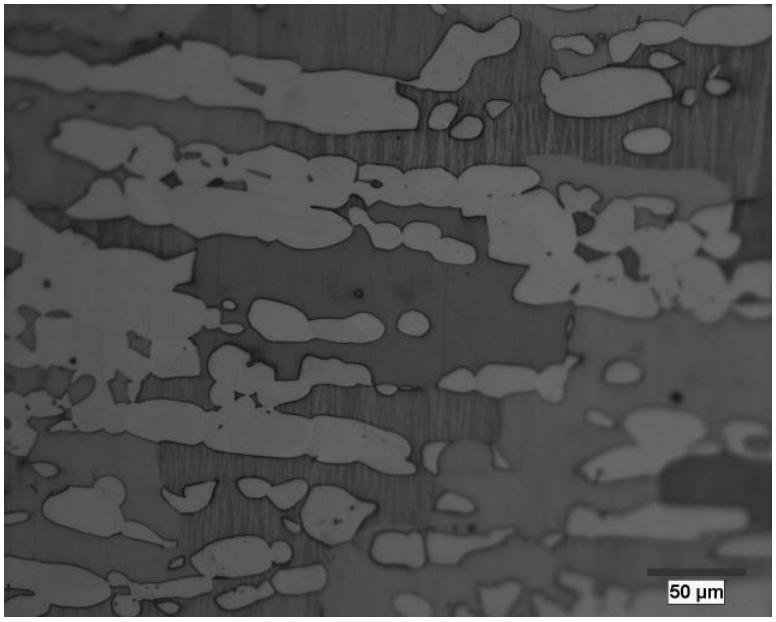

(e)

Figure 5.3 Continued.

Table 5.1 Volume fraction of ferrite phase and ferrite number

Annealing Temperature (°C)	Volume Fraction of Ferrite (%)	Measured Ferrite Number (FN)
1000	45.3±4.1	51.6±0.6
1040	50.2±4.6	54.0±2.9
1080	53.7±4.1	72.8±2.2
1120	56.7±6.0	72.1±1.1
1160	57.4±2.2	74.8±5.8

The content of major elements in both phases was analyzed using EDS analysis and the result is shown in Table 5.2. The ferrite phase has higher Cr and Mo content, while the elements such as Ni and Mn were preferentially partitioned to the austenite phase. At elevated annealing temperature, both Cr and Mo content in the ferrite phase dropped whereas the concentration of these elements did not change much for the austenite phase with annealing temperatures.

Table 5.2 EDS analysis of phase composition

	1000 °C		1080 °C		1120 °C	
	Austenite	Ferrite	Austenite	Ferrite	Austenite	Ferrite
Fe	67.8 ± 0.17	66.4 ± 0.12	67.5 ± 0.19	66.2 ± 0.12	66.4 ± 0.15	64.9 ± 0.44
Cr	19.9 ± 0.23	23.3 ± 0.08	20.0 ± 0.14	22.9 ± 0.09	19.7 ± 0.07	22.1± 0.26
Ni	4.68 ± 0.10	2.73 ± 0.05	4.70 ± 0.06	3.05 ± 0.08	4.58 ± 0.15	3.08 ± 0.05
Mn	2.0 ± 0.05	1.73 ± 0.05	1.98 ± 0.04	1.78 ± 0.04	1.94 ± 0.09	1.63 ± 0.05
Mo	1.18 ± 0.13	1.90 ± 0.08	1.15 ± 0.05	1.93 ± 0.10	1.16 ± 0.05	1.78 ± 0.10

5.3 Effects of annealing temperature on pitting corrosion of UNS S32003

To compare the pitting corrosion resistance of samples annealed at different temperatures, potentiodynamic cyclic polarization tests were conducted in 0.1 mol/L NaCl solution at 60 °C. Typical potentiodynamic cyclic polarization curves are shown in Figure 5.4 and average pitting potential of samples annealed at different temperature were compared in Table 5.3. Pitting potential first increased with annealing temperature and

reached a maximum for specimens annealed at 1080 ℃. Then the pitting potential of samples annealed at 1120 ℃ and 1160 ℃ dropped. Highest pitting corrosion resistance was obtained when the UNS S32003 material is annealed at 1080 ℃.

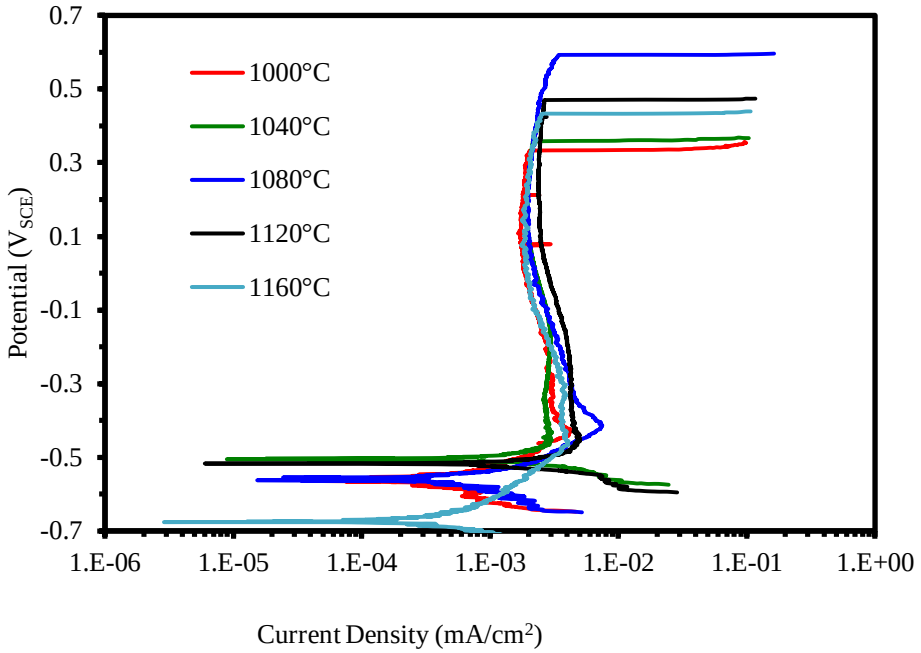

(a)

Figure 5.4 (a) Typical potentiodynamic polarization curves of annealed specimens. (b) Pitting potential as a function of annealing temperature.

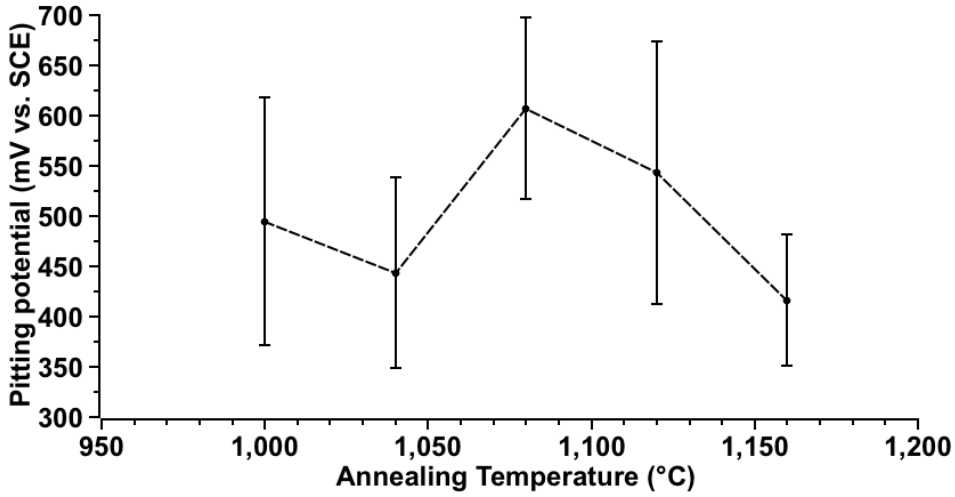

(b)

Figure 5.4 Continued.

Table 5.3 Pitting potential of samples annealed at different temperature

	1000 °C	1040 °C	1080 °C	1120 °C	1160 °C
E_{pit} (mV)	494.6 ± 123.4	443.5 ± 94.7	607.1 ± 90.3	543.2 ± 130.6	416.3 ± 65.7

To further compare the pitting corrosion resistance of the annealed UNS S32003 samples, potentiostatic polarization tests were conducted in 1 mol/L NaCl solution at 60 °C at different potentials. As shown in Figure 5.5(a), at 200 mV_{SCE}, stable pitting occurred on samples annealed at 1040 °C while samples annealed at 1080 °C and 1120 °C passivated over time. At 300 mV_{SCE}, samples annealed at 1080 °C and 1120 °C were passive and did not show stable pitting. At 400 mV_{SCE}, although both samples showed stable pitting event, but the induction time for pitting corrosion on the sample annealed at 1080 °C is longer than that

on the sample annealed at 1120 °C, which also indicates that the samples annealed at 1080 °C possess the highest pitting corrosion resistance among the three.

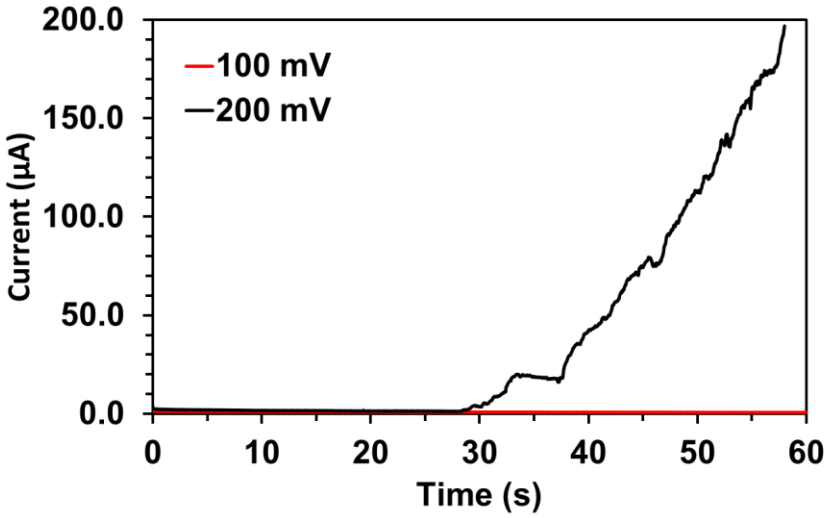

(a)

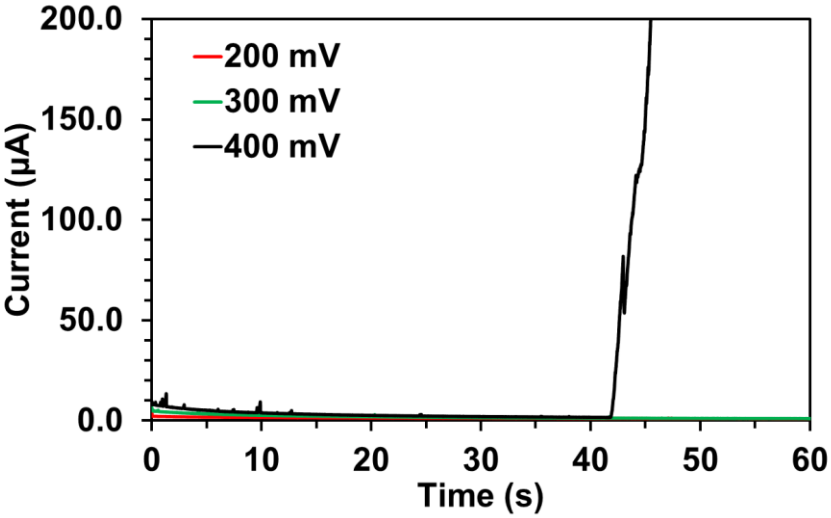

(b)

Figure 5.5 Potentiostatic polarization of samples annealed at (a) 1040 °C; (b) 1080 °C; (c) 1120 °C.

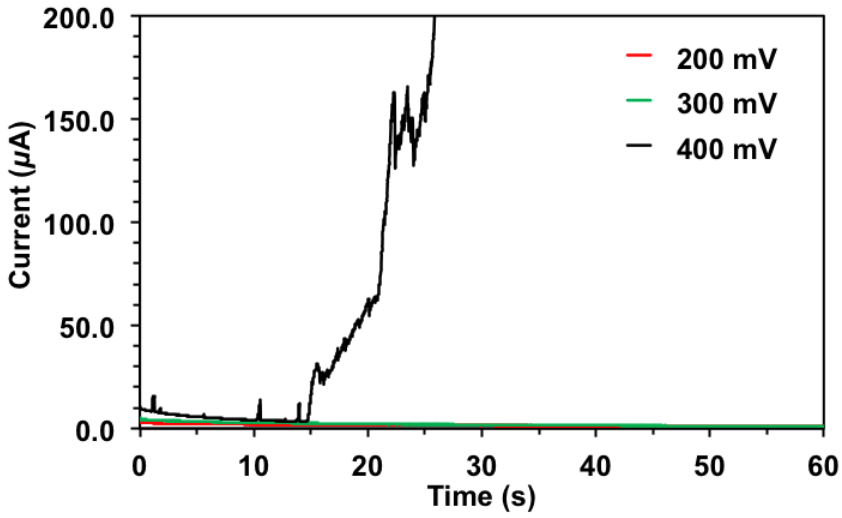

(c)

Figure 5.5 Continued.

In each cyclic polarization tests, the pits were allowed to grow till a certain current density was reached and then the sample was repassivated. In this way, the pits formed had a relatively large size. Figure 5.6 showed the morphology of these pits. It can be seen that the large pits that formed on the samples annealed at the lower temperature possessed a round shape while those formed on the samples annealed at higher temperatures were elongated. To observe the pit initiation sites in differently annealed samples, the tests were stopped when the current was less than two orders of magnitude higher than the passive current and the samples were rinsed immediately to stop the pits from further growth. Figure 5.7 shows the pit initiation sites for different samples. For the samples annealed at 1000 °C and 1040 °C, pits initiated in the austenite phase, while for the samples annealed

at 1080 °C, 1120 °C and 1160 °C, pit initiation sites were within the ferrite phase. The observed phenomena indicate that the susceptible sites changed from the austenite phase to the ferrite phase as the annealing temperature increases.

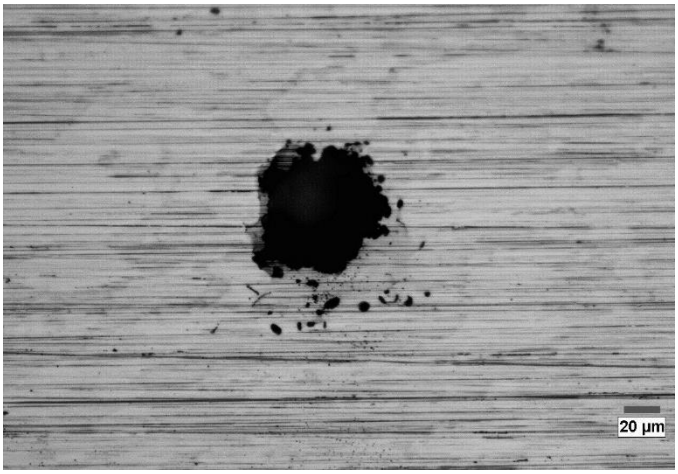

(a)

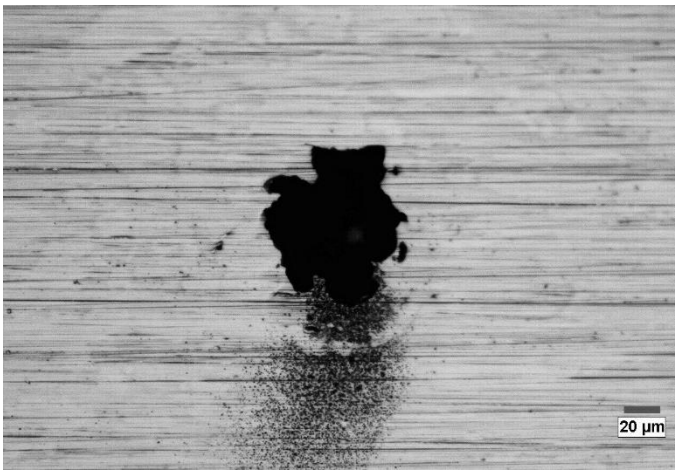

(b)

Figure 5.6 Optical microscope images of pits after potentiodynamic cyclic polarization tests. Pit formed in samples annealed at (a) 1000 °C, (b) 1040 °C, (c) 1080°C, and (d) 1120 °C.

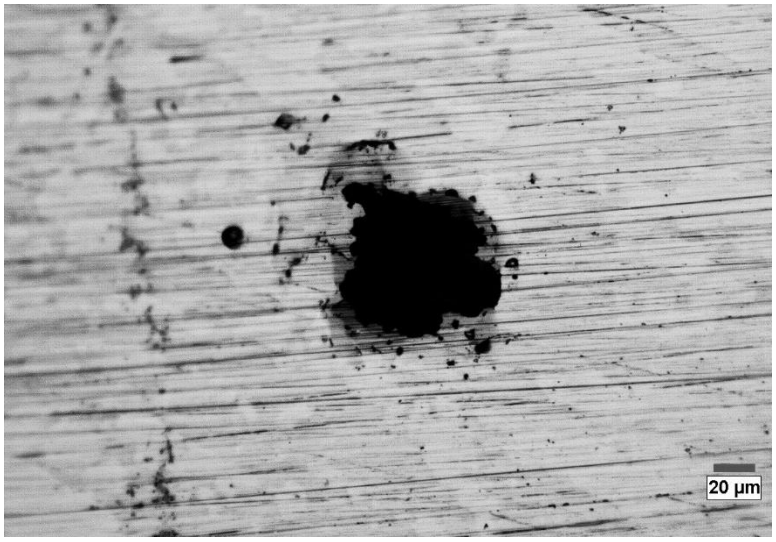

(c)

(d)

Figure 5.6 Continued.

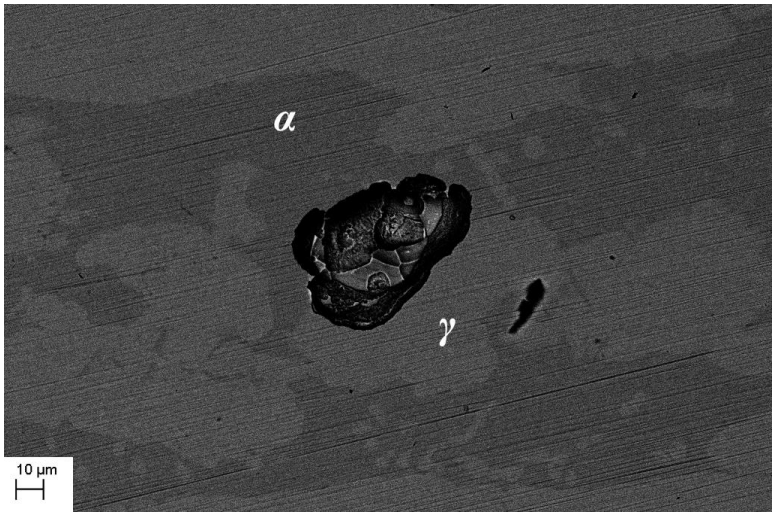

(a)

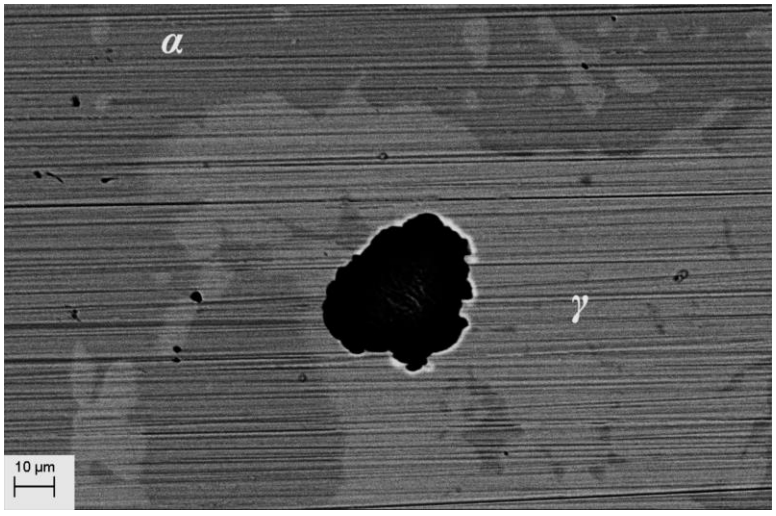

(b)

Figure 5.7 Pit initiation sites for specimens annealed at: (a) 1000 °C; (b) 1040 °C; (c) 1080 °C; (d) 1120 °C; and (e) 1160 °C.

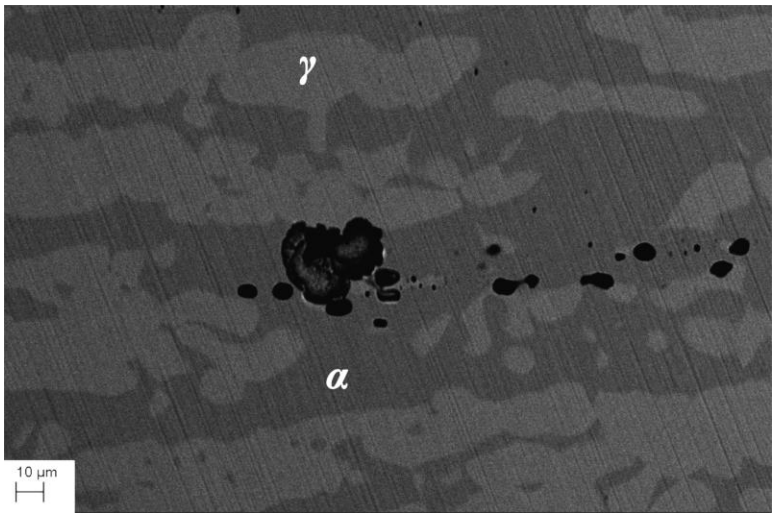

(c)

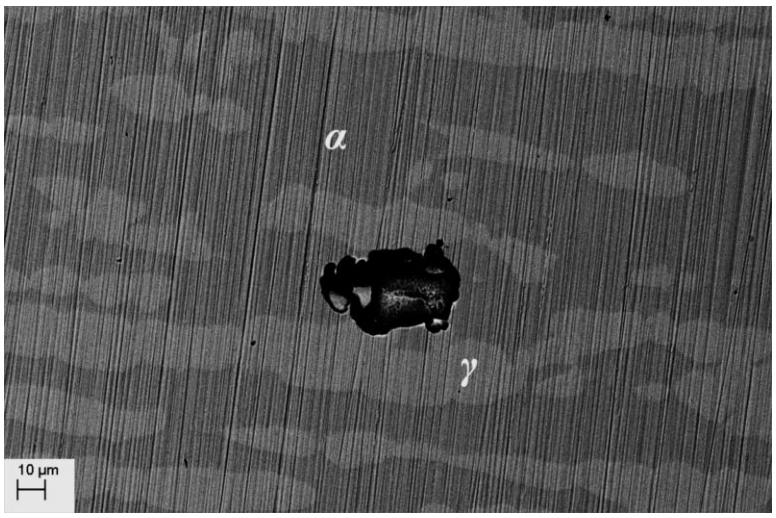

(d)

Figure 5.7 Continued.

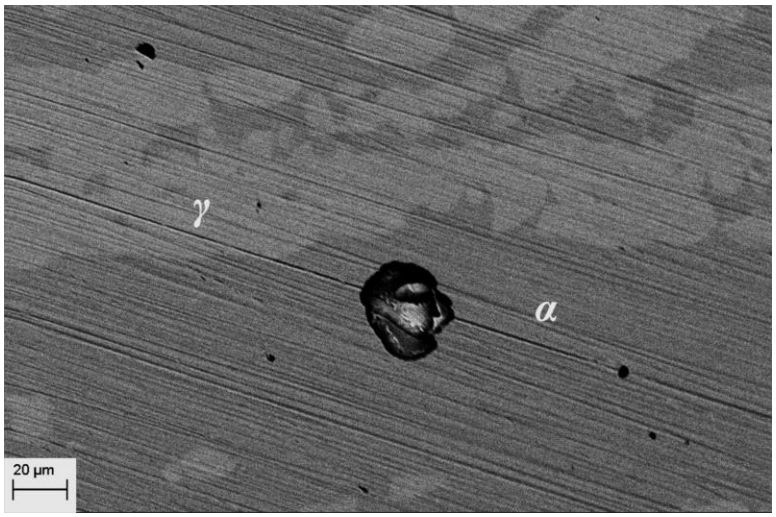

(e)

Figure 5.7 Continued.

5.4 Conclusions

Volume fraction of the ferrite phase increased with increasing the annealing temperature. For a given annealing time, the phases coarsened to a larger extent at 1160 °C compared with samples annealed at lower temperatures. Potentiodynamic cyclic polarization tests revealed that the samples annealed at 1080 °C possessed the highest pitting potential, indicating the highest resistance to pitting. Pit initiation sites in UNS S2003 changed from the austenite phase to the ferrite phase, indicating a higher pitting susceptibility of the ferrite phase when the material is annealed at a higher temperature, which could be attributed to the lower Cr and Mo content at the elevated annealing temperature.

CHAPTER 6. EFFECTS OF ISOTHERMAL AGING ON PITTING CORROSION BEHAVIOR OF LDSS

The optimum performance of DSSs is achieved when the volume ratio of the ferrite phase to the austenite phase is close to 50:50. However, processes such as welding, annealing treatment as well as aging can change the ferrite-to-austenite ratio, phase composition or lead to the formation of secondary phases including intermetallic phases or carbide and nitride precipitates, and thus further change the performance of DSSs.

Precipitation of σ phase and χ phase in standard UNS S31803 and super DSSs has been widely investigated.[54-58, 106, 107] σ phase forms within the temperature range of around 923 K (650 °C) to 1173 K (900 °C). In the DSS 2205 as well as in super DSSs it is precipitated within minutes of aging at the ferrite/austenite boundaries and grows into the ferrite phase because of the high content of Cr and Mo and higher diffusion rate in the ferrite phase.[55, 57, 58] Different from the fast formation of σ phase and χ phase in standard and super DSSs, the precipitation of intermetallic phases is sluggish in the lower alloyed LDSSs UNS S32101 and UNS S32304 because of their reduced Cr and Mo content. Cr_2N and $M_{23}C_6$ were found to precipitate after minutes of aging in LDSS 2101 along the ferrite/austenite interface and the ferrite/ferrite boundaries while the σ phase were detected after 24 hours of aging at 963 K (690 °C).[59]

The precipitation of secondary phases leads to the deterioration of both corrosion resistance and mechanical properties of DSSs.[50, 58, 62, 63, 107-110] Corrosion

resistance of DSSs has been found to decrease with aging times where the depleted zones in the vicinity of precipitates are the most susceptible sites for pitting corrosion initiation.

As a newly developed LDSS, the effects of aging treatment on the properties o UNS S32003 have rarely been studied. In this work, the effects of aging on the microstructural evolution and pitting corrosion behavior are studied in detail. Aging treatments were performed at temperatures in the range of 600 °C to 900 °C for up to two hours. The materials were also aged at 700 °C for different time periods to study the microstructural evolution over longer times. The samples were tested in 0.6 mol/L NaCl solution at 50 °C through potentiodynamic cyclic polarization to compare their pitting corrosion susceptibility.

6.1 Experimental details

Materials and heat-treatment conditions

The UNS S32003 material was cut into 10mm x 10mm x 3mm pieces for heat-treatment. The specimens were first annealed at 1040 °C in a pre-heated furnace for one hour and then water quenched. To study the phase transformation at different temperatures, the specimens were aged at temperatures within the range of 600 °C to 900 °C with 50 °C intervals for 30 minutes and 2 hours in furnace, respectively, followed by water quenching to preserve the microstructure formed after that aging treatment. To observe the evolution of microstructure over aging time, the specimens were aged at 700 °C for different time periods from 10 minutes up to 120 hours.

Corrosion tests

For corrosion test samples, a metal wire was attached at the back of the heat-treated specimens to ensure electric connection and the specimens were then mounted in epoxy. The surface of the mounted samples was ground to 2000 grit and ultrasonically cleaned in acetone before each test. The interface between the specimen and the epoxy was covered by an electroplating tape with a hole to avoid the crevice corrosion and to expose the same surface area of 0.6 cm^2 for each test.

Potentiodynamic cyclic polarization tests were done in deaerated 0.6 mol/L NaCl solution at 50 °C to compare the pitting corrosion resistance of differently heat-treated samples. The surface was first conditioned at -0.8 V_{SCE} for 20 minutes to remove the native oxide film formed in air, and then the open circuit potential (OCP) was measured for 1 hour. Then the potential was swept from 100 mV below the OCP to 1.2 V_{SCE} or until a current density of 0.2 mA/cm^2 was reached. The forward scan rate was 1mV/s and the reverse scan rate was 5 mV/s. Any data, where the sample showed signs of crevice corrosion after the test, was discarded. At least three polarization tests were conducted to ensure the reproducibility of data. In subsequent analysis of data, pitting potential (E_{pit}) was defined as the potential at which the current density exceeded 100 $\mu A/cm^2$ and the repassivation potential (E_{rp}) was defined as the potential where the backward scan curve intersected the forward scan curve, as shown in Figure 6.1.

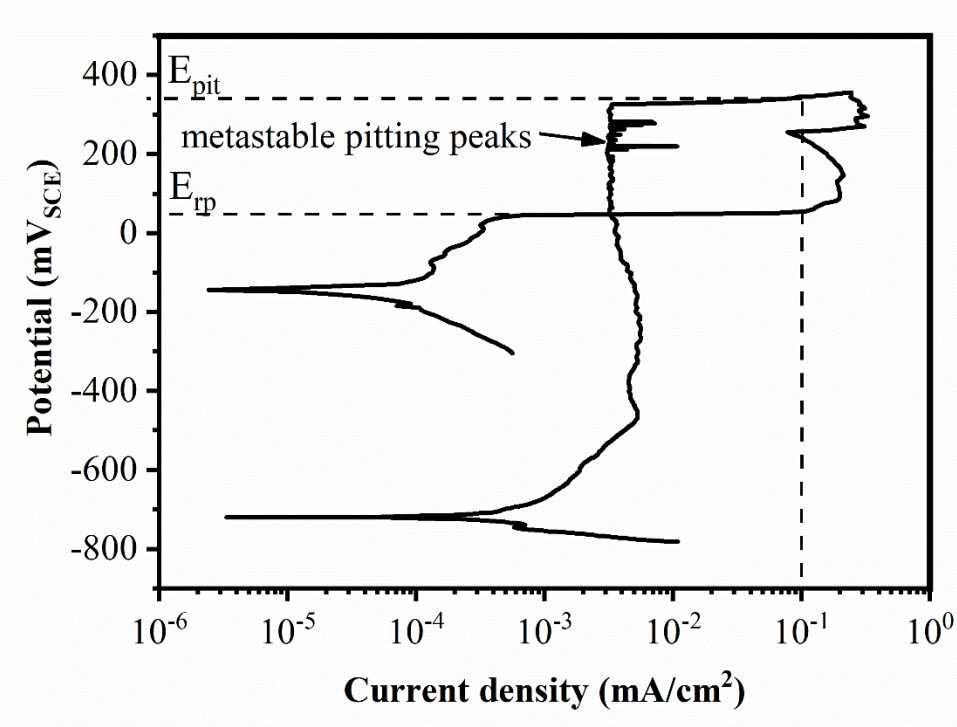

Figure 6.1 Typical cyclic potentiodynamic polarization curve of aged sample in 0.6 mol/L NaCl solution at 50 °C.

Metastable pitting events were also studied for the samples aged at 700 °C for different time periods. The current peaks during the forward scan before stable pitting represented the abrupt current increase followed by the repassivation of metastable pitting events. The numbers of peaks within every 100 mV intervals were counted after each test. The rate of occurrence of metastable pitting was defined as the number of metastable pitting events divided by the time period, which in this case is 100s for 100 mV interval with 1 mV/s forward scan rate.

Materials characterization

SEM coupled with EDS was used to characterize the microstructure and composition of different phases in the heat-treated samples. The samples were ground and

then polished to mirror finish using 0.05μm alumina. Two different etchants were used in this study. Electrolytic etching in 40 wt% NaOH etchant at 2.5 V was used to create better phase contrast for image analysis, but this method tends to etch out the precipitates. Chemical etching in Pellegrino's etchant, consisting of 25 ml nitric acid, 50 ml hydrochloric acid and 50 ml distilled water, has a slow etching rate and was used for positive identification of secondary phases.

To study the pit initiation sites, the samples were first polished to mirror finish using 0.05 μm alumina and etched in Pellegrino's etchant, and then potentiostatically polarized at 800 mV_{SCE} in 0.6 mol/L NaCl at 50 °C to induce pit initiation. Since the secondary phases remained after etching, it can be confirmed that the pits produced were not etch- pits. The pit nucleation locations were then characterized using SEM.

6.2 Effects of isothermal aging temperatures

The heat-treatment conditions are shown in Table 6.1.

Table 6.1 Sample ID under different isothermal aging conditions (change in aging temperatures)

Sample ID	Aging temperature (°C)	Aging time	Cooling
2003-600-30min	600	30 minutes	Water quenching
2003-600-2h	600	2 hours	Water quenching
2003-650-30min	650	30 minutes	Water quenching
2003-650-2h	650	2 hours	Water quenching
2003-700-30min	700	30 minutes	Water quenching
2003-700-2h	700	2 hours	Water quenching
2003-750-30min	750	30 minutes	Water quenching
2003-750-2h	750	2 hours	Water quenching
2003-800-30min	800	30 minutes	Water quenching
2003-800-2h	800	2 hours	Water quenching
2003-850-30min	850	30 minutes	Water quenching
2003-850-120h	850	2 hours	Water quenching
2003-900-30min	900	30 minutes	Water quenching
2003-900-2h	900	2 hours	Water quenching

6.1.1 Effects of aging temperature on microstructure evolution

The microstructure of UNS S32003 samples aged at different temperatures, from 600 °C to 900 °C, for 2 hours, is shown in Figure 6.2. Since the polished sample surface was etched in NaOH solution, the dark phase represents the ferrite phase, and the light phase is the austenite phase. The black spots are precipitates and they form mainly along the ferrite/austenite phase boundaries as well as within the ferrite phase. At 600 °C, the

precipitates can rarely be observed, indicating a very slow precipitation kinetics at 600 °C. The precipitates formed after 2 hours of aging at 700 °C to 900 °C and the amount of precipitates reached maximum at 800 °C. This was confirmed by image analysis, which calculated the volume fraction of the precipitates, as shown in Figure 6.3.

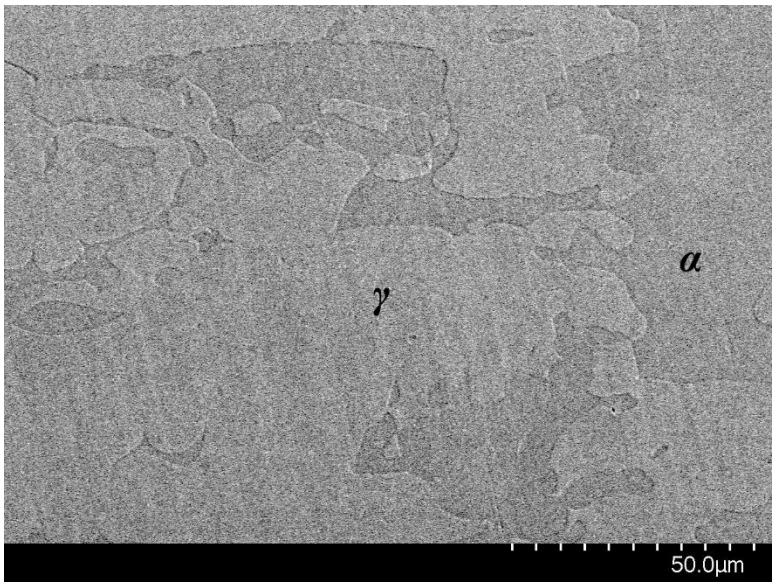

(a)

Figure 6.2 SEM images of microstructure of samples aged at: (a) 600 °C; (b) 700 °C; (c) 800 °C; (d) 900 °C.

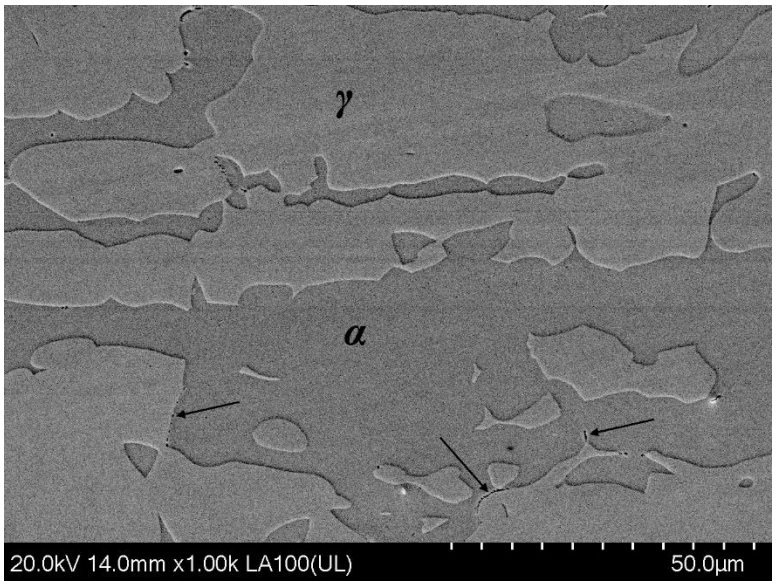

(b)

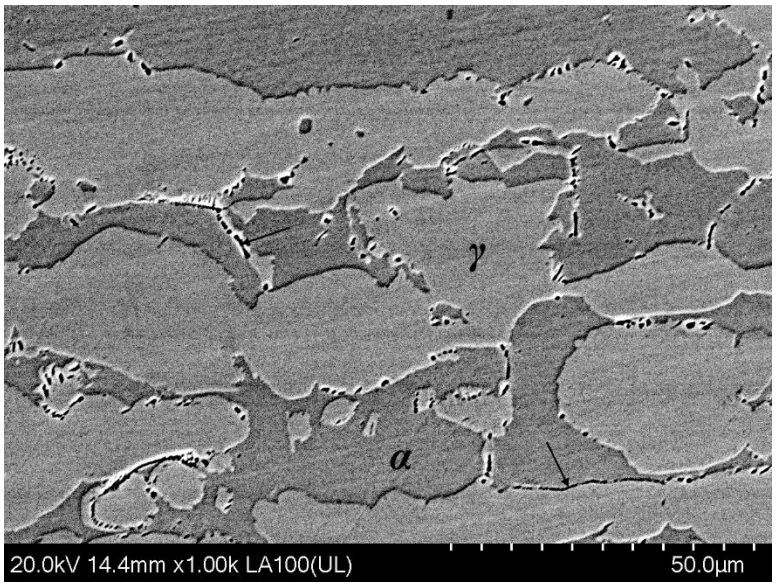

(c)

Figure 6.2 Continued.

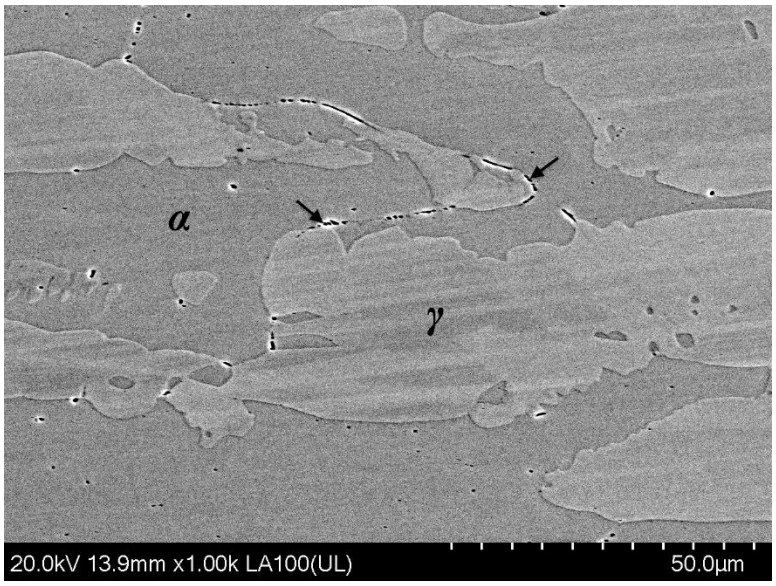

(d)

Figure 6.2 Continued.

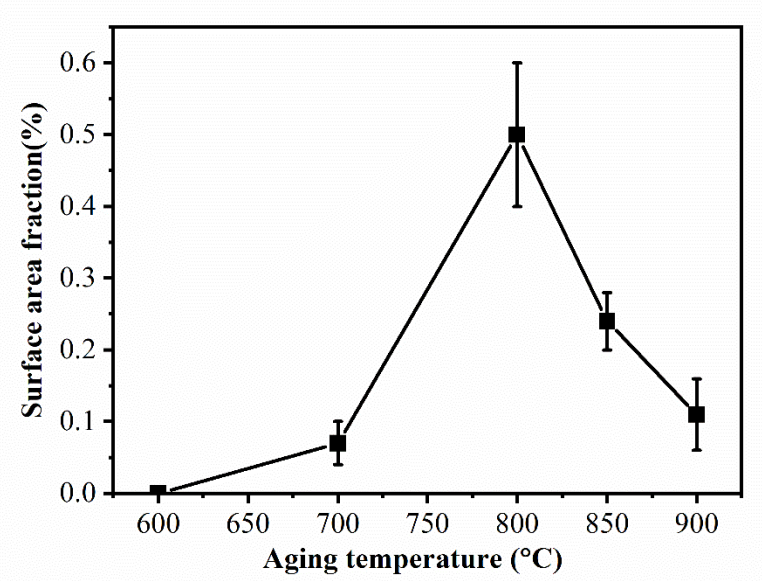

Figure 6.3 Change of volume fraction of precipitates with different aging temperature.

To positively identify the chemical composition of each phase, Pellegrino's etchant was used to preserve the precipitates. Figure 6.4 shows the microstructure of a sample aged at 850 °C for 2 hours and the chemical composition of each phase was characterized by EDS analysis, the results of which are shown in Table 6.2. Compared to the bulk phase, the precipitates are enriched in Cr and N, confirming that these precipitates are nitrides. It should be noted that EDS analysis of elements with light atomic weight (nitrogen in this case) is semi-quantitative, however, the contents of nitrogen in different phases can still be compared qualitatively using EDS.

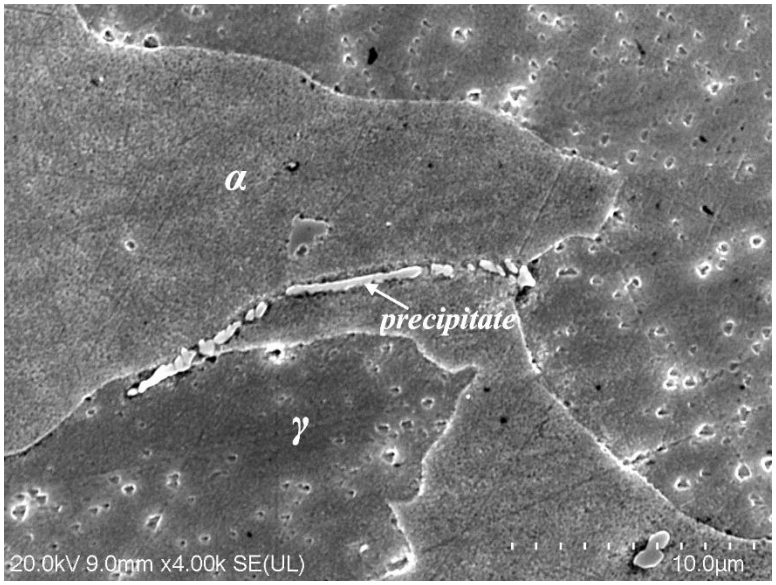

Figure 6.4 Secondary electron (SE)-SEM image of the microstructure of UNS S32003 sample aged at 850 °C for 2 hours. The polished surface was etched by Pellegrino's etchant.

Table 6.2 Chemical composition of the ferrite phase, austenite phase and precipitates in a UNS S32003 sample aged at 850 °C for 2 hours.

	Ferrite	Austenite	Precipitates
Cr	23.6 ± 1.1	19.8 ± 0.7	27.6 ± 2.8
Ni	2.3 ± 0.1	4.6 ± 0.4	3.1 ± 0.6
Mo	1.7 ± 0.4	1.1 ± 0.2	0.9 ± 0.4
Mn	1.6 ± 0.1	1.9 ± 0.1	1.2 ± 0.2
N	-	0.1 ± 0.1	4.5 ± 1.2

Because of the enrichment of Cr content in the precipitates, the areas surrounding the precipitates are often depleted in Cr. EDS line scan was performed across the precipitates formed in samples aged at 800 °C and 900 °C for 2 hours to identify if there is an existence of depleted zones, as shown in Figure 6.5 and Figure 6.6. Figure 6.5(b) shows the Cr profile across the precipitates formed along the ferrite/austenite boundary in a sample aged at 800 °C for 2 hours. The line-scan started from the ferrite phase and ended within the austenite phase. The Cr-depleted zones formed next to the precipitates and on the side of the ferrite phase. The Cr content in the depleted zone was lower than that for both the ferrite phase and the austenite phase. Cr-depleted zones also formed near the precipitates in the ferrite phase, as shown in Figure 6.5(c). The chemical composition of the depleted zones was compared with that of the bulk phases and was summarized in Table 6.3. However, for the sample aged at 900 °C for 2 hours, no distinct Cr-depleted areas were observed from BSE-SEM images close to the precipitates shown in Figure 6.6(a) and (c). Similar line-scans were performed across the precipitates, but the Cr content next to the precipitates along ferrite/austenite boundaries was similar as that for the austenite phase,

and there was no depletion of Cr at both sides of precipitates formed in the ferrite phase, as shown in Figure 6.6(b) and (d), respectively.

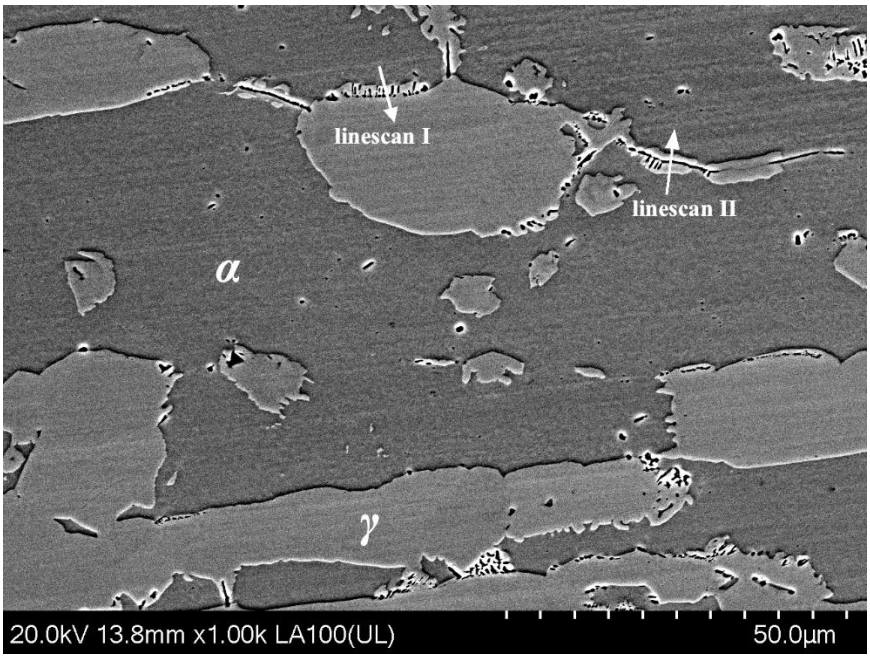

(a)

Figure 6.5 Cr content profile across precipitates formed in UNS S32003 samples aged at 1073 K (800 °C) for 2 hours. (a) BSE-SEM image showing the location of different linescans; (b) Cr K series line-scan I: across precipitates formed at the ferrite/austenite phase boundaries; (c) Cr K series line-scan II: across precipitates formed within the ferrite phase.

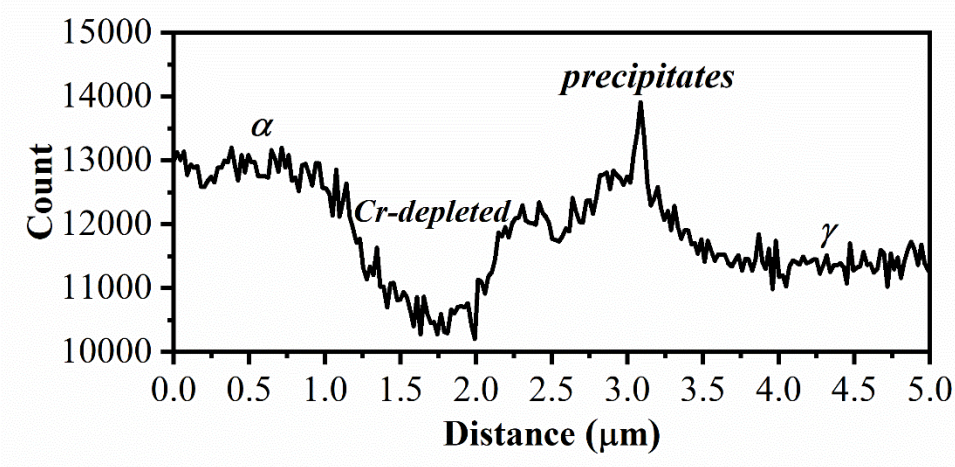

(b)

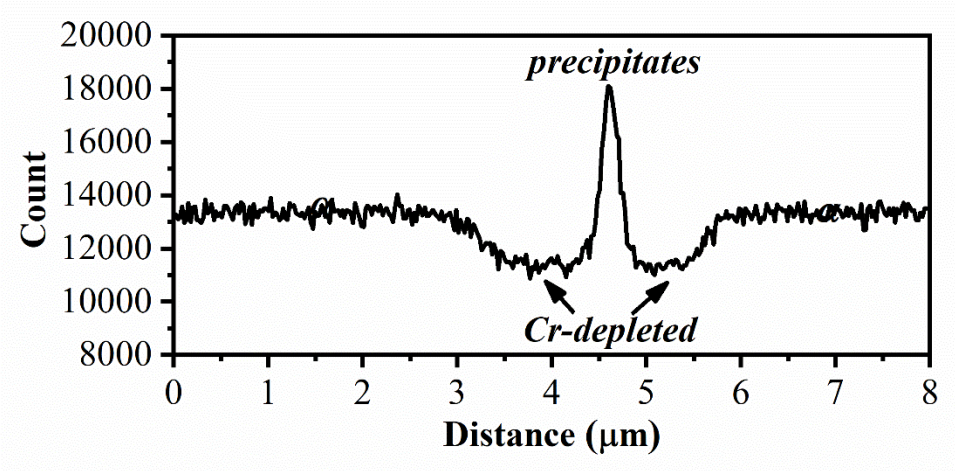

(c)

Figure 6.5 Continued.

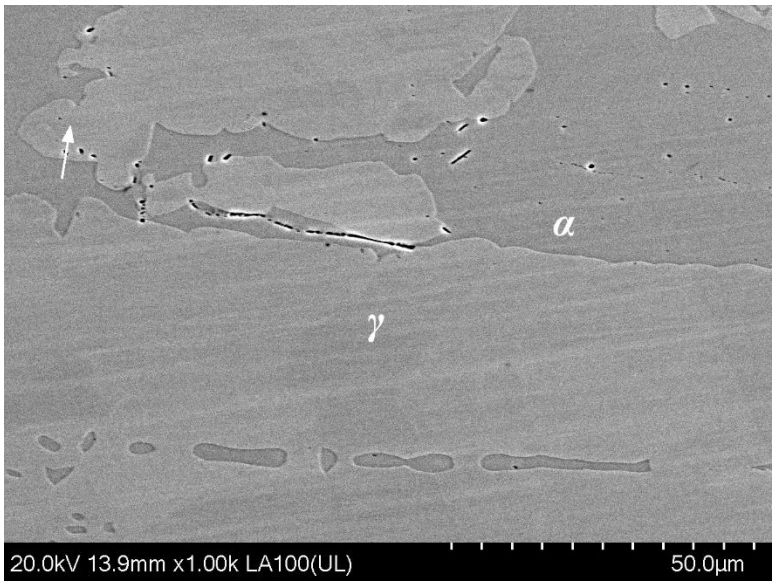

(a)

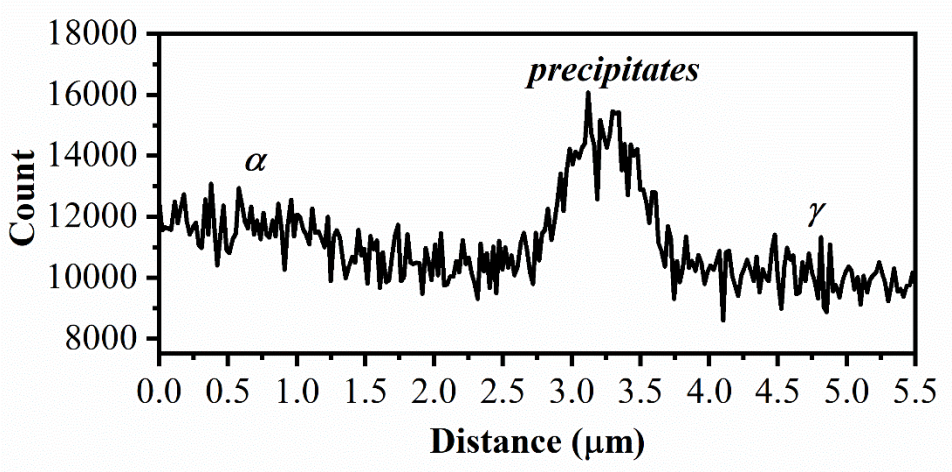

(b)

Figure 6.6 Cr profile across precipitates formed in a UNS S32003 sample aged at 1173 K (900 °C) for 2 hours. (a) BSE- SEM image showing line-scan across precipitates formed along ferrite/austenite boundaries; (b) Cr K series-line-scan across precipitates along ferrite/austenite phase boundaries; (c) BSE- SEM image showing line-scan across precipitates formed within the ferrite phase; (d) Cr K series-line-scan across precipitates within the ferrite phase.

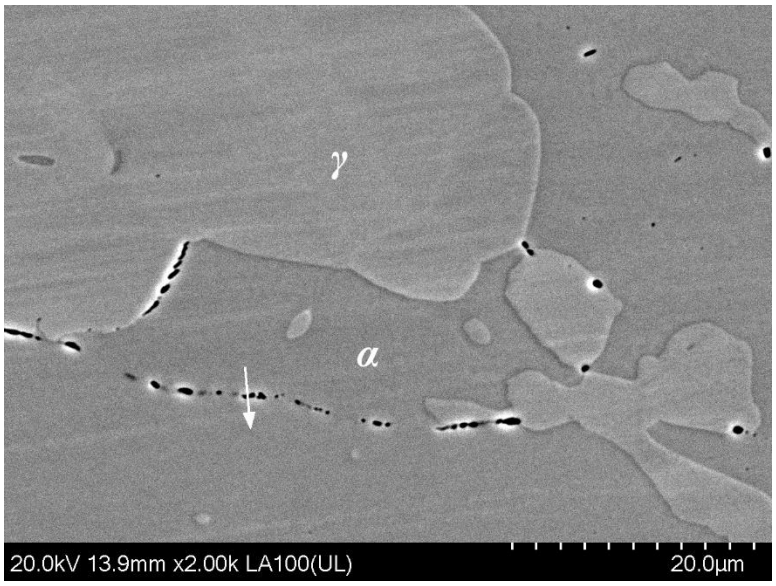

(c)

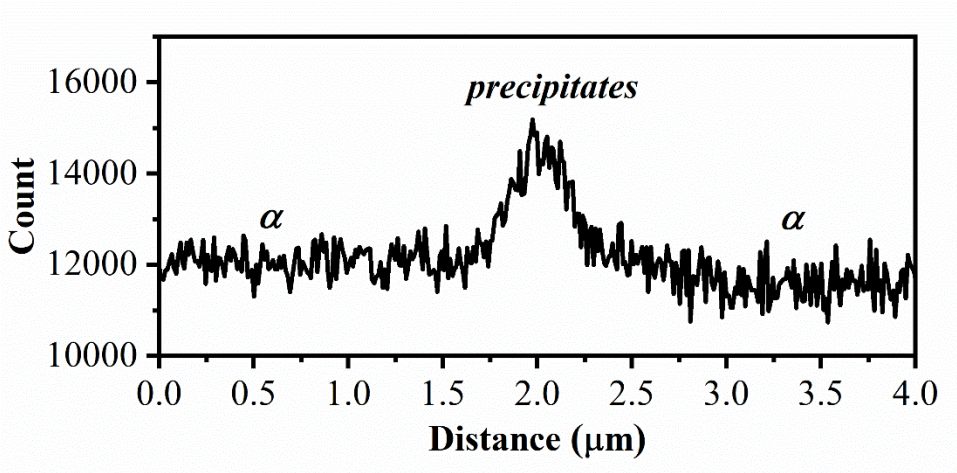

(d)

Figure 6.6 Continued.

Table 6.3 Comparison between the content of major elements in the ferrite phase, austenite phase and depleted zones in UNS S32003 samples aged at 800 ℃ for 2 hours.

	Ferrite	Austenite	Depleted zones
Cr	24.1±0.6	20.8±0.4	18.4±0.1
Ni	2.6±0.2	4.7±0.1	4.9±0.1
Mo	1.9±0.2	1.1±0.1	1.1±0.1
Mn	1.6±0.1	1.9±0	2.1±0.1
N	0.1±0.1	0.2±0.2	0.4±0.1

6.1.2 Pitting corrosion behavior of samples aged at different temperatures

The samples aged at different temperatures were tested in 0.6 mol/L NaCl at 50 ℃ to compare their pitting corrosion susceptibility. The pitting potential, E_{pit}, of different samples was acquired after each corrosion tests and compared, as shown in Figure 6.7. Pitting potential vs. aging temperatures curve showed a V shape, where the pitting potential first decreased from aging temperature of 650 ℃ and then reached a minimum for samples aged at 800 ℃ to 850 ℃. The pitting potential then increased again for the samples aged at temperature of 900 ℃, but it was lower than that for the samples aged at 700 ℃, as shown in Figure 6.7.

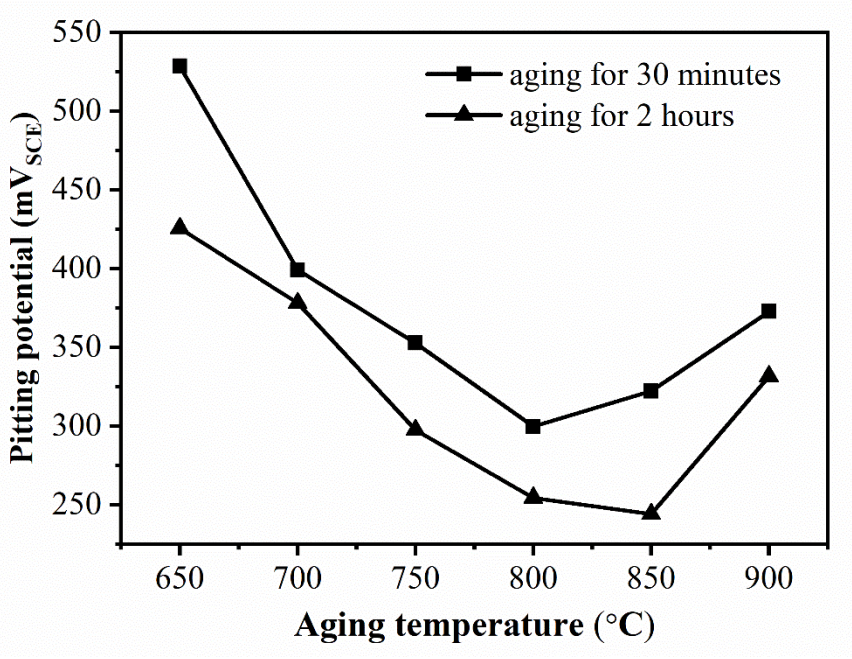

Figure 6.7 Change of pitting potential with different aging temperatures.

To identify the pit initiation site, very small pits were initiated on the polished and etched surface potentiostatically. Pit initiation site for a UNS S32003 sample aged at 850 ℃ for 2 hours is shown in Figure 6.8. A small pit with diameter of around 3 μm is located at the ferrite/austenite boundary, and close to the precipitates. The location of pit initiation site is where the depleted zones are located.

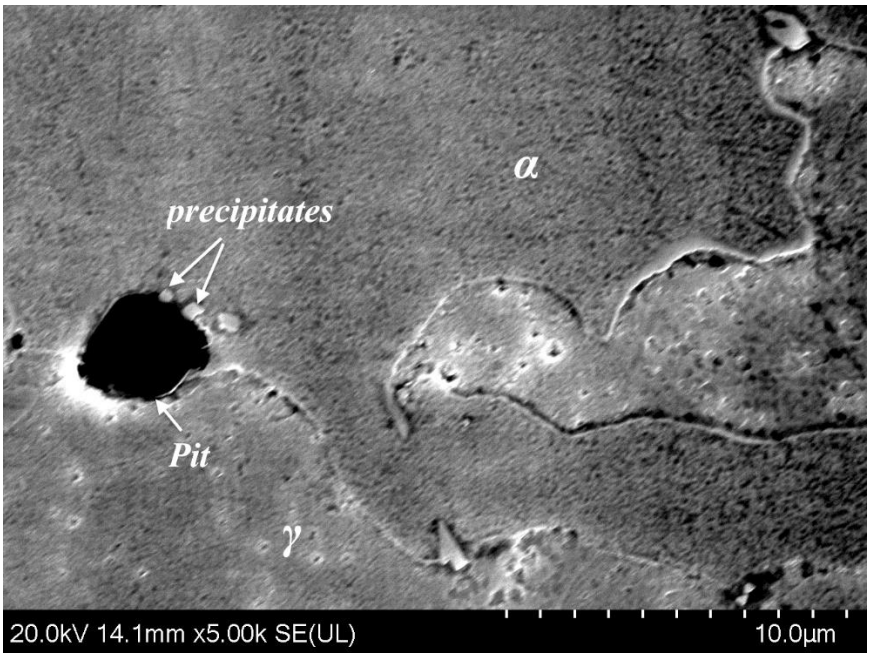

Figure 6.8 Secondary electron (SE)-SEM image showing the pit initiation site in the vicinity of precipitates in UNS S32003 sample aged at 850 ℃ for 2 hours.

6.2 Effects of isothermal aging time durations

UNS S32003 specimens were first annealed at 1040 ℃ and then water quenched, followed by isothermal aging at 700 ℃ for different time durations from 30 minutes up to 120 hours. The heat-treatment conditions are shown in Table 6.4.

Table 6.4 Sample ID under different isothermal aging conditions (change in aging time).

	Aging temperature (°C)	Aging time	Cooling
2003-700-10min	700	10 minutes	Water quenching
2003-700-30min	700	30 minutes	Water quenching
2003-700-2h	700	2 hours	Water quenching
2003-650-5h	700	5 hours	Water quenching
2003-650-12h	700	12 hours	Water quenching
2003-700-24h	700	24 hours	Water quenching
2003-700-120h	700	120 hours	Water quenching

6.2.1 Effects of aging time on microstructure evolution

To observe the microstructure evolution over time, the annealed UNS S32003 samples were aged at 700 ℃ for different time periods from 10 minutes up to 120 hours. For samples aged at 700 ℃ for 2 hours and 24 hours, only nitride precipitates were observed, which appeared as dark spots in the NaOH etched microstructure as shown in Figure 6.9(a) and (b). The volume fraction of precipitates increased from 0.07% to 0.41%. To reveal the detailed morphology of precipitates, high-magnification SEM images were taken on surfaces of samples etched in Pellegrino's etchant, as shown in Figure 6.10(a) and (b). EDS analysis also confirmed that the area in the vicinity of precipitates was depleted in Cr in the sample aged at 700 ℃ for 24 hours.

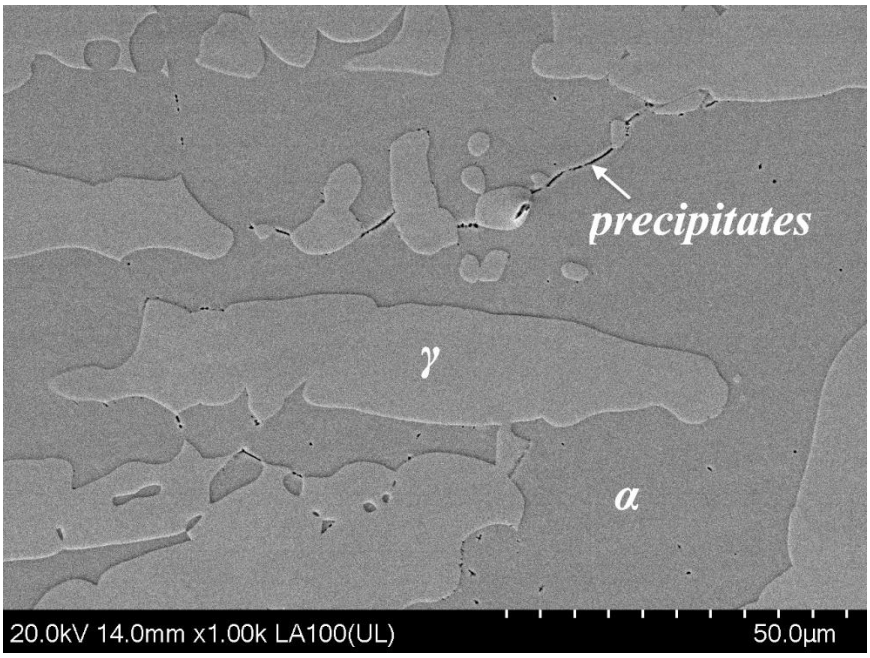

(a)

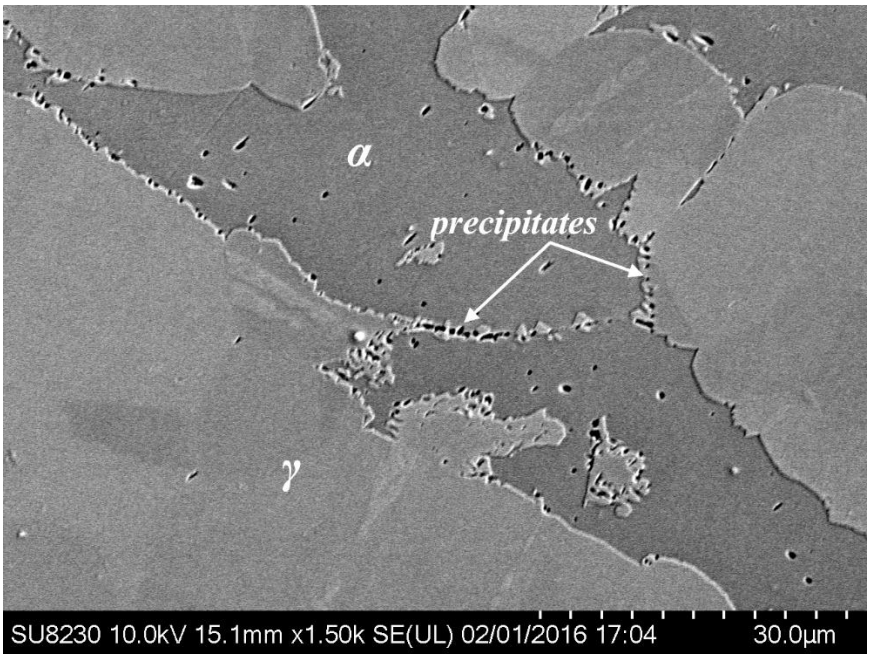

(b)

Figure 6.9 BSE-SEM images of samples aged at 700 °C for (a) 2 hours; (b) 24 hours; (c) 120 hours. Sample surface was etched in 40 wt% NaOH etchant.

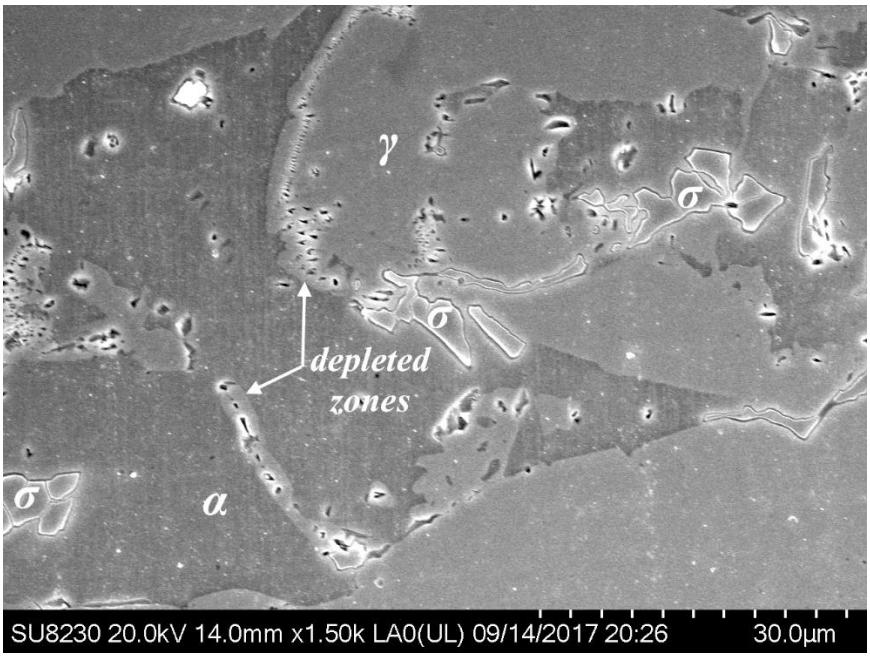

(c)

Figure 6.9 Continued.

Figure 6.9 (c) and Figure 6.10(c) show the microstructure of samples aged at 700 °C for 120 hours and etched in NaOH and Pellegrino's etchant. The surface fraction of the precipitates further increased to 0.97%. However, along with the formation of precipitates, intermetallic phase with larger size than the precipitates was also observed along the ferrite/austenite boundaries and within the ferrite phase in the sample aged for 120 hours. The chemical composition of intermetallic phases is shown in Table 6.5. The intermetallic phases are enriched in Cr and Mo and the Mo content is quite consistent with a value of around 4.6 wt%, confirming that they are σ phase.

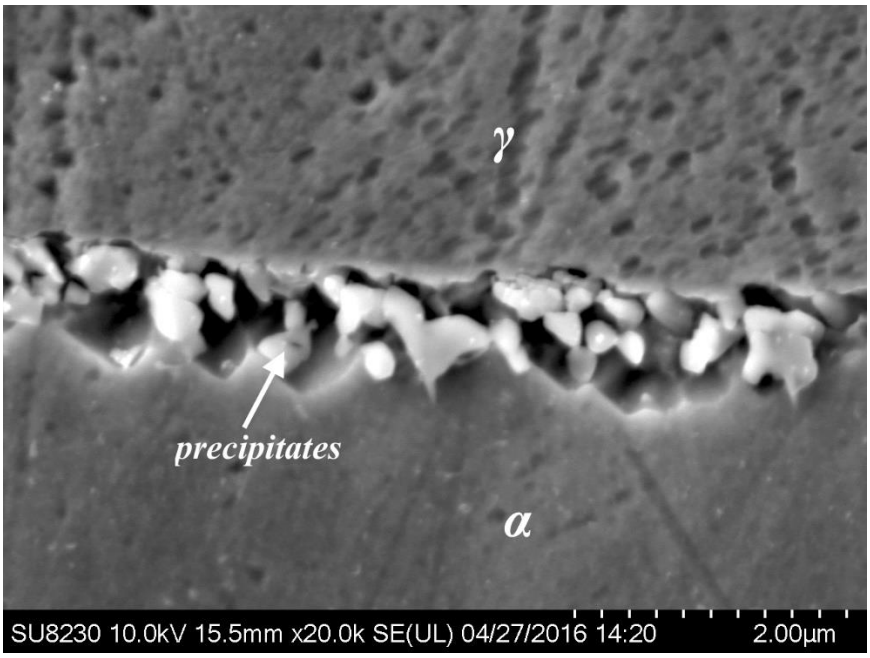

(a)

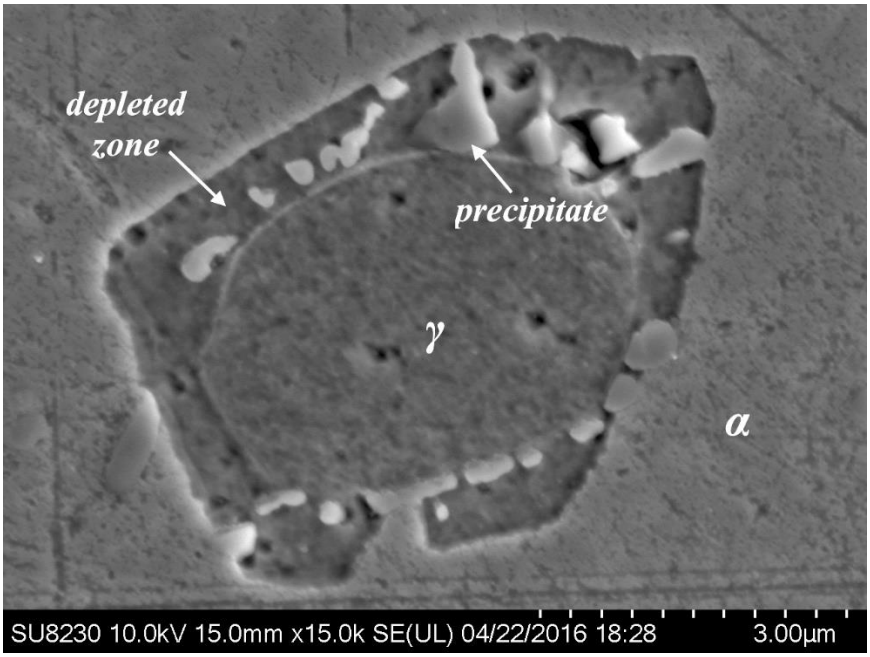

(b)

Figure 6.10 SEM images of microstructure of UNS S32003 samples aged at 700 °C for (a) 5 hours; (b) 24 hours; (c) 120 hours.

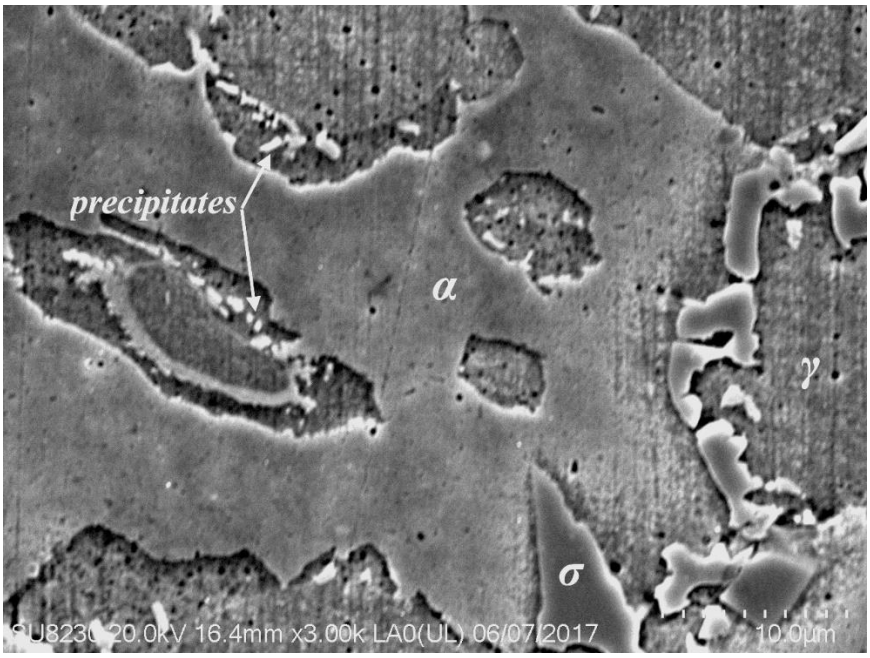

(c)

Figure 6.10 Continued.

Table 6.5 EDS analysis of chemical composition of different microstructural features in UNS S32003 samples aged at 700 °C for 120 hours.

	Ferrite	Austenite	σ phase	Depleted zones
Cr	23.0±0.3	20.0±0.1	28.5±1.9	18.4±0.1
Ni	2.0±0.2	4.6±0.0	2.1±0.2	4.9±0.1
Mo	1.5±0.3	1.0±0.2	4.6±0.4	1.1±0.1
Mn	1.5±0.1	1.9±0.0	1.8±0.1	2.1±0.1

X-ray diffraction (XRD) analysis was also carried out on the annealed specimen and two other specimens aged at 700 °C, as shown in Figure 6.11. The angles were scanned in the range of 35° to 60°. For the specimen annealed at 1040 °C, only ferrite phase (α) and

austenite phase (γ) peaks were detected. Although nitrides in the specimen aged at 700 ℃ for 24 hours were detected in the SEM/EDS analysis, their peaks were not observed in the XRD spectrum shown in Figure 6.11(b), probably due to their low amount (less than 0.41%). Only ferrite and austenite peaks were detected in the XRD analysis of the specimen aged at 700 ℃ for 24 hours. Further, for the specimen aged at 700 ℃ for 120 hours, in addition to the ferrite and austenite peaks, peaks corresponding to the σ phase were also detected. Corroborating with the fact that χ phase was not positively identified during SEM/EDS analysis of the specimen aged at 700 ℃ for 120 hours, it was confirmed that χ phase was not present in the microstructure of the specimen aged at 700 ℃ for 120 hours.

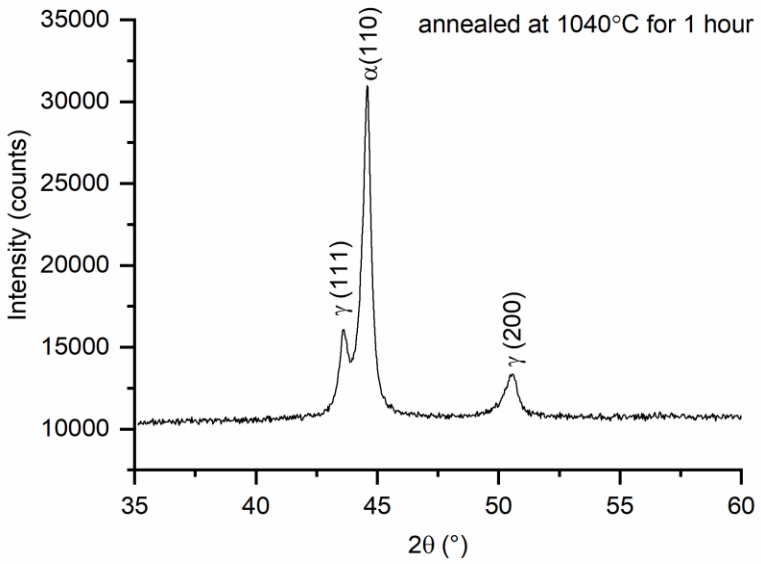

(a)

Figure 6.11 XRD patterns of specimens (a) annealed at 1040 ℃ for 1 hour; (b) aged at 700 ℃ for 24 hours; and (c) aged at 700 ℃ for 120 hours. γ: the austenite phase; α: the ferrite phase.

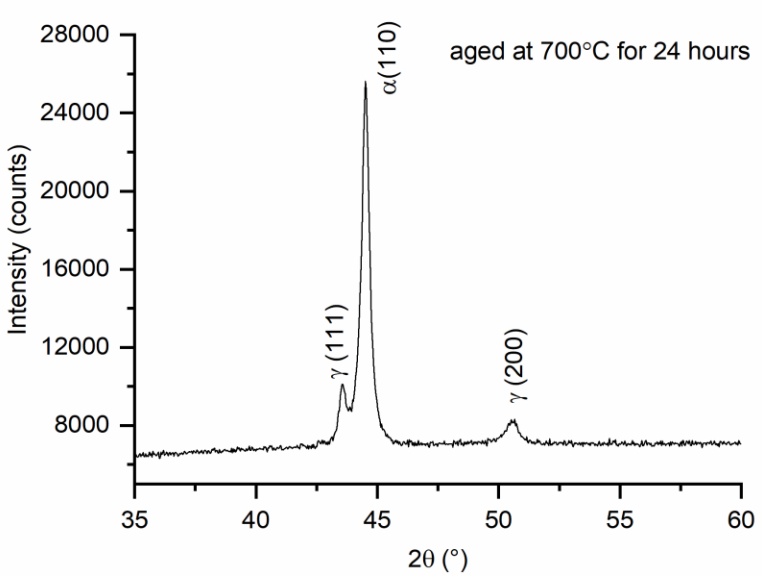

(b)

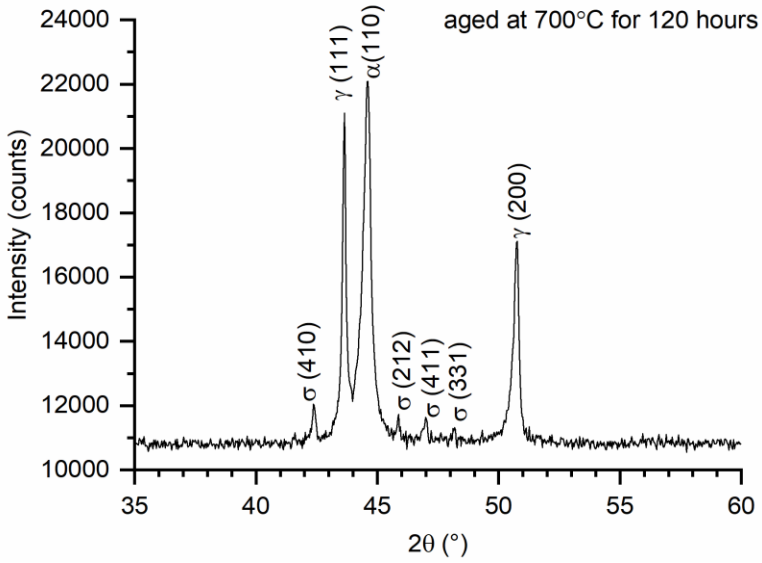

(c)

Figure 6.11 Continued.

6.2.2 Pitting corrosion resistance of samples aged at 700 °C for different aging time

Pitting corrosion behavior of samples aged at 700 °C for different time period was tested in 0.6 mol/L NaCl solution at 50 °C. The pitting potential and the repassivation potential dropped with longer aging time, as shown in Figure 6.12 and Table 6.6, indicating an increasing pitting corrosion susceptibility with aging time. The deviation of pitting potential is large for the samples aged for shorter periods of time up to 5 hours.

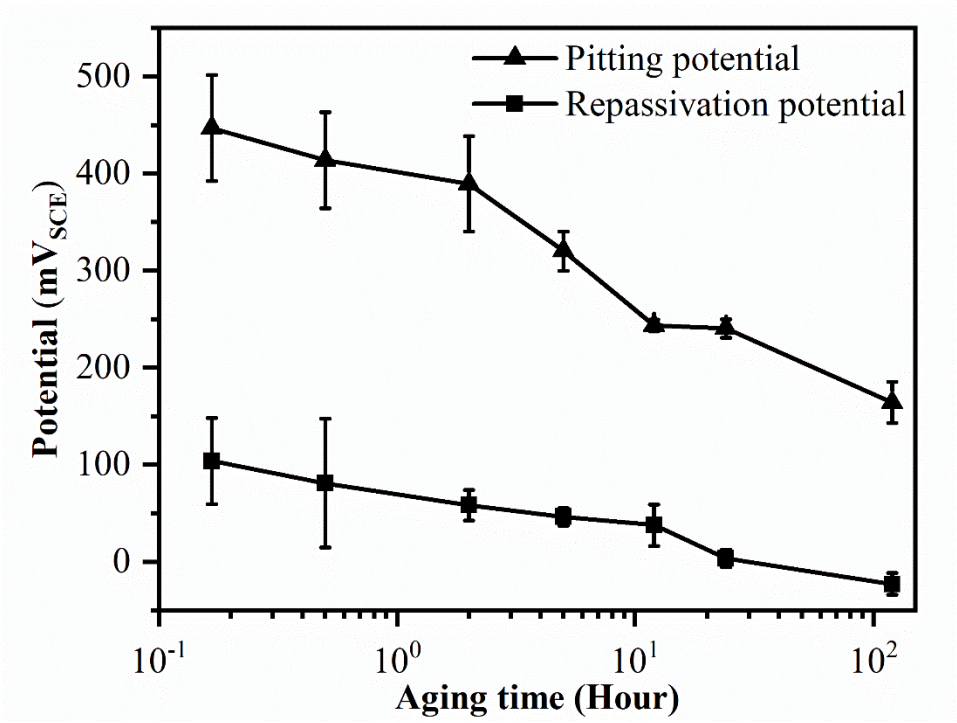

Figure 6.12 Change in pitting potential and repassivation potential with aging time at 700 °C.

Table 6.6 Values of pitting potential and repassivation potential.

Aging time (hour)	Pitting potential (mV_{SCE})	Repassivation potential (mV_{SCE})
0	451 ± 48	72 ± 22
0.17	447 ± 55	104 ± 45
0.5	414 ± 50	81 ± 66
2	390 ± 49	58 ± 16
5	320 ± 20	46 ± 9
12	243 ± 6	38 ± 21
24	241± 9	3 ± 9
120	164 ± 21	-23 ± 11

The approach used to study the effect of aging temperature on pitting corrosion behavior was also used to study the pit initiation site in samples aged at 700 °C. Similar to the small pits observed in the sample aged at 850 °C for 2 hours, the small pit initiated in the sample aged at 700 °C for 24 hours is also located at the ferrite/austenite boundary with nitride precipitation.

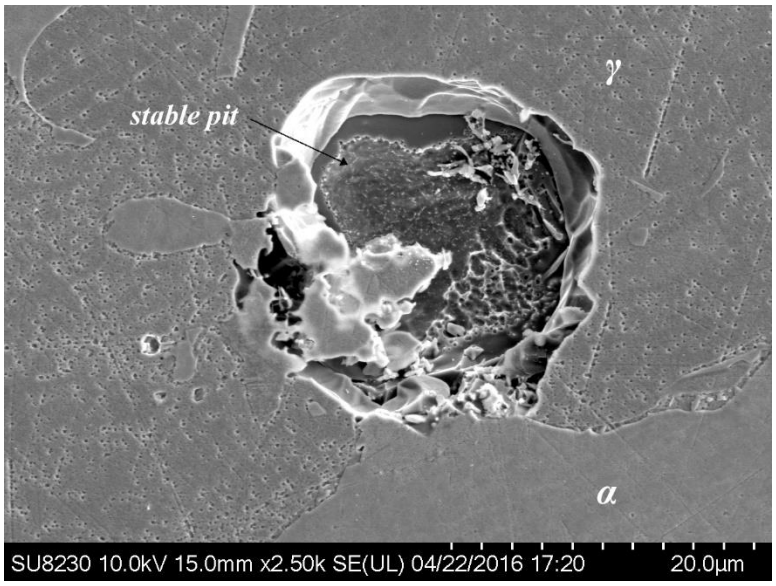

Figure 6.13 SE-SEM image showing the pit located at the ferrite/austenite boundary in sample aged at 700 °C for 24 hours.

Peaks resulting from metastable pitting events occurred below the pitting potential during potentiodynamic polarization, as shown in Figure 6.1. The rate of occurrence of metastable pitting events was defined as the number of metastable pitting events during each 100 mV intervals divided by the time spent (100s for 1mV/s scan rate). During potentiodynamic polarization, the occurrence of metastable pitting first increased to a peak value and then decreased at higher potentials, as shown in Figure 6.14(a). Although metastable pitting in the annealed sample occurred over a wide range of potential, but the metastable pitting rate in the annealed sample appeared to be the lowest. In Figure 6.14(b), metastable pitting rate in the potential range of 0-100 mV_{SCE} and 100-200 mV_{SCE} was compared since above 200 mV_{SCE}, stable pits would develop in the samples aged for 120 hours. Higher rate of metastable pitting indicates a higher frequency of film breakdown and repassivation, which is also an indication of higher pitting corrosion susceptibility. The

rate of occurrence of metastable pitting within the potential range of 0-100 mV and 100-200 mV increased with the longer aging time period, indicating that the aging for longer time periods deteriorate pitting corrosion resistance of UNS S32003.

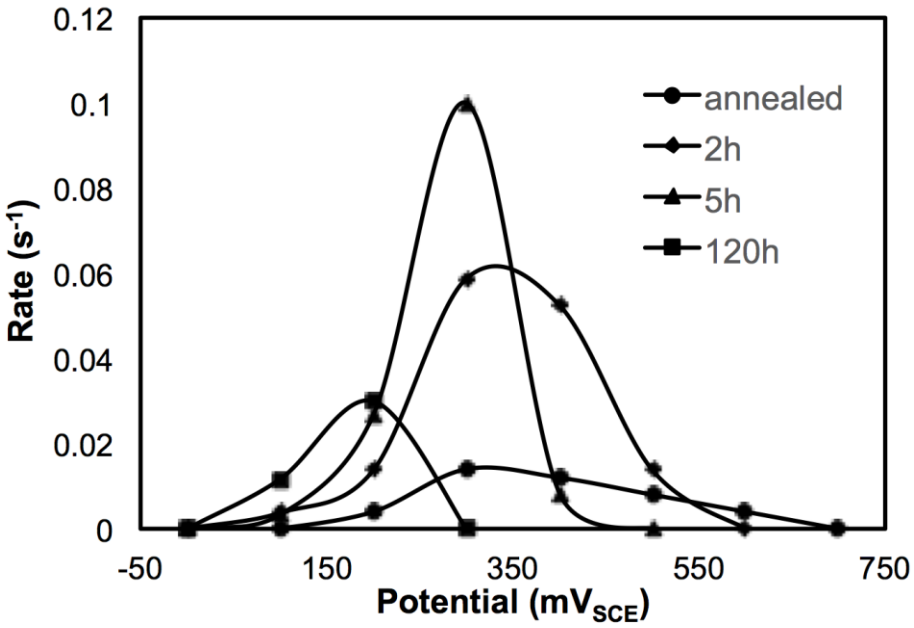

(a)

Figure 6.14 Rate of occurrence of metastable pitting for heat-treated specimens. (a) Change in the rate of occurrence with potential. (b) Change in the rate of metastable pitting in the potential range of 0-100 mV_{SCE} and 100-200 mV_{SCE} with aging time.

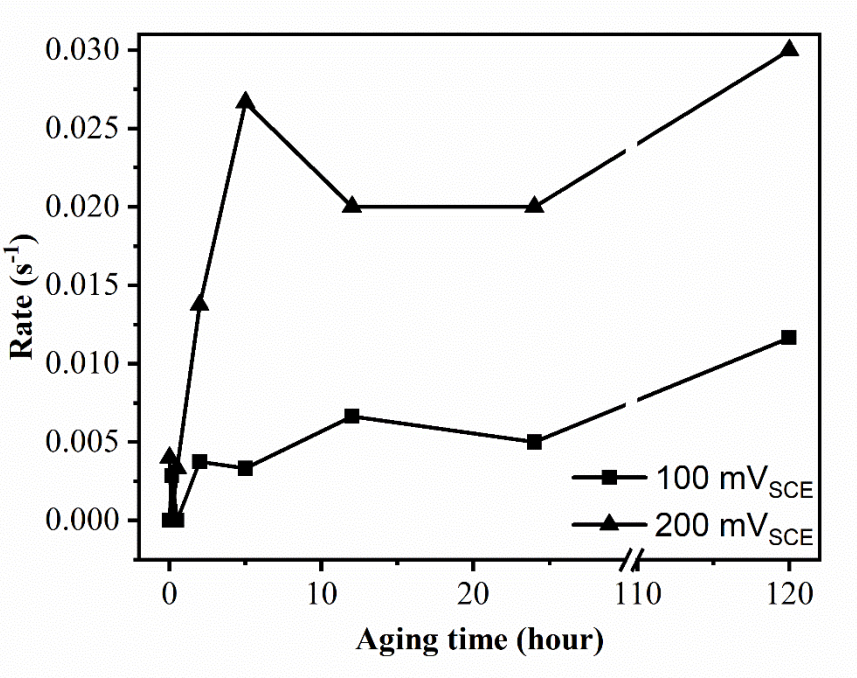

(b)

Figure 6.14 Continued.

6.3 Discussions

6.3.1 Phase transformations

After an isothermal aging of UNS S32003 within the temperature range of 600°C to 900°C for 2 hours, only nitride precipitates were positively identified while the intermetallic phases were not detected, as shown in Figure 6.2 and Figure 6.4. Similar phenomena have been reported for duplex stainless steels UNS S32101 and S32304 that also have leaner alloying content, especially lower Mo content, and only nitrides and carbides were detected after hours of aging in the temperature range of 700°C to 850°C. [111-113] However, for

standard S32205 and super DSSs, intermetallic phases form within minutes when aged at 800°C or 850°C.[58, 109, 112, 114] Since the intermetallic phases are enriched in Cr and Mo, the lower Cr and Mo content in UNS S32003 leads to the slow formation of intermetallic phases.

However, σ phase was detected after a long-term aging (120 hours) at 700°C in UNS S32003. Thermodynamic predication through Thermo-Calc indicates that σ phase is stable phase within temperature range of 500°C to 854°C, as shown in Figure 6.15. Although M_3P, $M_{23}C_6$ and MnS are also predicted to be stable within this temperature range, however, their volume fraction was in the order of 10^{-5} to 10^{-3} and they were not detected in all aged samples using SEM/EDS technique. This is probably because of the low content of element P, C and S in this alloy. $M_{23}C_6$ has been observed to precipitate along with Cr_2N using electron backscatter diffraction (EBSD) technique, [59] however, it's not possible to quantify $M_{23}C_6$ using SEM/EDS analysis because of the unavoidable carbon contamination in the SEM chamber. Although it has been reported that χ phase precipitated together with σ phase, [114, 115] it was not observed in the present study. Both χ phase and σ phase are enriched in Cr and Mo, however, χ phase has high Mo content more than 10wt%. [54, 56, 114, 115] Table 6.5 shows the chemical compositions of different phases in samples aged at 700°C for 120 hours, and the Mo content is 4.6 wt% with 95% confidence interval of 0.4 wt%, indicating that only σ phase is present after aging at 700°C for 120 hours. This may be because the χ phase is a metastable phase and after 120 hours of aging, it might have already transformed into σ phase. [115]

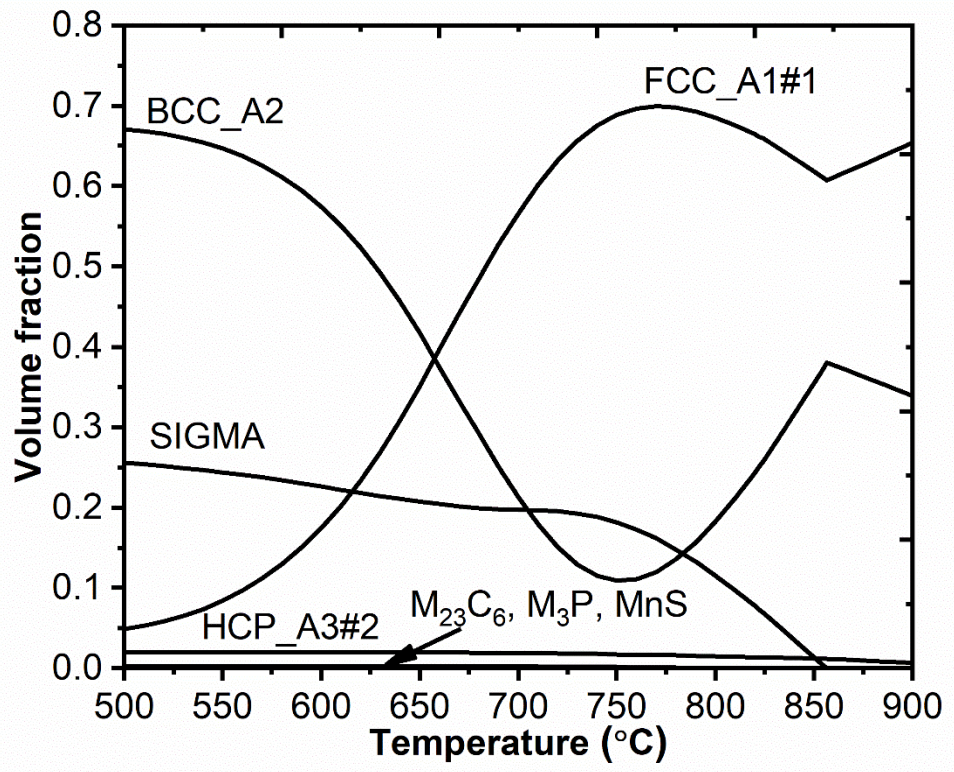

Figure 6.15 Thermo-Calc prediction of stable phases within the temperature range of 500 °C to 900°C. BCC_A2: the ferrite phase; FCC_A1#1: the austenite phase; SIGMA: σ phase; HCP_A3#2: nitride.

As shown in Figure 6.9 and Figure 6.10, phase transformation process during isothermal aging at 700°C in UNS S32003 involves first precipitation of nitrides and possibly carbides, and then the precipitation of σ phase after longer aging time. As shown in Figure 6.9(c), *σ* phase formed within the ferrite phase or along the ferrite/austenite boundaries and propagated into the ferrite phase, because of the higher diffusion rate and higher content of Cr and Mo in the ferrite phase. This process is similar to what has been observed in the lean duplex stainless steel UNS S32101 during isothermal aging at 690°C, where the *σ* phase was found to precipitate in the vicinity of nitride and carbide precipitates because of the local changes in the element content.[59]

6.3.2 Effects of aging on pitting corrosion behavior

Results in Figure 6.7 compare the pitting potential of samples aged at different temperatures for 30 minutes and 2 hours. Staring from 650 °C aged samples, the pitting potential first dropped with an increase in the aging temperature reaching a lowest value around 800 °C to 850 °C, and then the pitting potential increased for the samples aged at 900 °C. This is consistent with the microstructural evolution where for the samples aged at 800°C, the volume fraction of precipitates is the highest and the Cr-depleted zones is present, as shown in Figure 6.3. With the longer aging times at 700 °C, there is a decrease in the pitting potential as well as the repassivation potential, as shown in Figure 6.12. An increased metastable pitting rate was also observed with longer aging times, indicating the deteriorating effect of aging on pitting corrosion resistance, as shown in Figure 6.14(b).

Figure 6.8 and Figure 6.13 showed that the pit initiation sites reside at the ferrite/austenite boundary and close to the nitride precipitates. It is evident in Figure 6.8 that the pit initiation is closely related to the precipitate formation, probably because of the Cr-depleted zones associated with the precipitates. Since Cr is a major element in the passive film and is responsible for an increased corrosion resistance of stainless steels, the depletion of Cr in the vicinity of precipitates and σ phase seems to be the major reason for the deterioration of pitting corrosion resistance of aged samples. Except for the sample aged at 700 °C for 120 hours which also had σ phase precipitates, all aged samples had nitride precipitates, and the volume fraction of precipitates was below 1%. However, the change in the pitting corrosion resistance in terms of pitting potential, repassivation potential and metastable pitting event rates is very sensitive to the variation in the fraction of precipitates.

6.4 Conclusions

1. Only nitrides precipitates were positively detected along the ferrite/austenite phase boundaries and within the ferrite phase for the UNS S32003 samples aged in the temperature range of 873 K (600 °C) to 1173 K (900 °C) for up to 2 hours.
2. The precipitation kinetics was the fastest at 1073 K (800 °C) for the UNS S32003, where the Cr-depleted zones were observed to be in the vicinity of the precipitates.
3. For samples aged at 973 K (700 °C) for 120 hours, σ phase was detected along with an increase in the percentage of precipitates.
4. Precipitates were found to be at the edge of small pits, indicating the pit initiation is close to the precipitates and is probably associated with the Cr-depleted zones.
5. Pitting corrosion resistance decreased with higher fraction of nitride precipitates and the formation of σ phase. The change in the pitting corrosion resistance in terms of pitting potential, repassivation potential and metastable pitting rate is very sensitive to the precipitation of secondary phases even when the volume fraction of these precipitates is below 1%.

CHAPTER 7. PROPERTIES OF INDIVIDUAL-PHASES IN DUPLEX STAINLESS STEELS

7.1 Introduction

A preferential dissolution of the ferrite phase in UNS S32304 and S32101 samples in solutions containing $S_2O_3^{2-}$ and Cl^- was observed in this study, as described in Chapter 4. Because of the difference in the chemical composition, it is hypothesized that the pitting corrosion resistance is different for the individual ferrite or austenite phase. Also, in the aggressive pit solution with high acidity and high anion concentrations, there can be galvanic effects between the two constituent phases in DSSs. In order to study and compare the corrosion behavior of the two phases (ferrite and austenite), it is necessary to get the sample with single-phase microstructure.

One way to achieve that is to use super austenitic and super ferritic stainless steel samples to simulate the austenite phase and the ferrite phase in DSSs. However, since the chemical composition of each grade of DSSs is different, these alloys cannot fully represent the constituent phases in DSSs. In this chapter, a method following Tsai et. al. was used and the single ferrite phase and single austenite phase was separated in a mixed H_2SO_4 and HCl acid solution through preferential dissolution of the other phase. The process is described in the following experimental details.

After the single-phase microstructure was obtained, the pitting corrosion behavior of the single ferrite phase and single austenite phase was studied using potentiodynamic

cyclic polarization tests and scratch tests in solutions containing Cl^- and $S_2O_3^{2-}$. Galvanic effects between the two phases was studied in 2 mol/L HCl and (2 mol/L HCl + 0.02 mol/L $S_2O_3^{2-}$) solution to simulate the galvanic corrosion in pit solution.

7.2 Preparation of samples with single ferrite phase or single austenite phase

Figure 7.1 shows the potential region for active dissolution of UNS S32304 in mixed (2 mol/L H_2SO_4 + 0.5 mol/L HCl) solution at room temperature. There are two peaks in the active region, one at the potential of ~ -340 mV_{SCE}, while the other at the potential of ~ -265 mV_{SCE}. The two peaks during potentiodynamic polarization result from the maximum dissolution of the ferrite phase and the maximum dissolution of the austenite phase in UNS S32304 sample.

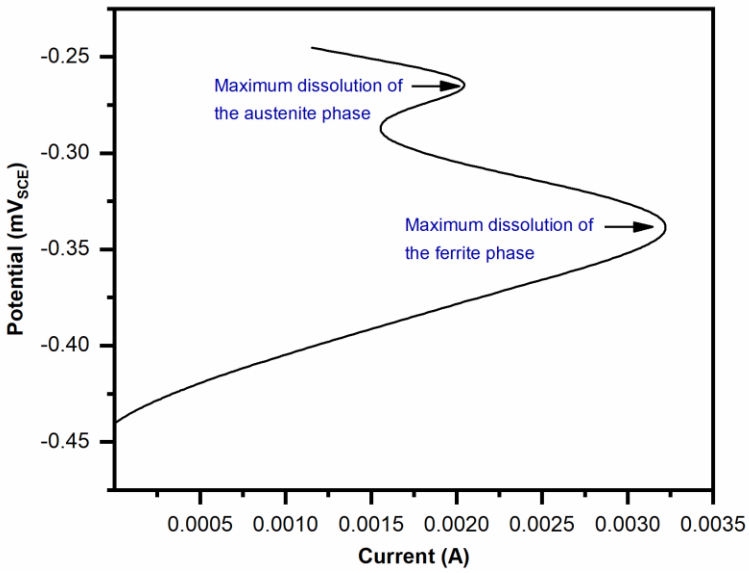

Figure 7.1 Active dissolution region of potentiodynamic polarization curve of UNS S32304 in (2 mol/L H_2SO_4 + 0.5 mol/L HCl) acidic solution at room temperature.

After potentiodynamic polarization, two UNS S32304 samples were polarized at those two potentials respectively for ten hours to selectively dissolve one phase and to get the single-phase microstructure of the other phase. The chemical composition of the remaining single phase was then characterized using EDS analysis and the results are shown in Table 7.1. It was confirmed that the rate of dissolution of the ferrite phase was the fastest at a lower potential of -340 mV_{SCE}, while the rate of dissolution of the austenite phase was the fastest at a higher potential of -265 mV_{SCE}.

Table 7.1 Chemical composition of individual phases in UNS S32304

Polarization potential	Cr	Ni	Mn	Mo	Phase remained	Phase selectively dissolved
-265 mV_{SCE}	25.7	3.1	1.0	0.4	Ferrite	Austenite
-340 mV_{SCE}	21.6	5.3	1.3	0.5	Austenite	Ferrite

The microstructure of the single ferrite phase and the single austenite phase was characterized under SEM and the top views are shown in Figure 7.2. The ferrite phase is interconnected while the austenite phase forms individual islands. The space previously occupied by the dissolved phase was then filled with lacquer to expose only one phase on the surface. The single-phase samples were also cross-sectioned and observed under SEM. Figure 7.3 shows the cross-sections of individual austenite and ferrite phase samples and the average depth of the single phase in tested samples was around 80-100 μm.

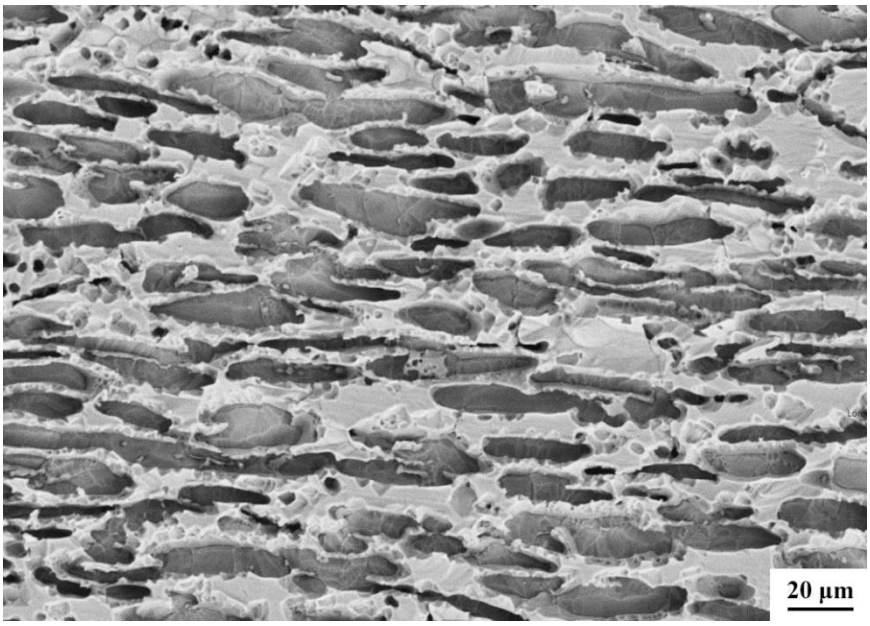

(a)

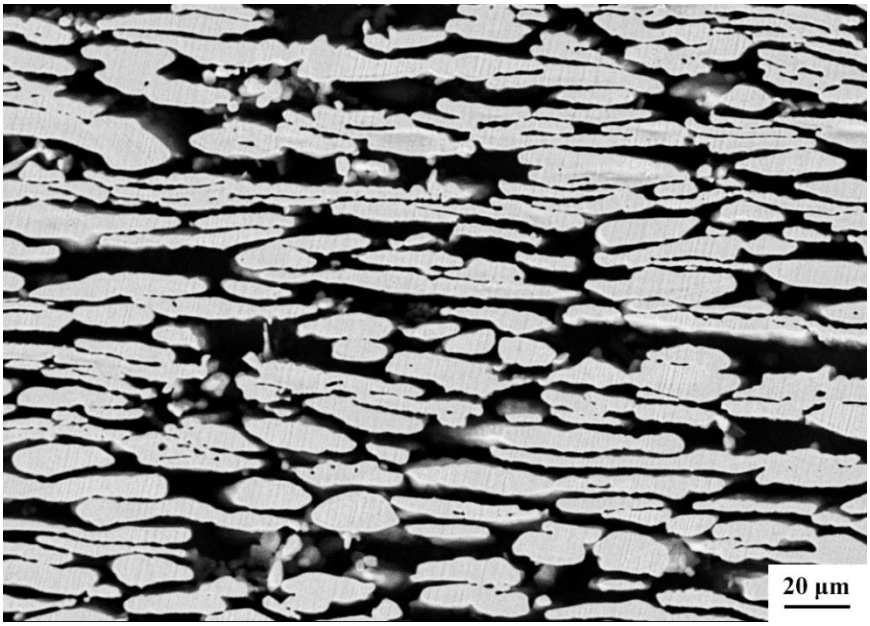

(b)

Figure 7.2 SEM images of microstructure with individual (a) ferrite phase after preferential dissolution of the austenite phase at -265 mV_{SCE}; and (b) austenite phase after preferential dissolution of the ferrite phase at -340 mV_{SCE}.

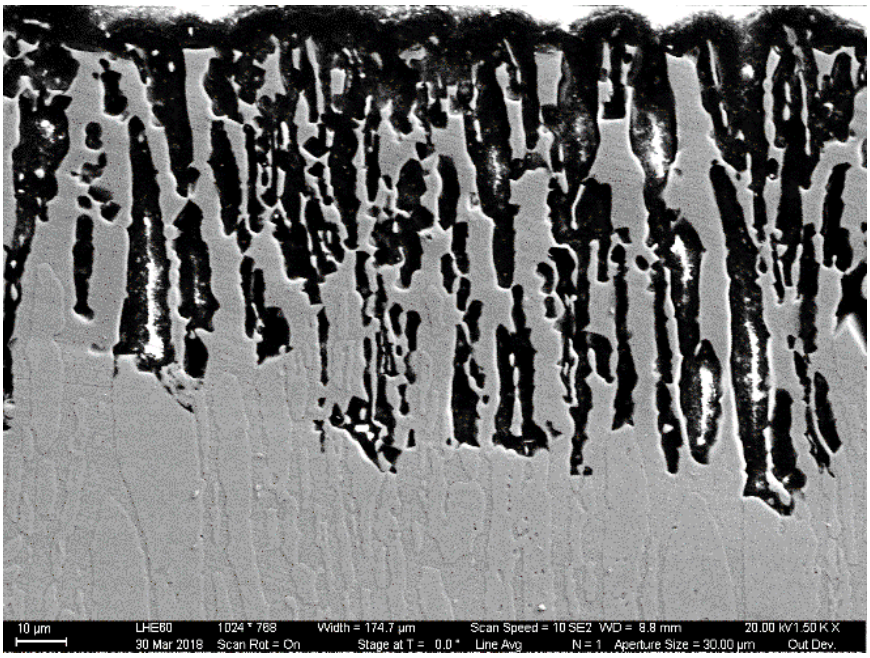

(a)

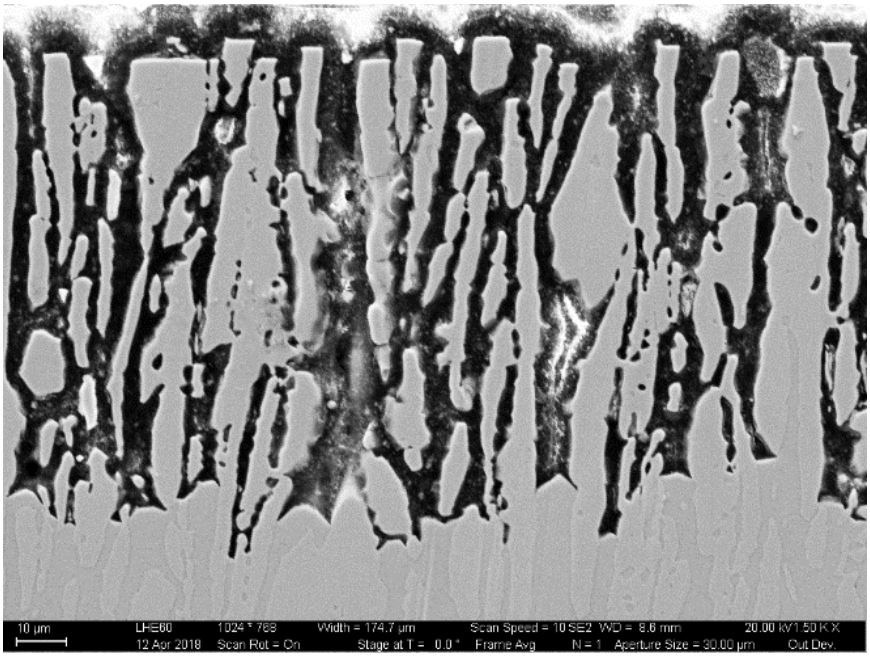

(b)

Figure 7.3 Cross-section of the separated individual phases: (a) Ferrite phase; (b) Austenite phase.

7.3 Scratch test results for single ferrite phase and single austenite phase samples

To study the pit growth and repassivation behavior of single-phase samples and to avoid crevice corrosion, scratch test method introduced in section **3.3.4** Potentiostatic scratch tests of this thesis was used. The current is allowed to stabilize for 60 seconds at the passive current and then the scratch is made using a diamond scriber to remove the passive film. The current is recorded for another 60 seconds. Continuous current increase indicates the development of localized corrosion. The test solution in this study was concentrated solution with (6000 mg/L Cl^- + 1160 mg/L $S_2O_3^{2-}$) at 50 °C. The single-phase samples were polarized at different potentials between -300 mV_{SCE} and 0 V_{SCE}. At least three tests were conducted under the same condition to check the reproducibility of test results.

Since the depth of single-phase microstructure was 80-100 μm, the depth of scratch should not exceed this value. In fact, the depth of the scratch made was far less than the depth of single-phase microstructure. Profilometry was used to characterize the scratch depth, as shown in Figure 7.4, and the depth of scratch was around 1μm.

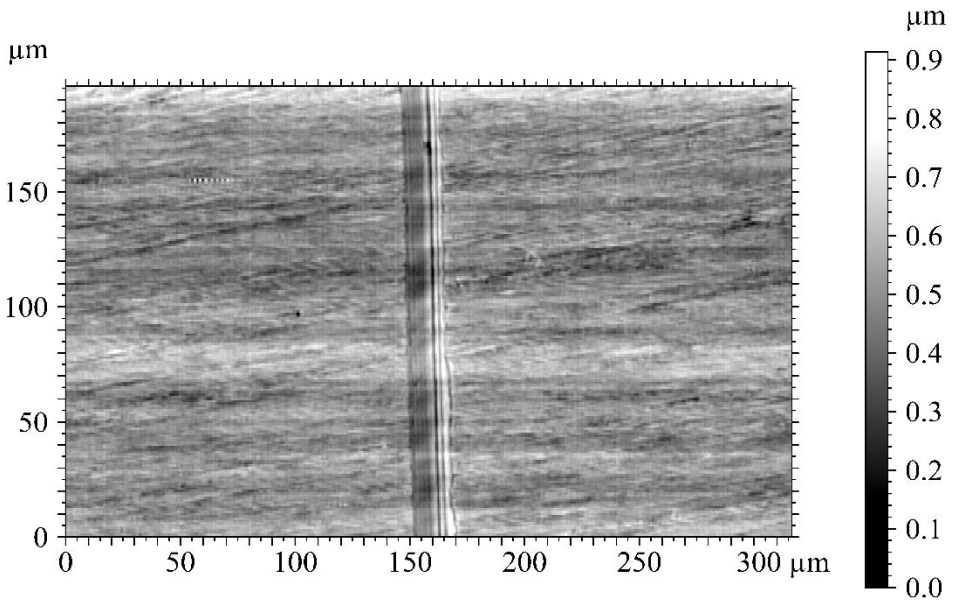

Figure 7.4 Profilometry image showing the depth of scratch.

For the single ferrite phase, the samples only repassivated after scratch when they are polarized at -300 mV_{SCE}, as shown in Figure 7.5. Since the applied potential was below the open circuit potential of the ferrite phase (-49 mV), cathodic reaction dominated at this potential, resulting in the negative current transients. The peak current during scratch at 0s was also negative, indicating that the cathodic reaction dominated on the bare alloy surface without passive film and there is no active dissolution on the bare alloy surface at -300 mV_{SCE}.

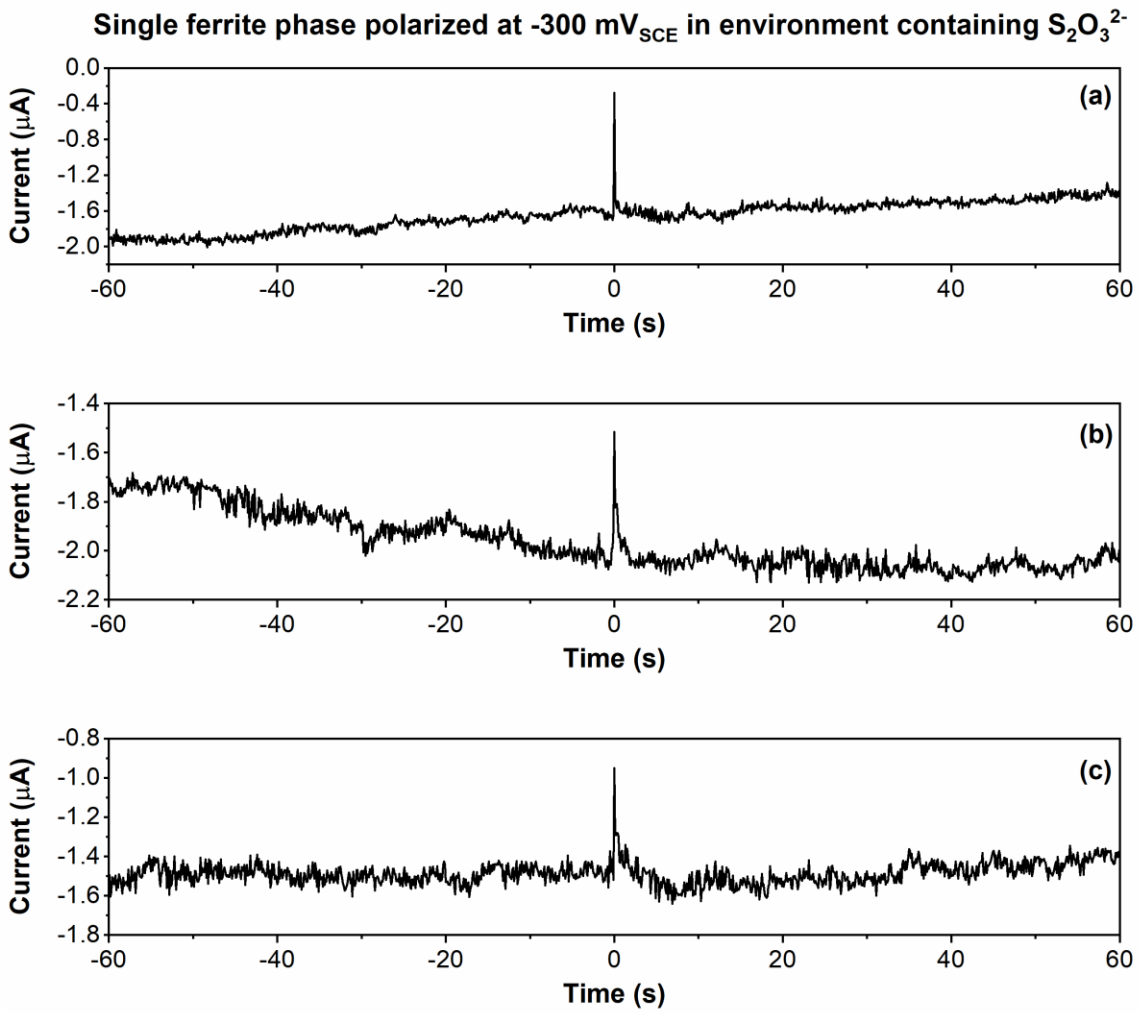

Figure 7.5 Current transients during potentiostatic polarization scratch tests of single ferrite phase in solution containing (6000 mg/L Cl^- + 1160 mg/L $S_2O_3^{2-}$). Potential: -300 mV_{SCE}. Graphs (a), (b) and (c) were the results under the same condition.

In comparison, Figure 7.6 shows the current transients during scratch tests of samples with single ferrite phase polarized at -200 mV_{SCE}. Before the scratch, the current on the surface with passive film was negative, which indicated a domination of the cathodic reaction. The current after the scratch did not decreased to the negative value, but increased continuously in the positive regime, indicating the anodic dissolution of the base alloy and the development of localized corrosion in the environment containing Cl^- and $S_2O_3^{2-}$ at -

200 mV_{SCE}. Since there are lacquer filled gaps on the surface of single ferrite phase samples, there was some randomness in whether the scratch was made on the ferrite phase or the lacquer. Therefore, the total current spike after scratch was different and thus the scale is different for the three test results shown in Figure 7.6. However, the current response was similar for the single ferrite samples at -200 mV_{SCE}.

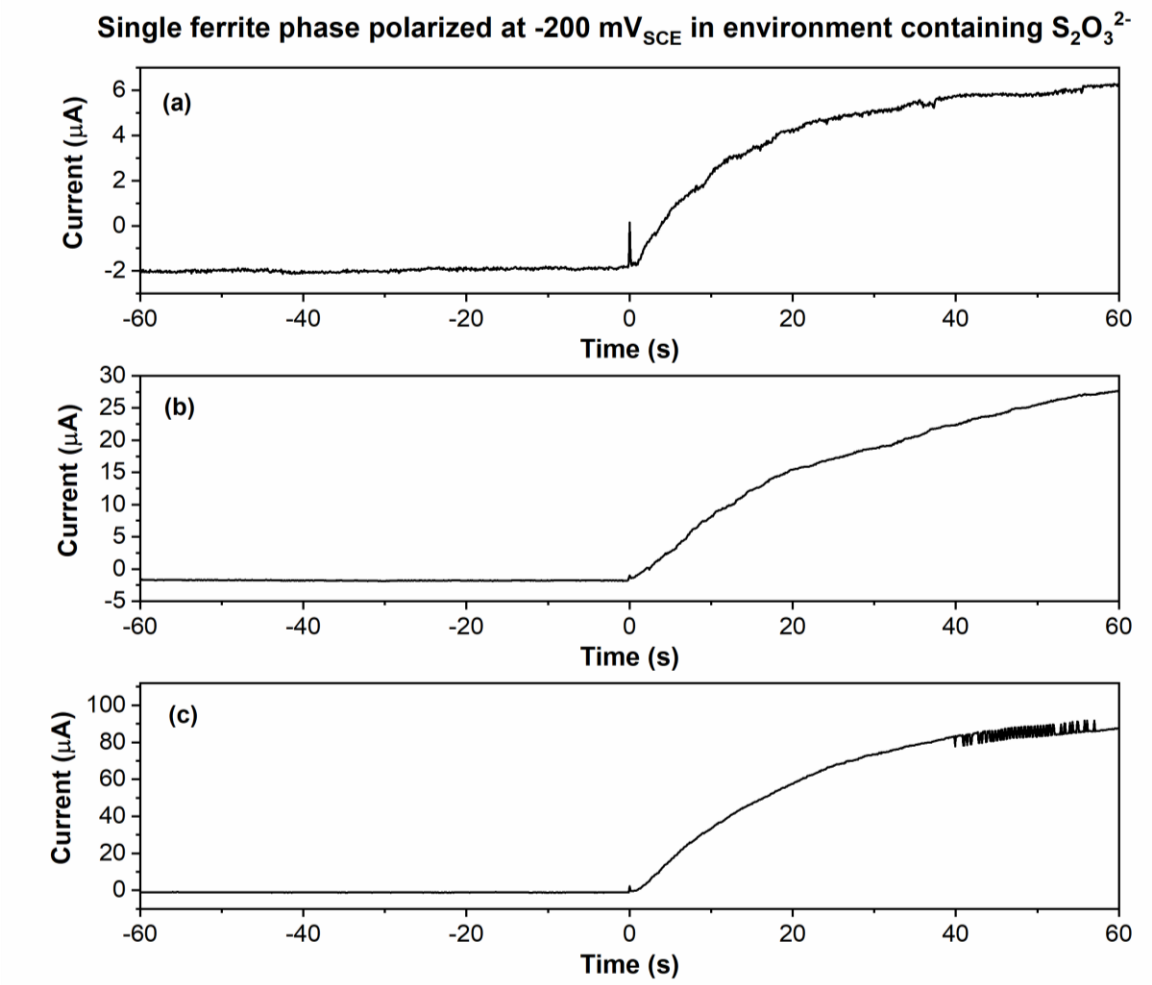

Figure 7.6 Current transients during potentiostatic polarization scratch tests of single ferrite phase in solution containing (6000 mg/L Cl^- + 1160 mg/L $S_2O_3^{2-}$). Potential: -200 mV_{SCE}. Graphs (a), (b) and (c) were the results under the same condition.

Further, the samples with single ferrite phase were polarized at -100 mV_{SCE} and the results are shown in Figure 7.7. Similar to the results when the samples were polarized at -200 mV_{SCE}, the current transient increased in the positive value regime as a result of the active dissolution of the bare alloy and pit growth. In addition, the pit growth rate is faster when the samples were polarized at -100 mV_{SCE}. The average value of the current at 10 seconds after scratch for single ferrite phase polarized at -200 mV_{SCE} was 15 μA, while that for single ferrite phase polarized at -100 mV_{SCE} was around eight times higher with the value of 124 μA.

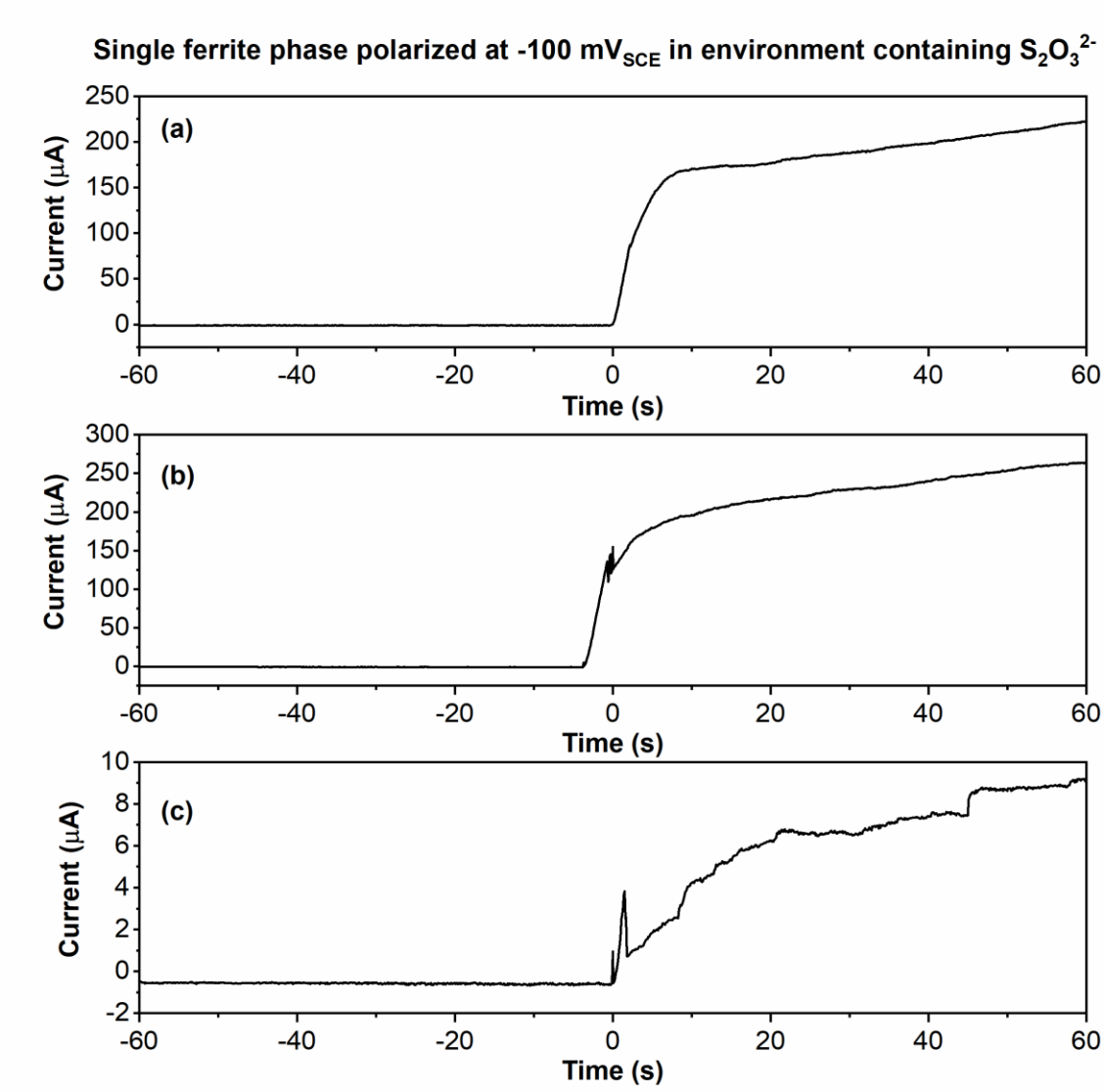

Figure 7.7 Current transients during potentiostatic polarization scratch tests of single ferrite phase in solution containing (6000 mg/L Cl^- + 1160 mg/L $S_2O_3^{2-}$). Potential: -100 mV_{SCE}. Graphs (a), (b) and (c) were the results under the same condition.

To understand the effect of $S_2O_3^{2-}$ on the pit growth of the single ferrite phase, scratch tests in pure NaCl solution were also conducted. Figure 7.8 shows the current transients during scratch test on the single ferrite phase polarized at -100 mV_{SCE} in environment containing 6000 mg/L Cl^- at 50 °C. Under this condition, the material

repassivated and there was no development of localized corrosion. Comparing results in Figure 7.7 and Figure 7.8, it can be concluded that the presence of $S_2O_3^{2-}$ promotes pit growth and hinders repassivation on the bare alloy surface.

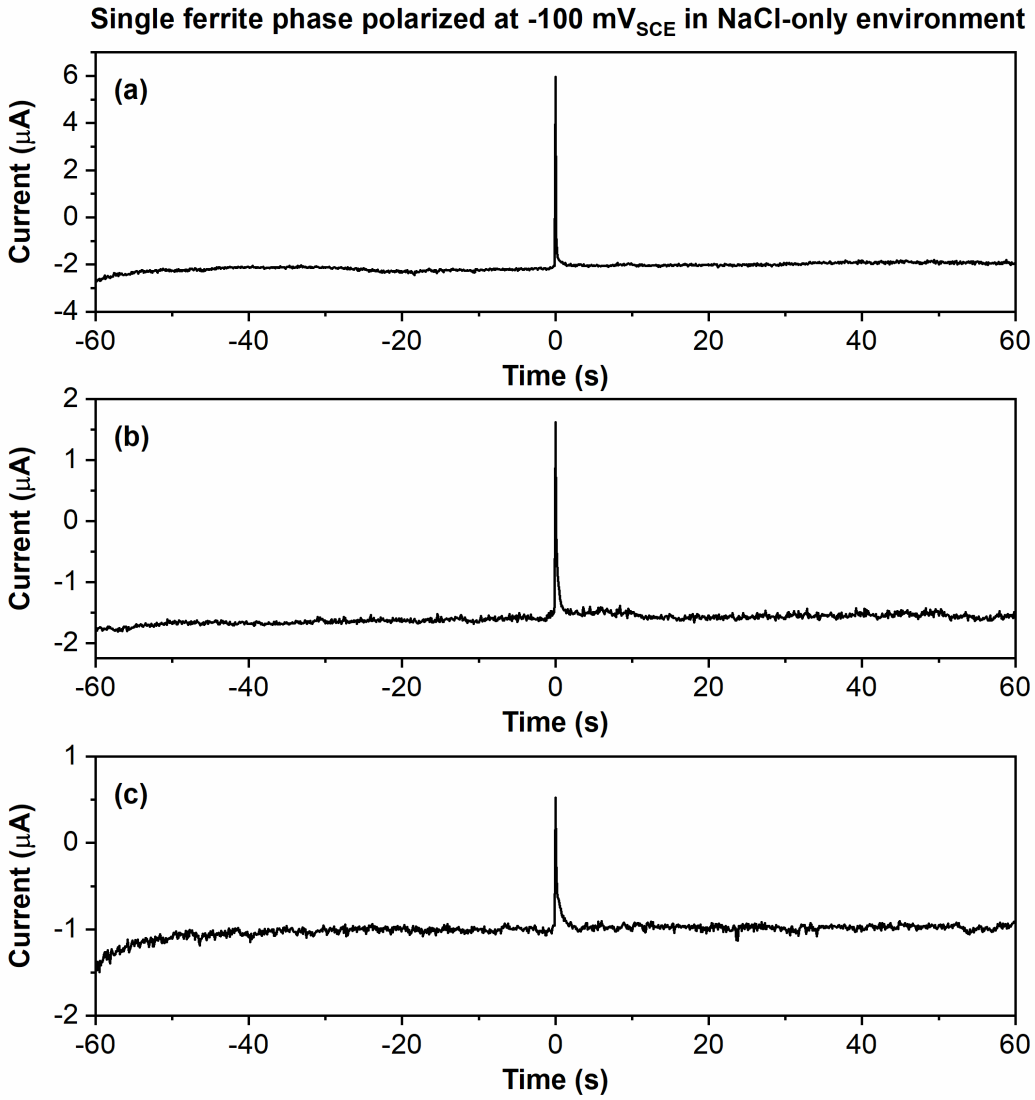

Figure 7.8 Current transients during potentiostatic polarization scratch tests of single ferrite phase in solution containing 6000 mg/L Cl^-. Potential: -100 mV_{SCE}. Graphs (a), (b) and (c) were the results under the same condition.

For the single austenite phase, the samples were first polarized at -200 mV_{SCE} during scratch test and the results are shown in Figure 7.9. Negative current transients before the scratch was because the polarized potential at -200 mV_{SCE} was below the open circuit potential of single austenite phase (-86 mV_{SCE}). After the passive film was removed through scratch, the current transients decreased to the current values before the scratch within one second, indicating there was no pitting corrosion when the austenite sample was polarized at -200 mV_{SCE}. Remember that the single ferrite phase sample had shown continuous increase in the current value that indicated localized corrosion after scratch under similar test conditions.

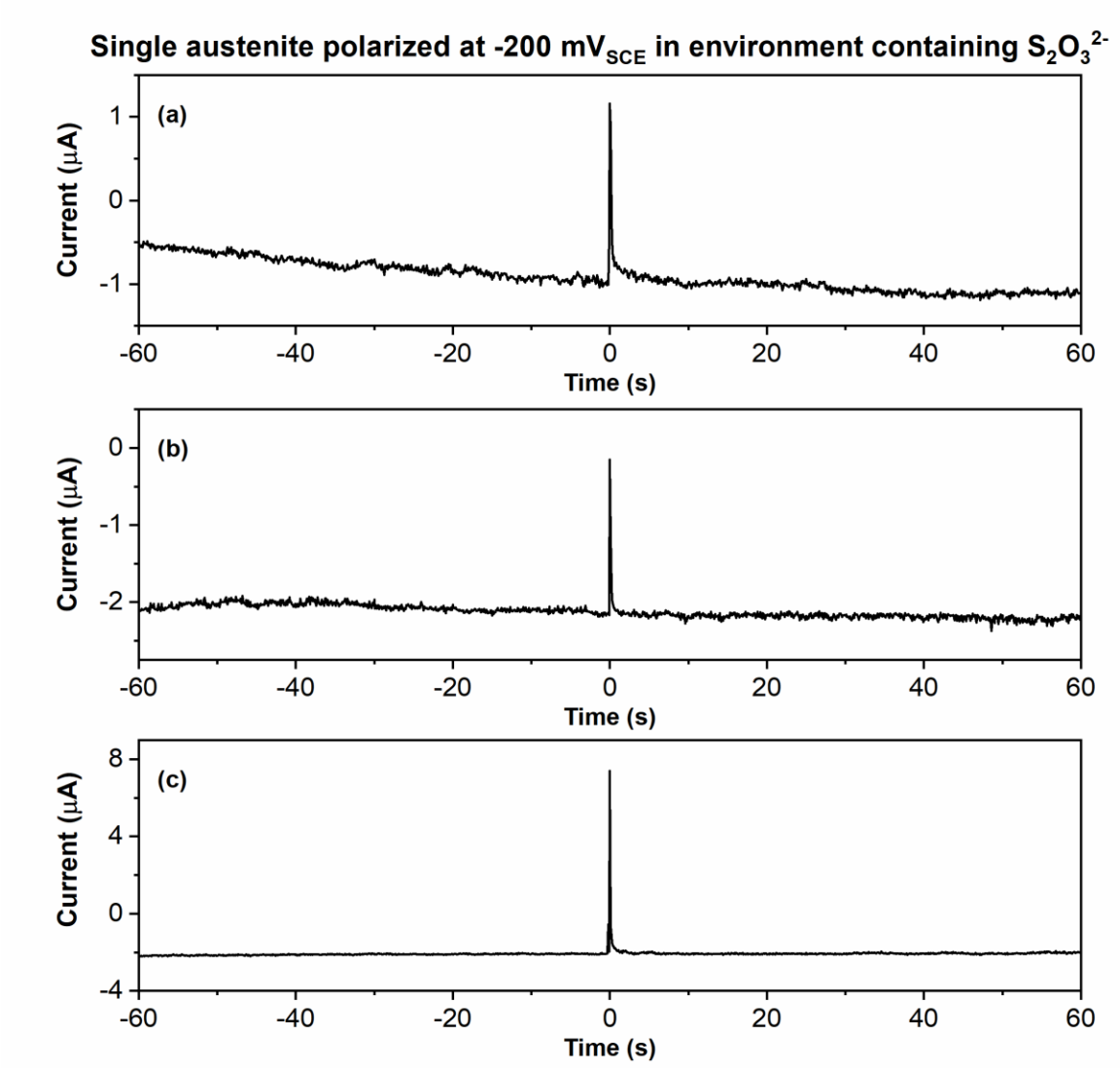

Figure 7.9 Current transients during potentiostatic polarization scratch tests of single austenite phase in solution containing (6000 mg/L Cl^- + 1160 mg/L $S_2O_3^{2-}$). Potential: -200 mV_{SCE}. Graphs (a), (b) and (c) were the results under the same condition.

Further, the single austenite phase was polarized at -100 mV_{SCE} in environment containing (6000 mg/L Cl^- + 1160 mg/L $S_2O_3^{2-}$) at 50 °C and the results are shown in Figure 7.10. After the scratch, the current transients also dropped back to the current values before the scratch was made. In Figure 7.10 (a), in addition to the sharp peak at 0s caused by the

removal of the passive film, there was another peak with gradual current increase and a fast drop, which indicated the presence of metastable pitting event.

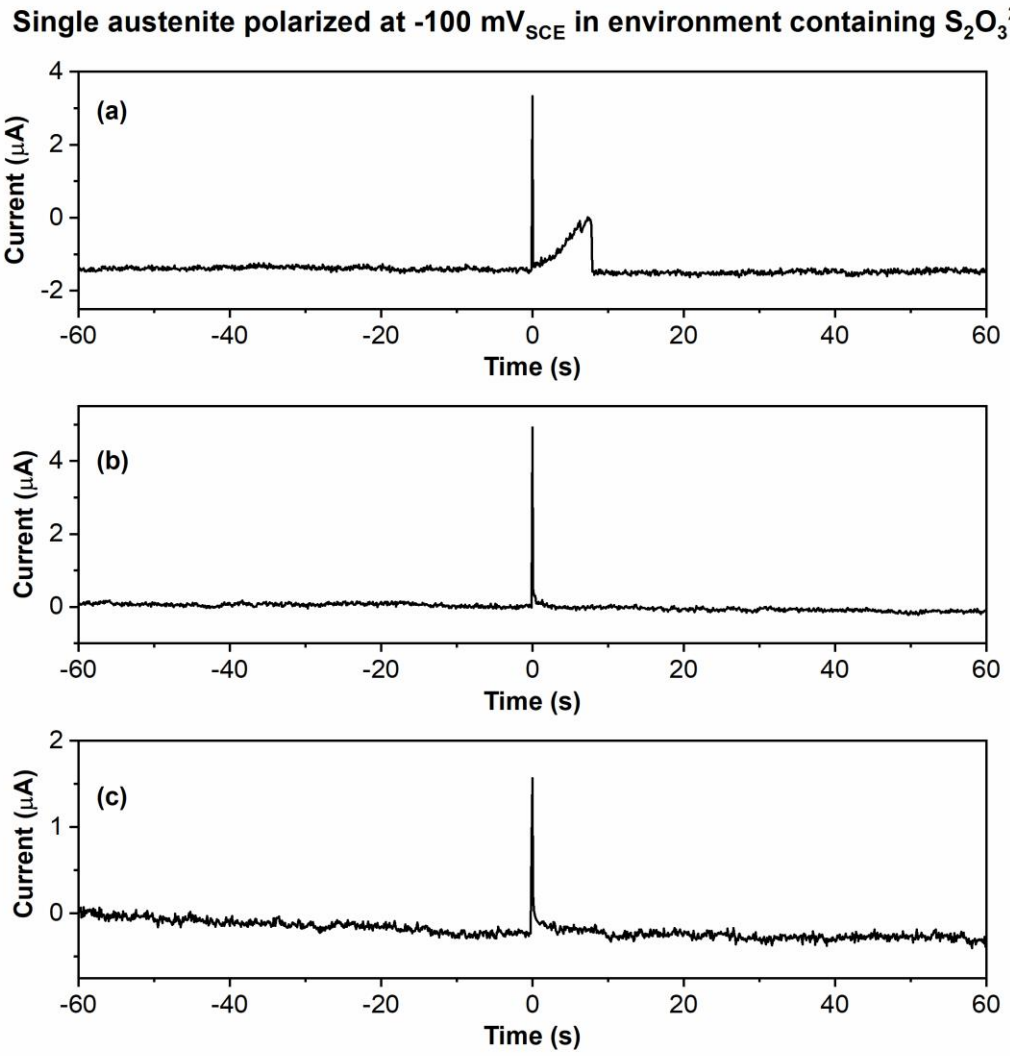

Figure 7.10 Current transients during potentiostatic polarization scratch tests of single austenite phase in solution containing (6000 mg/L Cl^- + 1160 mg/L $S_2O_3^{2-}$). Potential: -100 mV_{SCE}. Graphs (a), (b) and (c) were the results under the same condition.

The samples with single austenite phase were further polarized at 0 mV_{SCE} in environment containing (6000 mg/L Cl^- + 1160 mg/L $S_2O_3^{2-}$) at 50 °C. As shown in Figure 7.11, the current transients increased continuously in the anodic direction after the film was removed, indicating the growth of pits on the bare metal at this potential.

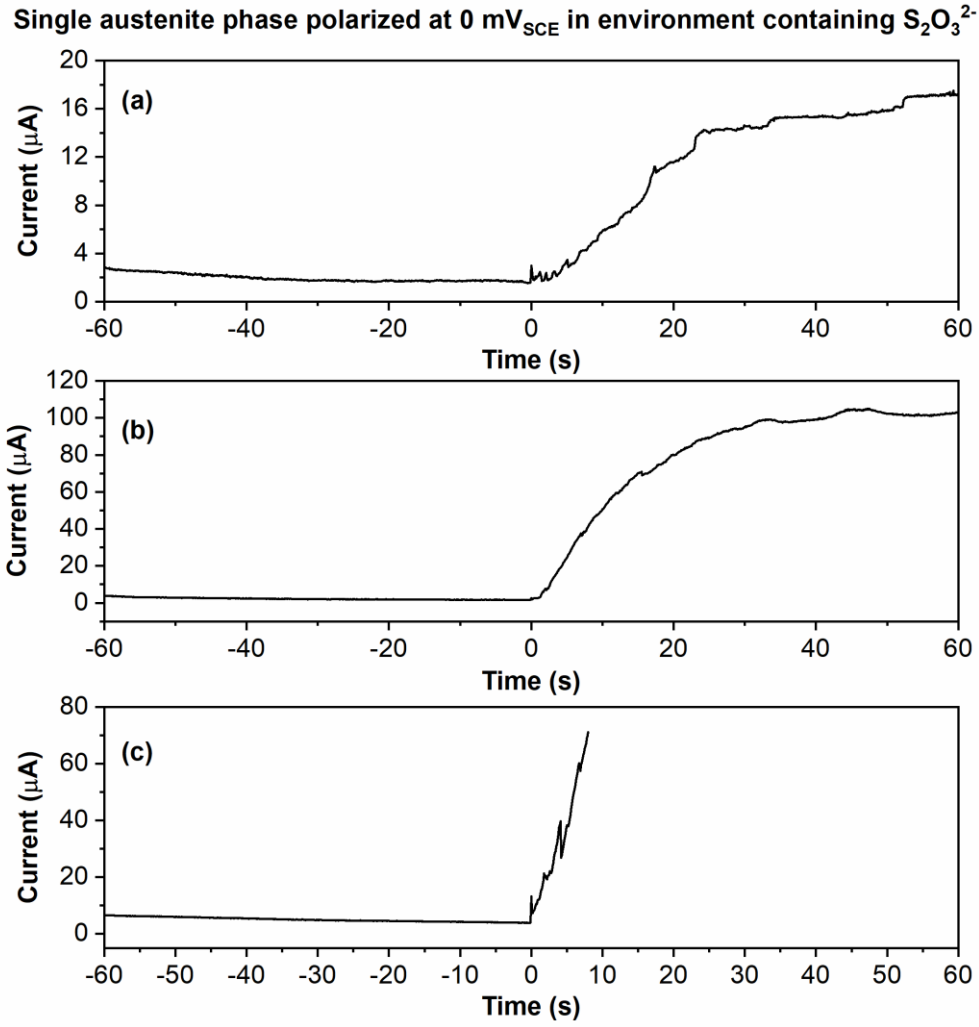

Figure 7.11 Current transients during potentiostatic polarization scratch tests of single austenite phase in solution containing (6000 mg/L Cl^- + 1160 mg/L $S_2O_3^{2-}$). Potential: 0 mV_{SCE}. Graphs (a), (b) and (c) were the results under the same condition.

Similar to the study on the ferrite phase, the effects of $S_2O_3^{2-}$ on the pit growth of the single austenite phase was also studied and scratch test method in pure NaCl solution was used. Figure 7.12 shows the current transients during scratch test on the single austenite phase polarized at 0 mV_{SCE} in environment containing 6000 mg/L Cl^- at 50 °C. Under this condition, the materials repassivated and there was no development of localized corrosion. Comparing results in Figure 7.11 and Figure 7.12, it can be concluded that the presence of $S_2O_3^{2-}$ promotes pit growth and hinders repassivation on the bare austenite surface as well.

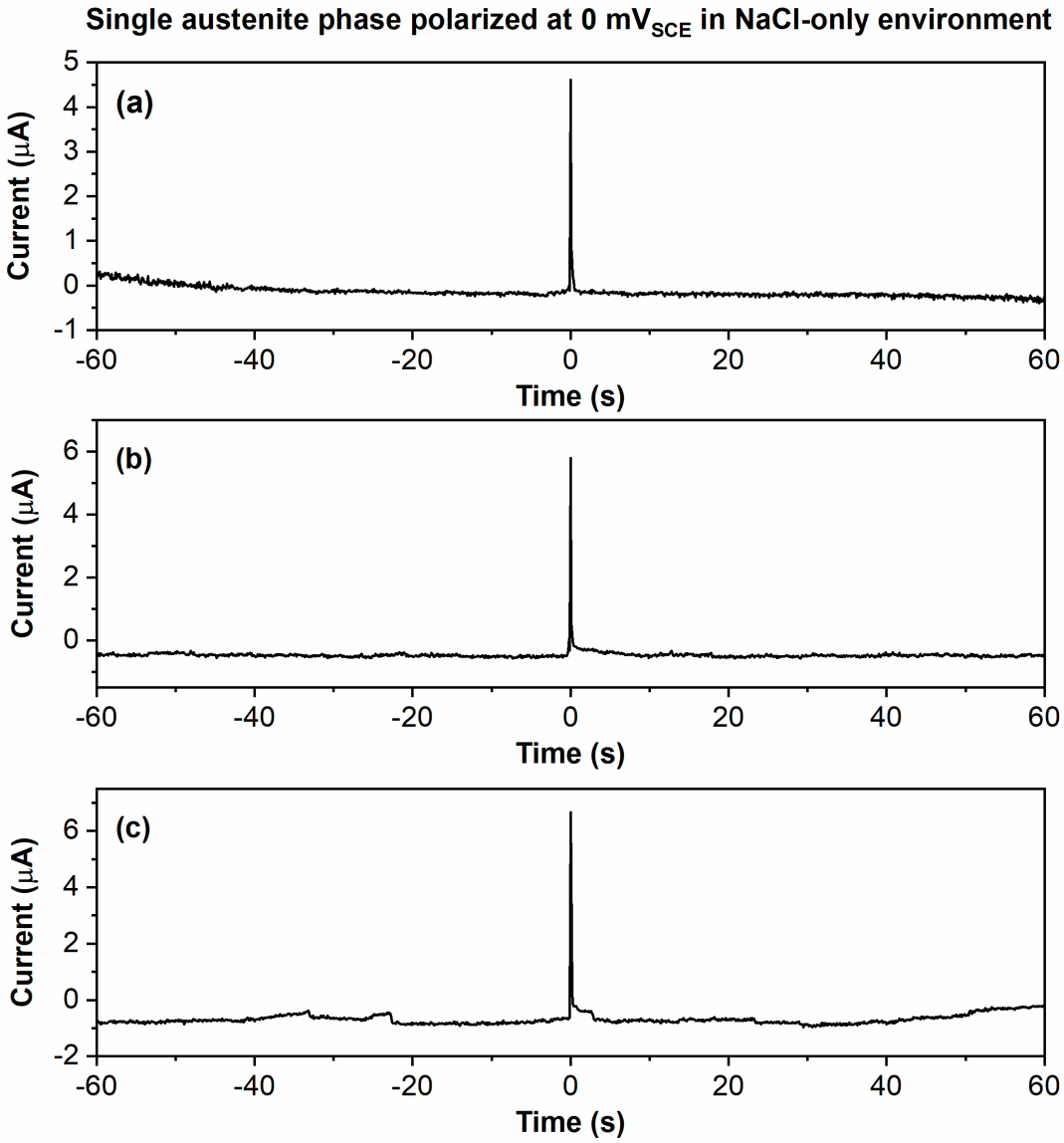

Figure 7.12 Current transients during potentiostatic polarization scratch tests of single austenite phase in solution containing 6000 mg/L Cl^-. Potential: 0 mV_{SCE}. Graphs (a), (b) and (c) were the results under the same condition.

For the single ferrite phase, during scratch test, the potential at which pit growth occurs is between -300 mV_{SCE} and -200 mV_{SCE} and above -200 mV_{SCE}, as can be concluded from Figure 7.5 to Figure 7.7. In comparison, for the single austenite phase, pit growth is

promoted when the potential is between -100 mV_{SCE} to 0 mV_{SCE} and above 0 mV_{SCE}, which is higher than the potential in the case of single ferrite phase. Thus, it can be concluded that the pitting corrosion resistance of the single austenite phase is higher than that of the single ferrite phase in UNS S32304.

7.5 Galvanic corrosion between the constituent phases of DSS

Hydrolysis of dissolved metal ions within pits leads to the acidification of pit solution, and the accumulation of cations attracts more aggressive anions from the bulk solution into the pit, making pitting corrosion an auto-catalytic process. For pits formed in NaCl, pH as low as -0.13 and Cl^- concentration as high as 6.47N were observed.[33] Hydrochloric acid solution with concentration as high as 5M has been used to simulate active dissolution within pits. [46, 50] In the present study, galvanic interaction between the ferrite phase and the austenite phase in 2 mol/L HCl simulated pit solution was studied for up to one hour. The single-phase samples were used in these galvanic tests, and their structures are shown in Figure 7.2 and Figure 7.3. Lower HCl concentration was used to achieve a lower corrosion rate of the anode in the galvanic couple and to ensure the single-phase microstructure of the anode is not totally removed so that the galvanic current reflect the true behavior of the single ferrite phase or single austenite phase.

The galvanic current between the ferrite phase and the austenite phase of UNS S32304 in 2 mol/L HCl at room temperature and at 50 °C is shown in Figure 7.13. According to the setup of the electrochemistry test cell and the potentiostat shown in Figure 3.7, positive current means that electrons flow from the ferrite phase to the austenite phase,

indicating that the ferrite phase is anodic to the austenite phase in 2 mol/L HCl solution. These results indicate that since the pit solution is highly acidic with high concentration of Cl^-, the presence of the austenite phase in the DSS will promote the active dissolution of the ferrite phase within pits, leading to the preferential dissolution of the ferrite phase within pits.

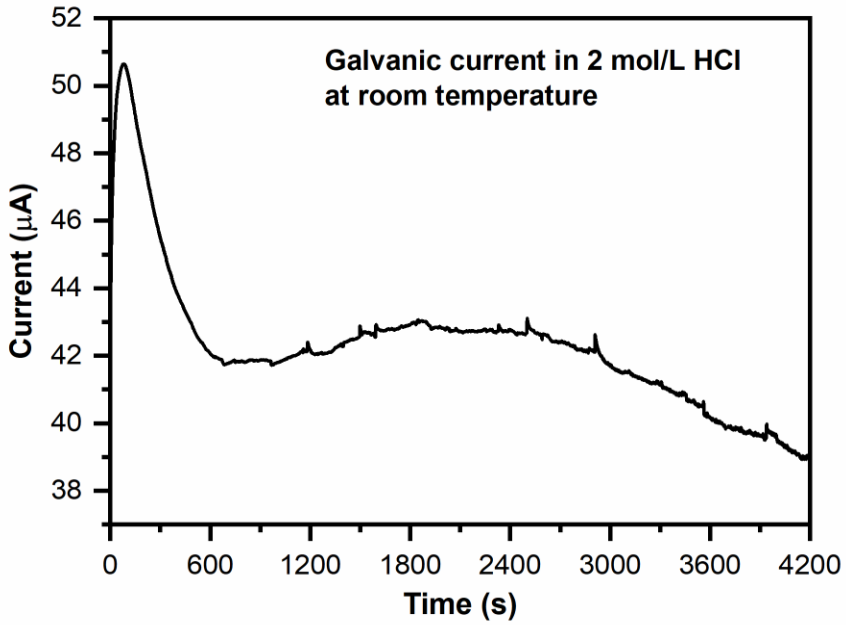

(a)

Figure 7.13 Galvanic current between the constituent phases of UNS 32304 at (a) room temperature and (b) 50 ℃.

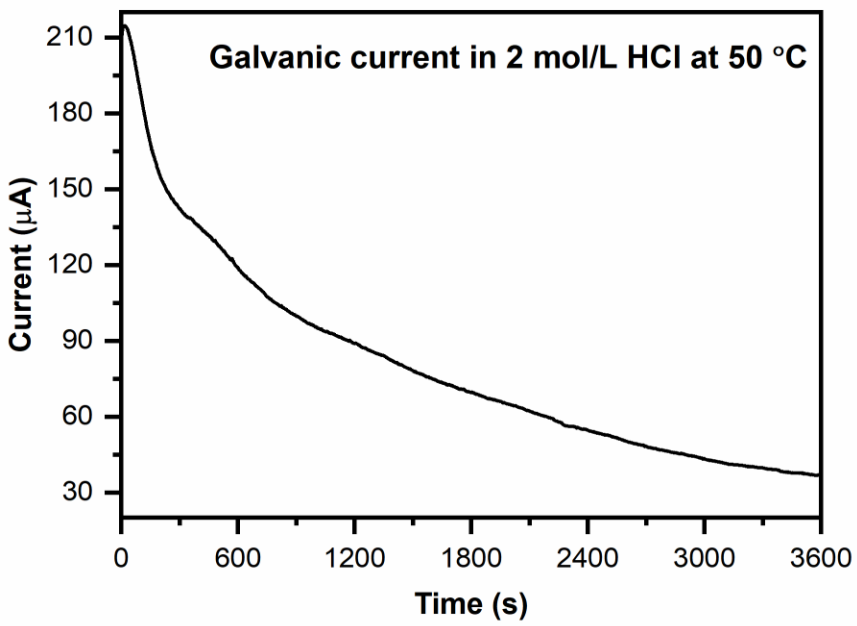

(b)

Figure 7.13 Continued.

Further, to observe the role of $S_2O_3^{2-}$ on the galvanic corrosion between the ferrite phase and the austenite phase, galvanic corrosion test was conducted in 2 mol/L HCl solution at room temperature for half an hour and then 50 mL $Na_2S_2O_3$ solution with a concentration of 0.02 mol/L was added to the test environment. The galvanic current between the ferrite phase and the austenite phase was constantly monitored, which is shown in Figure 7.14. In 2 mol/L HCl solution, the galvanic current was positive, indicating that the ferrite phase acted as the anode. With the addition of $Na_2S_2O_3$, the galvanic current increased drastically to a value that is three times as high as the value in the original 2 mol/L HCl, which indicates that the addition of $S_2O_3^{2-}$ promotes the galvanic corrosion between the ferrite phase and the austenite phase and increases the anodic dissolution of

the ferrite phase. After around 180 seconds, the galvanic current decreased with exposure time.

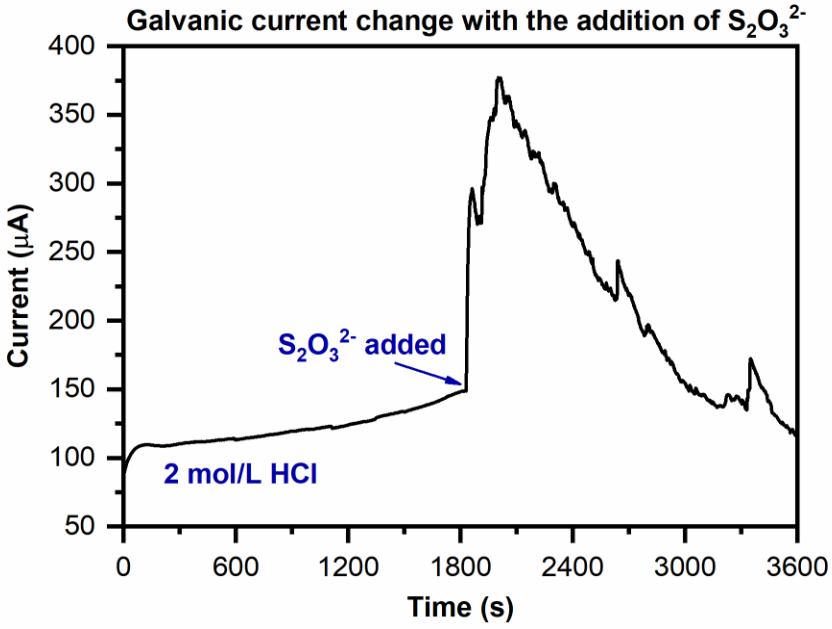

Figure 7.14 Galvanic current transients change with the addition of $S_2O_3^{2-}$ at room temperature. Original solution: 500 mL 2 mol/L HCl; added solution: 50 mL 0.02 mol/L $Na_2S_2O_3$.

The reactions that happen on the anode, the single ferrite phase, and the cathode, the single austenite phase, are discussed as follows. The anodic reaction is the anodic dissolution of the ferrite phase. In environment containing only HCl, the cathodic reaction is predominately the reduction reaction of proton:

$$2H^+ + 2e^- \rightarrow H_2 \tag{19}$$

With the addition of $S_2O_3^{2-}$, in addition of the cathodic reaction of proton, the $S_2O_3^{2-}$ is also reduced to sulfur (S), as described by Equation (20):

$$S_2O_3^{2-} + 6H^+ + 4e^- \rightarrow 2S + 3H_2O \quad (20)$$

And S may be further reduced to H_2S through the reaction:

$$S + 2H^+ + 2e^- \rightarrow H_2S \quad (21)$$

The total cathodic current is increased because of this additional cathodic reaction, which in turn will also increase the anodic dissolution of the ferrite phase according to the principle of charge conservation, as was seen as an increase in the anodic current upon the addition of thiosulfate. Once $S_2O_3^{2-}$ is consumed by the cathodic reaction and is totally reduced to element S, only H^+ reduction reaction predominates and the overall cathodic reaction rate is reduced, which in turn decreases the anodic dissolution rate of the ferrite phase, as was seen as a decrease in the anodic current after ~180 seconds of thiosulfate addition.

To check the proposed mechanism described above, the surfaces of the samples with single ferrite phase and single austenite phase after galvanic test were lightly rinsed in distilled water and dried. Then they were examined using SEM coupled with EDS techniques to observe their surface morphology as well as the elements present on the surface, and the results are shown in Figure 7.15 and Table 7.2. The bright area shown in Figure 7.15 (a) and (b) were due to the charging effect of the non-conductive lacquer that was used to fill the voids between the single phases.

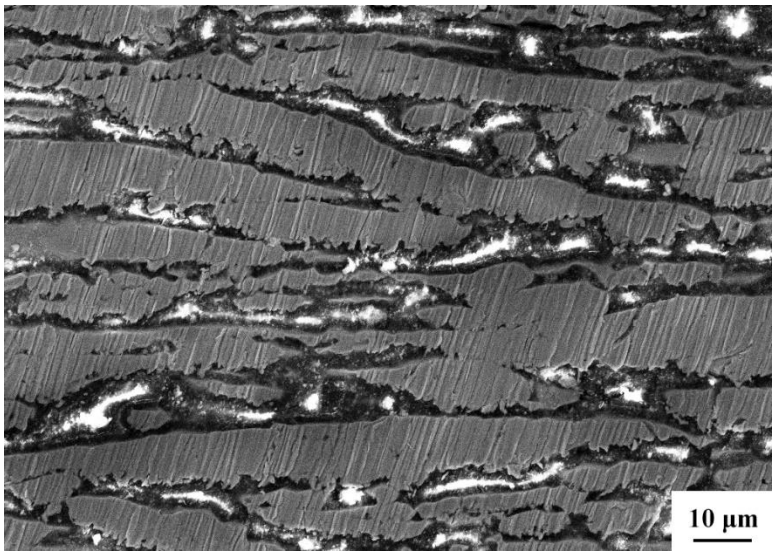

(a)

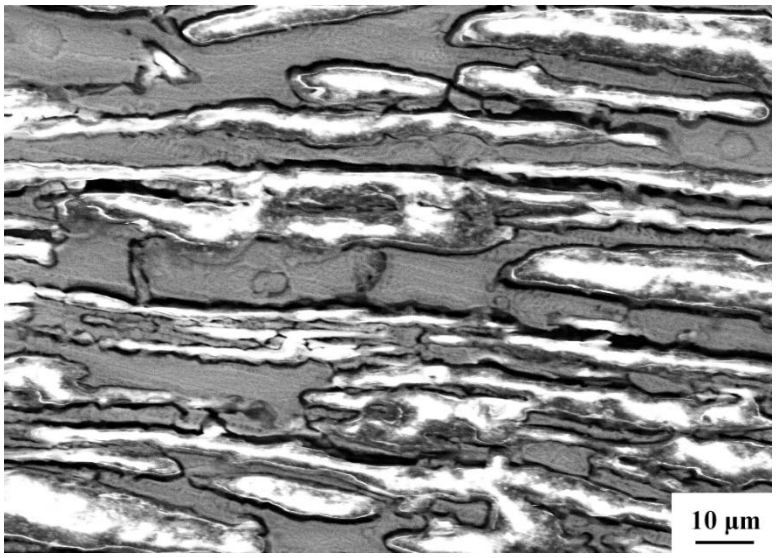

(b)

Figure 7.15 SEM images of the surface of (a) single austenite phase and (b) single ferrite phase after galvanic corrosion test in 500 mL 2 mol/L HCl with the addition of 50 mL 0.02 mol/L $Na_2S_2O_3$.

Figure 7.15 (a) shows the surface of the single austenite phase, and the polishing lines that were present before the galvanic test remained, which indicated that there was no detectable dissolution of the austenite phase during galvanic corrosion test and verified that it acted as the cathode in the galvanic couple. In comparison, Figure 7.15 (b) shows the surface of the single ferrite phase after the galvanic test, and the polishing lines were removed due to the active dissolution of the ferrite phase, which suggested that the ferrite phase was anodic to the austenite phase in the galvanic couple.

Table 7.2 Average contents of elements on the surface of single ferrite phase and single austenite phase after galvanic corrosion tests in environment containing $Na_2S_2O_3$.

	Cr	Ni	Mn	Mo	S
Single austenite	21.7 ± 0.3	5.5 ± 0.2	1.3 ± 0.1	0 ± 0	0 ± 0
Single ferrite	20.0 ± 2.0	10.6 ± 1.6	0.6 ± 0.4	2.4 ± 0.9	1.9 ± 0.7

Further, EDS analysis was conducted on at least nine spots on each sample shown in Figure 7.15. On all the spots tested on the single austenite phase, no element S was observed. In comparison, element S was detected on all the spots tested on the single ferrite phase. The average value and the 95% confidence interval of the contents of elements measured using EDS were calculated. The chemical composition of the austenite phase after galvanic corrosion test in environment containing $Na_2S_2O_3$ shown in Table 7.2 was similar to that tested on the polished surface of the austenite phase before galvanic tests shown in Table 7.1, which proved that there was no significant active dissolution of the austenite phase during galvanic corrosion. However, the tested chemical composition of

the surface of the ferrite phase after galvanic corrosion shown in Table 7.2 was different from the original polished surface before the galvanic test. This further proved that the ferrite phase was the anode in the galvanic couple with the austenite phase.

Although it was proposed that $S_2O_3^{2-}$ got reduced on the singe austenite phase sample (cathode), sulfur was not detected on the surface of the austenite sample during EDS analysis, but sulfur species were detected on the surface of the ferrite phase sample. This is probably due to the fact that elemental S reduced from $S_2O_3^{2-}$ was further reduced to H_2S, which according to the thermodynamic prediction shown in Figure 7.16 (a), is stable at the potential of the galvanic couple lower than -450 mV_{SCE} at pH close to 0. However, on the ferrite phase, the metal dissolution produces metal cations such as Fe^{2+}, Cr^{3+}, Mo^{2+} and Ni^{2+}, and may combine with reduced sulfur to form metal sulfide. According to the thermodynamic prediction shown in Figure 7.16 (b), under this condition, MoS_2 is the most stable compound to form.

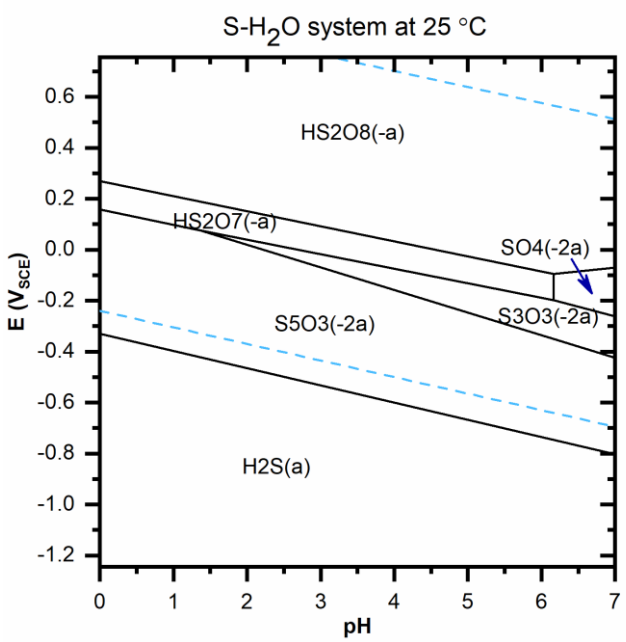

(a)

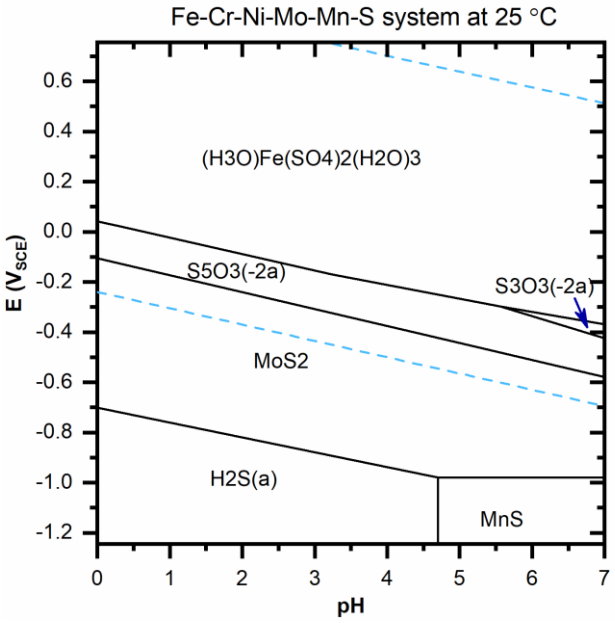

(b)

Figure 7.16 Pourbaix diagram for (a) S-H_2O system at 25°C and (b) Fe-Cr-Ni-Mo-Mn-S-H_2O system.

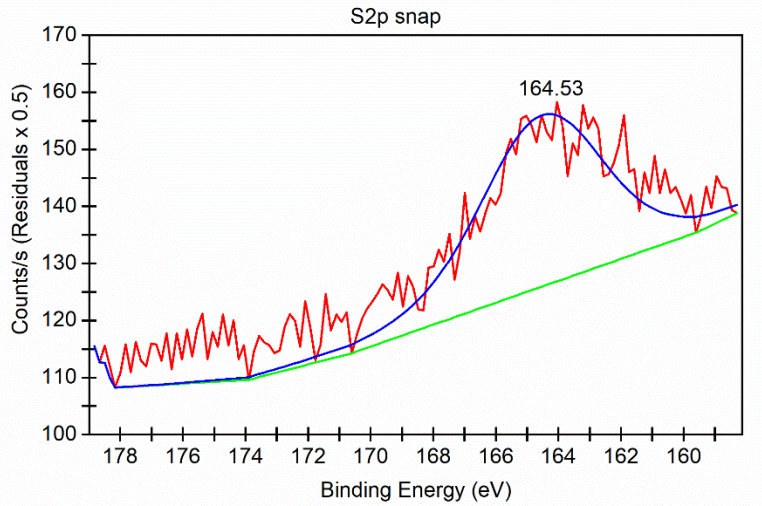

(a)

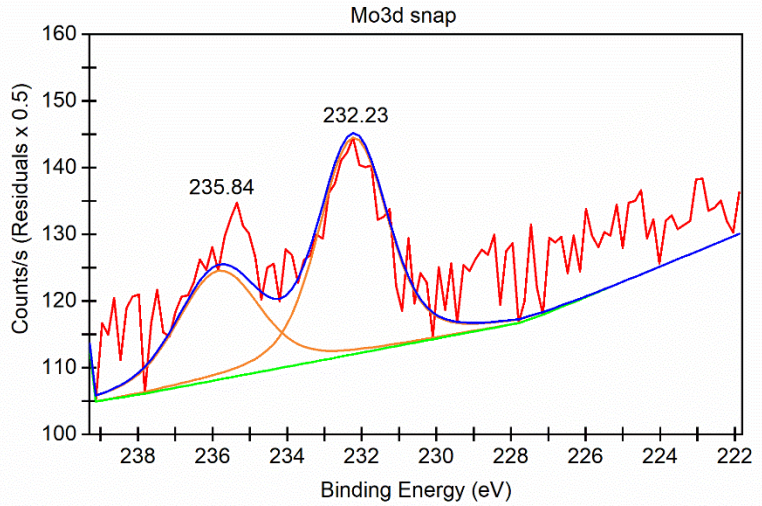

(b)

Figure 7.17 XPS analysis of element (a) Sulfur; (b) Molybdenum and (c) Chromium on the surface of the ferrite phase after galvanic corrosion 500 mL 2 mol/L HCl with the addition of 50 mL 0.02 mol/L $Na_2S_2O_3$.

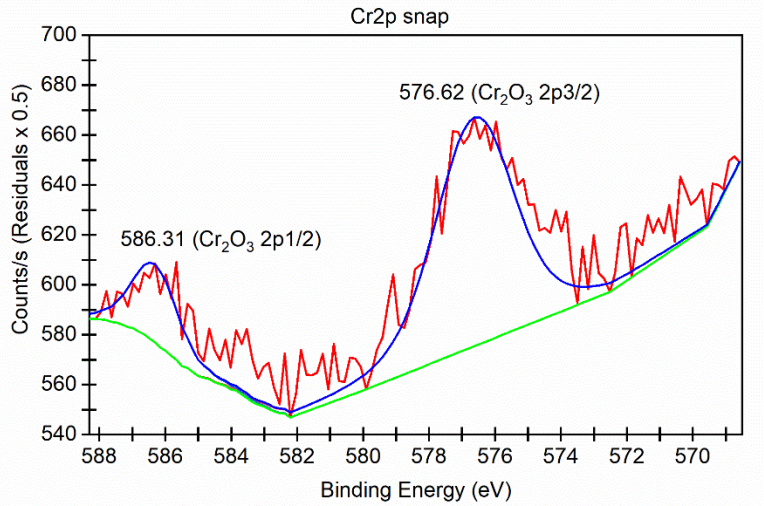

(c)

Figure 7.17 Continued.

XPS analysis was also carried out to figure out the state of elements and the results are shown in Figure 7.17. The energy level of XPS peaks were compared with NIST XPS database.[116] There are two peaks present in the Cr 2p snap scan. The one at 576.63 eV corresponds to Cr 2p3/2 in Cr_2O_3 and that at 586.3 eV corresponds to Cr 2p1/2 in Cr_2O_3. For Mo, there are two peaks present at 232.23 eV and 235.84 eV, which corresponds to Mo 3d in MoS_2 and molybdenum oxides (MoO_2 and MoO_3). There is one broad peak in S2p snap scan at 164.53 eV that can be attributed to S2p in MoS_2 and in elemental sulfur. For Mo and S, because of peak overlapping, it was not possible to distinguish different possible corrosion products. However, combining the thermodynamic prediction shown in Figure 7.16, sulfur should be reduced and formed metal sulfide and the most stable sulfide would be MoS_2.

7.6 Conclusions

In this chapter, the mechanism of preferential dissolution of the ferrite phase in UNS S32304 during pitting corrosion in environments containing NaCl and $Na_2S_2O_3$ was studied using scratch tests for repassivation kinetics and a galvanic corrosion test on samples with single ferrite phase and single austenite phase.

1. In the active region of the potentiodynamic polarization curve of UNS S32304 in (2 mol/L HCl + 0.5 mol/L H_2SO_4) solution, there are two peaks representing the maximum selective dissolution of the ferrite phase and the maximum selective dissolution of the austenite phase. Single ferrite phase and single austenite phase were separated by polarizing the DSS samples at the potentials of these two peaks.
2. During potentiostatic scratch tests, in environments containing (3000 mg/L Cl^- + 1160 mg/L $S_2O_3^{2-}$) at 50 °C, the transition from repassivation behavior to pitting corrosion behavior of single ferrite phase occurred at the potential between -300 mV_{SCE} and -200 mV_{SCE}, while that of the austenite phase occurred at the potential between -100 mV_{SCE} and 0 mV_{SCE}. The austenite phase possesses higher pitting corrosion resistance than the ferrite phase in tested environments.
3. Under the same polarization condition, single ferrite phase (polarized at -100 mV_{SCE}) and single austenite phase (polarized at 0 mV_{SCE}) showed repassivation behavior when the scratch test environment was 3000 mg/L Cl^-, while in comparison, pits developed when the scratch tests were done in (3000 mg/L Cl^-

+ 1160 mg/L $S_2O_3^{2-}$). These results clearly show that the presence of $S_2O_3^{2-}$ inhibits repassivation and promotes localized corrosion of the single phases.

4. In 2 mol/L HCl simulated pit solution, galvanic effect exists between the ferrite phase and the austenite phase, where the ferrite phase acts as an anode to the austenite phase in environments with high acidity and high chloride concentration.
5. The addition of $S_2O_3^{2-}$ promotes the galvanic effects between the ferrite phase and the austenite phase and the corrosion rate of the ferrite phase because of the increase in the cathodic reaction rate. $S_2O_3^{2-}$ was reduced to elemental S when added to HCl solution. EDS analysis of surfaces after the galvanic test indicated that elemental S was adsorbed on the ferrite phase in the galvanic couple and not on the cathodic austenite phase.

CHAPTER 8. CONCLUSIONS AND RECOMMENDATIONS

In this work, the pitting corrosion behavior of lean duplex stainless steels (LDSSs) in environments containing chloride and thiosulfate was studied. Four grades of lean duplex stainless steels were selected, including UNS S32101, S32304, S32003 and S82441, because they are less alloyed and more cost-effective in less aggressive environments compared with standard DSS UNS S31803. Effects of factors including anions in the environment, alloying elements in the LDSS materials, and heat-treatment such as annealing and aging were investigated.

8.1 Summary of results

Effects of addition of thiosulfate to environments containing chloride anions on the pitting corrosion behavior and repassivation behavior of the four LDSSs were studied in Chapter 4. Ranking of the four LDSSs based on their resistance to localized corrosion was also accomplished in Chapter 4. Annealing treatment of a relatively newly developed LDSS UNS S32003 and its effect on the pitting corrosion behavior was discussed in Chapter 5. Further, in addition to annealing, aging treatment of UNS S32003 was carried out and its effects on the microstructural evolution and pitting corrosion resistance were discussed in Chapter 6. Preferential dissolution of the ferrite phase was discovered in environments containing thiosulfate anions, and Chapter 7 explores the possible mechanism for this phenomenon using scratch tests and galvanic corrosion tests on the

single austenite phase and single ferrite phase in Cl^--containing environment and (Cl^- +$S_2O_3^{2-}$)-containing environment.

Potentiodynamic cyclic polarization tests were conducted on UNS S32101, S32304, S32003 and S82441 in four different environments containing 300 mg/L Cl^-, (300 mg/L Cl^-+29 mg/L $S_2O_3^{2-}$), (300 mg/L Cl^-+58 mg/L $S_2O_3^{2-}$) and (300 mg/L Cl^-+116 mg/L $S_2O_3^{2-}$) at 50 ℃. UNS S32003 and S82441 were resistant to pitting corrosion in all environments, while S32101 and S32304 were prone to pitting corrosion in 300 mg/L Cl^- solution and (300 mg/L+29 $S_2O_3^{2-}$) solution. Average pitting potential of UNS S32101 was ~370 mV lower than that of S32304 in 300 mg/L Cl^- solution and was ~480 mV lower than that of S32304 in (300 mg/L+29 $S_2O_3^{2-}$) solution at 50℃. In concentrated solution, UNS S32003 was prone to crevice corrosion, but S82441 did not show any pitting or crevice corrosion at 50 ℃. Ranking of resistance of LDSSs to localized corrosion is: S82441 > S32003 > S32304 > S32101.

Pitting potential of UNS S32101 increased ~70 mV and that of S32304 increased ~170 mV when 29 mg/L $S_2O_3^{2-}$ is added to 300 mg/L Cl^- solution. In comparison, the decrease of repassivation potential of both LDSSs was more than 400 mV and the hysteresis loop was not closed, indicating a stronger effect of $S_2O_3^{2-}$ on the repassivation of pits due to the formation of reduced sulfur species within pits. However, when the Cl^- /$S_2O_3^{2-}$ ratio was below eight with higher concentration of $S_2O_3^{2-}$, UNS S32304 became resistant to pitting corrosion, indicating that $S_2O_3^{2-}$ acts as inhibitor at higher concentration because of the preferential migration to the pit solution.

Preferential dissolution of the ferrite phase was observed in UNS S32101 and S32304 samples during pitting corrosion in environments containing $S_2O_3^{2-}$. The single ferrite phase and single austenite phase were separated from bulk UNS S32304 samples in (2 mol/L HCl + 0.5 mol/L H_2SO_4) through selective dissolution of selected phase using potentiostatic polarization. In the active region of the potentiodynamic polarization curve of UNS S32304 in (2 mol/L HCl + 0.5 mol/L H_2SO_4) solution, there are two peaks representing the maximum selective dissolution of the ferrite phase and the maximum selective dissolution of the austenite phase. The pitting corrosion resistance of the single ferrite phase and single austenite phase was compared using potentiostatic scratch tests in environments containing (3000 mg/L Cl^- + 1160 mg/L $S_2O_3^{2-}$) at 50 °C.

The transition from repassivation behavior to pitting corrosion behavior of single ferrite phase occurred at the potential between -300 mV_{SCE} and -200 mV_{SCE}, while that of the austenite phase occurred at the potential between -100 mV_{SCE} and 0 mV_{SCE}. The austenite phase possesses higher pitting corrosion resistance than the ferrite phase in tested environment. Under the same polarization condition, single ferrite phase (polarized at -100 mV_{SCE}) and single austenite phase (polarized at 0 mV_{SCE}) showed repassivation behavior when the scratch test environment was 3000 mg/L Cl^-, while in comparison, pits developed when the scratch tests were done in (3000 mg/L Cl^- + 1160 mg/L $S_2O_3^{2-}$). These results clearly show that the presence of $S_2O_3^{2-}$ inhibits repassivation and promotes localized corrosion of the single phases.

In 2 mol/L HCl simulated pit solution, galvanic effect exists between the ferrite phase and the austenite phase, where the ferrite phase acts as an anodic to the austenite phase in environments with high acidity and high chloride concentration. The addition of

$S_2O_3^{2-}$ promotes the galvanic effects between the ferrite phase and the austenite phase and the corrosion rate of the ferrite phase because of the increase in the cathodic reaction rate. $S_2O_3^{2-}$ was reduced when added to HCl solution. EDS analysis of surfaces after the galvanic test indicated that reduced sulfur species was adsorbed on the ferrite phase in the galvanic couple and not on the cathodic austenite phase.

In addition to the corrosion tests conducted on the as-received LDSSs samples, the effects of heat-treatment on the pitting corrosion behavior were also studied. Annealing treatment was performed on UNS S32003 in the temperature range of 1000 ℃ to 1160 ℃. Volume fraction of the ferrite phase increased with increasing the annealing temperature. For a given annealing time, the phases coarsened to a larger extent at 1160 ℃ compared with samples annealed at lower temperatures. Potentiodynamic cyclic polarization tests revealed that the samples annealed at 1080 ℃ possessed the highest pitting potential, indicating the highest resistance to pitting. Pit initiation sites in UNS S32003 changed from the austenite phase to the ferrite phase, indicating a higher pitting susceptibility of the ferrite phase when the material is annealed at a higher temperature, which could be attributed to the lower Cr and Mo content in the ferrite phase at the elevated annealing temperature.

Study on the effects of aging temperature and aging time was also carried out in this work. Only nitride precipitates were positively detected along the ferrite/austenite phase boundaries and within the ferrite phase for the UNS S32003 samples aged in the temperature range of 600 ℃ to 900 ℃ for up to 2 hours. The precipitation kinetics was the fastest at 800 ℃ for the UNS S32003, where the Cr-depleted zones were observed to be in the vicinity of the precipitates. For samples aged at 700 ℃ for 120 hours, σ phase was

detected along with an increase in the percentage of precipitates. Precipitates were found to be at the edge of small pits, indicating the pit initiation is close to the precipitates and is probably associated with the Cr-depleted zones. Pitting corrosion resistance decreased with higher fraction of nitride precipitates and the formation of σ phase. The change in the pitting corrosion resistance in terms of pitting potential, repassivation potential and metastable pitting rate is very sensitive to the precipitation of secondary phases even when the volume fraction of these precipitates is below 1%.

8.2 Practical impact and recommendations

In this research, pitting corrosion behavior of newly-developed LDSSs is studied in near-neutral environments that contain chloride, thiosulfate and sulfate anions, and the results provide knowledge about the corrosion performance of LDSSs and their possible applications in this type of environment. Without inhibitors in the environments or no surface treatment, UNS S32101 and S32304 are susceptible to pitting corrosion in near-neutral environments containing thiosulfate anions and are not recommended. However, if inhibitors are present or at higher thiosulfate concentration levels, UNS S32304 is resistant to pitting corrosion. In comparison, with higher Mo content and higher PREN number, UNS S32003 and S82441 are resistant to pitting corrosion in near-neutral environments with chloride and thiosulfate anions. In this type of environment, PREN number can still be applied to compare the pitting corrosion resistance of different grades of DSSs in the as-received state. Although it has been demonstrated that in caustic environment the presence of Mo can be detrimental, [117] it helps with the improvement of pitting corrosion resistance in near-neutral environments.

Although PREN number can be used as an estimation of the pitting corrosion resistance of DSSs in near-neutral environments, it cannot predict the change in the pitting corrosion resistance caused by the microstructural evolution. Annealing treatment of UNS S32003 in this work showed that the chemical composition in the ferrite phase and the austenite phase changes with annealing temperature. Thus, the pitting corrosion resistance is altered by annealing treatment and is determined by the more susceptible phase. Pitting resistance does not change monotonically with annealing temperature and higher annealing temperature does not indicate a higher pitting corrosion resistance. Also, a high annealing temperature above ~1150 ℃ should be avoided to prevent the supersaturation of nitride in the ferrite phase and the precipitation of nitrides, which is detrimental to the pitting corrosion resistance of DSSs.

Isothermal aging of UNS S32003 between the temperature range of 600 ℃ to 900 ℃ showed the precipitation of secondary phases. Although the precipitation of intermetallic phases is slower compared with that of standard and super DSSs, the formation of nitride precipitations occurs and deteriorates the pitting corrosion resistance with exposure time less than ten minutes. Thus, the cooling rate after high temperature exposure such as annealing treatment and welding should be fast to avoid a long exposure to the temperature range of 600 ℃ to 900 ℃.

8.3 Recommendations of future work

Although the work provides detailed study on the pitting corrosion behavior of LDSSs in terms of effects of aggressive anions, alloying elements, heat-treatment and

explored the possible mechanism for the preferential dissolution of the ferrite phase in pitting corrosion of DSSs, the are several recommendations for future work to deepen the understanding of this topic.

Scratch tests and galvanic corrosion tests were carried out in this work on the single ferrite phase and single austenite phase in environments containing chloride and thiosulfate, but they are mainly focused on the pit growth and repassivation after the passive film is removed. More work can be done to study the pit initiation on the single phases. The difficulty associated with pit initiation is the presence of lacquer/single phase interfaces and crevice corrosion can be activated before pitting corrosion, which does not fully represent the pit initiation on the constituent phases in the bulk material. It is recommended to passivate the surface of the separated single phases, so that the single phase materials are more resistant to crevice corrosion.

Although effects of isothermal aging and the formation of secondary phases have been studied in this work, they may not fully represent the microstructural evolution during actual materials treatment such as welding. Therefore, more work can be done to study the effects of welding on the precipitation formation and pitting corrosion resistance of LDSSs.

The electrochemical test method used in this research collects the response from the bulk surface of the tested samples, but does not provide detailed in-situ information about the pit initiation sites. Since pit initiation is related to the microstructure, micro-electrochemical test methods such as scanning vibrating electrode technique (SVET) and scanning electrochemical microscopy (SECM) can be used to study the correlation between the pitting initiation and microstructural features in DSSs.

REFERENCES

1. Garner, A., *Thiosulphate and Paper Machine Corrosion: Is the Problem Solved?* Pulp and Paper Canada, 2005. **106**(2).
2. Garner, A., *2010 Frank Newman Speller Award Lecture: Identifying the Critical Damage Mechanism.* CORROSION, 2011. **67**(6): p. 065006-1-065006-6.
3. Schneider, H., *Investment casting of high-hot strength 12% chrome steel.* Foundry Trade Journal, 1960. **108**: p. 562-563.
4. Bain, E.C., *An introduction to the iron-chromium-nickel alloys.*
5. Landolt, D., *Corrosion and surface chemistry of metals*. 2007: EPFL press.
6. Okamoto, G., *Passive film of 18-8 stainless steel structure and its function.* Corrosion Science, 1973. **13**(6): p. 471-489.
7. Lorang, G., et al., *Chemical Composition of Passive Films on AISI 304 Stainless Steel.* Journal of The Electrochemical Society, 1994. **141**(12): p. 3347-3356.
8. Schmutz, P. and D. Landolt, *In-situ microgravimetric studies of passive alloys: potential sweep and potential step experiments with Fe–25Cr and Fe–17Cr–33Mo in acid and alkaline solution.* Corrosion Science, 1999. **41**(11): p. 2143-2163.
9. Cho, E.-A., et al., *Quantitative analysis of repassivation kinetics of ferritic stainless steels based on the high field ion conduction model.* Electrochimica Acta, 2000. **45**(12): p. 1933-1942.

10. Verwey, E.J.W., *Electrolytic conduction of a solid insulator at high fields The formation of the anodic oxide film on aluminium.* Physica, 1935. **2**(1): p. 1059-1063.

11. Cabrera, N. and N.F. Mott, *Theory of the oxidation of metals.* Reports on Progress in Physics, 1949. **12**(1): p. 163.

12. Beck, T.R., *Electrochemistry of freshly-generated titanium surfaces—II. Rapid fracture experiments.* Electrochimica Acta, 1973. **18**(11): p. 815-827.

13. Lillard, R.S., G. Vasquez, and D.F. Bahr, *The Kinetics of Anodic Dissolution and Repassivation on Stainless Steel 304L in Solutions Containing Nitrate.* Journal of The Electrochemical Society, 2011. **158**(6): p. C194-C201.

14. Hoar, T.P., D.C. Mears, and G.P. Rothwell, *The relationships between anodic passivity, brightening and pitting.* Corrosion Science, 1965. **5**(4): p. 279-289.

15. Strehblow, H.H., *Nucleation and Repassivation of Corrosion Pits for Pitting on Iron and Nickel.* Materials and Corrosion, 1976. **27**(11): p. 792-799.

16. Marcus, P. and J.M. Herbelin, *The entry of chloride ions into passive films on nickel studied by spectroscopic (ESCA) and nuclear (36Cl radiotracer) methods.* Corrosion Science, 1993. **34**(7): p. 1123-1145.

17. Bardwell, J.A., B. MacDougall, and G.I. Sproule, *Use of SIMS to Investigate the Induction Stage in the Pitting of Iron.* Journal of The Electrochemical Society, 1989. **136**(5): p. 1331-1336.

18. Urquidi, M. and D.D. Macdonald, *Solute‐Vacancy Interaction Model and the Effect of Minor Alloying Elements on the Initiation of Pitting Corrosion.* Journal of The Electrochemical Society, 1985. **132**(3): p. 555-558.

19. Macdonald, D.D., *The history of the Point Defect Model for the passive state: A brief review of film growth aspects.* Electrochimica Acta, 2011. **56**(4): p. 1761-1772.

20. Uhlig, H.H., *Adsorbed and Reaction‐Product Films on Metals.* Journal of The Electrochemical Society, 1950. **97**(11): p. 215C-220C.

21. Hoar, T.P. and W.R. Jacob, *Breakdown of Passivity of Stainless Steel by Halide Ions.* Nature, 1967. **216**: p. 1299.

22. Heusler, K.E. and L. Fischer, *Kinetics of Pit Initiation at Passive Iron.* Materials and Corrosion, 1976. **27**(8): p. 551-556.

23. Heusler, K.E. and L. Fischer, *Kinetics of Pit Initiation at the Alloy Fe5Cr.* Materials and Corrosion, 1976. **27**(11): p. 788-791.

24. Frankel, G.S., *Pitting Corrosion of Metals: A Review of the Critical Factors.* Journal of The Electrochemical Society, 1998. **145**(6): p. 2186-2198.

25. Sato, N., *A theory for breakdown of anodic oxide films on metals.* Electrochimica Acta, 1971. **16**(10): p. 1683-1692.

26. Sato, N., K. Kudo, and T. Noda, *The anodic oxide film on iron in neutral solution.* Electrochimica Acta, 1971. **16**(11): p. 1909-1921.

27. Yushu, W., et al., *Effect of Thiosulfate on Metastable Pitting of 304L and S32101 in Chloride- and Thiosulfate-Containing Environment.* Corrosion, 2016. **72**(5): p. 628-635.

28. Frankel, G.S., et al., *Metastable Pitting of Stainless Steel.* CORROSION, 1987. **43**(7): p. 429-436.

29. Pistorius, P.C. and G.T. Burstein, *Metastable pitting corrosion of stainless steel and the transition to stability.* Philosophical Transactions of the Royal Society of London. Series A: Physical and Engineering Sciences, 1992. **341**(1662): p. 531.

30. Zuo, Y., et al., *The effects of some anions on metastable pitting of 316L stainless steel.* Corrosion Science, 2002. **44**(1): p. 13-24.

31. Burstein, G.T. and P.C. Pistorius, *Surface Roughness and the Metastable Pitting of Stainless Steel in Chloride Solutions.* CORROSION, 1995. **51**(5): p. 380-385.

32. Galvele, J.R., *Transport Processes and the Mechanism of Pitting of Metals.* Journal of The Electrochemical Society, 1976. **123**(4): p. 464-474.

33. Suzuki, T., M. Yamabe, and Y. Kitamura, *Composition of Anolyte Within Pit Anode of Austenitic Stainless Steels in Chloride Solution.* CORROSION, 1973. **29**(1): p. 18-22.

34. Schwenk, W., *Theory Of Stainless Steel Pitting.* CORROSION, 1964. **20**(4): p. 129t-137t.

35. Ke, R. and R. Alkire, *Initiation of Corrosion Pits at Inclusions on 304 Stainless Steel.* Journal of The Electrochemical Society, 1995. **142**(12): p. 4056-4062.

36. Isaacs, H.S., *The Behavior of Resistive Layers in the Localized Corrosion of Stainless Steel.* Journal of The Electrochemical Society, 1973. **120**(11): p. 1456-1462.

37. Beck, T.R. and R.C. Alkire, *Occurrence of Salt Films during Initiation and Growth of Corrosion Pits.* Journal of The Electrochemical Society, 1979. **126**(10): p. 1662-1666.

38. Alkire, R.C. and K.P. Wong, *The corrosion of single pits on stainless steel in acidic chloride solution.* Corrosion Science, 1988. **28**(4): p. 411-421.

39. Wong, K.P. and R.C. Alkire, *Local Chemistry and Growth of Single Corrosion Pits in Aluminum.* Journal of The Electrochemical Society, 1990. **137**(10): p. 3010-3015.

40. Laycock, N.J. and R.C. Newman, *Localised dissolution kinetics, salt films and pitting potentials.* Corrosion Science, 1997. **39**(10): p. 1771-1790.

41. Horvath, J. and H.H. Uhlig, *Critical Potentials for Pitting Corrosion of Ni, Cr - Ni, Cr - Fe, and Related Stainless Steels.* Journal of The Electrochemical Society, 1968. **115**(8): p. 791-795.

42. Newman, R.C., *The dissolution and passivation kinetics of stainless alloys containing molybdenum—II. Dissolution kinetics in artificial pits.* Corrosion Science, 1985. **25**(5): p. 341-350.

43. Elbiache, A. and P. Marcus, *The role of molybdenum in the dissolution and the passivation of stainless steels with adsorbed sulphur.* Corrosion Science, 1992. **33**(2): p. 261-269.

44. Marcus, P. and M. Moscatelli, *The Role of Alloyed Molybdenum in the Dissolution and the Passivation of Nickel - Molybdenum Alloys in the Presence of Adsorbed Sulfur.* Journal of The Electrochemical Society, 1989. **136**(6): p. 1634-1637.

45. Betts, A.J. and R.C. Newman, *The effect of alloyed molybdenum on the activation of anodic dissolution by reduced sulphur compounds.* Corrosion Science, 1993. **34**(9): p. 1551-1555.

46. Newman, R.C. and T. Shahrabi, *The effect of alloyed nitrogen or dissolved nitrate ions on the anodic behaviour of austenitic stainless steel in hydrochloric acid.* Corrosion Science, 1987. **27**(8): p. 827-838.

47. Jargelius-Pettersson, R.f.a., *Electrochemical investigation of the influence of nitrogen alloying on pitting corrosion of austenitic stainless steels.* Corrosion Science, 1999. **41**(8): p. 1639-1664.

48. Pardo, A., et al., *Pitting corrosion behaviour of austenitic stainless steels – combining effects of Mn and Mo additions.* Corrosion Science, 2008. **50**(6): p. 1796-1806.

49. Atamert, S. and J.E. King, *Elemental partitioning and microstructural development in duplex stainless steel weld metal.* Acta Metallurgica et Materialia, 1991. **39**(3): p. 273-285.

50. Naghizadeh, M. and M.H. Moayed, *Investigation of the effect of solution annealing temperature on critical pitting temperature of 2205 duplex stainless steel by measuring pit solution chemistry.* Corrosion Science, 2015. **94**: p. 179-189.

51. Zhang, L., et al., *Influence of annealing treatment on the corrosion resistance of lean duplex stainless steel 2101.* Electrochimica Acta, 2009. **54**(23): p. 5387-5392.

52. Yang, Y., et al., *Effect of Annealing Temperature on the Pitting Corrosion Behavior of UNS S82441 Duplex Stainless Steel.* CORROSION, 2012. **69**(2): p. 167-173.

53. Zhang, Z., et al., *Microstructural evolution and pitting resistance of annealed lean duplex stainless steel UNS S32304.* Nuclear Engineering and Design, 2012. **243**: p. 56-62.

54. dos Santos, D.C. and R. Magnabosco, *Kinetic Study to Predict Sigma Phase Formation in Duplex Stainless Steels.* Metallurgical and Materials Transactions A, 2016. **47**(4): p. 1554-1565.

55. Michalska, J. and M. Sozańska, *Qualitative and quantitative analysis of σ and χ phases in 2205 duplex stainless steel.* Materials Characterization, 2006. **56**(4): p. 355-362.

56. Calliari, I., et al., *The phase stability in Cr–Ni and Cr–Mn duplex stainless steels.* Journal of Materials Science, 2011. **46**(21): p. 6916.

57. Bhattacharya, A. and P.M. Singh, *Effect of Heat Treatment on Corrosion and Stress Corrosion Cracking of S32205 Duplex Stainless Steel in Caustic Solution.* Metallurgical and Materials Transactions A, 2009. **40**(6): p. 1388-1399.

58. Wilms, M.E., et al., *The effect of σ-phase precipitation at 800°C on the corrosion resistance in sea-water of a high alloyed duplex stainless steel.* Corrosion Science, 1994. **36**(5): p. 871-881.

59. Maetz, J.-Y., et al., *Precipitation and Phase Transformations in 2101 Lean Duplex Stainless Steel During Isothermal Aging.* Metallurgical and Materials Transactions A, 2016. **47**(1): p. 239-253.

60. Deng, B., et al., *Effect of annealing treatment on microstructure evolution and the associated corrosion behavior of a super-duplex stainless steel.* Journal of Alloys and Compounds, 2010. **493**(1–2): p. 461-464.

61. Deng, B., et al., *Evaluation of localized corrosion in duplex stainless steel aged at 850 °C with critical pitting temperature measurement.* Electrochimica Acta, 2009. **54**(10): p. 2790-2794.

62. Zhang, L., et al., *Effect of aging on the corrosion resistance of 2101 lean duplex stainless steel.* Materials Characterization, 2009. **60**(12): p. 1522-1528.

63. Zhang, Z., et al., *Effect of isothermal aging on the pitting corrosion resistance of UNS S82441 duplex stainless steel based on electrochemical detection.* Corrosion Science, 2015. **93**: p. 120-125.

64. Bhattacharya, A. and P.M. Singh, *Role of Microstructure on the Corrosion Susceptibility of UNS S32101 Duplex Stainless Steel.* CORROSION, 2008. **64**(6): p. 532-540.

65. Bhattacharya, A. and P.M. Singh, *Stress Corrosion Cracking of Welded 2205 Duplex Stainless Steel in Sulfide-containing Caustic Solution.* Journal of Failure Analysis and Prevention, 2007. **7**(5): p. 371-377.

66. Badji, R., et al., *Phase transformation and mechanical behavior in annealed 2205 duplex stainless steel welds.* Materials Characterization, 2008. **59**(4): p. 447-453.

67. Muthupandi, V., et al., *Effect of weld metal chemistry and heat input on the structure and properties of duplex stainless steel welds.* Materials Science and Engineering: A, 2003. **358**(1): p. 9-16.

68. Leif, *Welding Duplex Stainless Steels — A Review Of Current Recommendations.* Welding in the World, 2012. **56**(5): p. 65-76.

69. Chen, T.H. and J.R. Yang, *Microstructural characterization of simulated heat affected zone in a nitrogen-containing 2205 duplex stainless steel.* Materials Science and Engineering: A, 2002. **338**(1): p. 166-181.

70. Liou, H.-Y., R.-I. Hsieh, and W.-T. Tsai, *Microstructure and pitting corrosion in simulated heat-affected zones of duplex stainless steels.* Materials Chemistry and Physics, 2002. **74**(1): p. 33-42.

71. Nelson, D.E., W.A. Baeslack, and J.C. Lippold, *Characterization of the weld structure in a duplex stainless steel using color metallography.* Metallography, 1985. **18**(3): p. 215-225.

72. Tzaneva, B.R., L.B. Fachikov, and R.G. Raicheff, *Effect of halide anions and temperature on initiation of pitting in Cr–Mn–N and Cr–Ni steels.* Corrosion Engineering, Science and Technology, 2006. **41**(1): p. 62-66.

73. Assaf, F.H., S.S. Abd El-Rehiem, and A.M. Zaky, *Pitting corrosion of zinc in neutral halide solutions.* Materials Chemistry and Physics, 1999. **58**(1): p. 58-63.

74. Leckie, H.P. and H.H. Uhlig, *Environmental Factors Affecting the Critical Potential for Pitting in 18–8 Stainless Steel.* Journal of The Electrochemical Society, 1966. **113**(12): p. 1262-1267.

75. Newman, R.C., H.S. Isaacs, and B. Alman, *Effects of Sulfur Compounds on the Pitting Behavior of Type 304 Stainless Steel in Near-Neutral Chloride Solutions.* Corrosion, 1982. **38**(5): p. 261-265.

76. Laitinen, T.M.J., *Comparison of Stainless Steels in Simulated Paper Machine Environments.* Corrosion, 1999. **55**(9): p. 858-869.

77. Duret-Thual, C., et al., *The role of thiosulfates in the pitting corrosion of Fe-17Cr alloys in neutral chloride solution: Electrochemical and XPS study.* Corrosion Science, 1997. **39**(5): p. 913-933.

78. Garner, A., *Thiosulfate Corrosion in Paper-Machine White Water.* Corrosion, 1985. **41**(10): p. 587-591.

79. Newman, R.C., *Pitting of Stainless Alloys in Sulfate Solutions Containing Thiosulfate Ions.* Corrosion, 1985. **41**(8): p. 450-453.

80. Newman, R.C., et al., *Pitting of Stainless Steels by Thiosulfate Ions.* Corrosion, 1989. **45**(4): p. 282-287.

81. Laycock, N.J., *Effects of Temperature and Thiosulfate on Chloride Pitting of Austenitic Stainless Steels.* Corrosion, 1999. **55**(6): p. 590-595.

82. Yushu, W. and M.S. Preet, *Corrosion Behavior of Austenitic and Duplex Stainless Steels in Thiosulfate- and Chloride-Containing Environments.* Corrosion, 2015. **71**(8): p. 937-944.

83. Nakhaie, D., et al., *Effect of Thiosulfate on Pitting Corrosion of 316SS: II. Metastable Pitting and Transition to Stability.* Journal of The Electrochemical Society, 2015. **162**(4): p. C121-C127.

84. Choudhary, L., D.D. Macdonald, and A. Alfantazi, *Role of Thiosulfate in the Corrosion of Steels: A Review.* CORROSION, 2015. **71**(9): p. 1147-1168.

85. Pistorius, P.C. and G.T. Burstein, *Growth of corrosion pits on stainless steel in chloride solution containing dilute sulphate.* Corrosion Science, 1992. **33**(12): p. 1885-1897.

86. Ernst, P. and R.C. Newman, *Pit growth studies in stainless steel foils. II. Effect of temperature, chloride concentration and sulphate addition.* Corrosion Science, 2002. **44**(5): p. 943-954.

87. Rosenfeld, I.L. and I.S. Danilov, *Electrochemical aspects of pitting corrosion.* Corrosion Science, 1967. **7**(3): p. 129-142.

88. Sugimoto, K. and Y. Sawada, *The Role of Alloyed Molybdenum in Austenitic Stainless Steels in the Inhibition of Pitting in Neutral Halide Solutions.* CORROSION, 1976. **32**(9): p. 347-352.

89. Ürgen, M. and A.F. Çakir, *The effect of molybdate ions on the temperature dependent pitting potential of austenitic stainless steels in neutral chloride solutions.* Corrosion Science, 1991. **32**(8): p. 835-852.

90. Ruijini, G. and M.B. Ives, *The Influence of Addition of Molybdate Ions on Pit Growth in UNS S30100 Stainless Steel in Chloride Solution.* CORROSION, 1989. **45**(7): p. 572-574.

91. Moser, R.D., et al., *Chloride-induced corrosion resistance of high-strength stainless steels in simulated alkaline and carbonated concrete pore solutions.* Corrosion Science, 2012. **57**(Supplement C): p. 241-253.

92. He, L., P.M. Singh, and Y. Wang, *Pitting Behavior of Lean Duplex Stainless Steels in Thiosulfate-Containing Paper Machine Environments*, in *CORROSION 2017*. 2017, NACE International: New Orleans, Louisiana, USA. p. 8.

93. Ruel, F., et al., *On the Depassivation Mechanism of Lean Duplex Stainless Steels and the Influence of the Partitioning of the Alloying Elements.* CORROSION, 2014. **70**(6): p. 636-642.

94. Tsai, W.-T. and J.-R. Chen, *Galvanic corrosion between the constituent phases in duplex stainless steel.* Corrosion Science, 2007. **49**(9): p. 3659-3668.

95. Lo, I.H., et al., *Effect of electrolyte composition on the active-to-passive transition behavior of 2205 duplex stainless steel in H2SO4/HCl solutions.* Corrosion Science, 2006. **48**(3): p. 696-708.

96. Corrosion, J.J.A.N.C.o., *Standard Terminology and Acronyms Relating to Corrosion*. 2012.

97. Hack, H.P., *Galvanic Corrosion*, in *Reference Module in Materials Science and Materials Engineering*. 2016, Elsevier.

98. Mathieu, S., et al., *A corrosion study of the main constituent phases of AZ91 magnesium alloys.* Corrosion Science, 2003. **45**(12): p. 2741-2755.

99. Lee, J.-S., et al., *Corrosion behaviour of ferrite and austenite phases on super duplex stainless steel in a modified green-death solution.* Corrosion Science, 2014. **89**: p. 111-117.

100. Lee, J.-S., S.-H. Jeon, and Y.-S. Park, *Effects of Solution Annealing Temperature on the Galvanic Corrosion Behavior of the Super Duplex Stainless Steels.* Journal of Materials Engineering and Performance, 2013. **22**(2): p. 557-562.

101. Wang, Y., X. Cheng, and X. Li, *Electrochemical behavior and compositions of passive films formed on the constituent phases of duplex stainless steel without coupling.* Electrochemistry Communications, 2015. **57**: p. 56-60.

102. J .V. Pellegrino, H.H.S., J. D. Fritz, H. S. Ahluwalia, *Duplex Stainless Steel Atlas of Microstructures*. Vol. 2. 2014: Materials Technology Institute, Inc. 159.

103. Zanotto, F., et al., *Stress corrosion cracking of LDX 2101® duplex stainless steel in chloride solutions in the presence of thiosulphate.* Corrosion Science, 2014. **80**: p. 205-212.

104. Garfias-Mesias, L.F., J.M. Sykes, and C.D.S. Tuck, *The effect of phase compositions on the pitting corrosion of 25 Cr duplex stainless steel in chloride solutions.* Corrosion Science, 1996. **38**(8): p. 1319-1330.

105. Tan, H., et al., *Effect of annealing temperature on the pitting corrosion resistance of super duplex stainless steel UNS S32750.* Materials Characterization, 2009. **60**(9): p. 1049-1054.

106. Sieurin, H. and R. Sandström, *Sigma phase precipitation in duplex stainless steel 2205.* Materials Science and Engineering: A, 2007. **444**(1): p. 271-276.

107. Park, C.J., V.S. Rao, and H.S. Kwon, *Effects of Sigma Phase on the Initiation and Propagation of Pitting Corrosion of Duplex Stainless Steel.* CORROSION, 2005. **61**(1): p. 76-83.

108. Ravindranath, K. and S.N. Malhotra, *The influence of aging on the intergranular corrosion of 22 chromium-5 nickel duplex stainless steel.* Corrosion Science, 1995. **37**(1): p. 121-132.

109. Deng, B., et al., *Effect of thermal cycles on the corrosion and mechanical properties of UNS S31803 duplex stainless steel.* Corrosion Science, 2009. **51**(12): p. 2969-2975.

110. Deng, B., et al., *Evaluation of localized corrosion in duplex stainless steel aged at 850°C with critical pitting temperature measurement.* Electrochimica Acta, 2009. **54**(10): p. 2790-2794.

111. Wei, Z., et al., *Effect of ageing on precipitation and impact energy of 2101 economical duplex stainless steel.* Materials Characterization, 2009. **60**(1): p. 50-55.

112. Pezzato, L., et al., *Effect of the Heat Treatment on the Corrosion Resistance of Duplex Stainless Steels.* Journal of Materials Engineering and Performance, 2018. **27**(8): p. 3859-3868.

113. Calliari, I., et al., *New Lean Duplex Stainless Steels for Structural Applications.* Materials Science Forum, 2009. **604-605**: p. 419-426.

114. Chen, T.H., K.L. Weng, and J.R. Yang, *The effect of high-temperature exposure on the microstructural stability and toughness property in a 2205 duplex stainless steel.* Materials Science and Engineering: A, 2002. **338**(1): p. 259-270.

115. Melo, E.A. and R. Magnabosco, *Influence of the Heterogeneous Nucleation Sites on the Kinetics of Intermetallic Phase Formation in Aged Duplex Stainless Steel.* Metallurgical and Materials Transactions A, 2017. **48**(11): p. 5273-5284.

116. *NIST X-ray Photoelectron Spectroscopy Database*. National Institute of Standards and Technology: Gaithersburg MD.

117. Bhattacharya, A. and P.M. Singh, *Electrochemical behaviour of duplex stainless steels in caustic environment.* Corrosion Science, 2011. **53**(1): p. 71-81.